NETWORK OF NANOSCIENCES, MICRO NANOTECHNOLOGY
OF THE NATIONAL POLYTECHNIC INSTITUTE

(Volumen IV)

RESEARCH ADVANCES IN

NANOSCIENCES, MICRO AND NANOTECHNOLOGIES

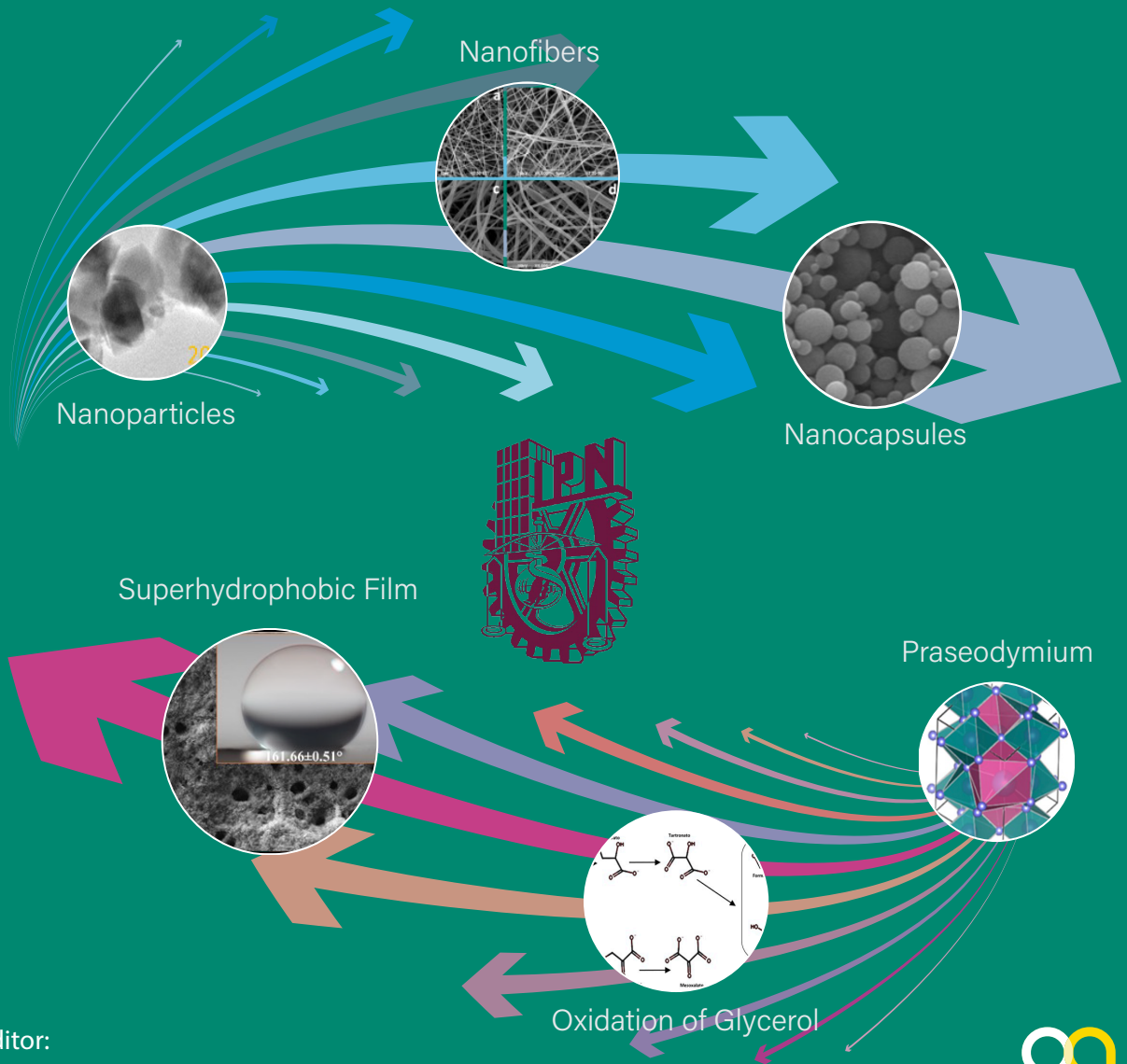

Editor:
Eduardo San Martín Martínez

open access

Research advances in nanosciences, micro and nanotechnologies

Volume 4

Editor

Eduardo San Martín Martínez Ph. D. •

Coordinator of the Nanoscience and Micro Nanotechnology Network

OmniaScience

España

Research advances in nanosciences, micro and nanotechnologies. Volume IV

Editor: Eduardo San Martin Martinez, PhD.

ISBN: 978-84-126475-2-5
DOI: https://doi.org/10.3926/oms.413

OmniaScience

Design cover: OmniaScience
Image cover: Eduardo Esteban San Martin Cordova, 2023

EDITORIAL COMMITTEE

HEALTH AREA

ENERGY AREA

FOOD AREA

Dr. José Abraham Balderas López
Interdisciplinary Professional Unit of Biotechnology, National Polytechnic Institute

Dr. Jorge Yáñez Fernández Unidad Profesional
Interdisciplinary Professional Unit of Biotechnology, National Polytechnic Institute

ENVIRONMENT AREA

Dr. Ricardo Cuenca Álvarez
Technological Research and Innovation Center, National Polytechnic Institute

Dra. Mónica de la Luz Corea Téllez
Higher School of Chemical Engineering and Extractive Industries, National Polytechnic Institute

Book editing secretarial support **Lic. Jocelyn Lissette Aguilar Bustamante**
Analyst of the Nanoscience and Micro Nanotechnology Network CORIyP - IPN

INDEX

FOOD AREA

ENERGY AREA

FOREWORD

What is nano? For an ordinary person, this is something quite small, minuscule, out of our perception… but it seems possible to imagine right now thanks to science-fiction movies. Nevertheless, to comprehend this, it is necessary to talk about nanoscale, which is a way of measuring things whose length is of the order of a few nanometers, being a nanometer a one billionth part of a meter. This is not a different world, it is just our world observed with a different point of view (and some different rules, of course), allowing us to understand how this world is built, and how we can rebuild it -and rebuild us- to improve it. Something similar happened before in 1667 when Leeuwenhoek reported the first detailed description of protists and bacteria living in the previously unknown microcosmos.

For the **Instituto Politécnico Nacional** of Mexico, the **Nanoscience and Micro Nanotechnology Network** (NMN Network) has a relevant role in the study and development of this kind of technology, which is intended to become a major element of our national industry in the next years. The **NMN Network** has as its main objectives to conduct basic and applied research in nanotechnology and nanoscience as well as to promote the training of postgraduate students of the highest level who will join the industry in the very near future.

The book **Research Advances in Nanosciences, Micro and Nanotechnologies Volume IV** compiles the latest scientific works developed by the members of the **NMN network**, covering multiple applications in different branches of science. Like its predecessors, the book's contributions stand out for in the originality and the scientific rigor with which various topics are addressed from the perspective of nanosciences and nanotechnology. Throughout several

chapters, the authors deal with distinct items where nanotechnology can offer new insight into the possible solutions to some unsolved problems like cancer, food quality, and conservation, energy conversion, generation of hydrogen, mechanical improvement of materials, etc.

The book is organized in five great areas: Health; Food; Energy; Environment; and Semiconductors and Materials.

In the first section, referred to as the **Health Area**, four topics are dealt with: the effect of particle size and polydispersity index on the design of the nanostructured lipid carriers for cancer treatment; the design of nanomaterials to improve the mammography images for a breast cancer diagnosis; the thermal study of nanocomposites seeking its application in medical studies; and the numerical simulation of biosensors and microfluidics.

In the second section, addressed to the **Food Area**, the authors develop three topics: for the first one, they studied the influence of the addition of organic compounds in obtaining gelatin nano-fibers; in the second, they analyzed the effects of nano-coatings on tomato quality during storage; the third topic concerns the effectivity of nano-encapsulation of riboflavin in biodegradable polymeric matrices when they use nano-spray drying.

Concerning the **Energy Area**, other members of the NMN Network have focused in four different items: the use of metal nanoparticles for energy conversion based on glycerol electroxidation; the exploration of water oxidation reaction through the incorporation of iron blocks into laminar hydroxides of iron and nickel; the evaluation of the structural properties of the solid state of fuel cells; and the hydrogen's photocatalytic generation using titanium and bismuth oxides.

The fourth section: **Environment**, is a unique chapter that focuses on studying the influence of the chemical structure of organic compounds in organogel formation for the removal of organic solvents.

Finally, the last section is dedicated to **Semiconductors and Materials**, with two chapters: the first one studies the reliability of flexible amorphous In-Ga-Zn-O (a-IGZO) thin-film transistors, while the second chapter shows an evaluation of the mechanical stability of the superhydrophobic nano-coating for buildings materials application.

I am sure that the contributions of this book, made by polytechnical researchers of the highest level, will be added to the host of solutions that are being developed worldwide to solve some of the major problems that afflict human beings with a different vision, but also to open the way for new investigations into unsuspected nano cosmos that we still do not know, but that has undoubtedly always been there.

We hope you enjoy reading.

Dr. Norberto Domínguez Ramírez
Coordinador de Operación y Redes de Investigación y Posgrado
Secretaría de Investigación y Posgrado Instituto Politécnico Nacional

Chapter 1 Health Area

NANOSTRUCTURED LIPID CARRIERS FOR CANCER TREATMENT: EFFECT OF PROCESS PARAMETERS ON PARTICLE SIZE AND POLYDISPERSITY INDEX USING EXPERIMENTAL DESIGN

Cándido Gómez Lara*, Mónica Rosalía Jaime Fonseca, Rocio Guadalupe Casañas Pimentel*

Instituto Politécnico Nacional, Centro de Investigación en Ciencia Aplicada y Tecnología Avanzada. Legaria 694, Irrigación, Miguel Hidalgo, CDMX, C. P. 11500, México

cgomezl1000@alumno.ipn.mx; rcasanas@ipn.mx

Gómez Lara, C., Jaime Fonseca, M. R., & Casañas Pimentel, R. G. (2023). Nanostructured lipid carriers for cancer treatment: effect of process parameters on particle size and polydispersity index using experimental design. In E. San Martín-Martínez (Ed.). *Research advances in nanosciences, micro and nanotechnologies. Volume IV* (pp. 15-52). Barcelona, Spain: Omniascience.

Abstract

Cancer is a global health problem with high incidence and mortality rates, to address this problem various strategies are being developed. The use of nanosystems for the targeted delivery of anticancer drugs used in chemotherapy is a strategy that has attracted a lot of attention because it promises to improve the efficacy of cancer treatment and reduce side effects, which may have a significant impact on the reduction in cancer mortality.

In the design of anticancer drug delivery nanosystems, aspects such as the size of the particles, the chemistry of their surface, the specificity with which they release the drug at the tumor site and the drug loading capacity, are fundamental to predict the treatment success. Understanding the effect of process parameters that determine the size and stability of drug delivery nanosystems is a major work.

Within drug delivery nanosystems, lipid-based systems have achieved wide success in their clinical application. Lipid particles include micelles, liposomes, solid lipid nanoparticles, and nanostructured lipid carriers. The latter are relevant because they provide greater stability and loading capacity of the drugs than the former.

Therefore, in this work a statistical study was developed to identify the significant variables that affect the size and the polydispersity index, seeking to obtain the conditions to develop nanostructured lipid carriers with small sizes and narrow size distributions. A robust analysis was performed using experimental designs, to provide a basis for the development of these nanosystems with specific sizes (less than 100 nm) with the aim of increase the particle penetration and drug accumulation in the tumor zone for future applications in anticancer drug delivery.

Keywords: cancer, nanostructured lipid carriers, experimental design.

1. Introduction

In the last century, cancer has significantly contributed to the decrease in life expectancy and represents the main cause of death in most countries [1, 2]. Cancer is one of the most important global health problems, in fact, the World Health Organization (WHO) in 2020 indicated that 18.8 million new cases were diagnosed, and 8.97 million deaths associated with this disease were reported [3 – 5]. Cancer, which is the name given to a group of diseases that share similar features, where the main characteristic is abnormal and uncontrolled growth of cells, can occur in almost any type of tissue. There are known more than 100 types of cancers [3]. Breast cancer and lung cancer are the main cause of death in women and men, respectively. A statistical study published in 2021 showed that of the 9.2 million cases of cancer in women (which includes all types) 24.5 % occur in the breast. A worldwide increase in cancer patients is expected in the next 50 years and an incidence of more than 34 million cancer cases is predicted for 2070 [2]. Researchers around the world have been working hard to protect humanity from numerous diseases [6, 7]. Although the advances in medicine have been significant in the last decade and have led to the improvement of existing treatments and the development of new strategies against cancer such as; targeted therapy [8 – 10], chemoradiation [8], vaccine therapies [8], immunotherapy [7, 9, 11, 12], fecal microbiota transplantation [13], archaeal-derived biological nanocarriers [14], infrasound [15], microbiome-associated therapy and host-host relationship [16], RNA (siRNA, miRNA) therapy [17, 18], bacteria-based cancer therapy (BBCT) [19] and cancer treatments based on hyperthermia [20], the administration of free chemotherapeutic drugs is the most widely used therapeutic alternative for the treatment of cancer.

Chemotherapy still shows inherent problems, for example, some drugs have very low solubility due to their bulky polycyclic nature (paclitaxel, etoposide, and docetaxel), which prevents them from hydrogen bonding with water [21, 22]. The poor solubility of drugs limits their bioavailability and reduces the efficacy of cytotoxic treatments. On the other hand, some molecules used as chemotherapeutics are unstable in the gastrointestinal tract and have very low permeability through the intestinal epithelium [22, 23] making them not viable for oral administration. New drugs under development such as 4-(N)-docosahexaenol 2',2'difluorodesoxycytidine show strong antitumor activity *in vitro* and *in vivo* in aggressive cancer models (e.g., pancreatic cancer, breast cancer, lung

cancer, and leukemia), but its clinical application has been limited due to its high instability in the intestine when it is administered in its free form [23, 24].

Similarly, Taxol® (paclitaxel) and Adriamycin® (doxorubicin) are drugs that have required chemical modifications to increase their solubility in water in order to be administered in therapeutic doses [22, 25]. Cancer treatments based on these drugs are not specific and generate side effects [26]. Sustained administration of paclitaxel may cause severe hypersensitivity [27, 28], immunosuppression-related bacterial infections [29], neurotoxicity, haematological cytotoxicity (mainly decreased blood neutrophil count) [30], myalgia [28, 31] and cardiac toxicity. In addition, prolonged use of chemotherapeutic agents can lead to multidrug resistance (MDR), which can greatly compromise treatment success [2, 32].

Alternative strategies for targeting drugs that avoid side effects are necessary. In this area, nanotechnology has been explored for anticancer drug delivery to the tumor site. Nanotechnology is the name given to the sum of those technologies applied in different areas of science and engineering that allow changing the properties and characteristics of materials at molecular and atomic levels [33, 34]. The sizes considered in nanotechnology should be 1–100 nm. These sizes give materials unique properties (optical, electrical, magnetic, etc.) that can be used in fields such as electronics and medicine [35, 36]. In general terms, nanomedicine can be defined as the branch of medicine that makes use of the knowledge and tools of nanotechnology for the prevention, diagnosis, delivery of drugs, repair, and regeneration of biological systems, as well as the monitoring and treatment of diseases through imaging technologies [37 – 40].

Based on their shape, nanomaterials can be classified as 0D (fullerenes, nanowires), 1D (nanotubes, carbon nanofibers), 2D (graphene, nanofilms) and 3D (nanostructured materials, nanocarriers) [41 – 44].

In nanomedicine, chemotherapy drugs are delivered into the body using 3D structures known as nanocarriers. Nanocarriers are used for the encapsulation, transport and targeting of drugs towards the tumor site [38]. Nanocarriers are synthesized from a large number of organic or inorganic precursors, the most popular are: polymeric nanoparticles, lipid nanoparticles (LNPs), hybrid polymer/lipid nanoparticles, carbon nanomaterials, among others [40, 44].

Lipids are amphipathic biomolecules, generally insoluble in water, non-toxic, biocompatible and biodegradable [45 – 47]. Thus, lipid-based nanocarriers have

been widely applied in nanomedicine; particularly, LNPs offer great potential for drug targeting. LNPs include a set of different spherical structures that surround an internal aqueous compartment. In recent years, two groups of LNPs with great therapeutic potential have been developed by combining advantageous properties [47], these are solid lipid nanoparticles (SLNs) and nanostructured lipid carriers (NLCs) (Figure 1) [48, 49].

SLNs and NLCs are composed of a lipid that is solid at room temperature or a mixture of lipids (solid and liquid) respectively (Figure 1). These nanoparticles generally undergo safe biodegradation [50]. The molecules that make up SLNs and NLCs have minimal influence on the extracellular and intracellular environment due to their chemical and physical similarity to the cell membrane components. These molecules also allow a controlled release of biological compounds [49]. SLNs and NLCs have a low average size (according to the method of synthesis) which allows them to simply flow in the blood avoiding uptake by the reticuloendothelial system (RES). SLNs and NLCs can be modified with various targeting molecules, including peptides, growth factors, aptamers, antibodies, and other small molecules that help them to increase their specificity towards cancer cells [48].

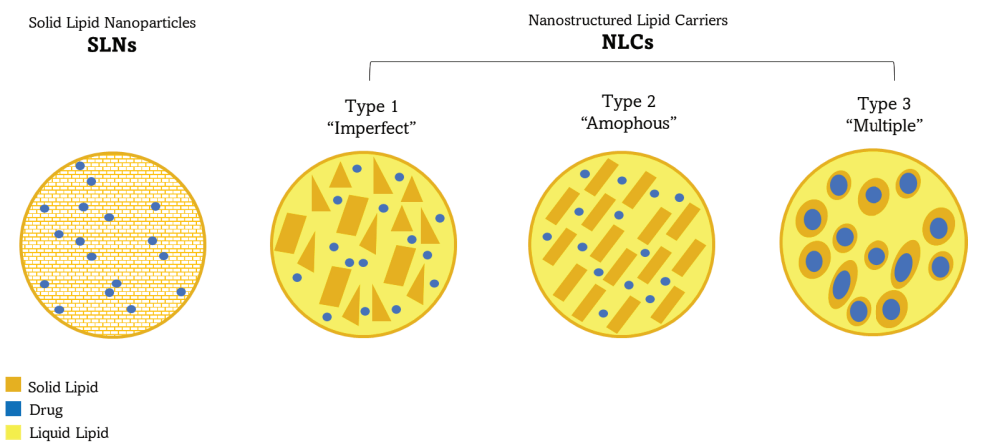

Figure 1. A schematic illustration of Solid Lipid Nanoparticles (SLNs) and Nanostructured Lipid Carriers (NLCs).

SLNs have the potential to be exploited as drug delivery systems, however, they present a drawback: the crystallinity of the matrix formed within them, caused by the perfect ordering of a single solid lipid, affects the entrapment capacity of the drug, and the chemotherapeutic agent internalized within the matrix

can become expelled from the nanoparticle quickly [49, 50]. As an alternative to SLNs, NLCs were developed; the presence of liquid lipids in the NLCs results in a non-perfect and amorphous network [46 – 51], given the presence of a liquid phase and the disordered structure, there is greater accumulation of the drug in the particle and the encapsulation and load capacity are improved [51].

The lipid mixture, the aqueous phase and the emulsifying agent constitute the main components in the synthesis of NLCs [52]. Low costs, low toxicity and sterilization capacity prior to its medical application are the main properties that materials must have for their use in the manufacture of nanocarriers. In general, the selection of lipids depends on their physiological tolerance, the structure, the solubility of the drug and the miscibility between the mixture of lipids. For the selection of lipids, it must first be considered that these are in the category of molecules generally recognized as safe (GRAS) [53], that is, that they do not produce toxic effects in the concentration employed. In addition, it is imperative to determine the solubility of the drug in the lipid mixture [54]. Triglycerides [55, 56], steroids (cholesterol) [57], waxes [52] and fatty acids [56], among others [58] are lipids commonly used to obtain NLCs.

Surfactants are chemical agents that reduce the surface tension between the lipid phase (organic phase) and the aqueous phase during the production of nanoparticles. These molecules are used as single agents or as mixtures and help to stabilize the lipid dispersion in the aqueous phase. [57, 59]. Some examples of surfactants widely used for lipid nanoparticles formulation include pluronic F68 (poloxamer 188), polysorbates (Tween), polyvinyl alcohol, and sodium deoxycholate (hydrophilic surfactants used in the synthesis of LNPs) [60].

In the last two decades, various techniques have been developed for the synthesis of NLCs, including: high-pressure homogenization (hot and cold) [61, 62], solvent diffusion [63], solvent emulsification-evaporation [64], emulsification sonication [65], microemulsion [66] and solvent injection [67]. The solvent injection method has been useful and more widely used, due to its easy handling and fast production speed, in addition to not requiring sophisticated or robust equipment during the process [52]. Using this technique, it has been possible to obtain particles of 64.00–440 nm [68 – 70]. However, there is not a complex study that analyzes the effect of the factors that influence the synthesis of NLCs to predict the particle size (PS) and obtain different particle sizes with the same composition and synthesis method.

The therapeutic effect of NLCs and nanoparticles in general is closely related to their composition, size, surface charge, and route of administration [21 – 23]. Initially, the design of nanodrugs was based on the enhanced permeability and retention effect (EPR) [71]. The EPR indicates that, in solid tumors, there is a formation of amorphous blood vessels with high permeability of plasmatic components due to the uncontrolled cell growth and the high nutrients demand; this, together with the poor drainage of waste components by the lymphatic system, allows that nanoparticles can easily leak through the capillary openings and reach the tumor stroma; so that, they can accumulate at the tumor site passively [72].

NLCs are highly relevant, and since 2017 more than 200 articles on this subject are published in PubMed annually [73]. The significant increase in the use of these nanoparticles suggests the great potential of NLCs for the treatment of cancer [74 – 79]. Despite the large number of publications, few pharmacological developments based on NLCs are in the final stage of clinical studies for application in humans, in most of them the particle sizes are >100 nm [68 – 70]. For large PS, the passive diffusion process established by the EPR is not the mechanism that promotes the accumulation of particles at the tumor site and other processes such as extravasation and active diffusion (which requires energy expenditure) [80] could be more relevant to enhance the accumulation of nanoparticles at the tumor site. Multiple physiological barriers [22] are involved from the administration of the nanodrug in the bloodstream to its internalization in the cancer cell.

As previously mentioned, the chemical composition and PS are factors that influence the accumulation of nanoparticles at the tumor site. It is still necessary to study the behavior of particles with sizes <100 nm, since most of the investigations focus on PS >100 nm, where the EPR effect has no relevance for the accumulation of NLCs [73 – 79]. To obtain small nanoparticles, which may be useful for the study of accumulation in tumors, the DoE Design of Experiments turns out to be a powerful tool for optimizing the synthesis process evaluating multiple factors [81]. DoE is a structured and organized method to determine the relationships between the factors that affect a process and its output [82]. The use of an experimental design will make it possible to obtain a useful model consciously and accurately for the formulation of particles <100 nm, which can be evaluated in vitro and in vivo with passive accumulation in the tumor site.

2. Materials and methods

2.1. *Materials*

The lipid mixture of the organic phase is composed of 18-carbon phospholipids, stearic acid and oleic acid (Figure 2). Stearic acid (C18, 93661C18H3602 MW:284.48 g/mol, Tm 71 °C, 97 % purity) and oleic acid (C18, 453036/1 12803315, C18H3402, MW:282.47, ρ=0.89 g/mL) were purchased from FlukaTM. Ethanol was used as solvent in the organic phase. Polysorbate 80/ Tween 80 (Hycel 9005-65-6) was used as surfactant. The aqueous phase use PBS phosphate buffer solution as solvent.

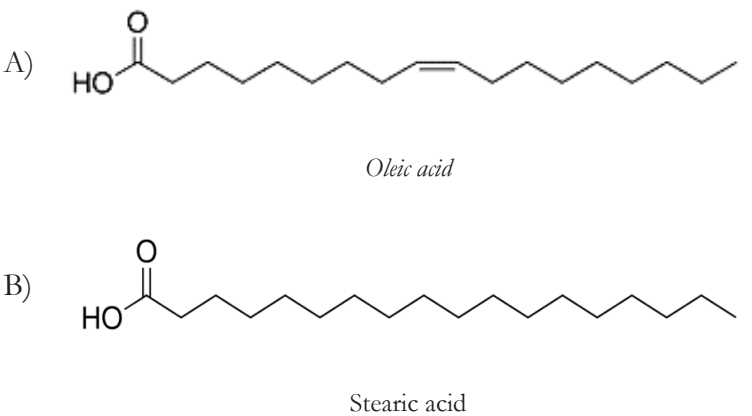

Figure 2. Chemical structure of the lipids used for the synthesis of NLCs. A) Liquid lipid (oleic acid) and B) Solid lipid (stearic acid).

2.2. *Synthesis of NLCs by solvent injection*

To obtain the NLCs, the solvent injection method, reported by Scubert *et al.* was used (Figure 3) [67], with some modifications. This method employs two phases, organic phase (lipid mixture in ethanol) and aqueous phase (surfactant in PBS).

The organic phase was prepared by heating ethanol (solvent) to 70 °C with indirect heat, stearic acid was added to the hot solvent and stirred for 15 min avoiding evaporation. The oleic acid was integrated when the solid lipid was completely dissolved, and it was kept stirring for 30 min. The aqueous phase was prepared by dissolving the necessary amount of surfactant in PBS phosphate

buffer (pH adjusted) at 40 °C and kept warm until synthesis. For the synthesis, the organic phase was rapidly injected into the aqueous phase under high agitation and at high temperature, using a syringe. Subsequently, the nanoparticles were kept stirring (5-15 min). The resulting suspension was sonicated at 70 % power, 45 kHz, for 15 min at 45 °C. The nanoparticle solution was kept at 25 °C for storage.

2.3. *Measurement of particle size and polydispersity index*

Particle size (PS) and polydispersity index (PDI) determination was performed by dynamic light scattering, using a Zetasizer Nano ZS series equipment (Malvern Instruments, USA), after appropriate dilution with PBS. The sample volume was constant (i.e. 1 mL).

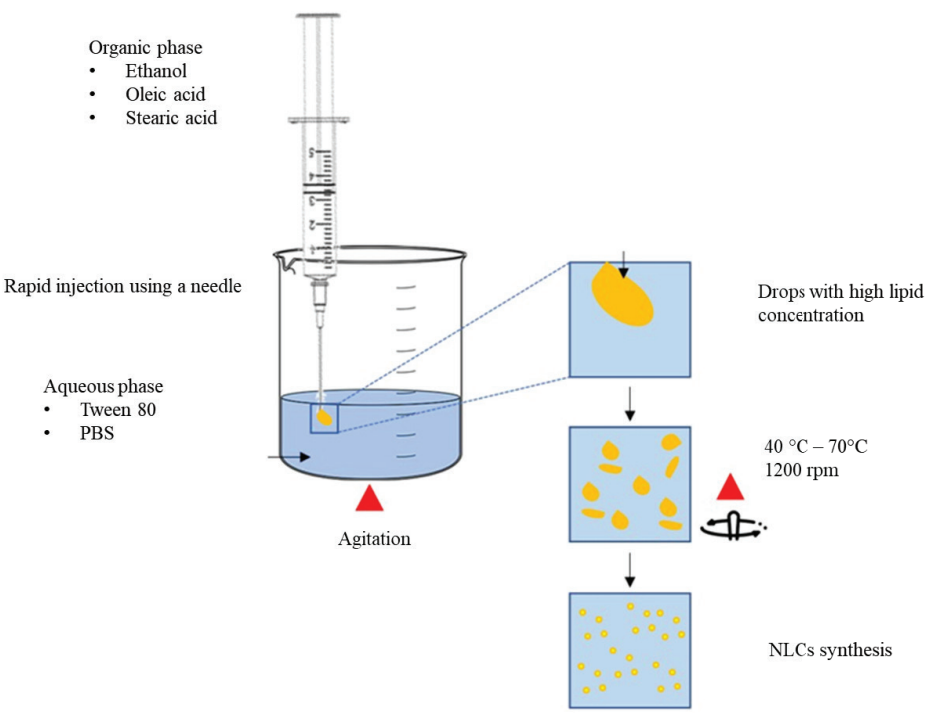

Figure 3. Solvent Injection Method. Obtaining NLCs by injecting a mixture of lipids at high speed in an aqueous phase at high temperature and stirring.

2.4. *Design of Experiments (DoE)*

As previously mentioned, DOE is an appropriate tool for the identification and optimization of critical parameters that interfere in a process [58]. For the selection, evaluation, screening, and optimization of the critical factors during the NLC synthesis, a structured study was carried out as shown in Figura4. First, the design factors were identified using a single factor design. A second step using a screening design allowed irrelevant factors to be discarded during the synthesis process. Subsequently, a full factorial 2^3 design was useful to identify the presence of curvature in the process. Afterwards, a Box-Behnken quadratic model was carried out for the optimization of the process and obtaining a mathematical model for the prediction of the PS and PDI (when the values of the optimized variables were modified). All statistical analysis were performed using Design expert 11 software.

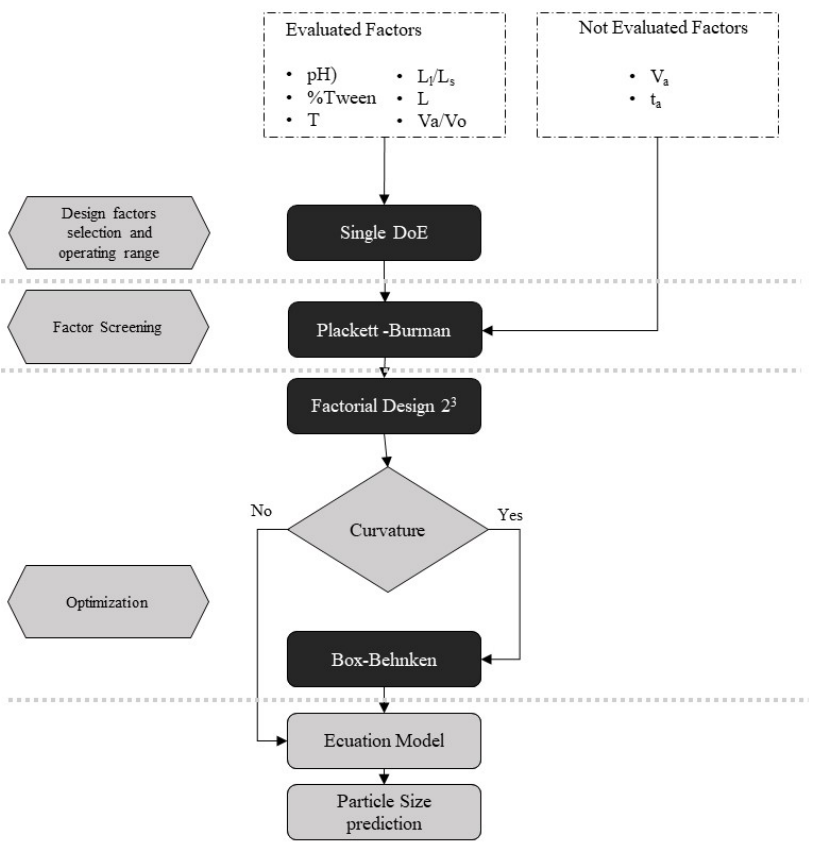

Figure 4. Flow diagram of DoE for the optimization of PS and PDI in obtaining NLCs using the solvent injection method.

2.5. *Selection of factors and operating ranges*

The operating ranges of the design factors were selected based on the effect on PS and PDI, using a single factor experimental design. The variables analyzed were the pH of the aqueous phase (pH), percentage v/v of surfactant (%tween 80), synthesis temperature (T), ratio of liquid lipid/solid lipid in the organic phase (L_l/L_s), total lipid concentration (L) and percentage of the organic phase in the final volume of synthesis (%V_o). The stirring speed (v_a) and stirring time (t_a) during the synthesis were not analyzed in this first phase of the study.

The evaluation of the pH effect was carried out by adjusting the pH of the buffer solution in the range of 3-11 using NaOH and 1.0 M HCl. The synthesis of NLCs was carried out in a range of 30-70 °C for the assessment of the influence of the temperature on the PS and PDI.

Different solutions (Table 1) for %V_o were prepared for the estimation of this factor on the PS and PDI.

Different concentrations of total lipids were evaluated (15, 20, 25, 30 and 35 mg/mL) during the preparation of the nanoparticles. To study the influence of surfactant concentration, different levels of Tween 80 in the aqueous phase were studied: 2 %, 3 %, 4 % and 5 %. It has been observed in previous works that a higher proportion of liquid lipid in the lipid mixture improves the stability of the NLCs [78, 83-86]. To evaluate this factor, the organic phase was prepared with a final concentration

Table 1. Experimental design for the evaluation of the effect of V_o (%) in the synthesis of NLCs.

Organic phase percentage (V_o %)		10 %	20 %	30 %	40 %	50 %
Organic phase						
	Ethanol (mL)	2.50	5.00	7.50	10.00	12.50
	Oleic acid (μL)	22.50	22.50	22.50	22.50	22.50
	Stearic acid (mg)	30.00	30.00	30.00	30.00	30.00
Aqueous phase						
	PBS (mL)	22.50	20.00	17.50	15.00	12.50
	Tween 80 (mL)	1.00	1.00	1.00	1.00	1.00

of total lipids equal to 20 mg/mL, making variations of the proportion of oleic acid from 30 % to 70 %. When one factor was analyzed, the remaining factors were kept constant as indicated below pH=3, %Tween 80=3 %, T=40 °C, L_l/L_s=70 %, L=20 mg/mL, $\%V_o$= 10 %, v_a 1200 rpm and t_a 10 min.

2.6. *Screening of significant variables by Plackett-Burman design of experiments*

Plackett-Burman is a screening design that evaluates and discards irrelevant experimental factors with a minimum of formulations and experimental runs during process optimization [87]. This step is important to eliminate factors that do not significantly affect the response variables. An experimental design of Filtered Plackett-Burman was proposed (Table 2) for the evaluation of the most significant variables during the synthesis of NLCs. Here, the proportion of oleic acid in the lipid mixture (L_l/L_s=70 %) and the percentage of the organic phase ($\%V_o$=10 %) were kept constant in all the experimental runs. Design factors and operating levels are shown in Table 3.

Table 2. Plackett-Burman experimental design runs for screening the significant independent variables affecting PS and PDI during NLCs synthesis.

Run	%tween	L	pH	T	v_a	t	PS	PDI
	(%)	(mg/mL)	-	(°C)	(rpm)	(min)	(nm)	-
1	4	25	3	70	1200	10	18.63	0.185
2	2	25	6	40	1200	10	84.69	0.207
3	4	15	6	70	800	10	11.19	0.158
4	2	25	3	70	1200	5	197.17	0.601
5	2	15	6	40	1200	10	11.01	0.225
6	2	15	3	70	800	10	20.15	0.183
7	4	15	3	40	1200	5	14.35	0.115
8	4	25	3	40	800	10	18.00	0.159
9	4	25	6	40	800	5	14.70	0.266
10	2	25	6	70	800	5	61.82	0.202
11	4	15	6	70	1200	5	12.10	0.163
12	2	15	3	40	800	5	127.17	1.000
13	3	20	4.5	55	1000	7.5	15.45	0.146
14	3	20	4.5	55	1000	7.5	18.18	0.178

Table 3. Level of independent factors selected in Placket-Burman design for screening independent variables.

Factor	Levels	
	(-1)	(1)
% Tween	2	4
L (mg/mL)	15	24
pH	3	6
T (°C)	40	70
v_a (rpm)	800	1200
t (min)	5	10

2.7. *Factorial design*

After discrimination of non-significant variables, the concentration of total lipids (L), concentration of surfactant (% tween 80) and pH of the aqueous solution (pH) were selected for a 2^3 factorial design. The effects of the factors were examined at two levels (+1 and -1) as shown in Table 4. The values of the levels were selected based on the results of the previous analysis (Plackett-Burman). For the experimental design process, nine different formulations were prepared and carried out in triplicate (27 runs) (Table 5). Statistical analysis was performed with Design Expert 11 software. For this design, the following factors were kept constant as indicated: pH=6, T=70 °C, L_l/L_s=70 %, $\%V_o$=10 % and v_a=1200 rpm.

2.8. *Box Benhken quadratic design*

After the system was characterized and the important factors were identified in a reasonable and accurate way (Table 6), the next objective was optimization. Using an optimization model, also called Response Surface/Box-Benhken (Table 7), levels +1, 0 and -1 were evaluated to obtain response surface plots and the mathematical model that describes the effect of the significant factors in the response variables PS and PDI, related to the process of obtaining the NLCs. The software was used to determine combinations of the factors studied to obtain NLCs of different sizes.

Table 4. Level of independent factors selected by screening method for full factorial 2^3 design.

Factor	Levels	
	-1	1
% Tween	2	4
L (mg/mL)	15	24
t (min)	5	10

Table 5. full factorial design 2^3 for robustness study.

Run	% Tween 80	t (min)	L (mg/mL)	PS (nm)	PDI
1	2	5	15	117.6	0.333
2	2	5	15	110.7	0.529
3	2	5	15	108.9	0.501
4	4	5	15	16.08	0.154
5	4	5	15	16.18	0.17
6	4	5	15	16.05	0.146
7	2	10	15	107.3	0.459
8	2	10	15	112	0.313
9	2	10	15	100.7	0.313
10	4	10	15	18.41	0.238
11	4	10	15	18.25	0.236
12	4	10	15	16.29	0.144
13	2	5	25	108.8	0.274
14	2	5	25	110	0.349
15	2	5	25	114.5	0.297
16	4	5	25	21.26	0.241
17	4	5	25	19.26	0.172
18	4	5	25	19.7	0.18
19	2	10	25	125.8	0.261
20	2	10	25	131.4	0.283
21	2	10	25	131.5	0.334
22	4	10	25	19.79	0.193
23	4	10	25	19.47	0.192
24	4	10	25	19.3	0.192
25	3	7.5	20	32.44	0.294
26	3	7.5	20	32.33	0.302
27	3	7.5	20	32.16	0.301

Table 6. Factor levels for Box Benhken response surface methodology.

Factor	Levels	
	-1	1
tween %	1.5	4.5
L (mg/mL)	15	30
t (min)	5	15

Table 7. Experimental design matrix for Box-Behnken Response Surface methodology.

Run	Tween 80 (%)	t (min)	L (mg/mL)	PS (nm)	PDI
1	1.50	5	22.5	104.20	0.420
2	4.50	5	22.5	15.39	0.186
3	1.50	15	22.5	92.00	0.300
4	4.50	15	22.5	14.66	0.166
5	1.50	10	15.0	29.61	0.510
6	4.50	10	15.0	13.75	0.170
7	1.50	10	30.0	116.00	0.406
8	4.50	10	30.0	21.36	0.307
9	3.00	5	15.0	70.23	0.122
10	3.00	15	15.0	15.34	0.225
11	3.00	5	30.0	95.25	0.693
12	3.00	15	30.0	132.00	1.000
13	3.00	10	22.5	18.41	0.164
14	3.00	10	22.5	17.66	0.240
15	3.00	10	22.5	19.32	0.249

3. Results and Discussion

3.1. *Effect of independent factors on the synthesis of NLCs*

3.1.1. Effect of the pH of the aqueous solution on PS and PDI during the synthesis of NLCs

As shown in Table 8, the PS of the NLCs obtained varies from 22.8–3511 nm with a PDI of 0.243 to 1.000 when NLCs were synthesized at pH 3-11. When alkaline solutions (pH>pKa) were used, the PS underwent a significant increase, related to the ionization state of the fatty acids in the synthesis medium. The

lipids used in the mixture have an acidic character with pKa values of 10.15 and 9.85 for stearic acid and oleic acid, respectively [88]. When the lipids are in a medium with a pH greater than their pKa, the molecules reduce the ionization state and therefore the repulsion between them, thus causing a crystallization process that results in the aggregation of the molecules and therefore in the increase in PS [89]. Likewise, under alkaline conditions there is no uniformity in the particle size (PDI 0.900-1.000) and a polydisperse solution is obtained. On the other hand, acidic conditions of the aqueous solution (pH<pKa) produced a better particle size distribution (PDI 0.243-0.270) and clearly the size of NLCs decreased (PS 22.68-31.37 nm) (Figure 5), which results convenient when we want to increase stability and storage time, since it has been reported that larger particles have less stability during storage time [55]. The pH of the aqueous phase is also relevant when it is desired to integrate a drug into the nanocarriers, the pH conditions will also influence the ionization of the drug and could increase or decrease the solubility, which will be reflected in the efficiency of drug entrapment and release [73, 90].

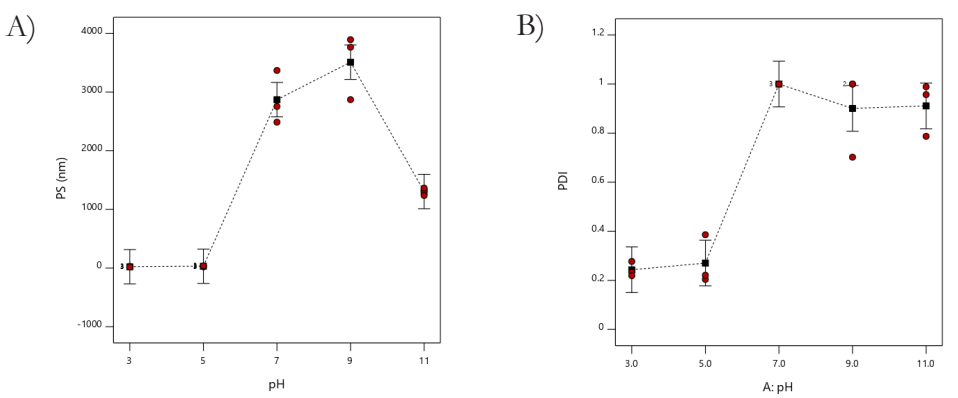

Figure 5. Effect of the aqueous solution pH on
A) PS and B) PDI in NLCs synthesis. *$p<0.05$, $R^2=0.97$.*

3.1.2. Effect of temperature on PS and PDI during the synthesis of NLCs

The effect of temperature on PS during NLC synthesis is shown in Table 8 and Figure 6. After statistical analysis, no significant effects were observed in the different treatments ($p<0.05$) and PS was in the range of 15.04-19.93 nm. The highest PS was observed when the synthesis temperature was 30 °C and although lower synthesis temperatures were not analyzed, it has been observed in previous

Table 8. Evaluated factors by single-factor design during the NLCs synthesis.

Factor		PS (nm)	PDI
pH			
	3	22.68 ± 6.00	0.243 ± 0.030
	5	31.37 ± 8.82	0.270 ± 0.100
	7	2871 ± 452	1.000 ± 0.000
	9	3511 ± 557	0.900 ± 0.172
	11	1305 ± 63.4	0.921 ± 0.116
Temperature (°C)			
	30	19.93 ± 7.40	0.160 ± 0.026
	40	16.17 ± 0.11	0.155 ± 0.005
	50	15.61 ± 0.38	0.146 ± 0.021
	60	15.99 ± 0.54	0.189 ± 0.008
	70	15.04 ± 0.44	0.149 ± 0.003
% V_o			
	10	16.67 ± 0.98	0.204 ± 0.035
	20	21.55 ± 1.36	0.231 ± 0.086
	30	821 ± 651	0.621 ± 0.344
	40	4567 ± 1146	1.000 ± 0.000
	50	2867 ± 1218	1.000 ± 0.000
L (mg/mL)			
	15	15.3 ± 1.32	0.136 ± 0.050
	20	17.2 ± 0.08	0.199 ± 0.080
	25	17.85 ± 0.96	0.283 ± 0.060
	30	102.69 ± 14.78	0.383 ± 0.081
	35	125.30 ± 36.60	0.430 ± 0.123
% tween 80			
	2	60.43 ± 5.67	0.208 ± 0.009
	3	30.27 ± 5.46	0.389 ± 0.004
	4	17.22 ± 0.26	0.510 ± 0.019
	5	16.44 ± 0.36	0.218 ± 0.003
% L_l/L_s			
	30	18.13 ± 0.90	0.194 ± 0.007
	40	17.98 ± 2.43	0.156 ± 0.030
	50	20.45 ± 3.18	0.198 ± 0.084
	60	19.91 ± 2.69	0.256 ± 0.020
	70	17.78 ± 0.96	0.203 ± 0.019

works [56] that PS increases when working at 20 °C. It is convenient to work at temperatures higher than the melting point of the solid lipid used in the organic phase mixture (stearic acid Tm=71 °C) [91], because, although it is not reflected in the PS, the structure and morphology of the NLCs is affected and may not be uniform. When working at low temperatures, the fast solidification and formation of the lipid network during the formation of NLCs (when the organic phase is rapidly injected into the aqueous phase) can cause low encapsulation of the drug [65, 75] and produce particles of variable composition that will give less stability to the particle suspension. Due to this, and because there are no differences between experimental treatments, the working temperature was kept constant at 70 °C during the subsequent optimization phases.

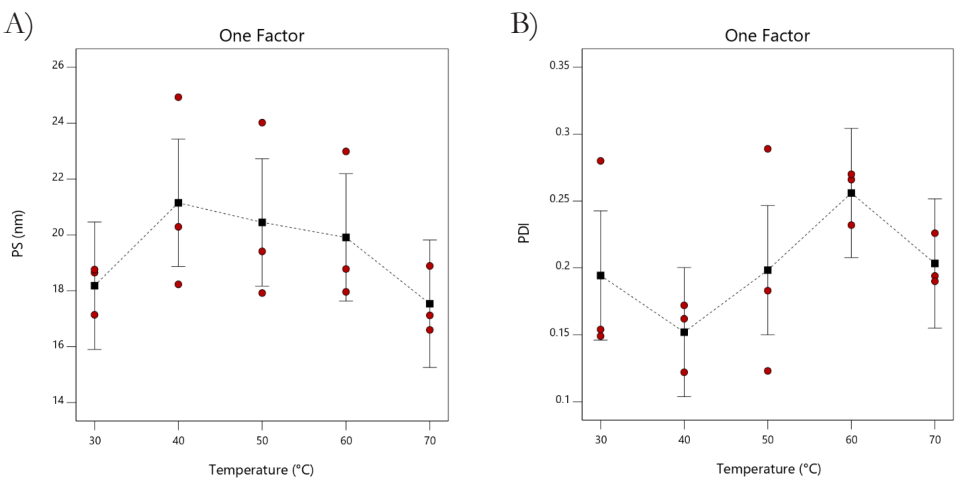

Figure 6. Effect of the temperature on A) PS and B) PDI in NLCs synthesis. $p<0.05$, $R^2=0.31$.

3.1.3. Effect of %V_o on PS and PDI during the synthesis of NLCs

Different volumes of ethanol during the synthesis of NLCs were used to study the effect of %V_o. As shown in Table 8 and Figure 7, the increase in %V_o results in a considerable increase in PS, but even more so in PDI, which drastically changes from 0.204 to 0.621 when the ethanol volume is increased from 10 % to 30 %. The stability of NLCs (data not shown) is considerably affected and percentages of 20 % ethanol led to the separation of the phases (organic and aqueous) in less than 24 h. As suggested by Scubert *et al.* [67], it is crucial to avoid exceeding the critical solvent/water ratio as this would result in coarser particles with large PS.

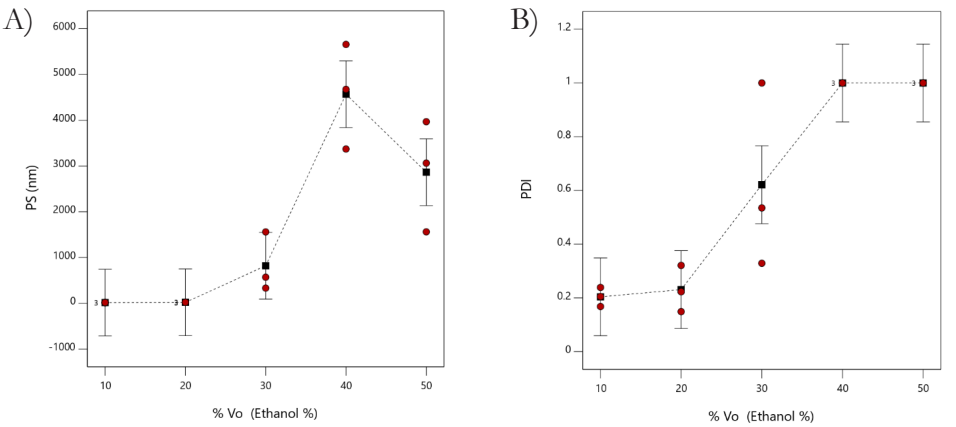

Figure 7. Effect of $\%V_o$ on A) PS and B) PDI in NLCs synthesis. *p>0.05, R^2=0.88.*

3.1.4. Effect of total lipid concentration (L) on PS and PDI during the synthesis of NLCs

Consistent with previous research [77, 78, 85], where the PS was considerably affected in direct proportion to the amount of total lipids dissolved in the organic phase, in this work PS increased from 15.3 to 125.30 nm (Figure 8) when lipid concentration increased. Harshad *et al.* evaluated different levels of lipid concentration achieving a decrease from 349.2 nm to 218.6 nm when working from a high level to a low level of lipid concentration [77]. In this part of the process (evaluation of independent factors) the lipid concentration varied from 15-35 mg/mL. No significant effects were observed at first treatments of 15 to 25 mg/mL, however, increases beyond 30 mg/mL led to larger PS. These results can be attributed to the increase in the viscosity of the organic phase, which makes it difficult to break the lipid droplets formed when they are injected into the aqueous phase. In the same way, these results suggest that the lipid concentration, as one of the factors with greater ease of control, could be a critical factor for the optimization of the process. Since the objective of the study is to obtain particle sizes ≤100 nm, the operating range of this variable for subsequent analyzes was established at 15-25 mg/mL.

3.1.5. Effect of surfactant concentration in the aqueous phase on PS and PDI during the synthesis of NLCs

Those NLCs prepared with the lowest concentration of surfactant (2 % Tween 80) showed a considerably large PS (60.40 nm) compared to the rest of the treatments (Figure 9). The gradual addition of Tween 80 results in smaller

particle sizes [92]. The sizes of NLCs obtained are the result of the reduction of the surface tension between the organic and aqueous phases, which inhibits the aggregation of small droplets during lipid injection [93]. Increases of 4 % to 5 % surfactant in the aqueous phase do not further reduce the particle size, however, smaller sizes are not required in the process. For all the above, 4 %-2 % Tween 80 was selected as the operating range for the screening designs.

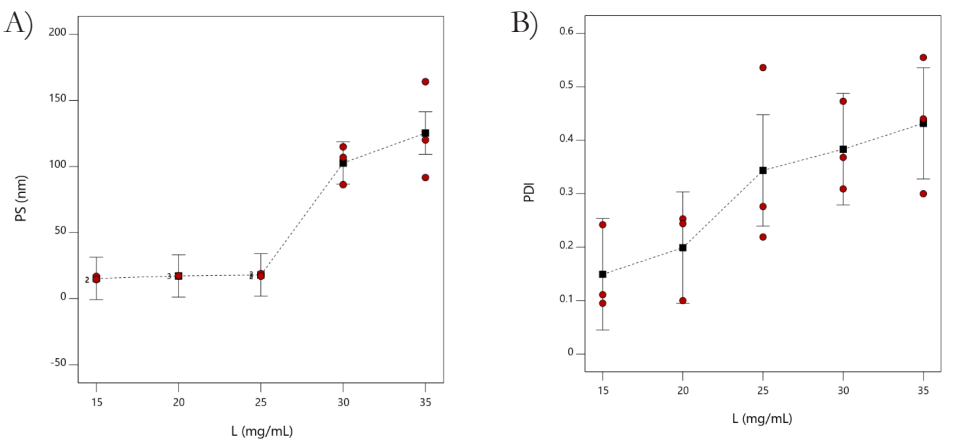

Figure 8. Effect of lipid concentration in the organic phase (L) on A) (PS) and B) (PDI) of NLCs. $p<0.05$, $R^2=0.92$.

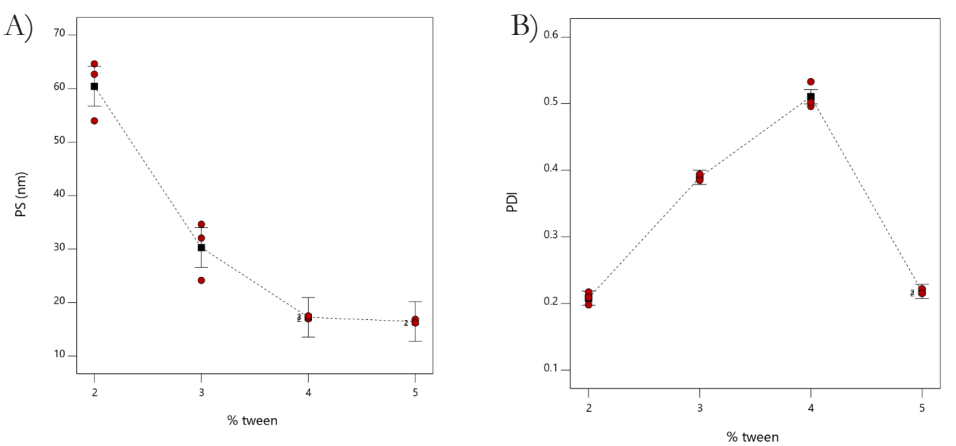

Figure 9. Effect of the surfactant concentration (%tween 80) on A) (PS) and B) (PDI) of NLCs. $p<0.05$, $R^2=0.99$.

3.1.6. Effect of the percentage of liquid lipid in the mixture on the PS and PDI during the synthesis of NLCs

In order to investigate the effect of the proportion of oleic acid in the lipid mixture, 5 different oleic acid:stearic acid (30-70 %) formulations were prepared (Table 8). Figure 10 shows that there are no significant changes in both PS and PDI response variables between the treatments. The PS were from 17.98 to 20.45 with a PDI 0.156-0.256, indicating that the particles exist in a monodisperse solution at all levels.

Previously, Chahinez *et al.*, evaluated liquid and solid lipid variations in different mixtures (triglycerides, short, medium and long chain phospholipids, glycerols, etc.) [79], showing multiple effects in all of them, however, the results of the study in medium chain phospholipids (MCF) are comparable with those obtained in this study (which uses two MCF), since there are no significant changes in PS when the percentage of liquid lipid increases. Since there are no significant differences in the response variables and since the high percentages of liquid lipid in the mixture increase the stability of the nanocarriers, it was decided to work with 70 % oleic acid in the subsequent experimental designs.

3.2. *Plackett-Burman (PB) screening design*

Plackett-Burman (PB) designs are filtering designs that involve a large number of factors and relatively few experiments [87]. PB has been widely used for the identification of the most significant independent factors affecting a process. A total of 14 experiments were performed involving six independent factors as shown in Table 2. The independent factors and their levels are shown in Table 3. The selected response variables (PS and PDI) exhibit great variation suggesting that the independent variables have a significant effect on them. The analysis of variance (ANOVA, Table 9, Table 10) for both response variables confirms that only some factors are relevant in the synthesis of NLCs. T and v_a ($p>0.05$) do not have significant effects during the synthesis of NLCs.

On the other hand, the surfactant concentration and the agitation time ($p<0.05$) are really significant, and it is suggested that they are two of the factors that govern the PS, which was verified in subsequent analyses. The statistics for L and pH show different values in both ANOVAs and suggests that they may not influence the PS. The screening analyzes are not used for the optimization and obtaining of a mathematical model [87], but rather as a method of selecting

variables for more robust methods, since in PB the effects of some factors may be hidden by the alias formed between them [94]. For this reason, although L is not significant in this part of the study, it was decided to include it in the factorial designs, since previous tests (Section 3.1.4) [67, 76, 77, 85] have shown a significant effect on PS, when there are variations in lipid concentration.

Table 9. DoE Plackett-Burman ANOVA for PS.

Source	SS	SM	F-value	p-value	
Model	35284.07	5040.58	7.47	0.0209	*significant*
%tween	14129.54	14129.54	20.93	0.006	
L	3343.67	3343.67	4.95	0.0766	
pH	3289.81	3289.81	4.87	0.0784	
T	224.21	224.21	0.3321	0.5894	
v_a	611.33	611.33	0.9055	0.385	
t	5760.14	5760.14	8.53	0.033	

Table 10. DoE Plackett-Burman ANOVA for PDI.

Fuente de variación	SS	SM	F-value	p-value	
Model	0.6995	0.0874	6.6	0.0263	*significant*
%tween	0.1402	0.1402	10.58	0.0226	
L	0.0071	0.0071	0.5325	0.4983	
pH	0.0988	0.0988	7.46	0.0412	
T	0.0142	0.0142	1.07	0.3478	
v_a	0.0249	0.0249	1.88	0.2285	
t	0.1419	0.1419	10.71	0.0221	

3.3. *Factorial design 2^3*

During the preliminary studies, three significant design variables were determined: % tween 80, L and v_a . A factorial design allows detecting possible interactions between these factors [95], which may affect the NLCs synthesis process. The factorial design is a much more effective tool to interpret and implement the results of the study of the process, considering simultaneous changes in the parameters studied. The effects of % tween, L and v_a were evaluated on the response variables PS and PDI using a 2^3 factorial design (Table 4, Table 5).

24 experimental runs (8 tests in triplicate and 3 central points) were prepared and the NLCs were synthesized by the solvent injection method.

As mentioned in previous works, the presence of a surfactant is necessary and irreplaceable for the formulation of NLCs [55, 73, 90], but there is a limit that can be used to avoid being irritant and toxic. For this reason, the objective of evaluating its interaction with other process variables is to minimize the concentration of tween 80. The results obtained were treated statistically by ANOVA and it was determined that the design model is significant ($p<0.05$) and is capable of describe more than 99 % of the events that occurred for the PS (Table 11). Clearly the %tween 80 factor is the most significant during the synthesis of NLCs. Center points were used in this design, since factorial designs assume that there is a linear relationship between each X & Y. Therefore, if the relationship between any X and Y shows curvature, a factorial design should not be used because the results may not be reliable [96]. Then, the ANOVA (Table 11) concludes that curvature exists, and it is necessary to use a response surface experimental design (RSM). Although this design (factorial 2^3) can detect curvature and predict some responses, an RSM must be used to model the curvature and acquire a fitted mathematical model.

Table 11. ANOVA of factorial design 2^3.

Source	Sum of quares	Mean Square	F-value	p-value	
Model	56925.88	8132.27	968.5	< 0.0001	significant
Tween %	55985.5	55985.5	6667.48	< 0.0001	
t	70.66	70.66	8.41	0.0095	
L	282.36	282.36	33.63	< 0.0001	
(tween)* % (t)	51.69	51.69	6.16	0.0232	
(tween)* % (L)	93.14	93.14	11.09	0.0037	
(t)*(L)	183.15	183.15	21.81	0.0002	
(tween)* % (t)*(L)	259.38	259.38	30.89	< 0.0001	
Curvature	3141.88	3141.88	374.18	< 0.0001	

3.4. *Box-Behnken /Response Surface Method*

The response surface method allows to evaluate a limited number of variables at different levels with a small series of experiments [85]. This approach was used selecting the experimental level for each variable based on the results of preliminary experiments. The surface and contour plots (Figure 10) show the interaction

of different factors on PS. The influence of the factors investigated on the PS using Box Behnken is shown in Table 7.

The ANOVA statistical analysis (Table 12), when the model was adjusted eliminating non-significant interactions, confirms that the model is significant ($p<0.05$) and that it can describe 97 % of the events. Table 7 shows that the PS can vary from 13.75-132 nm, suggesting it to be an adequate model for obtaining small particle sizes of NLCs useful in nanomedicine applications against cancer.

Analyzing the coded equation (Eq. 1), the most significant factor contributing to the variation in PS was the concentration of tween 80, this is evident when observing the value of its coefficient. The %tween 80 factor shows a negative effect on the PS, which translates into a decrease in the size value, thus being favorable for obtaining smaller particles, necessary for this study, and a monodisperse solution of particles. The observation of the increase of the PS with the increase of the concentration of lipids (L) in the organic phase had already been observed in this study and in previous works [83 – 86]. This can be associated with the observations presented in section 3.3.4, where the increase in the viscosity of the medium, caused by the increase in the percentage of lipids, and the difficulty in breaking the lipid droplets, is reflected in the particle size.

$$PS(nm) = 20.02 - 34.58\, Z_1 + 29.46\, Z_3 - 19.70\, Z_1 Z_3 + 22.91 Z_2 Z_3 + 35.37\, Z_2^2 + 23.98 Z_3^2$$

Eq. 1

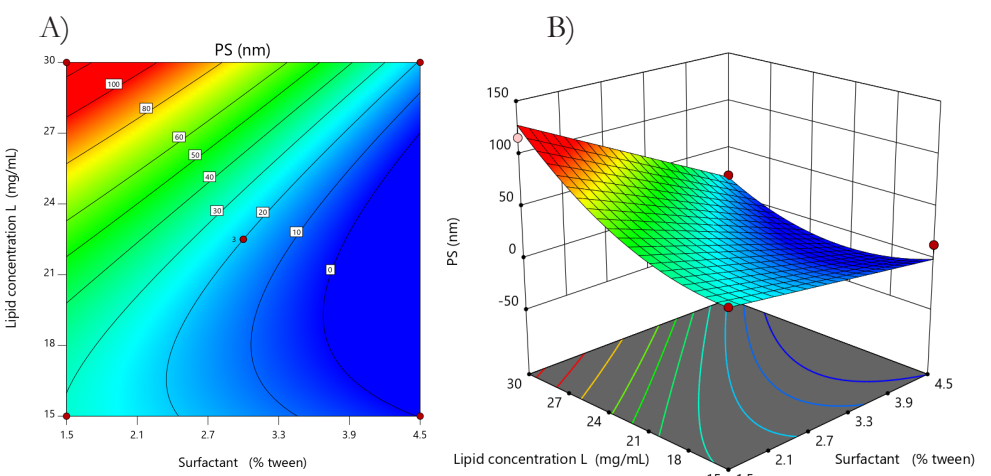

Figure 10. Influence of investigated parameters on PS: (A) counter plot and (b) surface plot $p<0.0001$, $R^2=0.97$.

Table 12. ANOVA of factorial design 2^3.

Source	Sum of Squares	df	Mean Square	F-value	p-value	
Model	26526.01	6	4421	41.44	< 0.0001	significant
%tween	9566.9	1	9566.9	89.68	< 0.0001	
L	6943.13	1	6943.13	65.09	< 0.0001	
(%tween) (L)	1551.57	1	1551.57	14.55	0.0051	
(v_a) (L)	2099.47	1	2099.47	19.68	0.0022	
v_a^2	4645.9	1	4645.9	43.55	0.0002	
L^2	2136.65	1	2136.65	20.03	0.0021	

3.5. *Optimization*

The Design Expert 11 software was used as a tool to determine the values of the different process factors, when a certain particle size is established. The values for each factor when it is desired to obtain particles with PS of 20, 60 and 100 nm are shown in Table 13. The experimental results show that the model is useful for predicting PS and PDI.

Table 13. Predicted and Experimental PS using RSM.

Tween (%)	v_a (min)	L (mg/mL)	Predicted PS (nm)	Experimental PS (nm)	Predicted PDI	Experimental PDI
4.37	14.51	23.13	20	19.25 ± 0.45	0.265	0.253 ± 0.02
2.57	5.54	17.01	60	71.35 ± 4.50	0.246	0.136 ± 0.13
2.74	12.26	27.73	100	102.93 ± 2.19	0.481	0.426 ± 0.01

When nanocarriers are used, the particle size is a determining factor in increasing the efficacy of cancer treatments. Previous work has shown the importance of particle size and distribution, for example, Caster *et al.*, in 2017 [96] demonstrated, by comparing 50, 100 and 150 nm particles in in vitro studies, that particles with a size of 50 nm and a better size distribution between them can more easily penetrate cells and carry out their therapeutic effect. A small particle size allows to increase the circulation time in the blood, by being able to evade RES. If a smaller particle size is enough to evade the immune system, the use of polyethylene glycol (PEG) can be limited. Recently, a particle size less than 100 nm is

a frequently observed feature in cancer treatment and most medically approved nanodrugs are usually >50 nm in size [91].

To identify in subsequent work whether particle sizes smaller than 100 nm are sufficient to evade all biological barriers, it is relevant to obtain small-sized nanocarriers, with a narrow distribution, but all of them with the same chemical composition.

4. Conclusions

In this study, NLCs were obtained by solvent injection method. Despite the simplicity of the technique, the solvent injection method has not been extensively studied to analyze the factors involved in NLC synthesis. Previous works had been analyzing the effect of independent variables (a single factor at a time) on the PS and the PDI, thus ignoring the interactions between independent factors. The DoE is a useful method to discriminate irrelevant factors in the production process of NLCs and based on a series of precise and well-founded experimental designs, it manages to determine the factors that have a significant effect on the synthesis of nanocarriers.

Using DoE and the solvent injection method, eight process factors (pH, %tween, T, L_l/L_s, L, %Vo, v_a and ta) that directly affect the PS and PDI of the NLCs were evaluated. By evaluating each factor independently, it was determined that the percentage of solvent and the percentage of liquid lipid in the lipid mixture do not have a real effect on PS and PDI and work levels other than the established critical values ($\%V_o$ =10 % and L_l/L_s, =70 %) destabilizes the particle suspension. Using Plackett-Burman, the temperature and the stirring speed were discriminated, since they do not present significant effects during the process. For the factorial experimental design, only %tween, L and v_a were used, the presence of curvature suggested adjusting the design to a quadratic model using RSM/Box-Benhken. The quadratic model indicates that two factors are critical during the synthesis of NLCs; firstly, the surfactant concentration negatively affects the particle size, allowing small particle sizes, which is convenient to obtain particles with PS<100 nm. On the other hand, the concentration of total lipids is another critical factor that will directly affect the size of the nanocarriers when their levels increase, that is, a higher concentration of lipids in the aqueous phase promotes particles with PS>100 nm.

The adjusted method is useful to predict the PS when variations of %tween and L (maintaining constant pH=6.0, T=70 °C, L_l/L_s L=70 %, $\%V_o$=10 %, v_a=1200 rpm and t_a=10 min) are performed. With the model adjusted it is

possible to obtain NLCs with PS 20, 60 and 100 nm with the same chemical composition. Particles of these sizes are theoretically adequate for anticancer drug delivery applications.

Acknowledgment and Funding

This work has been supported by the multidisciplinary project IPN-SIP 20232196. Cándido Gómez Lara thanks to CONACYT-Mexico for the doctorate fellowship N° 2022000002-01NACF.

References

1. Gonzalez-Valdivieso, J., Girotti, A., Schneider, J, & Arias, F. J. (2021). Advanced nanomedicine and cancer: Challenges and opportunities in clinical translation. *International Journal of Pharmaceutics*, 599. Elsevier B.V. https://doi.org/10.1016/j.ijpharm.2021.120438

2. Lei, S., Zheng, R., Zhang, S., Wang, S., Chen, R., Sun, K. *et al.* (2021). Global patterns of breast cancer incidence and mortality: A population-based cancer registry data analysis from 2000 to 2020. *Cancer Communications*, 41(11), 1183-1194. https://doi.org/10.1002/cac2.12207

3. Ferlay, J., Colombet, M., Soerjomataram, I., Parkin, D. M., Piñeros, M., Znaor, A. *et al.* (2021). Cancer statistics for the year 2020: An overview. *Internationa Journal of Cancer*, 149(4), 778-789. https://doi.org/10.1002/ijc.33588

4. Huang, L., Zhao, S., Fang, F., Xu, T., Lan, M., & Zhang, J. (2021). Advances and perspectives in carrier-free nanodrugs for cancer chemo-monotherapy and combination therapy. *Biomaterials*, 268. Elsevier Ltd. https://doi.org/10.1016/j.biomaterials.2020.120557

5. Hallan, S. S., Sguizzato, M., Esposito, E., & Cortesi, R. (2021). Challenges in the physical characterization of lipid nanoparticles. *Pharmaceutics*, 13. MDPI. https://doi.org/10.3390/pharmaceutics13040549

6. Zottel, A., Paska, A.V., & Jovčevska, I. (2019). Nanotechnology meets oncology: Nanomaterials in brain cancer research, diagnosis and therapy. *Materials*, 12. MDPI AG. https://doi.org/10.3390/ma12101588

7. Pliarchopoulou, K., & Pectasides, D. (2009). Pancreatic cancer: Current and future treatment strategies. *Cancer Treatment Reviews*, 35, 431-437. https://doi.org/10.1016/j.ctrv.2009.02.005

8. Sexton, R. E., Al Hallak, M. N., Diab, M., & Azmi, A. S. (2020). Gastric cancer: a comprehensive review of current and future treatment strategies. *Cancer and Metastasis Reviews*, 39, 1179-1203. Springer. https://doi.org/10.1007/s10555-020-09925-3

9. Tamura, T., Ohira, M., Tanaka, H., Muguruma, K., Toyokawa, T., Kubo, N. *et al.* (2015). Programmed Death-1 Ligand-1 (PDL1) Expression Is Associated with the Prognosis of Patients with Stage II/III Gastric Cancer. *Anticancer Res.* [Internet], 35(10), 5369-5376. Available from: http://www.ncbi.nlm.nih.gov/pubmed/26408698

10. Parmar, K., Mohamed, A., Vaish, E., Thawani, R., Cetnar, J., & Thein, K. Z. (2022). Immunotherapy in head and neck squamous cell carcinoma: An updated review. *Cancer Treatment and Research Communications,* 33. Elsevier Ltd. https://doi.org/10.1016/j.ctarc.2022.100649

11. Sahu, M., & Suryawanshi, H. (2021). Immunotherapy: The future of cancer treatment. *Journal of Oral Maxillofacail Pathology* [Internet], 25(2), 371. https://doi.org/10.4103/0973-029X.325257

12. Borody, T. J., Eslick, G. D., & Clancy, R. L. (2019). Fecal microbiota transplantation as a new therapy: from Clostridioides difficile infection to inflammatory bowel disease, irritable bowel syndrome, and colon cancer. *Current Opinion in Pharmacology*, 49, 43-51. Elsevier Ltd. https://doi.org/10.1016/j.coph.2019.04.017

13. Moghimipour, E., Abedishirehjin, S., Baghbadorani, M. A., & Handali, S. (2021). Bacteria and Archaea: A new era of cancer therapy. *Journal of Controlled Release*, 38, 1-7. Elsevier B.V. https://doi.org/10.1016/j.jconrel.2021.08.019

14. Vahl, J. M., von Witzleben, A., Reiter, R., Theodoraki, M. N., Wigand, M., Hoffmann, T.K. *et al.* (2022). Infrasound a new weapon in cancer therapy? *Explore*, 18, 366-370. Elsevier Inc. https://doi.org/10.1016/j.explore.2021.03.001

15. Singh, A., Nayak, N., Rathi, P., Verma, D., Sharma, R., Chaudhary, A. *et al.* (2021). Microbiome and host crosstalk: A new paradigm to cancer therapy. *Seminars in Cancer Biology*, 70, 71-84. https://doi.org/10.1016/j.semcancer.2020.05.014

16. Yang, C., Han, H., & Lin, S. (2022). RNA epitranscriptomics: A promising new avenue for cancer therapy. *Molecular Therapy. Cell Press,* 30, 2-3. https://doi.org/10.1016/j.ymthe.2021.12.008

17. Kumar, K., Rani, V., Mishra, M., & Chawla, R. (2022). New paradigm in combination therapy of siRNA with chemotherapeutic drugs for effective cancer therapy. *Current Research in Pharmacology and Drug Discovery*, 3. Elsevier B.V. https://doi.org/10.1016/j.crphar.2022.100103

18. Gupta, K. H., Nowicki, C., Giurini, E. F., Marzo, A. L., & Zloza, A. (2021). Bacterial-based cancer therapy (Bbct): Recent advances, current challenges, and future prospects for cancer immunotherapy. *Vaccines*, 9. https://doi.org/10.3390/vaccines9121497

19. Crezee, J., Franken, N. A. P, & Oei, A. L. (2021). Hyperthermia-based anti-cancer treatments. *Cancers*, 13, 1-4. https://doi.org/10.3390/cancers13061240

20. Lukyanov, A. N., & Torchilin, V. P. (2004). Micelles from lipid derivatives of water-soluble polymers as delivery systems for poorly soluble drugs. *Advanced Drug Delivery Reviews*, 56(9), 1273-1289.
https://doi.org/10.1016/j.addr.2003.12.004

21. Narvekar, M., Xue, H. Y., Eoh, J. Y., & Wong, H. L. (2014). Nanocarrier for poorly water-soluble anticancer drugs - Barriers of translation and solutions. *AAPS PharmSciTech,* 15, 822-833. Springer New York LLC.
https://doi.org/10.1208/s12249-014-0107-x

22. Lorscheider, M., Gaudin, A., Nakhle, J., Veiman, K. L., Richard, J., & Chassaing, C. (2021). Challenges and opportunities in the delivery of cancer therapeutics: Update on recent progress. *Therapeutic Delivery*, 12(1), 55-76.
https://doi.org/10.4155/tde-2020-0079

23. Valdes, S. A., Alzhrani, R. F., Rodriguez, A., Lansakara-P, D. S. P., Thakkar S. G., & Cui Z. (2019). A solid lipid nanoparticle formulation of 4-(N)-docosahexaenoyl 2', 2'-difluorodeoxycytidine with increased solubility, stability, and antitumor activity. *International Journal of Pharmaceutics*, 30, 570.
https://doi.org/10.1016/j.ijpharm.2019.118609

24. Surapaneni, M. S., Das, S. K., & Das, N. G. (2012). Designing Paclitaxel Drug Delivery Systems Aimed at Improved Patient Outcomes: Current Status and Challenges. *International Scholarly Research Notices*, 623139.
https://doi.org/10.5402/2012/623139

25. Marupudi, N. I., Han, J. E., Li, K. W., Renard, V. M., Tyler, B. M., & Brem, H. (2007). Paclitaxel: A review of adverse toxicities and novel delivery strategies. *Expert Opinion on Drug Safety*, 6, 609-621.
https://doi.org/10.1517/14740338.6.5.609

26. Kloover, J. S., Bakker, M. A. den, Gelderblom, H., & Meerbeeck, J. P. van. (2004). Fatal outcome of a hypersensitivity reaction to paclitaxel: a critical review of premedication regimens. *British Journal of Cancer*, 90(2), 304-305.
https://doi.org/10.1038/sj.bjc.6601303

27. Chou, P. L, Huang, Y. P., Cheng, M. H., Rau, K. M., & Fang, Y. P. (2020). Improvement of paclitaxel-associated adverse reactions (ADRs) via the use of nano-based drug delivery systems: A systematic review and network meta-analysis. *International. Journal of Nanomedicine*, 15, 1731-1743.
https://doi.org/10.2147/IJN.S231407

28. Javeed, A., Ashraf, M., Riaz, A., Ghafoor, A., Afzal, S., & Mukhtar, M. M. (2009). Paclitaxel and immune system. *European Journal of Pharmaceutical Sciences*, 38, 283-290.
https://doi.org/10.1016/j.ejps.2009.08.009

29. Perez, E. A., Vogel, C. L., Irwin, D. H., Kirshner, J. J., & Patel, R. (2001). Multicenter Phase II Trial of Weekly Paclitaxel in Women with Metastatic Breast Cancer. *Journal of Clinical Oncology*, 19(22), 4216-4223.
https://doi.org/10.1200/JCO.2001.19.22.4216

30. Lam, A. P., Sparano, J. A., Vinciguerra, V., Ocean, A. J., Christos, P., Hochster, H. *et al.* (2010). Phase II study of paclitaxel plus the protein kinase C inhibitor bryostatin-1 in advanced pancreatic carcinoma. *American Journal of Clinical Oncology: Cancer Clinical Trials*, 33(2), 121-124. https://doi.org/10.1097/COC.0b013e3181a31920

31. Chistiakov, D. A., Myasoedova, V. A., Orekhov, A. N., Bobryshev, Y. V. (2017). Nanocarriers in Improving Chemotherapy of Multidrug Resistant Tumors: Key Developments and Perspectives. *Current Pharmaceutical. Design*, 23(22). https://doi.org/10.2174/1381612823666170407123941

32. Gökçay, B., & Arda, B. (2015). Nanotechnology, nanomedicine; ethical aspects. *Rev. Rom. Bioet.,* 13(3).

33. Kumar, R., Aadil, K. R., Ranjan, S., & Kumar, V. B. (2020). Advances in nanotechnology and nanomaterials based strategies for neural tissue engineering. *Journal of Drug Delivery Science and Technology*, 57. Editions de Sante. https://doi.org/10.1016/j.jddst.2020.101617

34. Sim, S., & Wong, N. K. (2021). Nanotechnology and its use in imaging and drug delivery (Review). *Biomedical Reports,* 14(5). https://doi.org/10.3892/br.2021.1418

35. Rizzo, L. Y., Theek, B., Storm, G., Kiessling, F., & Lammers, T. (2013). Recent progress in nanomedicine: Therapeutic, diagnostic and theranostic applications. *Current Opinion in Biotechnology*, 24, 1159-1166. https://doi.org/10.1016/j.copbio.2013.02.020

36. Liz-Marzán, L. M., Nel, A. E., Brinker, C. J., Chan, W. C. W., Chen, C., Chen, X. *et al.* (2022). What Do We Mean When We Say Nanomedicine? *ACS Nano. American Chemical Society*, 16, 13257-13259. https://doi.org/10.1021/acsnano.2c08675

37. Lu, W., Yao, J., Zhu, X., & Qi, Y. (2021). Nanomedicines: Redefining traditional medicine. *Biomedicine and Pharmacotherapy*, 134. Elsevier Masson S.R.L. https://doi.org/10.1016/j.biopha.2020.111103

38. Svenson, S. (2014). What nanomedicine in the clinic right now really forms nanoparticles? *WIREs Interdisciplinary Reviews. Nanomedicine and Nanobiotechnology*, 6(2), 125-135. Wiley. https://doi.org/10.1002/wnan.1257

39. Taher, M., Susanti, D., Haris, M. S., Rushdan, A. A., Widodo, R. T., Syukri, Y. *et al.* (2023). PEGylated liposomes enhance the effect of cytotoxic drug: A review. *Heliyon*, 9(3). https://doi.org/10.1016/j.heliyon.2023.e13823

40. Aguilar, Z. P. (2013). Types of Nanomaterials and Corresponding Methods of Synthesis. In: *Nanomaterials for Medical Applications*, 33-82. Elsevier. https://doi.org/10.1016/B978-0-12-385089-8.00002-9

41. Khan, I., Saeed, K., & Khan, I. (2019). Nanoparticles: Properties, applications and toxicities. *Arabian Journal of Chemistry*, 12, 908-931. Elsevier B.V. https://doi.org/10.1016/j.arabjc.2017.05.011

42. Ealias, A. M., & Saravanakumar, M. P. (2017). A review on the classification, characterisation, synthesis of nanoparticles and their application. In: *IOP Conference Series: Materials Science and Engineering. Institute of Physics Publishing.*

43. Dastidar, D. G., Ghosh, D., & Das, A. (2022). Recent developments in nanocarriers for cancer chemotherapy. *OpenNano*, 8. Elsevier Inc. https://doi.org/10.1016/j.onano.2022.100080

44. Jaiswal, P., Gidwani, B., & Vyas, A. (2016). Nanostructured lipid carriers and their current application in targeted drug delivery. *Artificial Cells, Nanomedicine and Biotechnology*, 44, 27-40. Taylor & Francis Ltd. https://doi.org/10.3109/21691401.2014.909822

45. Mohd Nordin, U. U., Ahmad, N., Salim, N., & Mohd Yusof, N. S. (2021). Lipid-based nanoparticles for psoriasis treatment: a review on conventional treatments, recent works, and future prospects. *RSC Advances. Royal Society of Chemistry*, 11, 29080-29101. https://doi.org/10.1039/D1RA06087B

46. Scioli Montoto, S., Muraca, G., & Ruiz, M. E. (2020). Solid Lipid Nanoparticles for Drug Delivery: Pharmacological and Biopharmaceutical Aspects. *Frontiers in Molecular Biosciences*, 7. Frontiers Media S.A. https://doi.org/10.3389/fmolb.2020.587997

47. Alexis, F., Rhee, J. W., Richie, J. P., Radovic-Moreno, A. F., Langer, R., & Farokhzad, O. C. (2008). New frontiers in nanotechnology for cancer treatment. *Urologic Oncology: Seminars and Original Investigations*, 26, 74-85. https://doi.org/10.1016/j.urolonc.2007.03.017

48. Jeitler, R, Glader, C., Tetyczka, C., Zeiringer, S., Absenger-Novak, M., Selmani, A. *et al.* (2022). Investigation of Cellular Interactions of Lipid-Structured Nanoparticles with Oral Mucosal Epithelial Cells. *Frontiers in Molecular Biosciences,* 9. https://doi.org/10.3389/fmolb.2022.917921

49. Li, Q., Cai, T., Huang, Y., Xia, X., Cole, S. P. C., & Cai, Y. (2017). A review of the structure, preparation, and application of NLCs, PNPs, and PLNs. *Nanomaterials*, 7. https://doi.org/10.3390/nano7060122

50. Üner, M., & Yener, G. (2007). Importance of solid lipid nanoparticles (SLN) in various administration routes and future perspectives. *International Journal of Nanomedicine*, 2.

51. Majumdar, A., Dubey, N., & Malviya, N. (2019). Nanostructure lipid carriers: A promising tool for the drug delivery in the treatment of skin cancer. *Asian Journal of Pharmaceutical and Clinical Research*, 12(5), 15-26.

52. Chauhan, I., Yasir, M., Verma, M., & Singh, A. P. (2020). Nanostructured lipid carriers: A groundbreaking approach for transdermal drug delivery. *Advanced Pharmaceutical Bulletin*, 10, 150-165. Tabriz University of Medical Sciences. https://doi.org/10.34172/apb.2020.021

53. Elmowafy, M., & Al-Sanea, M. M. (2021). Nanostructured lipid carriers (NLCs) as drug delivery platform: Advances in formulation and delivery strategies. *Saudi Pharmaceutical Journal*, 29(9), 999-1012. https://doi.org/10.1016/j.jsps.2021.07.015

54. Kovacevic, A., Savic, S., Vuleta, G., Müller, R. H., & Keck, C. M. (2011). Polyhydroxy surfactants for the formulation of lipid nanoparticles (SLN and NLC): Effects on size, physical stability and particle matrix structure. *International. Journal of Pharmaceutics*, 406(1–2), 163-172. https://doi.org/10.1016/j.ijpharm.2010.12.036

55. Duong, V. A., Nguyen, T. T. L., Maeng, H. J., & Chi, S. C. (2019). Preparation of Ondansetron Hydrochloride-Loaded Nanostructured Lipid Carriers Using Solvent Injection Method for Enhancement of Pharmacokinetic Properties. *Pharmaceutical Research,* 36(10), 138. https://doi.org/10.1007/s11095-019-2672-x

56. Varshosaz, J., Sadeghi, H., Andalib, S., & Hassanzadeh, F. (2012). Optimization of LDL targeted nanostructured lipid carriers of 5-FU by a full factorial design. *Advanced Biomedical Research*, 1(1), 45. https://doi.org/10.4103/2277-9175.100147

57. Elbrink, K., Van Hees, S., Holm, R, & Kiekens, F. (2023). Optimization of the different phases of the freeze-drying process of solid lipid nanoparticles using experimental designs. *International Journal of. Pharmaceutics,* 635. https://doi.org/10.1016/j.ijpharm.2023.122717

58. Sheoran, S., Arora, S., Samsonraj, R., Govindaiah, P., & Vuree, S. (2022). Lipid-based nanoparticles for treatment of cancer. *Heliyon*, 8. Elsevier Ltd. https://doi.org/10.1016/j.heliyon.2022.e09403

59. McClements, D.J., & Rao, J. (2011). Food-Grade nanoemulsions: Formulation, fabrication, properties, performance, Biological fate, and Potential Toxicity. *Critical Reviews in Food Science and Nutrition*, 51, 285-330. https://doi.org/10.1080/10408398.2011.559558

60. Huang, Z. R., Hua, S. C., Yang, Y. L., & Fang, J. Y. (2008). Development and evaluation of lipid nanoparticles for camptothecin delivery: A comparison of solid lipid nanoparticles, nanostructured lipid carriers, and lipid emulsion. *Acta Pharmacologica Sinica,* 29(9), 1094-1102. https://doi.org/10.1111/j.1745-7254.2008.00829.x

61. Fang, Y. P., Lin, Y. K., Su, Y. H., Fang, J. Y. (2011). Tryptanthrin-Loaded Nanoparticles for Delivery into Cultured Human Breast Cancer Cells, MCF7: The Effects of Solid Lipid/Liquid Lipid Ratios in the Inner Core. *Chemical and Pharmaceutical Bulletin*, 59. https://doi.org/10.1248/cpb.59.266

62. Bondi, M. L., Azzolina, A., Craparo, E. F., Lampiasi, N., Capuano, G., Giammona, G. *et al.* (2007). Novel cationic solid-lipid nanoparticles as non-viral vectors for gene delivery. *Journal of Drug Targetting,* 15(4), 295-301. https://doi.org/10.1080/10611860701324698

63. Charcosset, C, El-Harati, A, & Fessi, H. (2005). Preparation of solid lipid nanoparticles using a membrane contactor. *Journal of Controlled Release*, 108(1), 112-120. https://doi.org/10.1016/j.jconrel.2005.07.023

64. Taha, E., Nour, S. A., Mamdouh, W., Selim, A. A., Swidan, M. M., Ibrahim, A. B. *et al.* (2023). Cod liver oil nano-structured lipid carriers (Cod-NLCs) as a promising platform for nose to brain delivery: Preparation, *in vitro* optimization, *ex vivo* cytotoxicity & *in vivo* biodistribution utilizing radioiodinated zopiclone. *International Journal of Pharmaceutics X,* 100160. https://doi.org/10.1016/j.ijpx.2023.100160

65. Das, S., & Chaudhury, A. (2011). Recent Advances in Lipid Nanoparticle Formulations with Solid Matrix for Oral Drug Delivery. *AAPS PharmSciTech.,* 12(1), 62-76. https://doi.org/10.1208/s12249-010-9563-0

66. Schubert, M. A., & Müller-Goymann, C. C. (2003). Solvent injection as a new approach for manufacturing lipid nanoparticles-evaluation of the method and process parameters. *European Journal of Pharmaceutics and Biopharmaceutics.,* 55(1), 125-131. https://doi.org/10.1016/S0939-6411(02)00130-3

67. Arıca Yegin, B., Benoît, J. P., & Lamprecht, A. (2006). Paclitaxel-Loaded Lipid Nanoparticles Prepared by Solvent Injection or Ultrasound Emulsification. *Drug Development and Industrial Pharmacy,* 32(9), 1089-1094. https://doi.org/10.1080/03639040600683501

68. Jiang, H., Geng, D., Liu, H., Li, Z., & Cao, J. (2016). Co-delivery of etoposide and curcumin by lipid nanoparticulate drug delivery system for the treatment of gastric tumors. *Drug Delivery*, 23(9), 3665-3673. https://doi.org/10.1080/10717544.2016.1217954

69. Mallappa Dandagi, P., Anant Dessai, G., Panchakshari Gadad, A., & Desai V. B. (014). Formulation and evaluation of nanostructured lipid carrier (NLC) of Lornoxicam. *International Journal of Pharmacy and Pharmaceutical Sciences,* 6(2), 73-77.

70. Wu, J. (2021). The enhanced permeability and retention (Epr) effect: The significance of the concept and methods to enhance its application. *Journal of Personalized Medicine*, 11(8), 771. https://doi.org/10.3390/jpm11080771

71. Bazak, R., Houri, M., Achy, S. El., Hussein, W., & Refaat, T. (2014). Passive targeting of nanoparticles to cancer: A comprehensive review of the literature. *Molecular and Clinics Oncology,* 2(6), 904-908. https://doi.org/10.3892/mco.2014.356

72. Song, C. X., Labhasetwar, V., Murphy, H., Qu, X., Humphrey, W. R., Shebuski, R. J. *et al.* (1997). Formulation and characterization of biodegradable nanoparticles for intravascular local drug delivery. *Journal of Controlled Release*, 43. https://doi.org/10.1016/S0168-3659(96)01484-8

73. Zhou, J., Guo, B., Zhu, W., Sui, X., Ma, X., Qian, J. *et al.* (2021). Novel biomimetic nanostructured lipid carriers for cancer therapy: preparation, characterization, and *in vitro* / *in vivo* evaluation. *Pharmaceutical Development and Technology,* 26(1),81-91. https://doi.org/10.1080/10837450.2020.1835957

74. Akhoond Zardini, A., Mohebbi, M., Farhoosh, R., & Bolurian, S. (2018). Production and characterization of nanostructured lipid carriers and solid lipid nanoparticles containing lycopene for food fortification. *Journal of Food Science and Technology*, 55(1), 287-298. https://doi.org/10.1007/s13197-017-2937-5

75. Krambeck, K., Silva, V., Silva, R., Fernandes, C., Cagide, F., Borges, F. *et al.* (2021). Design and characterization of Nanostructured lipid carriers (NLC) and Nanostructured lipid carrier-based hydrogels containing Passiflora edulis seeds oil. *Internationa Journal of Pharmaceutics,* 600. https://doi.org/10.1016/j.ijpharm.2021.120444

76. Vaghasiya, H., Kumar, A., & Sawant, K. (2013). Development of solid lipid nanoparticles based controlled release system for topical delivery of terbinafine hydrochloride. *European Journal of Pharmaceutical Sciences*, 49(2), 311-322. https://doi.org/10.1016/j.ejps.2013.03.013

77. Joshi, A. S., Patel, H. S., Belgamwar, V.S., Agrawal, A., & Tekade, A. R. (2012). Solid lipid nanoparticles of ondansetron HCl for intranasal delivery: Development, optimization and evaluation. *Journal of Materials Science: Materials in Medicine*, 23(9), 2163-2175. https://doi.org/10.1007/s10856-012-4702-7

78. Houacine, C., Adams, D., & Singh, K. K. (2020). Impact of liquid lipid on development and stability of trimyristin nanostructured lipid carriers for oral delivery of resveratrol. *Journal of Molecular Liquids*, 316. https://doi.org/10.1016/j.molliq.2020.113734

79. Subhan, M. A., Yalamarty, S. S. K, Filipczak, N., Parveen, F, & Torchilin, V. P. (2021). Recent advances in tumor targeting via EPR effect for cancer treatment. *Journal of Personalized Medicine*, 11(6), 571. https://doi.org/10.3390/jpm11060571

80. Weissman, S., & Anderson, N. G. (2014). Design of Experiments (DoE) and Process Optimization. A Review of Recent Publications. *Organic Process Research & Development*, 19(11), 140904154728003. https://doi.org/10.1021/op500169m

81. Gujral, G., Kapoor, D., & Jaimini, M. (2018). An updated review on design of experiment (DOE) in pharmaceuticals. *Journal of Drug Delivery and Therapeutics,* 8(3). https://doi.org/10.22270/jddt.v8i3.1713

82. Tamjidi, F., Shahedi, M., Varshosaz, J., & Nasirpour, A. (2017). Stability of astaxanthin-loaded nanostructured lipid carriers as affected by pH, ionic strength, heat treatment, simulated gastric juice and freeze–thawing. *Journal of Food Science and Technology,* 54(10), 3132-3141. https://doi.org/10.1007/s13197-017-2749-7

83. Kovács, A., Berkó, S., Csányi, E., & Csóka, I. (2017). Development of nanostructured lipid carriers containing salicyclic acid for dermal use based on the Quality by Design method. *European Journal of Pharmaceutical Sciences,* 99, 246-257. https://doi.org/10.1016/j.ejps.2016.12.020

84. Kudarha, R., Dhas, N. L., Pandey, A., Belgamwar, V. S., & Ige, P. P. (2015). Box-Behnken study design for optimization of bicalutamide-loaded nanostructured lipid carrier: Stability assessment. *Pharmaceutical Development and Technology*, 20(5), 608-618. https://doi.org/10.3109/10837450.2014.908305

85. Loo, C., Basri, M., Ismail, R., Lau, H., Tejo, B., Kanthimathi, M. *et al.* (2013). Effect of compositions in nanostructured lipid carriers (NLC) on skin hydration and occlusion. *International Journal of Nanomedicine*, 8, 13-22. https://doi.org/10.2147/IJN.S35648

86. Plackett, R. L., & Burman, J. P. (1946). The Design of Optimum Multifactorial Experiments. *Biometrika*, 33(4), 305-325. https://doi.org/10.1093/biomet/33.4.305

87. Kanicky, J. R., & Shah, D. O. (2002). Effect of degree, type, and position of unsaturation on the pKa of long-chain fatty acids. *Journal of Colloid and Interface Science,* 256(1), 201-207. https://doi.org/10.1006/jcis.2001.8009

88. Kanicky, J. R., & Shah, D. O. (2003). Effect of premicellar aggregation on the pKa of fatty acid soap solutions. *Langmuir*, 19(6), 2034-2038. https://doi.org/10.1021/la020672y

89. Govender, T., Stolnik, S., Garnett, M. C., Illum, L., & Davis, S. S. (1999). PLGA nanoparticles prepared by nanoprecipitation: drug loading and release studies of a water soluble drug. *Journal of Controlled Release*, 57(2), 171-185. https://doi.org/10.1016/S0168-3659(98)00116-3

90. Attia, M. (2013). Formulation and Evaluation of Betamethasone Sodium Phosphate Loaded Nanoparticles for Ophthalmic Delivery. *Journal of Clinical and Experimental Ophthalmology,* 4(2).

91. Sukmawati, A., Utami, W., Yuliani, R., Da'I, M., & Nafarin, A. (2018). Effect of tween 80 on nanoparticle preparation of modified chitosan for targeted delivery of combination doxorubicin and curcumin analogue. *IOP Conference Series: Materials Science and Engineering, 311. International Conference on Sensors, Materials and Manufacturing 24-26 Nov 2017, Chiayi, Taiwan.* https://doi.org/10.1088/1757-899X/311/1/012024

92. Chaudhari, S. R., & Shirkhedkar, A. A. (2020). Application of Plackett-Burman and central composite designs for screening and optimization of factor influencing the chromatographic conditions of HPTLC method for quantification of efonidipine hydrochloride. *Journal of Analytical Science and Technology,* 11(1). https://doi.org/10.1186/s40543-020-00246-2

93. de Oliveira, M., Lima, V. M., Yamashita, S. M. A., Alves, P. S., & Portella, A.C. (2018). Experimental Planning Factorial: A brief Review. *International Journal of Advanced Engineering Research and Science,* 5(6), 166-177. https://doi.org/10.22161/ijaers.5.6.28

94. Lloyd, D. K., Bergum, J., & Wang, Q. (2020). Application of quality by design to the development and validation of analytical methods. In: *Specification of Drug Substances and Products: Development and Validation of Analytical Methods*, (2nd Ed.). Elsevier. pp. 59-99. https://doi.org/10.1016/B978-0-08-102824-7.00004-X

95. Caster, J. M., Yu, S. K., Patel, A. N., Newman, N. J., Lee, Z. J., Warner, S. B. *et al.* (2017). Effect of particle size on the biodistribution, toxicity, and efficacy of drug-loaded polymeric nanoparticles in chemoradiotherapy. *Nanomedicine*, 13(5), 1673-1683. PMID: 28300658; PMCID: PMC5483200. https://doi.org/10.1016/j.nano.2017.03.002

96. Hoshyar, N., Gray, S., Han, H., & Bao, G. (2016). The effect of nanoparticle size on *in vivo* pharmacokinetics and cellular interaction. *Nanomedicine,* 11(6), 673-692. PMID: 27003448; PMCID: PMC5561790. https://doi.org/10.2217/nnm.16.5

CHAPTER 2 HEALTH AREA

DESIGN OF NANOMATERIALS TOWARD THE CONTRAST ENHANCEMENT IN MAMMOGRAPHY IMAGES FOR BREAST CANCER DIAGNOSIS

Y. M. Hernández-Rodríguez, A. Ashok, Oscar E. Cigarroa-Mayorga*

Dept. Advanced Technologies, UPIITA-Instituto Politécnico Nacional, Av. IPN No. 2580, C.P. 07340, México

ocigarroam@ipn.mx

Hernández-Rodríguez, Y. M., Ashok, A., & Mayorga-Cigarroa, O. E. (2023). Design of nanomaterials toward the contrast enhancement in mammography images for breast cancer diagnosis. In E. San Martín-Martínez (Ed.). *Research advances in nanosciences, micro and nanotechnologies. Volume IV* (pp. 53-72). Barcelona, Spain: Omniascience.

Abstract

In this chapter, the characteristics of several materials for application in medical imaging are discussed. This text is focused on breast cancer, and thus, it is mentioned in deep since the effects on human health until the medical tools to give a medical diagnosis. A complete panorama of breast cancer is offered to the reader in the introduction section. Thus, the chapter starts with the meaning of cancer and the statistics of this disease. Then, the mammography images are mentioned as the current techniques for the diagnosis, particularly the use of X-ray beams and the physics involved in the image generation. Afterward, experimental results about Mn-oxide based nanoparticles are shown. The synthesis of nanoparticles was performed through accessible methods of synthesis from chlorides compounds. And then, the nanoparticles were functionalized with silicon oxide for enhancing the biocompatibility of the material. The physical properties of nanoparticles were studied by X-ray diffraction, scanning electron microscopy, transmission electron microscopy, energy dispersive X-ray spectroscopy, Raman spectroscopy, and X-ray photoelectron spectroscopy. Artificial breast tissue was obtained to test the nanoparticles and studied the behaviour in the tissue. The possibility of employing the nanoparticles as contrast enhancement material for breast cancer diagnosis is discussed.

Keywords: breast cancer, accessible methods of synthesis, nanoparticles, early diagnosis, hydrothermal, artificial breast tissue.

1. Introduction

Cancer is a complex disease where a group of cells in the human body tend to grow out of control. It is known that one of the most common cancer-associated death among women is the breast cancer in the world. Invasive ductal carcinoma and invasive lobular carcinoma are the two main kinds of cancer found in the breast of women. These cancer cells begin in ducts and lobules parts of the breast, respectively [1]. A variety of factors, mainly genetic, aging, and environmental factors, are associated with the initiation and progression of breast cancer. The new cases of breast cancer patients have been rising day by day. However, the death rate through breast cancer is reduced by 43 % during 1990-2020 due to the development of various types of therapies for the early detection and monitoring of patients [2]. Generally, breast cancer is diagnosed using various techniques, namely breast ultrasound, diagnostic mammogram, imaging techniques, biopsy, etc. The imaging techniques are suitable for the detection of early breast cancer stages, which include mammography, positron emission tomography (PET), magnetic resonance imaging (MRI), computed tomography (CT) scan, and single-photon emission computed tomography (SPECT) scan, ultrasound, and X-rays, among others . These imaging technologies constitute a tool for determining the type and stage of breast cancer by the creation of visual representations from the mama and the medical interpretation of these medical analyses. Among these imaging techniques, the mammography technique has been attractive for the detection of cancers at an early stage of development that can reduce the risk of dying due to breast cancer disease. The mammography imaging technique utilizes a low-dose X-ray system as a source for visualizing the tissue inside the breasts [3]. It contains several advantages (i.e., high sensitivity and specificity, inexpensive, well tolerated, etc.) for diagnosis and monitoring of patients in the early stages of cancer. Besides these various benefits, mammography imaging is limited by technical performance, quality of practices, and the patient-centered way of working. It has been shown from previous studies that the utilization of external substances or materials or nanomaterials will be needed for developing emerging opportunities.

Breast cancer detection is categorized into three distinct stages: identification of an abnormality in the breast tissue by an imaging technique (usually mammography), diagnosis of cancer using imaging modalities plus a biopsy assay, and characterization of abnormalities to determine a prognosis and an appropriate course of treatment [4 – 6]. Mammography is designed for detecting breast cancer

using radiographic examination. The performance of mammography imaging has been improving for several decades by developing advanced detector technologies and powerful computers [7, 8]. Recently, digital mammography is used for the early detection of breast cancer, which offers the promise of revolutionizing mammography imaging and effective screening through its superior dose, diagnostic accuracy, and control performance. The physical principles of mammography are connected with breast composition, radiation energy, X-ray spectra, compression, scattered radiation control, and magnification [9]. Breast tissue is composed of milk glands, ducts and lobules, fatty tissues, and supportive tissues. Depending on the compositions of these components, breast tissue is divided into dense breast tissue and non-dense breast tissue. Mammography is helpful to detect early breast cancer by determining the ratio of non-dense tissue and dense tissue. Mammography uses X-rays to get images from breast tissue, which has a modest impact on contrast. The shape of the X-ray spectrum in mammography is dependent on the energy of applied potential and target/filter combination [9, 10]. Higher X-ray energies can provide lower doses or better image quality even for patients with dense breasts. The energies of X-rays used in mammography are generally found in the range of 22-49 keV. Therefore, finding the optimum X-ray spectrum provides valuable information about image quality and dose efficiency. Breast compression is another important parameter in mammography imaging techniques. For effective early breast cancer detection, the amount of exposed breast tissue should be increased. Breast compression reduces radiation or improves image quality by lowering scatter radiation, geometric blurring, and anatomical super-position [2, 9]. After interacting X-rays with the breast tissues, the radiation will be scattered in various directions. More scattered radiation produces by denser and thicker glandular tissue than by the thinner, fatty, and transparent tissues. To get high-contrast imaging, lower amounts of scattered radiation are preferred. The grid generally consists of strips of lead, which are used to reduce undesired scattered radiation that damages the image quality. The performance of image quality is related to the grid ratio (i.e., the ratio of strip height to strip spacing). The greater grid ratio is suitable to achieve the high efficiency of the grid and required radiation dose [9]. The increment of image quality is performed by reducing breast thickness and air-gap technique. The imaging radiation then reaches the image receptor system that consists of a single intensifying screen with a luminescent coating and a special single-emulsion film. The film must be exposed to the proper film-screen system and radiation quality to visualize the diagnosis in the optimum range. Afterward, film processing is required for changing the image contrast, fog, noise, and sensitivity. Solid-state detectors are utilized to record the scattered radiation that converts

the scattered radiation into electronic signals. These electronic signals are sent to a computer for displaying images on the monitor. The analysis of image quality can visualize the characteristic morphology of a mass, the shape and spatial configuration of calcifications, distortion of the normal architecture of the breast tissue, the asymmetry between images of the left and right breasts, development of anatomically definable new densities [10]. The quantitative and qualitative descriptions of image quality are influenced by the nature of the X-ray spectrum, X-ray absorption properties at the anatomic region, geometric sharpness, the resolution characteristic curve, noise properties of the imaging system, etc. The complete process of the mammography imaging technique is presented in Figure 1. All the parameters used in mammography should be optimized properly to achieve effective resolution of the image so that it will be useful for detecting cancer present in the breast.

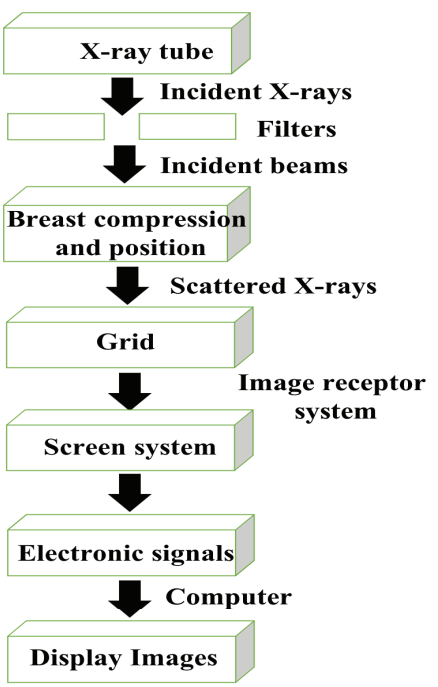

Figure 1. Components of mammographic imaging techniques.

Nowadays, the development of new testing devices as well as materials has been improved for facilitating the detection of cancer. Nanotechnology is a growing field of research, which involves the understanding and control of matter at the nanometer scale [11]. Nanotechnology offers new opportunities for the

reduction of cost, working time, as well as environmental pollution. Nanocarriers used for cancer diagnosis and therapeutic cancer drugs are divided mainly into organic and inorganic, which are made from lipids, polymers, proteins nucleic acid, metals, carbon, micelles, liposomes, dendrimers, and nanoparticles [12, 13]. The development of these nanoparticles is dependent on various factors, such as the shape and size of the particle, surface chemistry, composition, potential, elasticity, etc. Many of the applications of nanotechnology utilize nanomaterials for designing devices and systems due to their unique physical as well as chemical properties. Nanomaterials are characterized by unique physicochemical properties, such as small feature size in the range of 1-100 nanometers, large surface area to mass ratio, and high reactivity that can be metals, ceramics, biomaterials, polymeric materials, or composite materials. These properties of nanomaterials make them different from bulk materials in general design processes and their objectives. Based on dimensions, nanomaterials are divided into four different classes: zero-dimensional nanomaterials (i.e., quantum dots, fullerenes, and nanoparticles, etc.), one-dimensional nanomaterials (i.e., nanotubes, nanofibers, nanorods, nanowires, and nanohorns, etc.), two-dimensional nanomaterials (i.e., nanosheets, nanofilms, and nanolayers, etc.), three-dimensional nanomaterials (i.e., bulk powders, dispersions of nanoparticles, arrays of nanowires and nanotubes, etc.) [3, 13]. The variety of nanomaterials and their new properties have been applied from extraordinarily tiny electronic devices to biomedical devices. Nanomaterials can serve as vehicles for the delivery of therapeutic agents, detectors, or guardians against early disease and perhaps repair of metabolic or genetic defects. Various types of nanomaterials, namely nanoparticles (i.e., Ag, Au, SiO_2, TiO_2, Fe_2O_3, etc.), quantum dots, carbon structures (i.e., graphene, graphene oxide), dendrimers, and nanogels (i.e., polypeptides, collagen) have been using since several decades for medical imaging. With growing advances in mammography imaging, several nanomaterials using different nanoparticles of gold, silver, platinum, aluminum, palladium, copper, iron, silica, gold-coated Fe_3O_4, gold-silver alloy, silver sulfide, silica encapsulated silver, etc. have been employed by various research groups [11 – 16]. Nanomaterials are also used as imaging agents. The use of these nanomaterials in early cancer detection and therapy is promising to overcome the limitations found in the conventional diagnosis methods and identification of abnormalities.

There are several examples of nanomaterials that have been used to enhance the detection and diagnosis of cancers, namely quantum dots, carbon-based nanomaterials (carbon nanotubes, buckyballs, nanodiamond), metal- or oxide-based nanomaterials (gold, silver, aluminum, magnetic iron oxide, titanium

dioxide, zinc oxide, silica, etc.), liposomes, and polymer-based nanomaterials (polysaccharides, polypeptides, polyelectrolytes, dendrimers, and polynucleotides). These nanomaterials have desirable characteristics that facilitate their use for screening and imaging. These nanomaterials contain unique characteristic properties, namely small size and shape in nanoscale, large surface area to mass ratio, increased fraction of atoms at the surface, chemical compositions, multifunctional capabilities, and high reactivity. The mechanical properties (i.e., strength, brittleness, hardness, toughness, fatigue strength, plasticity, elasticity, ductility, rigidity, yield stress, etc.), thermal properties (thermal conductivity, thermoelectric power, heat capacity, and thermal stability, etc.), magnetic properties (diamagnetic, paramagnetic, ferromagnetic, antiferromagnetic, ferrimagnetic, etc.), electrical, optical, and catalytic properties are the most important physicochemical properties of nanomaterials [13, 17, 18]the understating of nanotechnology, cancer biology, immunomedicine, and nanoparticle surface chemistry has provided a better clue to prepare the effective immuno-nanomedicine for cancer therapy. Moreover, the selection of nanoparticles type and its composition is essential for development of efficient drug delivery system (DDS. These properties are mainly dependent on the size and shape of nanomaterials, which are different from bulk materials of the same composition. For improving the contrast in mammography imaging, various properties of nanomaterials have been studied thoroughly. The nanomaterials should have the properties, such as small size and shape, high X-ray absorbance, low cytotoxicity, high permeability and retention, chemically inert, high adaptability, strong near-infrared absorber, ability to alter electromagnetism properties, easily controlled features, high stability, good tolerability, etc. for contrast enhancement [3, 18]including in ultrasonography, computed tomography, scintigraphy, and magnetic resonance imaging. Nanoparticles have become more prevalent in reports of novel contrast agents, especially for molecular imaging and detecting cellular processes. Fluorescent nanoparticles can easily be tuned for specific imaging purposes. They offer a more intense fluorescent light emission, longer fluorescence lifetimes, and a much broader spectrum of colors than conventional fluorophores. Nanoparticle contrast agents for ultrasound have also been developed, which may enhance the sensitive detection of vascular and cardiac thrombi, as well as solid tumors of the colon, liver, and breast, in a noninvasive manner. Most common materials that have been used for the development of photo-based nanoparticles (NPs. To enhance the quality of imaging compared with the conventional technique, various techniques, namely a combination of nanomaterials with a superconducting quantum interface device, metal alloys, a

combination of metal nanoparticles with semiconductors, magnetic nanoclusters, etc. are also employed. With these recent developments for enhancing contrast, nanomaterials could improve the chances of locating tumors, and tracking their levels and microcalcifications in the breast tissue with high selectivity, special resolution, and sensitivity for early detection [12]. Although these nanomaterials are promising in the field of medical imaging, the use of nanomaterials is limited by their cost, time, safety, and complexity. Various types of nanomaterials, such as thin films, multilayers, nanotubes, nanofilaments, nanometer-sized particles, etc. have been synthesized by many different techniques. The choice of the particular synthesis techniques for nanomaterials depends on diverse features such as source materials, nature of substrate, required film thickness, specific application of nanomaterials, material's purity, material's stability, repeatability, uniformity, flexibility, etc. These features are directly related to the material properties and production costs. Depending on the quality of synthesized nanomaterials and fabrication cost, techniques for the synthesis of nanomaterials are generally divided into two categories: physical-based and chemical-based techniques. The physical-based methods like thermal evaporation, sputtering, molecular beam epitaxy, pulsed laser deposition, etc., are normally designed to synthesize high-quality materials with fewer impurities, showing more reliable and reproducible techniques. Electrochemical processes, chemical polymerization, sol-gel, chemical vapor deposition, colloidal dispersion, hydrothermal route, etc., are some examples of chemical-based techniques for the synthesis of nanomaterials. Solution-based techniques possess cost-effective devices due to their simplicity of the deposition process, ease to handle, require less energy usage, better material utilization, and use of potentially low energetic incentives (i.e., low substrate temperatures, atmospheric environment, etc.). The completed information about these methods and their respective advantages, disadvantages, and types of nanomaterials to be synthesized is found in the reported literature [1, 19, 20]. The synthesis of nanomaterials is a complex process, which can be categorized into various steps: generation of the atoms/molecules from the source, transport of the source atoms/molecules to the substrate (or container), nucleation process, and growth of nanomaterials. At present, the synthesis techniques play a vital role in controlling the structures of nanomaterials at the nanoscale. The optical, electrical, magnetic, biological, structural, and morphological properties of nanomaterials can be tailored depending on the synthesis techniques and synthesis parameters. Based on these properties, nanomaterials can be used in a variety of applications. Image processing is a vital step in the quantification of structural features from images. Morphology is another

technique of image processing, which is based on the shape and form of objects. Generally, morphology utilizes a structuring element to an input image for creating an output image of the same size. Morphological operations such as erosion, dilation, opening, and closing are used to perform morphological image analysis [21]. The Breast Imaging-Reporting and Data System classified mammographic features into various categories of morphology, namely punctuated (round or oval shape), amorphous (rounding or flaking shaped), coarse heterogeneous (irregular and conspicuous), fine pleomorphic (more conspicuous), and fine linear and fine linear branching (thin, irregular linear) [22]. These morphologies are mainly dependent on the size and shape of images. The formation of an image of an object or breast cancer tissue involves different steps, such as capturing the image, digitization, transmission, etc. The technique adopted for enhancing the quality of an image is also called contrast enhancement. Numerous contrast enhancement methods, namely, histogram stretching or histogram equalization technique, algorithms, thresholding, classical image filtering, wavelet transformation, mathematical morphology techniques, multifractal models, etc., have been proposed to improve the contrast of images [21 – 26]. All these techniques are designed to improve the contrast of images by analyzing multicomponent images, removing the noise in high frequency, increasing the distribution of gray levels, analyzing the quantitative description of complex structures, minimizing the homogeneity of co-occurrence matrix of the original image, sharpening medical images, removing the clouds to achieve more clarity, among others. Recently, techniques based on mathematical morphology are applied for contrast enhancement due to their advantages over other techniques for providing better visualization of images. Mathematical morphology uses mathematical principles and relationships to extract the components of images, which are based on the structural properties of objects [23, 24]. It uses an input image and processing operator for image processing that involves selective extraction of the features followed by contrast enhancement.

2. Experimental procedure

Two materials were explored: (1) Mn_3O_4, and (2) $MnFe_2O_4$ nanoparticles. To synthesize the Mn_3O_4 nanoparticles, manganese (II) chloride, deionized water with 18 MΩ as resistivity value, two inches epi ready silicon wafers (1 0 0) were commercially acquired from MERK (SIGMA-ALDRICH). On the other hand, to obtain the $MnFe_2O_4$ nanoparticles, iron chloride, and manganese chloride

were used as metal sources, and sodium dodecyl sulfate, ethanol, and sodium hydroxide, were commercially obtained from the same provider. The functionalization of nanoparticles with silicon oxide was performed by using ammonia, and tetraethyl orthosilicate, which were commercially obtained. In addition, artificial breast tissue was made based on our previous work [27] to evaluate the behavior of synthesized materials. Thus, xylene, benzalkonium chloride, ammonium hydroxide, alumina, hydrogen peroxide, acetone, glycerin, agar, silicon carbide, and methanol were commercially acquired from MERK (SIGMA-ALDRICH). All the reagents were used without further purification process.

To raise the Mn_3O_4 nanoparticles the known spray pyrolysis methodology was employed according to our previously reported methodology [28]. Thus, the manganese chloride was used to prepare a 0.5 M aqueous solution. The solution was fogged to nebulize the substance and guide it by a 21 % Oxygen flux to the surface of a silicon substrate at 450 °C. Then, the sample was cleaned in a subsequent bath of ethanol and water. Finally, it was dried in nitrogen flux. To collect the nanoparticles, the sample was undergone in an ultrasonic source for 30 min and then, was centrifugated at 10,000 RPM for 10 min. On the other hand, to raise the $MnFe_2O_4$ nanoparticles the hydrothermal method was used following the procedure reported in our previous research work [29]. Thus, manganese chloride and an iron chloride solution were made in water. Afterward, the solutions were mixed in a proportion of 2:1 for Fe: Mn and bubbled for 30 min with a 21 % oxygen atmosphere. The solution was placed in an autoclave for performing the hydrothermal methodology. The entire system was heated to 180 °C for 4h to obtain nano-icosahedrons. The sample was recovered after synthesis and cleaned by a subsequent bath of ethanol and water. Then, it was dried into a 20 L/ min nitrogen flux.

For functionalization with SiO_2, both kinds of nanoparticles were placed in a chemical water according to the procedure previously reported [29]. Ethanol, deionized water, and ammonia were mixed in a rate of 20:20:4 respectively. The mix was sonicated for 10 min to homogenize it. Then, the nanoparticles, Mn_3O_4 and $MnFe_2O_4$, were combined with tetraethyl orthosilicate plus the mix previously obtained in separately events. The mix was held at room temperature and was stirred for 8 h to bring the Mn_3O_4 nanoparticles-SiO_2 and $MnFe_2O_4$ nanoparticles-SiO_2 complex, respectively.

The artificial breast tissue (ABT) was made from the reagents shown in Table 1. Thus, benzalkonium chloride, glycerin, and water were placed in a beaker and

mixed at 30 °C. Afterward, alumina powder with an average diameter of 1 μm and 0.3 μm was mixed separately with silicon carbide and agar. Both mixings were incorporated to constitute the ABT at 91 °C with constant stirring of 40 RPM/min for 3 h. Then it was cooled down in the water for 1 h and then was placed on a surface at room temperature. The dispersion of the nanoparticles was studied before and after functionalization with SiO_2.

Table 1. List of reagents and materials with the corresponding proportion used to constitute the artificial breast tissue.

Chemical Reagent	Wt. % composition
deionized water	82.97
Glycerin	11.21
benzalkonium chloride	0.46
Agar	3
silicon carbide (17 μm)	0.53
alumina (particle size of 1 μm)	0.95
alumina (particle size of 0.3 μm)	0.88

All the samples were characterized by X-ray diffraction (XRD, Bruker D8 Eco Advance diffractometer) by using a radiation Cu kα = 1.5418 Å, scanning electron microscopy (SEM, JEOL 7401F microscope) with a system for energy dispersive X-ray spectroscopy (EDS), dynamic light scattering (DLS, an Anton Paar Litesizer 500), transmission electron microscopy (TEM, JEOL ARM200F), X-ray photoelectron spectroscopy (XPS, Thermo Fisher Scientific K-alpha model) with Al kα monochromatic beam as beam source, and atomic force microscopy (AFM, SOL instruments NT-MDT model).

3. Results and discussion

To analyze the morphology of nanoparticles, scanning electron microscopy images were recorded. Figure 2a and b shows the comparison between the Mn_3O_4 and $MnFe_2O_4$ nanoparticles, where both kinds of nanoparticles are obtained with a high grade of dispersion. Transmission electron microscopy images evidence in great detail the morphology of as synthesized nanoparticles, where the Mn_3O_4 nanoparticles have a sphere-like shape (Figure 2c) and the $MnFe_2O_4$ nanoparticles have an icosahedron-like shape. The difference in shape could be attributed to the methodology due to Mn_3O_4 nanoparticles being synthesized

by spray pyrolysis and $MnFe_2O_4$ nanoparticles being obtained by hydrothermal method. Morphology could have an important effect on the application as a contrast enhancement agent in mammography images because of the surface charge linked to the staking of materials [30].

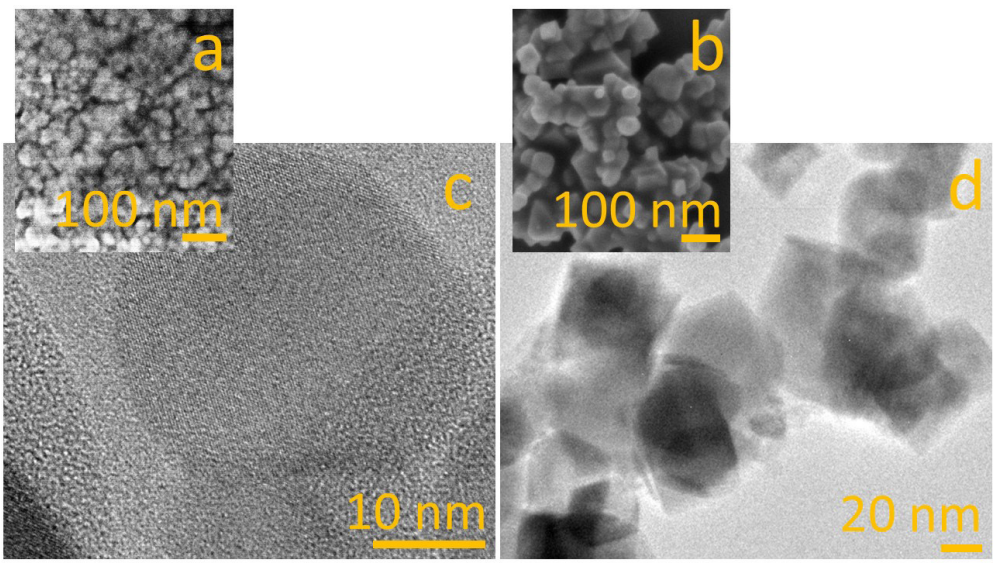

Figure 2. Scanning electron microscopy images of (a) Mn_3O_4 and (b), $MnFe_2O_4$ nanoparticles. Transmission electron microscopy images of (c) Mn_3O_4 and (d), $MnFe_2O_4$ nanoparticles.

The phase present in the samples was analyzed by X-ray diffraction. Figure 3 shows a comparison between the signal obtained from the Mn_3O_4 and $MnFe_2O_4$ nanoparticles. The diffraction of (011), (112), (013), (121), (004), (220), (015), (231), (033), (224), (125), (040) and (143) planes were found in good agreement for Mn_3O_4 phase [28]. The (220), (311), (400), (422), (511), and (440) planes are in good agreement for the cubic phase of $MnFe_2O_4$ [29]. In addition, the elemental contents were analyzed by energy dispersive X-ray spectroscopy (EDS), finding the elemental proportion according to Mn_3O_4 and $MnFe_2O_4$ phase, Figure 3b and 3c, respectively. Thus, the nanoparticles have a homogeneous phase according to obtained results.

Moreover, the $MnFe_2O_4$ nanoparticles were characterized by X-ray photoelectron spectroscopy (XPS) in four different morphologies: (i) flakes, (ii) rough-octahedrons, (iii) regular-octahedrons, and (iv) icosahedrons. Figure 4 shows the comparison between the recorded signal of the different analyzed morphologies. As can be seen in Figure 4, the proportion rate between the Fe and Mn ions is different among the samples. On the other hand, the oxygen signal (after applying

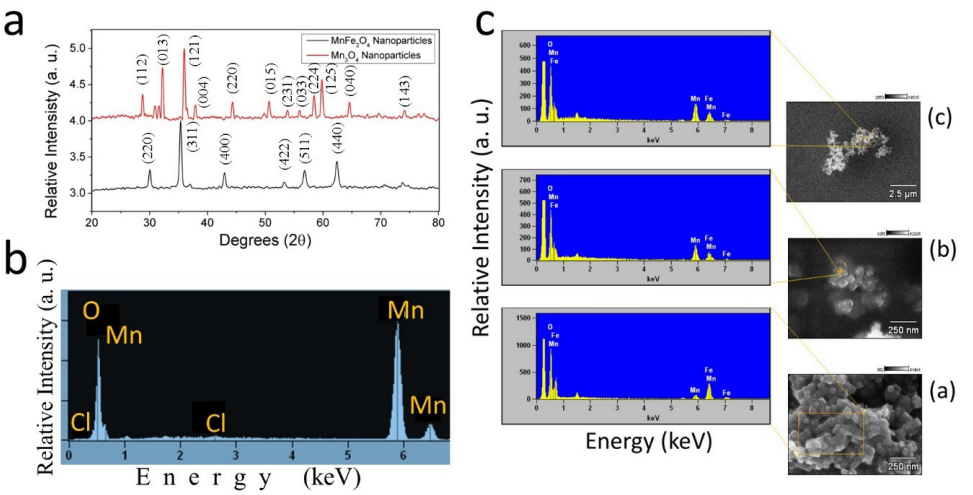

Figure 3. (a) XRD pattern comparison between Mn_3O_4 (red) and $MnFe_2O_4$ (black) nanoparticles. EDS spectra of (b) Mn_3O_4 nanoparticles and (c) $MnFe_2O_4$ nanoparticles.

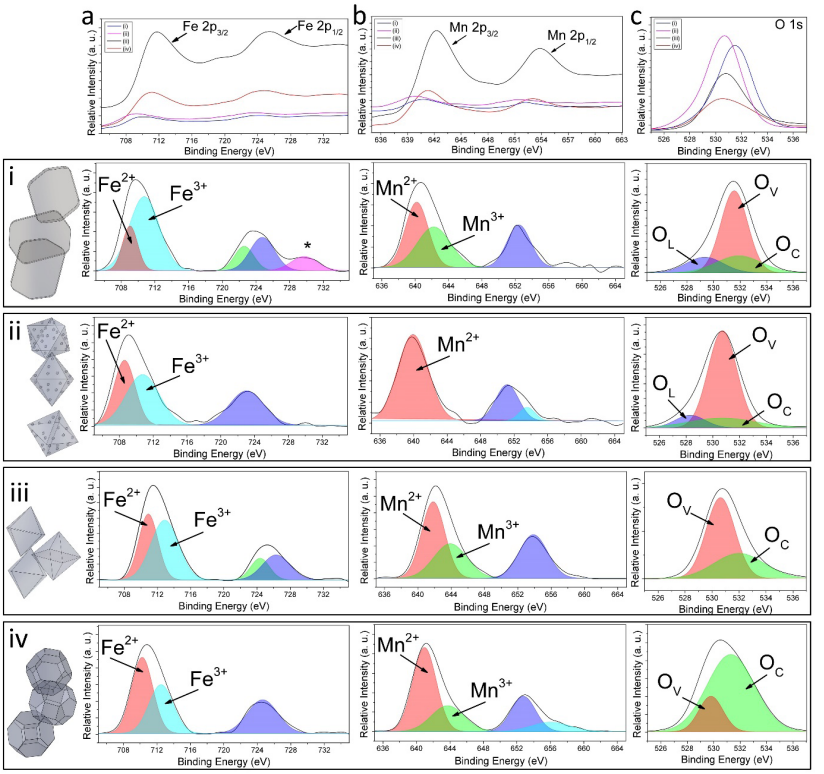

Figure 4. XPS spectra of $MnFe_2O_4$ nanoparticles (a) 705–735 eV, (b) 635–665 eV, and (c) 525–537 eV BE range. The gaussian fit of XPS spectra was recorded from different morphologies: (i) flakes, (ii) rough-octahedrons, (iii) regular-octahedrons, and (iv) icosahedrons. Taken from reference [29].

a Gaussian fit) unveils a strong difference in the oxygen components, and oxygen vacancy density could be the main factor linked to morphology [31, 32]. This variation in oxygen vacancies can confer an enhancement for distribution into the breast tissue and for functionalization toward drug carriers' formation.

The artificial breast tissue (ABT) is shown in Figure 5a. Figures 5b and c show a comparison between two dispersions of nanoparticles into the ABT (1 μg/mL, and 600 μg/mL). And Figures d and e show the profile of the selected region. Can be seen a clear difference in nanoparticles once they are incorporated into the ABT. The nanoparticles are well incorporated into the ABT as can be seen in the TEM image (see Figure 5f). Figures 5g and 5h show the distance between the nanoparticles according to the concentration induced by the ABT. The nanoparticles can be dispersed according to the concentration rate in the ABT, this is useful for contrast enhancement application due to dispersion guarantee a major efficiency in the material employed for this application.

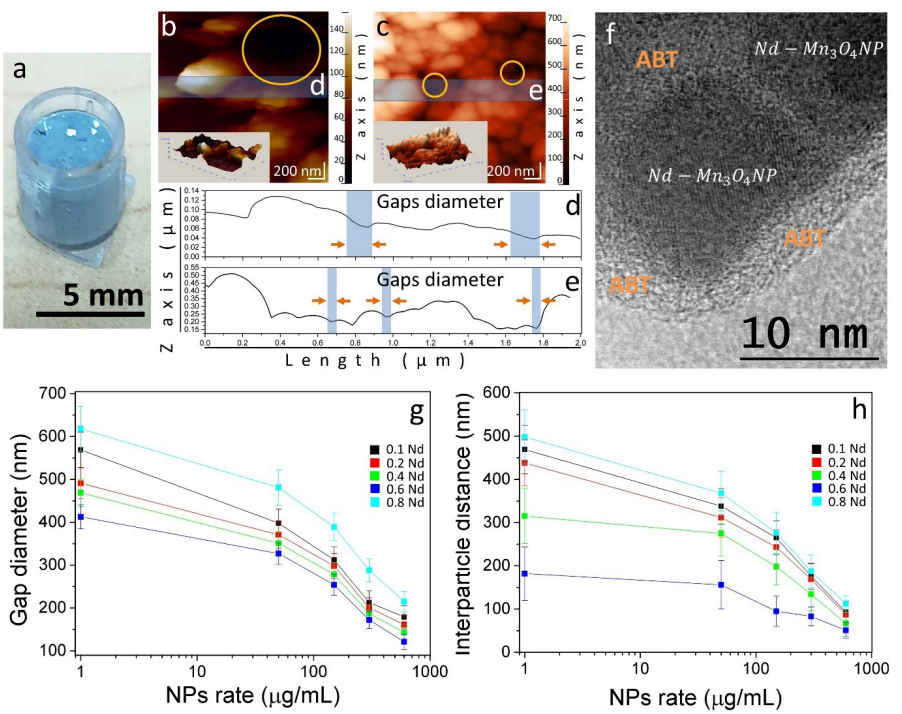

Figure 5. (a) Photograph of the ABT with nanoparticles incorporated. AFM image of Mn_3O_4 nanoparticles into ABT with a nanoparticle mass rate of (b) 1 μg/mL and (c) 600 μg/mL (Inserts show the 3D projection of shown area, respectively). The (d) and (e) show the roughness profile of sections depicted in (b) and (c), respectively. (f) Mn_3O_4 nanoparticles into ABT imaged by HRTEM. The relationship between the nanoparticles rate in ABT and (g) the size of the gaps, and (h) interparticle distance. Taken from reference [28].

Once the nanoparticles were functionalized, they were exposed to a breast cancer cell (BT_20 cell line) for 24 hours. After the time was reached, the sample was prepared for visualization in a transmission electron microscope. Figure 6 shows the nanoparticles inside the cell, this could be useful for specific targeting of breast cancer disease and specific targeting.

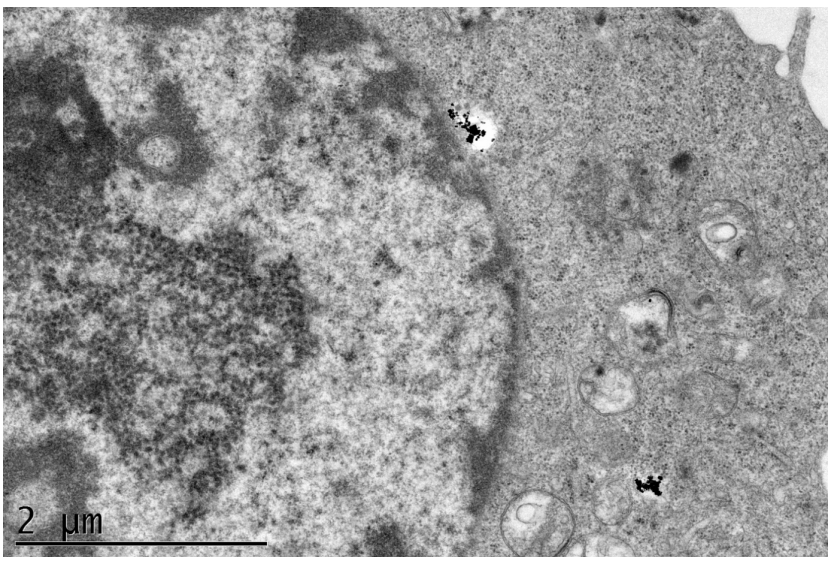

Figure 6. Transmission electron microscopy image of a breast cancer cell after 24 h of interaction with Mn_3O_4 and $MnFe_2O_4$ nanoparticles.

4. Conclusions

This chapter described detailed information about mammography imaging for early breast cancer detection. Although the mammography imaging technique is efficient for identifying cancer tissue, it will not always provide the best resolution of images due to the complex structure of human tissue. Therefore, the use of nanomaterials in mammography imaging will be a promising alternative as a contrast agent to detect abnormal tissue appropriately. Many studies regarding the use of different nanomaterials in mammography imaging have been found to improve the performance of imaging techniques. Despite the development of more nanomaterials in mammography imaging, the use of these nanomaterials is still associated with some limitations regarding synthesis techniques for commercialization, sensitivity, specificity, etc. To solve these challenges or limitations, highly dynamic synthesis techniques and optimization of synthesis parameters for nanomaterials should be done to get high-quality material at low-cost. Since

nanomaterials can greatly improve the survival rates for breast cancer patients, future studies should also aim at their features, their safety and efficacy profile, their potential applications, their experimental observations, etc. The Mn_3O_4 (red) and $MnFe_2O_4$ nanoparticles can be applied for contrast enhancement in mammography images for early breast cancer diagnosis.

Acknowledgement and Funding

The authors acknowledge the Consejo Nacional de Humanidades, Ciencia y Tecnología (CONAHCYT) for the economic support to this work through the FORDECYT-PRONACES/6005/20 project. The authors also thank the Secretaría de Investigación y Posgrado of the IPN for the partial financial support to this research.

References

1. Mukhopadhyay, S., & Chanda, B. (2000). A multiscale morphological approach to local contrast enhancement. *Signal Processing*, 80(4), 685-696. https://doi.org/10.1016/S0165-1684(99)00161-9
2. Wang, L. (2017). Early diagnosis of breast cancer. *Sensors* (*Switzerland*), 17(7). https://doi.org/10.3390/s17071572
3. Keservani, R. K., Kesharwani, R. K., & Sharma, A. K. (2016). Nanobiomaterials involved in medical imaging technologies. In: *Nanomaterials in Medical Imaging*, 303-337. Elsevier Inc. https://doi.org/10.1016/B978-0-323-41736-5.00010-8
4. Yaffe, M. J. (1990). AAPM tutorial. Physics of mammography: image recording process. *Radiographics*, 10(2), 341-363. https://doi.org/10.1148/radiographics.10.2.2183301
5. Jacobs, L., & Finlayson, C. (2010). Early Diagnosis and Treatment of Cancer Series: Breast Cancer-E-Book: Expert Consult. Elsevier Health Sciences. ISBN: 9781437736106 https://books.google.com.mx/books?id=LCqw_pJc5MIC
6. Paci, E. (2002). Mammography and Beyond: Developing Technologies for Early Detection of Breast Cancer. *Breast Cancer Research*, 4(3), 123-125. https://doi.org/10.1186/bcr429
7. Hansmann, M., Hackelöer, B.-J., & Staudach, A. (1986). Diagnosis of Breast Disease. *Ultrasond Diagnosis in Obstetrics and Gynecology*, 407-428. https://doi.org/10.1007/978-3-642-70423-9_18
8. Oliver A., Freixenet, J., Martí, J., Pérez, E., Pont, J., Denton, R. R. E. *et al.* (2010). A review of automatic mass detection and segmentation in mammographic images. *Medical Image Analysis*, 14(2), 87-110. https://doi.org/10.1016/j.media.2009.12.005
9. Heywang-köbrunner, S. H., Dershaw, D. D., & Schreer, I. (2001). Diagnostic breast imaging Mammograpghy, sonograpghy, magnetic resonance imaging, and interventional procedures. *Journal of Medical Radiation Sciences*, 62(1), 86-87. https://doi.org/10.1002/jmrs.90
10. Jafari, S. H., Saadatpour, Z., Salmaninejad, A., Momeni, F., Mokhtari, M., Nahand, J. S. *et al.* (2018). Breast cancer diagnosis: Imaging techniques and biochemical markers. *Journal of Cellular Physiology*, 233(7), 5200-5213. https://doi.org/10.1002/jcp.26379
11. Han, X. Xu, K. Taratula, O., & Farsad, K. (2019). Applications of nanoparticles in biomedical imaging, *Nanoscale*, 11(3), 799-819. https://doi.org/10.1039/C8NR07769J

12. Zeineldin, R. (2020). Nanotechnology for cancer screening and diagnosis: from innovations to clinical applications.
https://doi.org/10.1016/B978-0-08-102983-1.00010-7

13. Saravanakumar, K., Anbazhagan, S., Usliyanage, J. P., Naveen, K. V., Wijesinghe, U., Xiaowen, H. *et al.* (2022). A comprehensive review on immuno-nanomedicine for breast cancer therapy: Technical challenges and troubleshooting measures. *International Immunopharmacology*, 103, 108433.
https://doi.org/10.1016/j.intimp.2021.108433

14. Silva A. D. R., Stocco, T. D., Granato, A. E. C., Harb, S.. V., Afewerki, S., Bassous, N. J. *et al.* (2019). Recent Advances in Nanostructured Polymer Composites for Biomedical Applications. *Micro and Nano Technologies*, 21-52.
https://doi.org/10.1016/B978-0-12-816771-7.00002-8

15. Shahbazi, N., Zare-Dorabei, R., & Naghib, S. M. (2021). Multifunctional nanoparticles as optical biosensing probe for breast cancer detection: A review. *Materials Science and Engineering* C, 127, 112249.
https://doi.org/10.1016/j.msec.2021.112249

16. Chapman, S., Dobrovolskaia, M., Farahani, K., Goodwin, A., Joshi, A., Lee, H. *et al.* (2013). Nanoparticles for cancer imaging: The good, the bad, and the promise. *Nano Today*, 8(5), 454-460.
https://doi.org/10.1016/j.nantod.2013.06.001

17. Waller, J., DeStefano, K., Chiu, B., Jang, I., Cole, Y., Agyemang, C., et al, (2022). An update on nanoparticle usage in breast cancer imaging. *Nano Select*, 3(7), 1103-1111.
https://doi.org/10.1002/nano.202100320

18. Joudeh, N., & Linke, D. (2022). Nanoparticle classification, physicochemical properties, characterization, and applications: a comprehensive review for biologists. *Journal of Nanobiotechnology*, 20(1), 1-29.
https://doi.org/10.1186/s12951-022-01477-8

19. Tulinski, M., & Jurczyk, M. (2017). Nanomaterials Synthesis Methods. *Metrology and Standardization of Nanotechnology*, 1, 75-98.
https://doi.org/10.1002/9783527800308.ch4

20. Rane, A., V., Kanny, K., Abitha, V. K. & Thomas, S. (2018). Methods for Synthesis of Nanoparticles and Fabrication of Nanocomposites. In: *Synthetic of Inorganic Nanomaterials*. Elsevier Ltd.
https://doi.org/10.1016/B978-0-08-101975-7.00005-1

21. Sreedhar, K., & Panlal, B. (2012). Enhancement of Images Using Morphological Transformations. *International Journal of Computer Science and Information Technology*, 4(1), 33-50.
https://doi.org/10.5121/ijcsit.2012.4103

22. Hofvind, S., Iversen, B. F., Eriksen, L., Styr, B. M. Kjellevold, K., & Kurz, K. D. (2011). Mammographic morphology and distribution of calcifications in ductal carcinoma in situ diagnosed in organized screening. *Acta Radiologica*, 52(5), 481-487. https://doi.org/10.1258/ar.2011.100357

23. Reljin, B. Milošević, Z. Stojić, T., & Reljin, I. (2009). Computer aided system for segmentation and visualization of microcalcifications in digital mammograms. *Folia Histochemica et Cytobiologica*, 47(3), 525-532. https://doi.org/10.2478/v10042-009-0076-1

24. Kimori, Y. (2013). Morphological image processing for quantitative shape analysis of biomedical structures: Effective contrast enhancement. *Journal of Synchrotron Radiation*, 20(6), 848-853. https://doi.org/10.1107/S0909049513020761

25. Kimori, Y. (2011). Mathematical morphology-based approach to the enhancement of morphological features in medical images. *Journal of Clinical Bioinformatics*, 1(1), 1-10. https://doi.org/10.1186/2043-9113-1-33

26. Hassanpour, H., Samadiani, N., & Mahdi Salehi, S. M. (2015). Using morphological transforms to enhance the contrast of medical images. *Egyptian Journal of Radiology and Nuclear Medicine*, 46(2), 481-489. https://doi.org/10.1016/j.ejrnm.2015.01.004

27. Gaona-Esquivel, A., Hernandez-M, D. M., Hernández-Rodríguez, Y. M., & Cigarroa-Mayorga, O. E. (2022). The role of Nd as a dopant in Mn_3O_4NPs on the heat induction of artificial breast tissue due to the irradiation of microwaves. *Materials Chemistry and Physics*, 292, 126822. https://doi.org/10.1016/j.matchemphys.2022.126822

28. Gaona-Esquivel, A., Hernández-M, D., Sánchez-Trujillo, P. J., Cigarroa-Mayorga, O. E., & Meléndez-Lira, M. (2020). Hyperthermia Effect on Phantom of Breast Carcinoma Tissue Induced by Mn_3O_4 Nanoparticles Synthesized by One-Step Spray Pyrolysis Method. *Key Engineering Materials*, 853, 56-60. https://doi.org/10.4028/www.scientific.net/KEM.853.56

29. Cigarroa-Mayorga, O. E. (2021). Tuning the size stability of $MnFe_2O_4$ nanoparticles: Controlling the morphology and tailoring of surface properties under the hydrothermal synthesis for functionalization with myricetin. *Ceramics International*, 47(22), 32397-32406. https://doi.org/10.1016/j.ceramint.2021.08.139

30. Palomino, J., Varshney, D., Weiner, B. R., & Morell, G. (2015). Study of the structural changes undergone by hybrid nanostructured Si-CNTs employed as an anode material in a rechargeable lithium-ion battery. *Journal of Physical Chemistry C*, 119, 21125-21134. https://doi.org/10.1021/acs.jpcc.5b01178

31. Raj, A.M.E., Victoria, S.G., Jothy, V.B., Ravidhas, C., Wollschläger, J., Suendorf, M. *et al.* (2010). XRD and XPS characterization of mixed valence Mn_3O_4 hausmannite thin films prepared by chemical spray pyrolysis technique. *Applied Surface Science*, 256(9), 2920-2926. https://doi.org/10.1016/j.apsusc.2009.11.051

32. He, M., Zeng, Y., Zhou, F., Kong, G., Lu, Y., Chen, W. *et al.* (2020). $MnFe_2O_4$ nanoparticles anchored on the surface of MgAl-layered double hydroxide nanoplates for stable magnetorheological fluids *Journal of Molecular Liquids*, 319, 114098. https://doi.org/10.1016/j.molliq.2020.114098

Chapter 3 Health Area

THERMAL STUDY OF NANOCOMPOSITES FOR MEDICAL APPLICATIONS

José Luis Luna Sánchez[1], José Luis Jiménez Pérez[1*], Zormy Nacary Correa Pacheco[2], Omar Usiel García Vidal[1], Ruben Gutiérrez Fuentes[3], Genaro López Gamboa[4], Misha Jessica del Castillo Aguirre[1], Rigoberto Carbajal Valdez[5], Alfredo Cruz Orea[5]

[1]Unidad Profesional Interdisciplinaria en Ingeniería y Tecnologías Avanzadas-Instituto Politécnico Nacional, Av. Instituto Politécnico Nacional No. 2580, Col. Barrio la Laguna Ticomán, Alcaldía Gustavo A. Madero, C.P. 07340, Ciudad de México, México.

[2]Centro de Desarrollo de Productos Bióticos-Instituto Politécnico Nacional. Centro de Desarrollo de Productos Bióticos. Carretera Yautepec-Jojutla, km. 6, Calle CEPROBI, No. 8, San Isidro, Yautepec, C.P. 62731, Morelos, México.

[3]Tecnológico Nacional de México Campus Toluca, dirección Avenida Tecnológico s/n. Colonia Agrícola Bellavista, Metepec, C.P. 52149, Estado de México, México.

[4]Instituto Tecnológico de Toluca, Avenida Tecnológico s/n. Colonia Agrícola. Bellavista, La Virgen, CP 52149 Metepec, Estado de México, México.

[5]Departamento de Física, CINVESTAV-IPN, Av. Instituto Politécnico Nacional, No. 2508, Col. San Pedro Zacatenco, 07360, Estado de México, México.

jimenezp1957@gmail.com

Luna Sánchez J. L., Jiménez Pérez, J. L., Correa Pacheco, Z. N., García Vidal, O. U., Gutiérrez Fuentes, R., López Gamboa, G. et al (2023 Thermal study of nanocomposites for medical applications. In E. San Martín-Martínez (Ed.). *Research advances in nanosciences, micro and nanotechnologies. Volume IV* (pp. 73-92). Barcelona, Spain: Omniascience.

Abstract

Technological advances in stereolithography 3D printing have allowed the development of new composites. Nowadays the trend is toward composites containing nanostructures modifying their physicochemical properties while maintaining their processability. In this work, the elaboration and characterization of silver nanoparticles (AgNPs) and silver nanowhiskers (AgNWs) and its nanocomposites in an acrylic resin is presented. The AgNPs were synthesized using a green method from Jalapeño Chili (Capsicum Annuum var Annuum) extract. The AgNWs were synthesized using the polyol method. Complementary studies were carried out to determine morphology, functional groups, the crystalline structure and the plasmon resonance by transmission electron microscopy (TEM), Fourier transform infrared spectroscopy (FTIR), X ray diffraction (XRD) and UV-vis spectroscopy, respectively. The resin nanocomposites were formulated with AgNPs or AgNWs at different concentrations and their thermal diffusivity was measured by Thermal Lens (TL). On the other hand, using photoacoustic spectroscopy (PAS), the characteristic curing time of the nanoresins was determined. It was found an increase in thermal diffusivity and curing time with the increase in concentration of the nanostructures and higher curing time for the AgNWs nanocomposite. on the curing process. Samples were printed using SLA to find possible applications in 3D printing structures for medical application.

Keywords: 3D printing, nanocomposites, thermal properties, physicochemical characterization

1. Introduction

In the 80's a new manufacturing process to obtain solid prototypes from 3D digital images with relative high speed and ease of printing was developed. Layer by layer, thin films of a polymeric material, which is sensitive to UV light, are deposited. After the process is repeated many times, a solid piece of cured polymer is obtained, although curing time is short. Moreover, cost-energy savings are high and complex pieces can be obtained [1, 2].

Usually, the size of the printed objects is between 5-30 cm; therefore, to obtain pieces in the millimeter scale, is necessary to modify the printing technique. This also depends on the material to be used and the process itself. There main 3D additive manufacturing technologies are material extrusion, material jetting, Vat photopolymerization, powder bed fusion, sheet lamination, directed energy deposition, and binder jetting [3].

The additive manufacturing, 3D printing, or rapid modeling is focused on reducing printing time and improving the properties of the printed material. Among its advantages are speed is faster than other techniques, cheapness, complex geometries for printed pieces are obtained, higher availability, reduction of waste material.

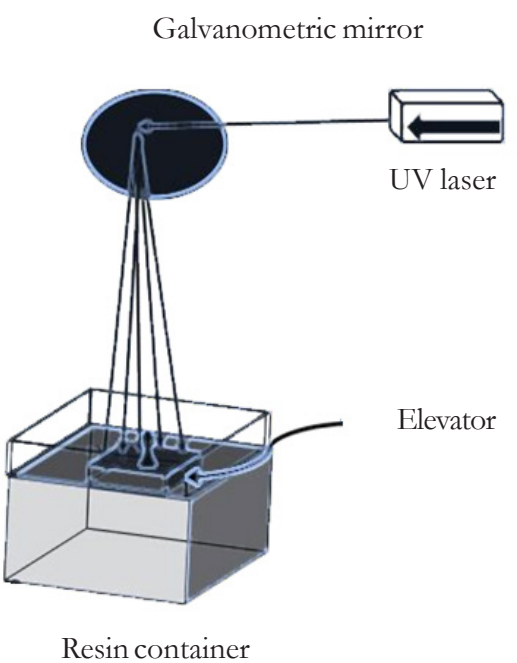

Figure 1. 3D printing by stereolithography.

On the other hand, among its disadvantages are limitations in materials used for printing, size limitation, accuracy, and is not possible mass production [4].

Among 3D additive manufacturing techniques, stereolithography (SLA) comes originally for lithography [5]. It uses the hydrophilic physical properties of a clay substrate on which the design is drawn with graphite. Due to the hydrophobic properties of graphite, the design is transferred from the clay plate to the substrate [6].

Nowadays, epoxy, vinyl or polyester resins are employed as well as bio-based resins based on starch, lactic acid or natural derivatives. In general, UV light and light-curing resins are used as shown in Figure 1. The laser light is directed by a galvanometric mirror which polymerizes the photocurable resin layer by layer by and UV laser, until the 3D figure is obtained.

The typical formulation for curing involves the use of a photo initiator, which generates the reactive species for starting the polymerization process, the monomers to be cured, and oligomers which can modify the structure of the resin [7]. The printed pieces currently have applications that range from biology to electronics and medicine [8]. The development of Nanotechnology has led the use resins in which nanometric-sized structures are incorporated, known as nanoresins or nanocomposites with the subsequent modification of the physicochemical properties of the final printed product. Metallic nanostructures such as Fe, Ti, Ag, Co and Au have been incorporated to polymers such as polyethylene and polylactic acid, among others. However, main problems faced up are poor incorporation of nanostructures into the polymer, agglomerations, changes in the size and shape of the nanostructures, before and during the polymer photocuring process [9].

Among photothermal techniques used to study the thermal properties and curing of resins used for 3D printing, photoacoustic (PA) and thermal lens (TL) are of special interest. In PA a beam of light in contact with a material causes a deformation on its surface with a subsequent expansion of the crystalline network and the release of energy in the form of waves in its surrounding environment. It is a sensitive and non-destructive technique. The experimental set up is shown in Figure 2. In this technique, a modulated beam of laser light hits the sample placed on a metal sheet generating thermal waves with pressure changes in the air adjacent to the metal sheet. Then, the acoustic signal produced is received by a microphone and sent to and amplifier for further processing [10 – 12].

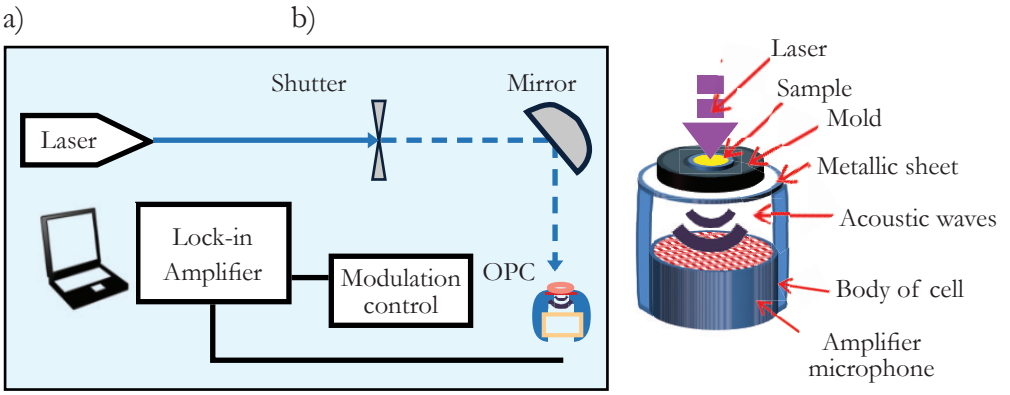

Figure 2. a) Experimental set up for PA. b) Open Cell Microphone (OPC).

Thermal lens (TL) is a phenomenon formed when a beam of laser light (pump laser) excites the sample. A second beam of laser light (probing laser) passes through that point being its trajectory modified due to the change in the refractive index caused by an increase in the temperature on the sample with respect to the surrounding environment [13 – 15]. The experimental set up is shown in Figure 3.

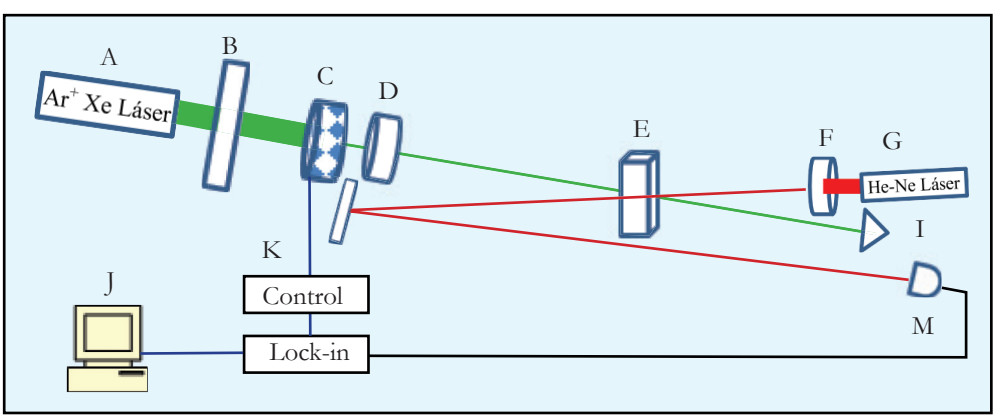

Figure 3. Experimental set up for TL: A) Ar^+ Xe ion pump laser, B) Filter, C) Shutter, D) Focusing lens 1, E) Liquid sample, F) Focusing lens 2, G) He-Ne probing laser, H) Mirror, I) Energy container, J) Computer, K) Shutter control, L) Lock-In, M) Detector.

The Fresnel theory as a function of time describes the TL phenomena as shown in Eq. 1.

$$I(t) = I(0) \cdot \left[1 - \frac{\theta}{2} \tan^{-1} \left(\frac{2 \cdot m \cdot V}{[(1+2 \cdot m)^2 + V^2] \cdot \frac{t_c}{2 \cdot t} + 1 + 2 \cdot m + V^2} \right) \right]^2 \quad (1)$$

being the probe laser beam at any time t. $I(0)$. is the initial value of $I(t)$ for t=0, θ is the shift of the phase in the probe beam after passing through the sample caused by the increase in temperature. $V=\left(\frac{z_1}{z_c}\right)$, z_c is the confocal distance of the probe beam and z_1 is the distance from the probe beam waist to the sample. ω_p and ω_e are the beam spot sizes of the probe and excitation beams at the sample, respectively, $m=\left(\frac{\omega_p}{\omega_e}\right)^2$ and $\theta=-\frac{P_e \cdot A_e \cdot L}{k \cdot \lambda}\left(\frac{ds}{dT}\right)$, P_e is the excitation beam power, is the optical absorption coefficient of the sample, L is the sample thickness, k is the thermal conductivity, λ is the laser wave-length of the probe beam, and $\left(\frac{ds}{dT}\right)$ is the change of the optical path length with temperature of the probe beam. The characteristic time constant of the thermal lens is related to the thermal diffusivity as follows $D=\frac{\omega_e^2}{4 \cdot t_c}$, in which θ and t_c can be determined by fitting Eq. 1 to the experimental data obtained [16 – 18].

In this work, silver nanoparticles (AgNPs) and silver nanowires (AgNWs) were synthesized and added to an acrylic resin to elaborate and nanocomposite with possible applications in biomedicine. Samples were physicochemically characterized and thermal properties were measured.

2. Materials and methods

2.1. *Synthesis of nanostructures*

2.1.1. AgNPs synthesis

The methodology of Li *et al.* [19] was used for green synthesis of AgNPs from Capsicum annum L. extract (Jalapeño chili pepper). Chilis were bought at a local market in Mexico City. They were washed with distilled water. An extract was elaborated, centrifuged at 4000 rpm for 1 h and filtered. Later, the extract was made up to 250 mL in distilled water. As a precursor, 0.1 M of AgNO3 was used. Then, 10 mL of the precursor were added to 50 mL of the reducer at room temperature and stirred. Every hour (up to 11 h), a sample was taken, and absorbance was determined by UV-vis. Color changed from transparent to translucent white, reddish brown and finally dark cherry after 11 h of reaction time.

2.1.2. AgNWs synthesis

The AgNWs were synthesized using the polyol method [20]. Silver nitrate, glycerol and PVP were used as a precursor, solvent and reducer and protective agent were used. For that, 0.489 M of AgNO3 was dissolved in 19 mL of a

solution containing 0.284 mol of PVP in glycerol and stirred. On the other hand, 0.5 mL of a 2 M NaCl aqueous solution was dissolved in 1 mL of glycerol and homogenized. Both solutions were mixed and heated at 220 °C at a heating rate of 2.75 °C/min and stirred at 50 rpm. The reaction was stopped using deionized in a 1:1 ratio with respect to the volume of the reactant system and the resulting product was precipitated by centrifugation at 7000 rpm. The solids were washed with deionized water three times. Finally, the precipitate was dispersed in water for its characterization.

2.2. *Nanocomposites elaboration*

The AgNPs and AgNWs were added to an acrylic resin to form two different nanocomposites. For that, 1.5 to 6 mg of dry nanostructures were dispersed in 5 mL of the resin (INKTEK, Mexico) using and ultrasonic bath for 1 h. For further use as characterization and printing, the composites were homogenized in an ultrasonic bath for 30 minutes.

2.3. *Characterization*

2.3.1. Physicochemical characterization

The UV-vis absorption coefficient was determined using a Genesis® 10S Spectrometer, in absorbance mode, range of 190-1100 nm, and a step of 5 nm. Functional groups were identified in a Bruker ® Alpha FTIR (Fourier Transformed Infrared Spectroscopy) equipment with a range of 400 – 4000 cm^{-1} and a step of 2 cm^{-1}. Nanostructures' morphology was observed using a JEOL® JEM-1010 Transmission Electron Microscope (TEM) at an acceleration voltage of 60 kV. The X-ray diffraction (XRD) patterns were obtained using a Rigaku® Smart Lab diffractometer (Cu Kα, λ = 1.5418 Å), with a step of 0.02 °/s, and 2θ from 20-80°, voltage and current were 45 kV and 200 mA, respectively.

2.3.2. Thermal measurements

2.3.2.1. Thermal diffusivity

Thermal diffusivity measurements of the nanoresin were carried out using the experimental set up shown in Figure 3. Briefly, the probing laser passes through the sample, reflects off the mirror and is directed towards the light intensity sensor. Then, the excitation laser beam penetrates in the interior of the liquid

sample, increasing the temperature in the surrounding medium, causing a deviation in its trajectory. Constant parameters used were Pe= 40 mW, (power of the Ar+Xe excitation laser at 514.5 nm (me= 4.9 ×10−3 cm the diameter of the excitation laser light beam; λp=632.8 nm (He-Ne probe laser wavelength), mp= 1.81 ×10−2 cm (probe beam diameter, red), m=13.691, V=1.22; zc=6.56 cm focal length; z1=2 m, L=1.0 cm (length of sample cell).

2.3.2.2. Curing time determination

The curing time was determined using the OPC set up shown in Figure 2. The liquid resin was placed inside a neoprene O-ring (5x2 mm) as a container on a metallic aluminum film (0.0012 mm thick). The sample was irradiated with a modulated laser beam at 17 Hz; with a wavelength of 400 to 450 nm and an average power of 2 mW. An Electret® microphone connected to the cell detects the wave generated due to temperature increase.

3. Results and discussion

3.1. *UV-vis of nanostructures resin and nanocomposites*

In Figure 4 the UV-vis of the resin with reaction time for the AgNPs can be seen. The curves show a band centered at 395nm, and an incipient growth of a band centered at 475 nm which corresponds to the surface plasmon resonance of silver. As the reaction progresses, the band at 475 nm is increased while the band at 395 nm is decreased. This behavior is like that reported by Li *et al.* [19].

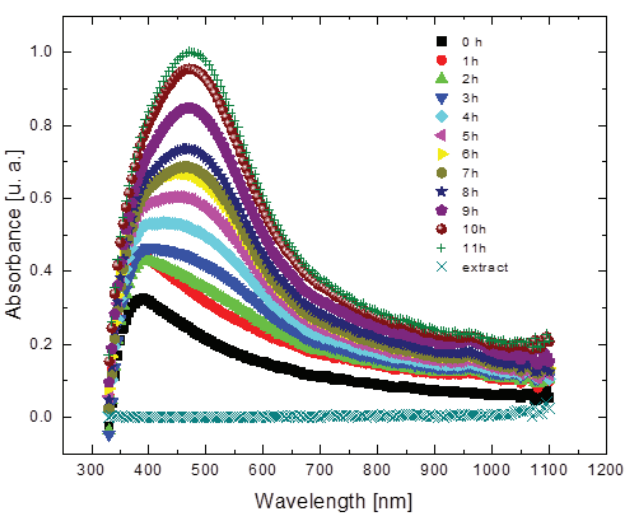

Figure 4. Kinetics of AgNPs synthesis followed by UV-vis spectrometry.

As seen in Figure 4 for AgNPs a main peak centered at 475 is observed because the vibrational mode is isotropic. On the other hand, AgNWs present two vibrational modes, one transversal and the other longitudinal corresponding to a shoulder centered at 350 nm assigned to transverse vibration and a band centered at 380 nm assigned to longitudinal vibration (spectra not shown) [21, 22].

In the UV-vis spectra of the acrylic resin (not shown) a band in the range from 277 to 429 nm was observed, the range in which the resin polymerizes.

For the nanocomposite, a band is observed from 420 to 435 nm (not shown), which remains in the same region, but changes slightly in intensity. The highest absorption started from 435nm and increases as the wavelength decreases.

3.2. *FTIR of nanostructures resin and nanocomposites*

In Figure 5, the FTIR spectra of the samples was taken every hour from the reacting system. All curves were similar. The characteristic absorption bands observed were at 3709-2803 cm^{-1} for the symmetric and asymmetric vibration of the O-H bond and stretching vibrations of the N-H bonds of primary and secondary amines [23]. At 2816-1904 cm^{-1}, for water, corresponding to the symmetrical stretching of oxygen, -O- and the stretching of the S-H, NH2+, NH+ bonds, maybe from vitamins and thiols of the extract. The band at 1635 cm^{-1} is related to the bending of the H-O-H bonds, to the amide bonds and to the C=O, -C=N bonds. Only small changes in the intensity of the band at 3709-2803 cm^{-1} during the synthesis correlates with the kinetics found by UV-vis spectrometry in Figure 4. For AgNWs, the same peaks were observed (spectra not shown).

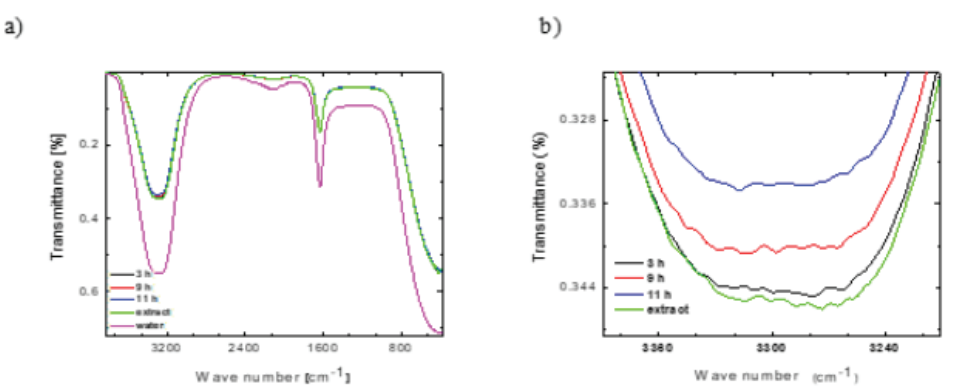

Figure 5. a) Kinetic monitoring of the synthesis of AgNPs.
b) Detail of the band at 3709-2803 cm-1.

The FTIR spectrum of the acrylic resin is shown in Figure 6. The most important absorption bands are 2869-2970 cm^{-1} related to the stretching of the C-H bond (-CH_3 and -CH_2), at 1723 cm^{-1} corresponding to the stretching of the C=O bond, a small band at 1635-1616 cm^{-1} due to the stretching of the RCO-NH2 bond. At 1450 cm^{-1}, and a peak corresponding to the -CO-CH_2 bond. A broad band between 1016 and 1193 cm^{-1}, corresponding to the ester group and another broad band between 3600 and 3350 cm^{-1} due to O-H stretching and amino group.

In the case of the nanocomposite, the FTIR spectra (not shown) had the bands corresponding to both, the nanostructures, and the resin.

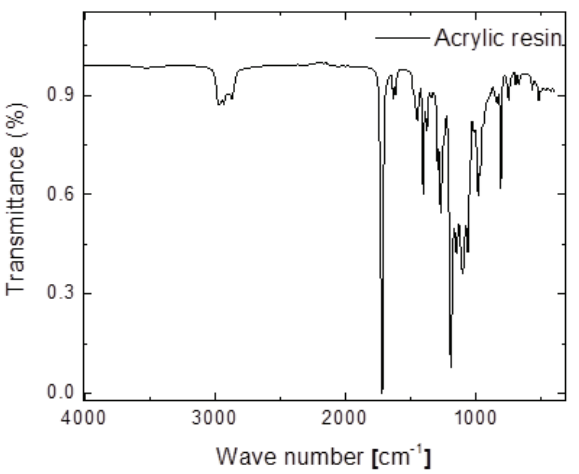

Figure 6. FTIR spectrum of the INKTEK acrylic resin

3.3. *TEM of nanostructures*

TEM images were used to determine the diameter of the AgNPs. The kinetics for 0, 5, and 11 h was observed. In Figure 7, a) an example of AgNPs at time 5 h is shown along with b) the particle size distribution histogram.

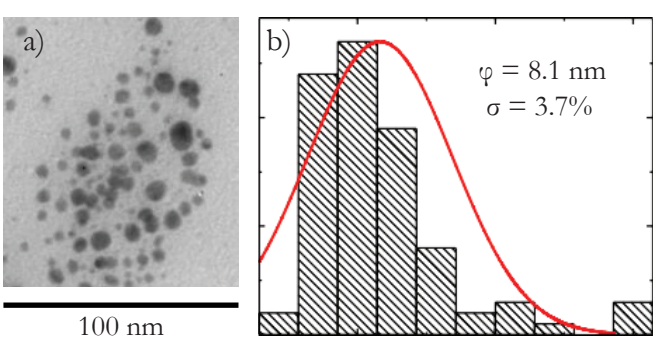

Figure 7. TEM images after 5 h reaction time for AgNPs synthesis.

The particles are spherical in shape and size distribution varies. In Table 1 the particle size for the different reaction times is shown.

Table 1. Particle diameter statistics.

Particle size [nm]			
Time [h]	0	5	11
Minimun diameter	2.5	2.9	5.9
Maximum diameter	12.7	21.3	35.8
SD	1.6	3.7	4.6
Mean	6.2	7.6	15.7

From TEM micrographs of AgNWs in Figure 8, linear, straight structures are observed, which different thickness and length (Figure 8a). No branches are observed. Considering these nanostructures as straight cylinders, the calculated diameter is 56.8 nm and the average length l=1451.7 nm with a mean aspect ratio of 25.6 (Figure 8b).

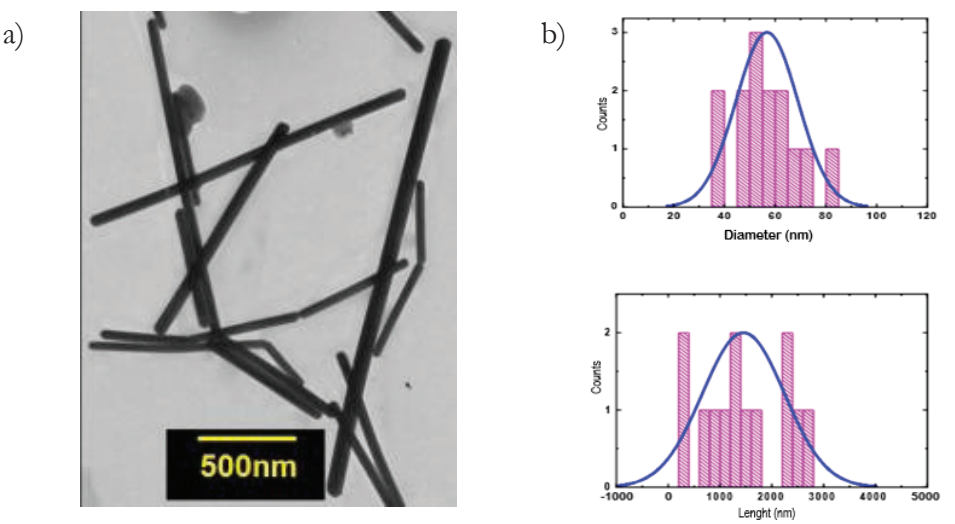

Figure 8. TEM images for AgNWs.

3.4. *XRD of nanostructures*

The structural properties of the AgNPs powders were analyzed by X-ray diffraction (diffractogram not shown). The obtained peaks corresponded to the planes of the cubic structure, FCC of silver [24], according to the Ag

crystallographic chart (JCPDS-ICDD chart04-0783) [25]. The peaks were observed at 37.8° corresponding to the (111) plane, at 45.9°, corresponding to the (200) plane, at 67.2 corresponding to the (220) plane, and at 76.5° corresponding to the (311) plane. Similar results were reported for AgNPs green syntheses using extracts of Santalum album fruits, Oryza Sativa seeds and Coleus aromaticus leaves [26].

For the AgNWs (diffractogram not shown), the signals corresponding to the FCC cell planes of silver were identified, which agree with the JCPDS standard file number 04-0783 of ASTM [27]. The crystallites that constitute them have a preferential orientation in the direction (111).

3.5. *Thermal properties of the nanocomposites*

3.5.1. Diffusivity of nanocomposites by TL

In Figure 9 it can be seen that the thermal diffusivity of the nanocomposites increased as the concentration of nanostructures in the composite increased. For the same concentration, the thermal diffusivity of the AgNPs composites is higher than for the AgNWs nanocomposites due to the higher aspect ratio to volume of nanoparticles compared to nanowhiskers [28].

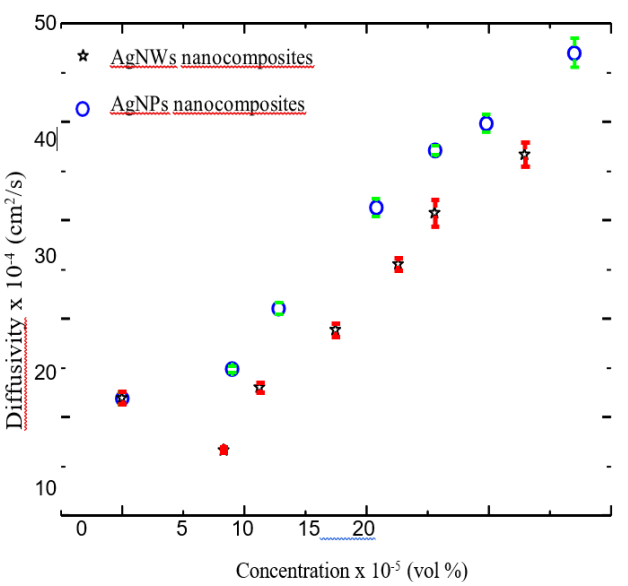

Figure 9. Thermal Diffusivity of the nanocomposites versus AgNPs or AgNWs nanostructures concentration (vol %) (in red and green the SD of the measurements).

3.5.2. Curing time of nanocomposites by PAS

In Figure 10, the relationship between the AgNPs or AgNWs concentration and the characteristic curing time, τ. For the same concentration, it is observed that for the composites containing AgNWs the curing time is higher than for the nanocomposites containing the AgNPs. This may be due to the UV light with generates free radicals increasing the interfacial thermal resistance and then, curing time is higher [29]. Also, as concentration is increased, the curing time increased being more noticeable for the AgNWs. This increase is related to the number of reactive functional groups between the acrylic resin and the nanostructures. For lower nanostructures concentration, the characteristic time τ increases slowly. On the other hand, as concentration of nanostructures increased, the possibility of the reaction of these functional groups present on the surface of the nanostructures, increases the characteristic time τ [14].

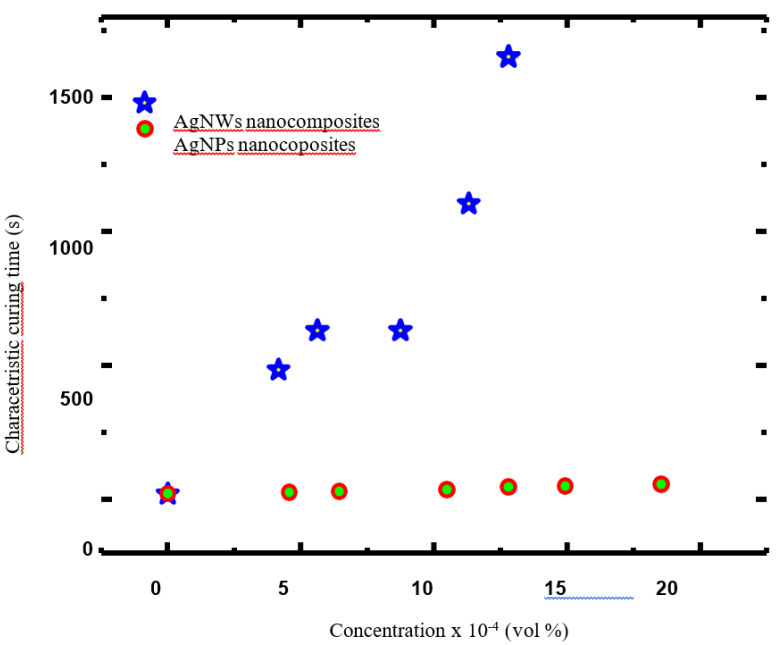

Figure 10. Characteristic curing time versus concentration for the nanocomposites.

3.5.3. SLA 3D Printing Process

The composites formulated with the AgNPs and AgNWs were 3D printed in the form of meshes (1 cm^2) for application as cellular scaffolds. AN UV laser with a wavelength of 405 nm was used. The system was illustrated in Figure 1 and the interior of the printer is shown in Figure 11.

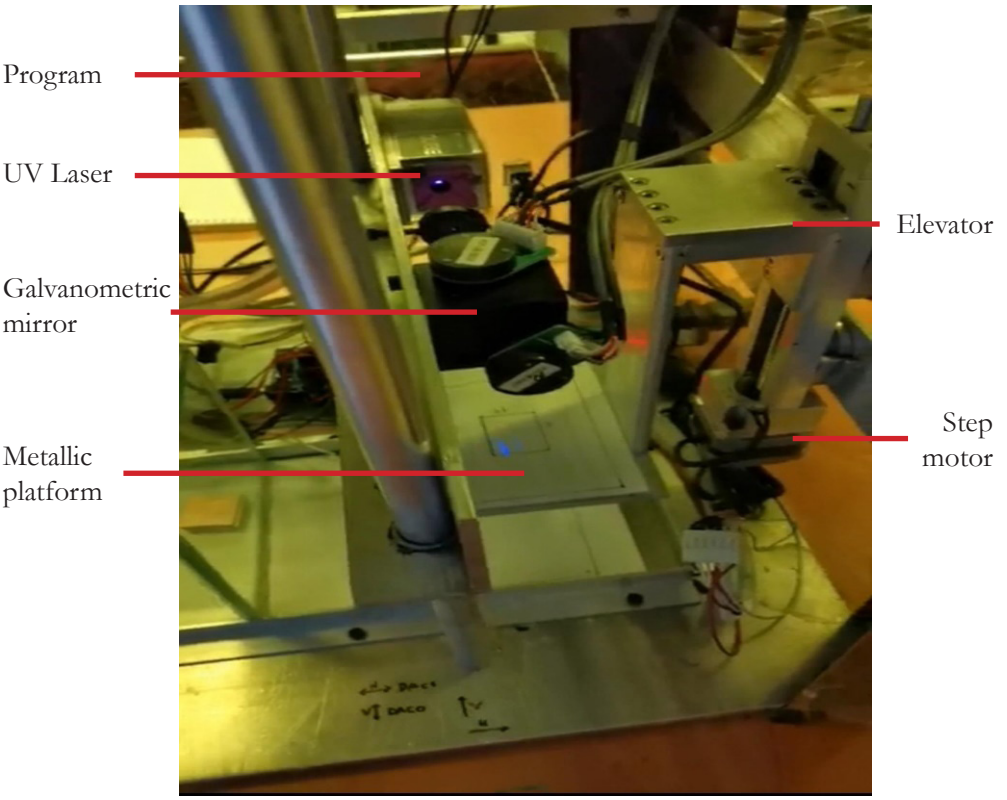

Figure 11. Inner part of the experimental 3D printer.

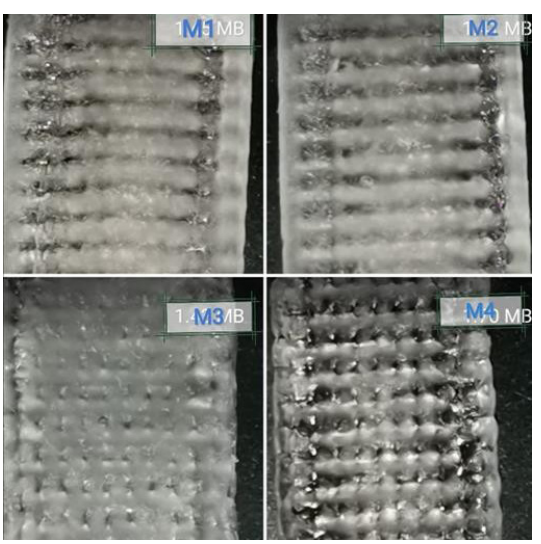

Figure 12. 3D printed structures.

The parameters considered for 3D printing are the numerical data to stablish the initial position of the laser, the height at which the printing starts, the total area of the printed mesh, the number, and the space between the vertical and horizontal lines for the printed mesh, the duration of time to cure light activate the composite resin and the displacement of the printer platform inside the resin. Examples of the 3D printed structures are shown in Figure 12.

4. Conclusions

In this work, 3D scaffolds by SLA from AgNPs or AgNWs and an acrylic resin nanocomposite were successfully printed. From the green synthesis, spherical AgNPs with size between 5.9-35.8 nm after 11 h reaction observed by TEM were obtained. Particles size depend on synthesis reaction time. Main functional groups for the nanostructures and nanocomposites were identified by FTIR. The obtained values for thermal diffusivity (D) measured by TL were between 14 and 47x10-8 m2/s for concentrations ranging from 5 to 19x10-5 wt% for the AgNPs. For the AgNWs the D values were between 6 and 37x10-8 m2/s for concentrations ranging from 4 to 17x10-5 wt%. Regarding the characteristic curing time (τ) a maximum of 58 s were obtained for the AgNPs nanocomposites and for the AgNWs nanocomposites maximum was 1651 s for the highest concentration of the nanostructures. Both D and τ increased with nanostructures concentration. The aim of this work was to find applications of 3D printed scaffolds nanocomposites in the biomedical field.

Acknowledgement and Funding

We would like to thank CONACYT, COFAA-IPN, EDI for their support.

References

1. Gibson, I., Rosen, D., & Stucker, B. (2015). *Additive Manufacturing Technologies 3D Printing, Rapid Prototyping and Direct Digital Manufacturing*. ISBN 978-1-4939-2112-6. https://doi.org/10.1007/978-1-4939-2113-3_1

2. Wohlers, T., & Gorne, T. (2014). *History of Additive Manufacturing*. Wohlers Report, Fort Collins, CO: Wohlers Associates, Inc. https://pdf4pro.com/amp/view/history-of-additive-wohlers-report-manufacturing-27057b.html

3. Srivatsan, T.S., & Sudarshan, T.S. (Eds.). (2016). *Additive Manufacturing Innovations, Advances, and Applications*. CRC Press, Taylor & Francis Group, LLC. ISBN-13: 978-1-4987-1478-5.

4. Aghakhanlouy, S., & Grieser, F. 3D Printing Speed: How Fast Do 3D Printers Go in 2023? Updated Jan 25, 2023 https://all3dp.com/2/3d-printer-speed/

5. Currículo e Historial de Litografía y Serigrafía (2010). http://blogdecienciassocialesyhumanas.blogspot.com/search?q=litograf%C3%ADa. Accessed 09 March 2023.

6. Ying, Y., Choong, C., Maleksaeedi, S., Eng, H., Chen, P., & Wei, J. (2017). Curing characteristics of shape memory polymers in 3D projection and laser stereolithography. *Virtual and Physical Prototyping*, 12(1), 77-84. https://doi.org/10.1080/17452759.2016.1254845

7. Gill, A. A. (2012). *Thesis: Applications of Microstereolithography in Tissue Engineering Department of Materials Science and Engineering University of Sheffield.* https://etheses.whiterose.ac.uk/3711/1/Andrew_Gill_Thesis_Final_Submission.pdf Accessed 09 March 2023.

8. Xu, W., Jambhulkar, S., Zhu, Y., Ravichandran, D., Kakarla, M., Vernon, B. *et al.* (2021). 3D printing for polymer/particle-based processing: A review. *Composites Part B: Engineering*, 223 109102. https://doi.org/10.1016/j.compositesb.2021.109102

9. Rosencwaig, A., & Gersho, A. (1976). Theory of the photoacoustic effect with solids. *Journal of Applied Physics*, 47(64), 64-69. https://doi.org/10.1063/1.322296

10. Gosselin, F., Di Renzo, M., Ellis, T. H., & Lubell, W. D. (1996). Photoacoustic FTIR Spectroscopy, a Nondestructive Method for SensitiveAnalysis of Solid-Phase Organic Chemistry. *Journal of Organic Chemistry*, 61(23), 7980-7981. https://doi.org/10.1021/jo961393g

11. Vieyra-Pincel, P., Jiménez-Pérez, J. L., Cruz-Orea, A., Correa-Pacheco, Z. N., & Hernández Rosas, J. (2015). Photoacoustic study of curing time by UV laser radiation of a photoresin. *Thermochimica Acta*, 606, 53-57. https://doi.org/10.1016/j.tca.2014.12.008

12. Rohling, J. H., Medina, A. N., Bento, A. C., Pereira, J. R. D., Rubira, A. F., Baesso, M. L. *et al.* (2001). Differential thermal lens temperature scanning approach to glass transition analysis in polymers: application to polycarbonate. *Journal of Physics D: Applied Physics*, 34, 407-412. https://doi.org/10.1088/0022-3727/34/3/326

13. Cabrera, H., Korte, D., & Franko, M. (2015) Mode-mismatched confocal thermal-lens microscope with collimated probe beam. *Review of Scientific Instruments* 86(053701), 1-7. https://doi.org/10.1063/1.4919735

14. Shen, J., Lowe, R. D., & Snook, R. D. (1992) A model for cw laser induced mode-mismatched dual-beam thermal lens spectrometry. *Chemical Physics*, 165(2-3), 385-396. https://doi.org/10.1016/0301-0104(92)87053-C

15. Stephen, B., Bialkowski, E., & Winefordner, J. D. (Ed). (1996). Photothermal Spectroscopy Methods for Chemical Analysis. *Journal of the American Chemical Society*, 119, 26, 6212. Utah State University. Wiley: New York. ISBN 0-471-57467-8. https://doi.org/10.1021/ja965536s

16. Villegas, O., & Castillo, J. (2018) Study of thermo-optical properties of nanofluids of gold and silver nanoparticles functionalized with polyethylene glycol and sodium dodecyl sulfate in water using thermal lens spectroscopy. Proc. SPIE 10672, *Nanophotonics VII*, 106723S, 1-6. https://doi.org/10.1117/12.2307284

17. Carbajal-Valdez, R., Jiménez-Pérez, J. L., Cruz-Orea, A., Correa-Pacheco, Z. N., Alvarado-Noguez, M. L., Romero-Ibarra, I. C. *et al.* (2017). Thermal properties of centrifuged oils measured by alternative photothermal techniques. *Thermochimica Acta*, 657, 66-71. https://doi.org/10.1016/j.tca.2017.09.014

18. Li, S., Shen, Y., Xie, A., Yu, X., Qiu, L., Zhang, L. *et al.* (2007). Green synthesis of silver nanoparticles using Capsicum annuum L. extract. *Green Chemistry*, 9, 852-858. https://doi.org/10.1039/b615357g

19. Carbajal-Valdéz, R., Rodríguez-Juárez, A., Jiménez-Pérez, J.L., Sánchez-Ramírez, J.F., Cruz-Orea, A., & Correa-Pacheco, Z. N. (2019). Experimental investigation on thermal properties of Agnanowires nanofluids at low concentrations. *Thermochimica Acta*, 671, 83-88. https://doi.org/10.1016/j.tca.2018.11.015

20. Lin, J., Hsueh, Y., & Huang, J. (2014). The concentration effect of capping agent for synthesis of silver nanowire by using the polyol method. *Journal of Solid State Chemistry*, 214, 2-6.
https://doi.org/10.1016/j.jssc.2013.12.017

21. Sun, Y., Gates, B., Mayers, B., & Xia, Y. (2002). Crystalline Silver Nanowires by Soft Solution. *Processing. Nano Letters*, 2(2), 165-168.
https://doi.org/10.1021/nl010093y

22. Socrates, G. (2004). *Infrared and Raman characteristic group frequencies: Tables and Charts*. 3rd Ed. Formerly of Brunel, The University of West London, Middlesex. UK. John Wiley & Sons, Ltd. ISBN 0 470 09307 2.
https://analyticalscience.wiley.com/do/10.1002/sepspec.9780470093078/full/

23. Mahakham, W., Sarmah, A. K., Maensiri, S., & Theerakulpisut, P. (2017). Nanopriming technology for enhancing germination and starch metabolism of aged rice seeds using photosynthesized silver nanoparticles. *Scientific Reports*, 7(8263), 1-21.
https://doi.org/10.1038/s41598-017-08669-5

24. Mehta, B. K., Chhajlani, M., & Shrivastava, B. D. (2017). Green synthesis of silver nanoparticles and their characterization by XRD. *Journal of Physics: Conference Series*, 836(012050), 1-5.
https://doi.org/10.1088/1742-6596/836/1/012050

25. Vanaja, M., & Annadurai, G. (2013) Coleus aromaticus leaf extract mediated synthesis of silver nanoparticles and its bactericidal activity. *Applied Nanoscience*, 3, 217-223.
https://doi.org/10.1088/1742-6596/836/1/012050

26. Mao, H., Feng, J., Ma, X., Wu, C., & Zhao, X. (2012). One dimensional silver nanowires synthesized by self-seeding polyol process. *Journal of Nanoparticle Research*, 14(887), 1-15.
https://doi.org/10.1007/s11051-012-0887-4

27. Rivière, L., Lonjon, A., Dantras, E., Lacabanne, C., Olivier, P., & Rocher Gleizes, N. (2016). Silver fillers aspect ratio influence on electrical and thermal conductivity in PEEK/Ag nanocomposites. *European Polymer Journal*, 85, 115-125.
https://doi.org/10.1007/s11051-012-0887-4

28. Valencia, L. M., Herrera, M., de la Mata, M., Delgado, F. J., & Molina, S. I. (2022). Synthesis of Silver Nanocomposites for Stereolithography: In Situ Formation of Nanoparticles. *Polymers*, 14(6), (1168), 1-14.
https://doi.org/10.1007/s11051-012-0887-4

29. Roberts, A. T., Yang, J., Reish, M., Alabastri, A., Halas, N. J., Nordlander, P. *et al.* (2018). Plasmonic nanoparticle-based epoxy photocuring: A deeper look. *Materials Today*, 27, 14-20.
https://doi.org/10.1007/s11051-012-0887-4

Chapter 4 Health Area

NUMERICAL SIMULATION OF A PDMS MICROFLUIDIC CHANNEL COMPATIBLE WITH BIOSENSORS

Verónica Iraís Solís-Tinoco[1, 3*], Tamara Jennifer Crisóstomo -Rodríguez[2], Marco Antonio Ramírez-Salinas[3], Miguel Ángel Alemán-Arce[3]

[1] Instituto de Ciencias Aplicadas y Tecnología, Universidad Nacional Autónoma de México, Ciudad de México 04510, Mexico. irais.solis@icat.unam.mx

[2] Unidad Profesional Interdisciplinaria en Ingeniería y Tecnologías Avanzadas UPIITA-IPN. Ingeniería Biónica. Ciudad de México, C.P. 07340.

[3] Centro de Investigación en Computación del Instituto Politécnico Nacional, Laboratorio de Microtecnología y Sistemas Embebidos. Ciudad de México 07738, Mexico.

irais.solis@cic.ipn.mx

Solís-Tinoco, V. I., Crisóstomo-Rodríguez, T. J., Ramírez Salinas, M. A., & Alemán-Arce, M. Á. (2023). Numerical simulation of a PDMS microfluidic channel compatible with biosensors. In E. San Martín-Martínez (Ed.). *Research advances in nanosciences, micro and nanotechnologies. Volume IV* (pp. 93-106). Barcelona, Spain: Omniascience.

Abstract

Microfluidics has promoted the development of sensors, whose designs, materials, and sizes have been adapted for application in areas such as biology, chemistry, and health. For this, the design of the microfluidic system studies the effect of those parameters on its operation, in addition, the microfluidic design must be compatible with the transducer characteristics. Numerical simulations are powerful tools that allow us to analyze whether microfluidic designs are appropriate, and thereby advance to the microfabrication phase. Nevertheless, performing a numerical simulation of a microfluidics system is not an easy task. In this work, the design of a microfluidic channel is described using COMSOL Multiphysics 5.5. The material is polydimethylsiloxane (PDMS), and its dimensions are chosen to work with a laminar flow. Fluid flow patterns, pressure distribution, and velocity field of water were observed by using the simulation software. The results showed that the velocity and pressure of the water increased, from 0.0012 m/s to 0.06 m/s and from 0.06 Pa to 174.37 Pa, when increasing the flow ratios from 10 μL/h to 500 μL/h. The 3D and 2D graphs showed that the distribution of the water velocity decreased in the walls, due to the interaction between the PDMS and water. Finally, this study provides information to analyze the design of the microchannel and to organize the experimental measurements, establishing suitable geometries, materials, and injection flow ratios.

Keywords: microfluidics, numerical simulation, PDMS, microchannel, pressure, velocity.

1. Introduction

Microfluidics is a field focused on the engineered manipulation of fluids and molecules at the microscale [1]. It studies fluids confined in microchannels typically smaller than 500 μm. It is a growing field of research which is having a significant effect on point-of-care diagnostics and clinical studies[2, 3]. Additionally, microfluidics is very well established in academia [4, 5] and it is rapidly gaining positions in the industry mainly for the development of new methodologies and new products for life sciences [6].

The potential of microfluidics lies in size reduction, scaling down fluidic processes to the microscale, offering significant advantages, for instance; Miniaturized components and processes employing smaller volumes of fluid (pL-μL), thus leading to reduced reagent consumption, as a result, this decreases costs and permits optimized small quantities of expensive samples, thereby the quantities of waste products are reduced [7]. In the microfluidic devices, diffusive mixing is easy and fast, often increasing the velocity and accuracy of reactions. A microfluidic chip allows to reduce measurement times, improve sensitivity, higher selectivity, and greater repeatability [9].

A microfluidic chip is a pattern of microchannels, molded by techniques of microfabrication [4, 5, 9, 10]. Those microfluidic chips can be integrated with transducers (e.g., optical, mechanical, electrical, magnetic, etc.) to form as we know it as a lab on a chip sensor [5, 11, 12]. The microfluidic chip design is essential to obtain an optimized system. It requires analyzing on the effect of the geometry, material, fluids, and temperature etc. Numerical simulations are useful tools to perform preliminary physical tests and investigations on microfluidic chips, also to verify the quality of the microchannel fabrication [13]. A numerical simulation is a calculation to study the behavior of systems whose mathematical models are complex to provide analytical solutions. However, performing a numerical simulation is a very complex task. It requires knowledge about of the software and the physical concepts of microfluidics, to configure the simulation properly and thereby obtain correct results.

In this work, we use the COMSOL Multiphysics program [14] to describe the microfluidic chip design of a polydimethylsiloxane (PDMS) microchannel, with a radius of reservoir of 250 μm, with a length 1000 μm and with a width and height of 70 μm. Its geometry could be compatible with optic (e.g., gold)

[15] and mechanical [11] (e.g., lithium niobate) transducers to create lab on a chip sensors. This study is aimed to describe, step by step, the design of a single microfluidic channel in COMSOL Multiphysics. Additionally, we calculate and analyze the pressure and velocity of water using different flow ratios, commonly used in bio applications.

2. Methodology

2.1. *Setting*

The simulation of the microfluidic channel is carried out in the engineering modeling software COMSOL Multiphysics version 5.5. The settings are mentioned in Table 1.

Table 1. COMSOL configuration for the microfluidic channel

Settings	Details
Space Dimension	3D
Physic	Fluid Flow, Single-Phase Flow, Laminar Flow
Study Type	General Studies, Stationary
Module	Microfluidic

2.2. *Geometry of the PDMS microfluidic channel*

The Figure 1a shows the geometry of the microchannel, where L represents the length, it is parallel to the Y axis that connects two reservoirs, Ri for the inlet and Ro for the outlet, the radius is 250 µm. For a correct union between the

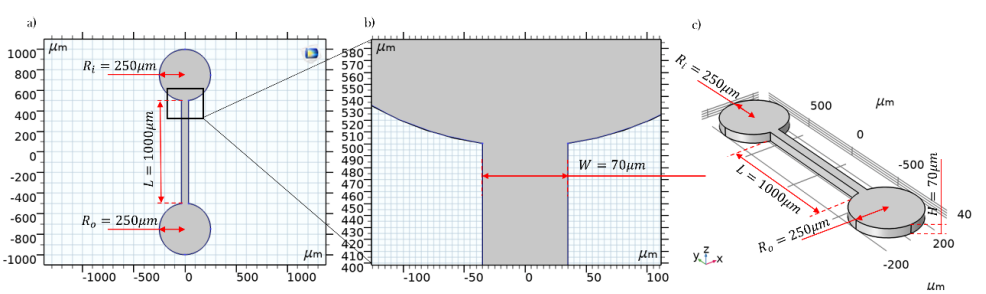

Figure 1. Geometry of the PDMS microfluidic channel. a) Top view of the reservoirs, inlet and outlet, with 250 µm of radius, b) Reservoir connecting to the rectangular part of the microchannel with a width (W) of 70 µm, and c) Microchannel dimensions.

rectangular part of the channel and the reservoir, it is necessary to extend the length of the channel as shown in the Figure 1b. An extrusion of 70 μm is set for the height (H) as shown in Figure 1c.

2.3. *Materials of the microfluidic channel*

Polydimethylsiloxane (PDMS) is chosen as the material for the walls due to its excellent properties that allow molding at microscale a channel. This polymer is transparent, and a biocompatible polymer widely used in microfluidics due to its compatibility with biosensors. [5, 16] as for example cellular adhesion. Cellular adhesion is a multipart process with crucial implications in physiology (i.e. immune response, tissue nature, architecture maintenance, or behaviour and expansion of tumor cells We can set its Young's modulus, so we have the option to modify the design or make the study more efficient.

Water is chosen as fluid because it is the universal dissolvent and its properties are used as a reference to understand the behavior of the fluid through the microchannel, and thereby, we could compare the behavior with other biological fluids.

The PDMS and water do not need to be registered, COMSOL software has their properties in the library. The properties are specified in the following Figure 2. We select the entire microchannel for water, it must be configured as one solid, see Figure 2a-b. We select the walls, one by one, to configure PDMS material as shown in the Figure 2c-d.

2.4. *Inlet and outlet port microfluidic channel*

In this section, the inlet and outlet of the microchannel are configured as well as the water as a laminar flow. The inlet reservoir (Ri) is selected as shown in Figure 3a, where a tubing is connected to inject the water inside the microchannel, then, due to the same pressure, water passes through the microchannel and reaches the outlet reservoir as shown in Figure 3b. The water leaves the microchannel due to the pressure and through another tubing connected at the outlet reservoir as shown in Figure 3c. We test three different flow ratios, 2.778×10^{-12} m^3/s, 9.772×10^{-12} m^3/s, and 1.3889×10^{-10} m^3/s which are equivalent to 10 μL/h, 35 μL/h, and 500 μL/h, respectively. These flow ratios are commonly used in biofunctionalization and droplet generation processes [2]. It's important to verify that at the end of this configuration, when entering the Inlet, Outlet and Wall option, the selection is displayed as shown in Figure 3.

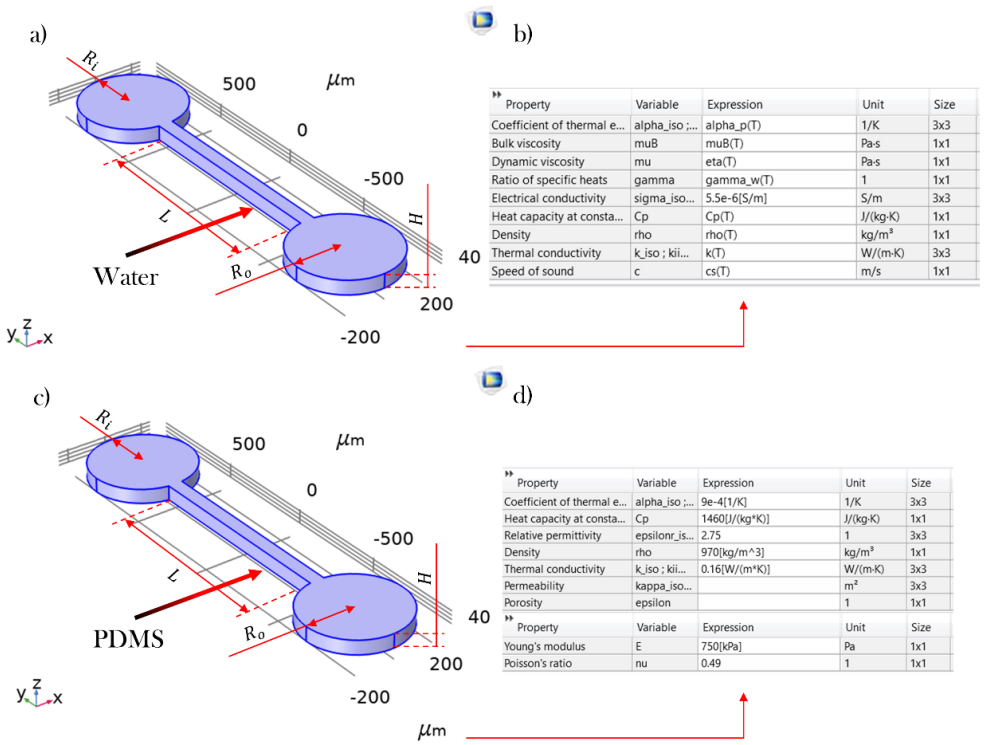

Figure 2. a) Scheme showing the selected parts of the microchannel where the water will flow, b) Properties of water, c) Selected geometry of the microchannel to configure the PDMS material, and d) Properties of PDMS polymer.

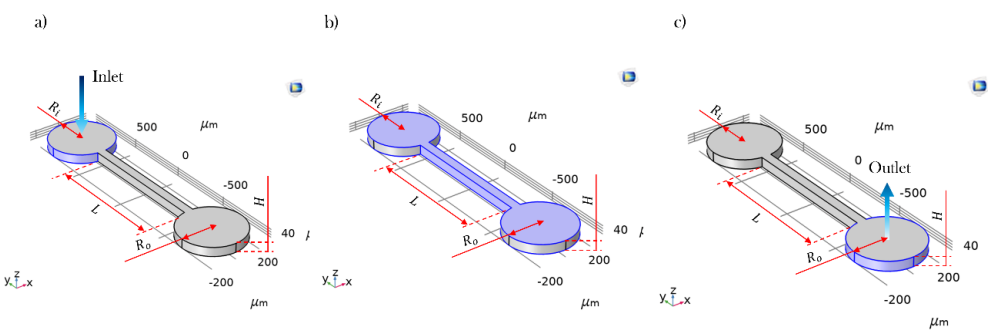

Figure 3. Port settings. a) Inlet port settings, reservoir Ri where the water enters, b) Walls port settings where the water flows and c) Outlet port settings, reservoir Ro where the water comes out.

2.5. *Mesh settings*

In this section, we select a normal mesh for a stationary study, this configuration has a suitable characteristic to perform it, see Figure 4c. Each crossing of lines in the mesh, called nodes, is where the resolution of equations is generated

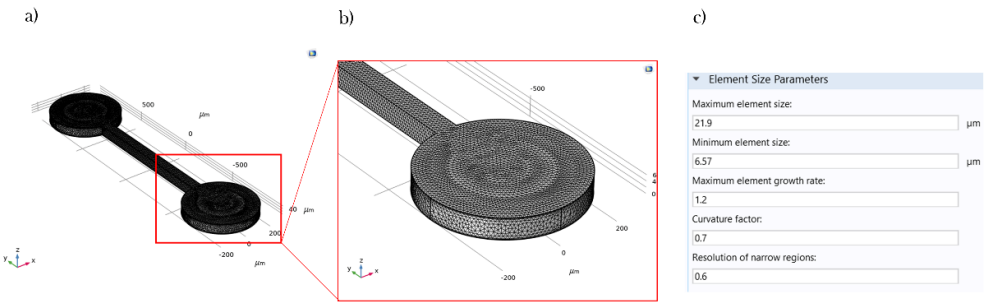

Figure 4. Normal mesh settings. a) Normal mesh along the entire geometry, b) Outlet reservoir with the mesh and c) Default properties of a normal mesh for a stationary study.

by COMSOL to obtain, speed, pressure, among other parameters. Figure 4a-c shows the main parameters for a normal mesh as well as an approach to the mesh produced in the outlet reservoir.

2.6. *Study Settings*

To generate a stationary study, slices of the areas of interest are needed. In this case, three types of slices are generated. The slice 1 is parallel to the microchannel in the yz plane, and it is in middle of the microchannel, as shown in the Figure 5a. The second plane (slice 2) is created parallel to the microchannel in the yx plane, see Figure 5b. Finally, we configure five slices in the zx plane, in the transversal form, as shown in the Figure 5c.

The slices are used to generate the stationary study in which the speed appears in each one to calculate the pressure and velocity of the water at different flow ratios.

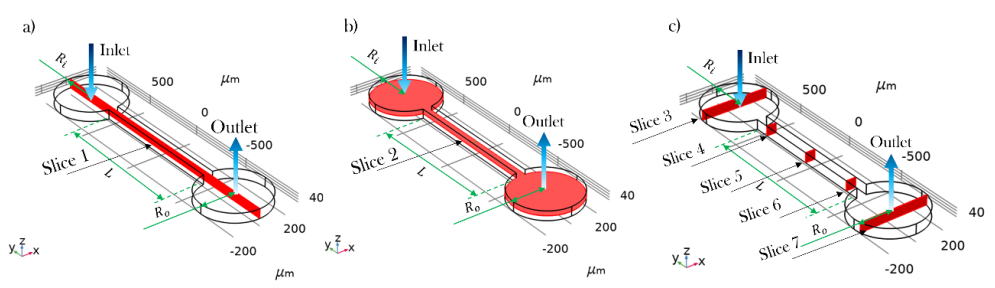

Figure 5. Settings of the slices. a) Slice 1 is parallel to the microchannel in the yz plane. b) Slice 2 is parallel to the microchannel in the yx plane. c) Slice 3 to Slice 7 is transversal to the microchannel in the zx plane.

3. Results and Discussion

3.1. *Velocity of the water through the PDMS microchannel*

To calculate the results, it is necessary to indicate the type of study that COMSOL will perform, if it is not given by default in the options box on the left of interphase, we must create it by selecting a new study in the tool ribbon at the top of interphase. Once this is done, to obtain the velocity, we select a 3D PLOT GROUP in the same tool ribbon and configure it to refer to Slice 1, created in the previous section, see Figure 5a. Once inside the 3D PLOT GROUP configurations, we will find a variable selector indicated with a red and a green triangle, in this section, we will search the variable of interest to analyze (e.g., velocity). Once this is done, we return to the study settings and press the Compute button to generate the study, as shown in Figure 6.

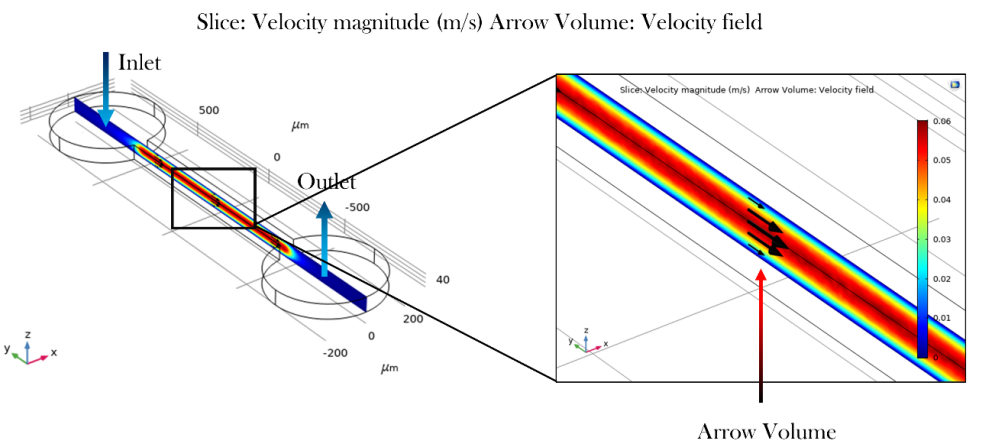

Figure 6. Slide 1 of velocity flowing through the microchannel and flow lines of that velocity indicating the direction from the inlet to outlet.

We can see in Figure 6 that the water velocity is less than 0.02 m/s in the inlet reservoir and in the outlet reservoir, while through the microchannel the velocity can reach 0.06 m/s. We can observe the water direction from the inlet to the outlet. For the second stationary study referenced to Slice 2, see Figure 5b. We repeat the previously mentioned steps but selecting the Slice 2. Then, we can see in Figure 7 that the velocity is transversely along the microchannel.

In the case of Slice 3-7 (see Figure 5), we obtain two results. The first one in 3D PLOT GROUP, with the velocity referenced to the transverse planes as

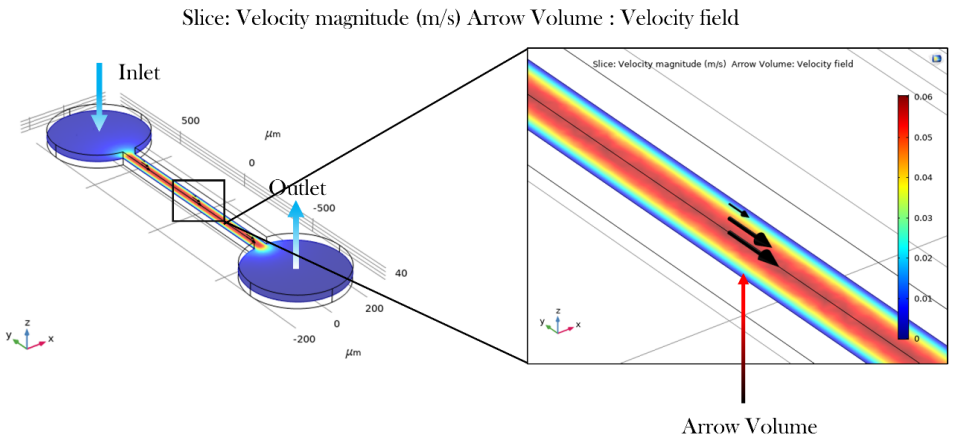

Figure 7. Velocity through the microchannel and flow lines of that velocity in the slice 2.

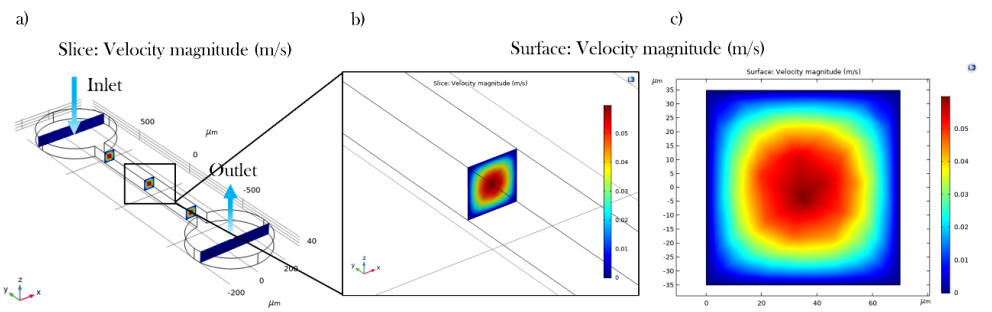

Figure 8. a) Velocity magnitude in the slices 3-7, b) 3D plot of the central slice 5, and c) Surface of the transversal velocity in 2D of the slice 5.

shown in Figures 8a and 8b, following the steps already mentioned. We plot a 2D PLOT GROUP and reference it to Slice 5, which is a central transverse plane, to observe the behavior of the water as shown in Figure 8c.

We can see in the Figure 8 the results of the slides 3-7, the scale is shown that goes from 0.0 m/s to 0.06 m/s, which is the velocity range calculated through the PDMS microchannel. We note that the velocity in the center reaches the largest value (0.06 m/s) while in the base (sensor) and walls (PDMS) the velocity reaches the lowest values (0.01 m/s). We attribute this behavior to the PDMS, due to it is a polymer with a Young´s modulus of 750 kPa that affects the flow of the water. With this simulation, it is possible to calculate the time that the water takes to pass through the entire microfluidic channel at different flow ratios, the results are shown in Table 2.

Table 2. Water injection flow ratios. Calculated pressure and velocity values by numerical simulation, and the travel time of the water through the microchannel.

Water Flow at inlet reservoir		Velocity (m/s)d		Pressure (Pa)e		Maximum Time (s)c
(µL/h)a	(m^3/s)b	min	max	min	max	
10	2.778 e-12	0.0	0.0012	0.06	3.48	0.833
35	9.722 e-12	0.0	0.0040	0.21	12.19	0.250
500	1.389 e-10	0.0	0.0600	2.93	174.37	0.016

a Flow ratio used for microfluidics applications.
b Flow ratio in unit accepted by COMSOL Multiphysics.
c Fill Time of water to pass through the entire microfluidic channel with 1000 µm of length.
d Calculated values of water velocity at Slice 2.
e Calculated values of water pressure at Slice 2.

3.2. *Pressure of the water through PDMS microchannel*

To obtain the water pressure inside the PDMS microfluidic channel, we select a 3D PLOT GROUP, in its settings, in the green and red triangle, we choice the pressure variable. We select the surface of the entire microchannel to obtain pressure values and pressure curves, to appreciate the behavior of the microchannel, as shown in Figure 9 a-d.

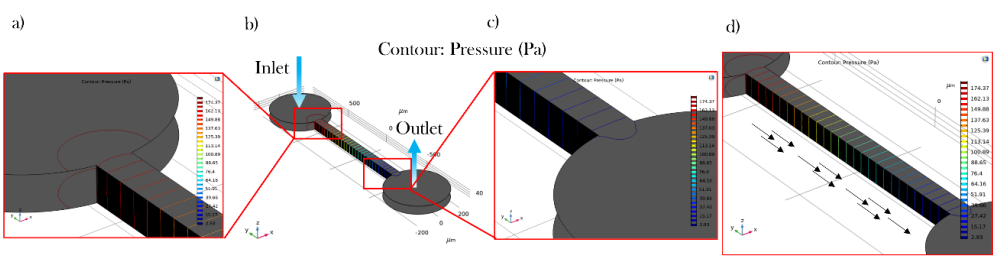

Figure 9. a) Pressure curves in the inlet reservoir, b) Pressure curves along the entire geometry of the PDMS microchannel, c) Pressure curves in the outlet reservoir and d) Pressure curves along the entire PDMS microchannel.

We can see in Figure 9 a-d, that the flow is distributed along the PDMS microchannel causing different pressures from 2.93 Pa to 174.37 Pa for a flow ratio of 500 µL/h. Thus, we can calculate and observe the maximum pressure values that the microchannel supports, without suffering damage or leaks, by varying the flow ratios of the water.

The data of pressure and velocity of water provide information to analyze the design of the microfluidic channel and to organize the experimental measurements, establishing suitable geometries, materials, and injection flow ratios. The pressure values at different flow ratios are shown in Table 2. As we expected, the values increase as the flow ratio increases. On the contrary, the time decreased as the flow ratio increased.

4. Conclusions

In this work, we presented a numerical simulation of a PDMS microfluidic channel whose geometry could be compatible with optic and mechanical sensors. We configured the microchannel geometry to analyze a laminar behavior, and to calculate the pressure and velocity using water.

PDMS material was selected for its well-known biocompatibility, thereby the PDMS microchannel can be applied in biology and chemistry. Water is used as a fluid and as a reference in these simulations.

The design is the basic microfluidic channel with an inlet and outlet. The radius of reservoirs is 250 μm with a length of 1000 μm, a width of 70 μm and a height of 70 μm. The PDMS microchannel can be fabricated with 3D printer or photolithography techniques.

In this work, we described the configuration of ports to analyze the behavior of pressure and velocity of water since this is the universal solvent and the most used in bio applications.

The results showed that the velocity goes from 0.0 m/s to 0.06 m/s decreasing in the walls, due to the interaction between the PDMS and water. The minimum filling time was 0.016 seconds using a flow ratio of 500 μL/h. The pressure goes from 2.93 Pa to 174.37 Pa. In the case of 35 μL/h, the velocity goes from 0 m/s to 0.0040 m/s, with a pressure that goes from 0.21 Pa to 12.19 Pa, with a filling time of 0.250 s.

For the flow ratio of 10 μL/h, the velocity goes from 0.0 m/s to 0.0012 m/s, with a pressure that goes from 0.06 Pa to 3.48 Pa, with a filling time of 0.833 s.

These calculations required at computational cost of 1.61 GB with an execution time of 1 minute and 20 seconds. With this work, we demonstrate the potential of numerical simulations for the suitable design and microfabrication of microfluidic systems compatible with sensors, also by numerical simulation is possible to vary the water for other biochemical substances, modifying its properties according to the study.

Funding

We acknowledge the financial support from National Polytechnic Institute (IPN-Mexico) scholarship program, Beca de Estímulo Institucional de Formación de Investigadores (ID-BEIFI 151, student-2019640552) and for the scientific project SIP. 20230952.

References

1. Whitesides, G. M. (2006). The origins and the future of microfluidics. *Nature*, 442, 7101 (July 2006), 368-373. https://doi.org/10.1038/nature05058

2. Courtois, F., Olguin, L. F., Whyte, G., Bratton, D., Huck, W. T. S., Abell, C. *et al.* (2008). An Integrated Device for Monitoring Time-Dependent in vitro Expression from Single Genes in Picolitre Droplets. *ChemBioChem*, 9(3), 439-446. https://doi.org/10.1002/cbic.200700536

3. Yager, P., Edwards, T., Fu, E., Helton, K., Nelson, K., Tam, M. R., & Weigl, B. H. (2006). Microfluidic diagnostic technologies for global public health. *Nature*, 442(7101), 412–418. https://doi.org/10.1038/nature05064

4. Ochoa, A., Álvarez-Bohórquez, E., Castillero, E., & Olguin, L. F. (2017). Detection of Enzyme Inhibitors in Crude Natural Extracts Using Droplet-Based Microfluidics Coupled to HPLC. *Analytical Chemistry*, 89(9), 4889-4896. https://doi.org/10.1021/acs.analchem.6b04988

5. Solis-Tinoco, V., Marquez, S., Quesada-Lopez, T., Villarroya, F., Homs-Corbera, A., & Lechuga, L. M. (2019). Building of a flexible microfluidic plasmo-nanomechanical biosensor for live cell analysis. *Sensors and Actuators B Chemical*, 291, 48-57. https://doi.org/10.1016/j.snb.2019.04.038

6. Microfluidics Companies Worldwide | Biotech Careers. Retrieved March 2, 2023 from https://biotech-careers.org/company-core-activity/microfluidics

7. Campbell, Z. S., & Abolhasani, M. (2020). Facile synthesis of anhydrous microparticles using plug-and-play microfluidic reactors. *Reaction Chemistry & Engineering*, 5(7), 1198-1211. https://doi.org/10.1039/D0RE00193G

8. Sun, A. C., Steyer, D. J., Allen, A. R., Payne, E. M., Kennedy, R. T. *et al.* (2020). A droplet microfluidic platform for high-throughput photochemical reaction discovery. *Nature Communications*, 11(1), 6202. https://doi.org/10.1038/s41467-020-19926-z

9. Scott, S. M., & Ali, Z. (2021). Fabrication Methods for Microfluidic Devices: An Overview. *Micromachines*, 12(3), 319. https://doi.org/10.3390/mi12030319

10. Solis-Tinoco, V., Sepulveda, B., & Lechuga, L. M. (2015). Novel nanoplasmonic biosensor integrated in a microfluidic channel. Proceedings of *SPIE Microtechnologies, 2015, Barcelona, Spain*. 95190T. https://doi.org/10.1117/12.2178990

11. Agostini, M., Greco, G., & Cecchini, M. (2019). Full-SAW Microfluidics-Based Lab-on-a-Chip for Biosensing. *IEEE Access* 7, 70901-70909. https://doi.org/10.1109/ACCESS.2019.2919000

12. Chen, Y-S., Huang, C-H., Pai, P-C., Seo, J., & Lei, K. F. (2023). A Review on Microfluidics-Based Impedance Biosensors. *Biosensors*, 13(1), 83.

13. Hashim, U., Diyana, P. N. A., & Adam, T. (2012). Numerical simulation of Microfluidic devices. In 2012 *10th IEEE International Conference on Semiconductor Electronics (ICSE)*, 26-29. https://doi.org/10.1109/SMElec.2012.6417083

14. COMSOL Multiphysics® Software - Understand, Predict, and Optimize. *COMSOL*. Retrieved March 2, 2023 from https://www.comsol.com/comsol-multiphysics

15. Solis-Tinoco, V., Morales-Luna, G., Acevedo-Barrera, A., Ochoa, A., Vazquez-Estrada, O., Olguin, L. F. *et al.* (2022). An optical sensor combining surface plasmon resonance, light extinction, and near-critical angle reflection, for thin liquid film biochemical sensing. *Optics and Lasers in Engineering*, 158, 107137. https://doi.org/10.1016/j.optlaseng.2022.107137

16. Bauer, W. A. C., Fischlechner, M., Abell, C., & Huck, W. T. S. (2010). Hydrophilic PDMS microchannels for high-throughput formation of oil-in-water microdroplets and water-in-oil-in-water double emulsions. *Lab on a Chip*, 10(14), 1814-1819. https://doi.org/10.1039/C004046K

Chapter 1 Food Area

INFLUENCE OF THE ADDITION OF ORGANIC COMPOUNDS IN OBTAINING GELATIN NANOFIBERS

Wendy Magaly Arias Balderas, Ningel Omar Gama Castañeda, Eduardo San Martín Martínez, Miguel Ángel Aguilar Méndez*

Instituto Politécnico Nacional, CICATA Unidad Legaria, Calzada Legaria 694, Col. Irrigación, Ciudad de México. C.P. 11500. México.

*maguilarme@ipn.mx

Arias Balderas, W. M., Gama Castañeda, N. O., San Martín Martínez, E., & Aguilar Méndez, M. Á. (2023). Influence of the addition of organic compounds in obtaining gelatin nanofibers. In E. San Martín-Martínez (Ed.). *Research advances in nanosciences, micro and nanotechnologies. Volume IV* (pp. 107-122). Barcelona, Spain: Omniascience.

Abstract

Nanomaterials have been introduced to the food industry by developing packages and sensors containing active substances. These substances can be incorporated into nanofibers, prolonging the shelf-life of food. In this study, we developed nanofibers using a mixture of gelatin, citric acid, glycerol, and poly (ε-caprolactone) (PCL). The nanofibers were characterized using rheological, morphological, physical, and mechanical analyses. The results showed that adding citric acid increased the viscosity of the polymeric solution, but it did not reach the level of pure gelatin solution. The presence of citric acid conserved the pseudoplastic behavior required for electrospinning, decreased the fiber diameter, and provided greater tensile strength. The presence of citric acid and glycerol helped to improve the morphological characteristics of the nanofibers, resulting in continuous and homogeneous fibers with a better appearance. Fourier transform infrared spectra (FTIR) showed the presence of characteristic gelatin and PCL peaks, indicating the successful incorporation of the polymers. Nanofibers made from gelatin-citric acid and gelatin-glycerol mixtures are the most promising options for incorporating metabolites and active compounds, as they provide an accessible and biodegradable system in the food industry.

Keywords: Electrospinning, nanofiber, gelatin, poly (ε-caprolactone).

1. Introduction

The development of nanofibers has experienced a surge in recent years due to several benefits, such as higher surface area, smaller pore size, higher porosity, and tensile strength [1]. Different methods can produce these materials, including template synthesis, phase separation, self-assembly, and electrospinning [2]. Electrospinning is currently the most popular technique for nanofiber processing due to its practicality, versatility, high processing yield, low cost, and diverse morphologies [3]. This method involves applying high voltage to a polymer solution from a syringe tip. The droplet's surface becomes electrically charged, generating repulsive forces. The solvent evaporates during its trajectory to a metal collector (plate or cylinder), and the material is deposited as nanofibers [4]. Three key factors are considered when developing nanofibers: formulation factors (such as solvents and polymers used to generate the polymer solution, polymer solution concentration, concentration of a substance or active ingredient to be incorporated in the solution, etc.), processing factors (electrospinning parameters such as flow rate, applied voltage, syringe to collector distance, etc.), and environmental factors (ambient temperature and relative humidity). Electrospinning is an innovative technique that has found applications in various fields, initially in the biomedical and pharmaceutical industries, but recently expanded to areas such as food, particularly in developing smart packaging [5 – 6]. Electrospinning has proven successful in these areas as it serves as a release system for various substances, including active ingredients and/or metabolites, through an intelligent system known as "nano in a nano" [7] and is applicable in different fields. The selection of polymers plays a crucial role in this technique, as they must be suitable for electrospinning and have good mechanical properties [8]. A wide range of natural polymers, including zein [9], chitosan [10], cellulose [11], gelatin [12], pullulan [3], and even some plant and seed mucilage [13], have been used to develop nanofibers. Synthetic polymers such as ethyl cellulose [14], polyvinyl alcohol (PVA) [15], polylactic acid (PLA), and polyethylene glycol (PEG) [16] have also been used.

Gelatin is one of the most commonly used natural polymers due to its biocompatibility, accessibility, low cost, biodegradability, and high efficiency [17]. This soluble protein is obtained by breaking down the collagen structure into single chains [18]. Gelatin has been extensively studied, and electrospinning has yielded satisfactory results with this polymer [19]. Researchers have reported that fibers with a stable morphology, high water absorption capacity, and excellent

mechanical properties can be produced using gelatin [20]. Therefore, in this study, we formulated various gelatin compositions to evaluate the effect of adding a crosslinking agent, surfactant, and synthetic polymer on nanofiber production. These nanofibers will be utilized in the future for incorporating metabolites into the manufacture of smart packaging.

2. Material and methods

2.1. *Material*

Gelatin type A from porcine skin 300 bloom (Sigma Aldrich, USA) was used for nanofiber development. Other materials included glycerol, citric acid, and PCL (Mn= 800,000), also from Sigma Aldrich (USA). Glacial acetic acid, sourced from Fisher Scientific (Massachusetts, USA), was used as a solvent.

2.2. *Preparation of polymeric solutions*

Various formulations were created with a gelatin concentration of 20 % (w/v) and a water-acetic acid mixture in a 50:50 ratio. The ratio of the polymers and organic compounds utilized in each formulation is presented in Table 1. Each formulation was stirred at 350 rpm for 1 h at 60 °C. The GePCL combination was the only formulation prepared with a total polymer concentration of 10 % (w/v), using acetic acid as a solvent, and was stirred for 3 h to improve the incorporation between the two polymers. Finally, all solutions were cooled to 30 °C, loaded into a syringe, and utilized for electrospinning.

Table 1. Formulations of polymeric solutions.

Mixture	Ge (%)	GeCA (%)	GeGL (%)	GePCL (%)
Gelatin	100	99	100	70
Citric acid	-	1	-	-
PCL	-	-	-	30
Solvents				
Water	50	50	49.7	-
Acetic acid	50	50	50	100
Glycerol	-	-	0.3	-

2.3. *Electrospinning process*

Nanofibers were produced using electrospinning equipment from Bioinica & Fluidnatek LE-100 (Spain). The polymeric solution was loaded into a disposable syringe (5 mL) with an 18-gauge stainless steel needle tip. Each mixture was introduced into the injection pump, and a flow rate of 0.8-1.0 mL/h was used. Two electrodes (positive and negative) were placed near a high-voltage source. A voltage of +18 kV and -5 kV was applied between the syringe tip and the metallic collector plate, which was positioned 10 cm away, creating an electric field and facilitating the formation of nanofibers. Nanofibers were collected on wax paper (10 × 10 cm) previously placed on the collector. Finally, the nanofibers were stored in a desiccator for 24 h.

2.4. *Scanning electron microscopy (SEM)*

A small quantity of nanofibers was obtained and attached to a metal sample holder using double-sided tape. The samples were subsequently sputter-coated with a gold layer for 120 seconds (Desk IV, Denton Vacuum, USA) and imaged at an acceleration voltage of 20 kV. Micrographs were captured at various magnifications using SEM equipment from JEOL (JMS-6390LV, Japan).

2.5. *Fourier transform infrared (FTIR) spectra*

FTIR analysis was performed using a spectrophotometer (Cary 630, Agilent Technologies, USA). The analysis involved the identification of characteristic signals (peaks) present in an infrared spectrum. These signals arise from interatomic vibrations between functional groups present in the nanofibers, and peaks can be observed at different wave numbers within a range of 4000 to 500 cm^{-1}. An attenuated total reflectance cell was utilized with a resolution of 4 cm^{-1} and 32 scans.

2.6. *Rheological Characterization*

The viscosity behavior of the polymeric solutions was determined according to the method described by Kazemianrad [17], with some modifications. A rheometer (Anton Paar MCR 302, Austria) was utilized to measure the viscosity as a function of the shear rate. The required geometry was a cone-plate PP25-1 (24.981 mm diameter), and measurements were taken at shear rates ranging from 1 to 100 s^{-1} with 10 s^{-1} intervals, resulting in a total of 30 data points. The samples were measured at room temperature (25 °C) and with a 0.5 mm gap.

2.7. *Physical and mechanical test*

The thickness of the nanofibers was measured using a Mitutoyo 547-500S micrometer (Digimatic, Japan). Similarly, mechanical property characterization was conducted using the methodology described by Nilsuwan [21], with some modifications. A Texture Analyzer (TA-XT2i) software was employed using the ASTM D882-02 standard method. Nanofiber samples were cut into strips (50 × 20 mm) for analysis. The strips were positioned between equipment tongs spaced 30 mm apart. The software was configured to use a stretching speed of 1 mm/min, a test speed of 3 mm/s, and a force of 1 N. Tensile strength (TS) was then calculated.

2.8. *Statistical Analysis*

The results were presented as the mean ± standard deviation (SD). Data were analyzed using a one-way ANOVA, followed by mean comparisons using the Least Significant Difference (LSD) method, using OriginPro 8.5 software. Statistical significance was tested at $p < 0.05$.

3. Results and discussion

3.1. *Scanning electron microscopy (SEM)*

Figure 1 depicts SEM micrographs of four types of nanofibers: gelatin (Ge), gelatin-citric acid (GeCA), gelatin-glycerol (GeGL), and gelatin-polycaprolactone (GePCL). In most of the images, the nanofibers appear smooth, uniform, linear, and free of defects such as beading, dripping, and broken fibers. The desirable properties of gelatin, such as being a highly natural polymer, hydrophilic, with a low melting point, and good dispersibility, make it suitable for creating high-quality nanofibers with thickening, dispersing, and emulsifying properties [22, 23]. The smooth, uniform, and bead-free nanofibers in these micrographs are mainly due to the high concentration of Ge used in the polymer solution, which was 20 % (m/v). Okutan [24] has shown that a concentration greater than 14 % w/v is required to create nanofibers with uniform and defect-free structures. By increasing the polymer solution concentration, a stable solution stream is created that does not break, resulting in a uniform nanofiber deposit [25, 26]. In contrast, low-concentration gelatin polymer solutions have been reported to produce beads and droplets instead of nanofibers [27, 28].

Moreover, it has been observed that the viscosity of a polymer solution increases proportionally with its concentration and the molecular weight of its components [29]. Thus, the GePCL solution was expected to have the highest viscosity; however, it had a low viscosity because it was prepared at a lower concentration (10 %) than the other formulations (20 %). As a result, it showed a rheological behavior very close to Newtonian. The low concentration and viscosity of the solution, along with the partial phase separation between Ge and PCL, caused an unstable solution jet, resulting in fibers of large size and heterogeneous diameters, as well as solution droplets when deposited on the collector.

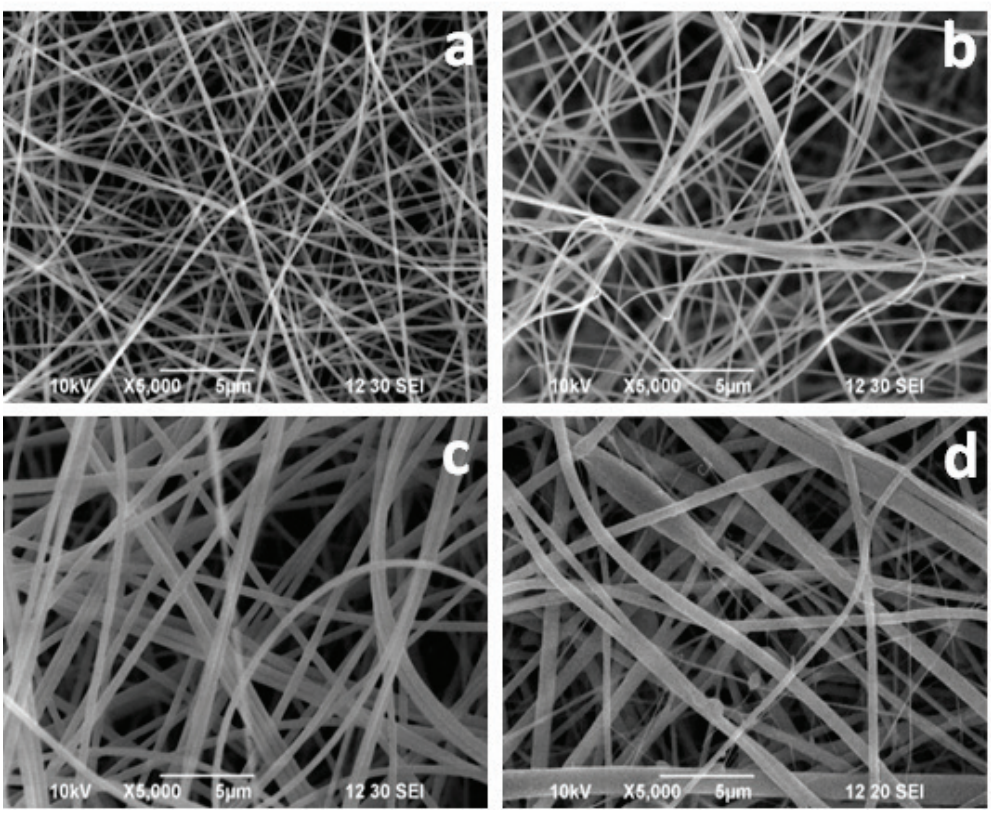

Figure 1. SEM images of nanofibers formulated with Ge (a), GeCA (b), GeGL (c) and GePCL (d).

Figure 2 displays the frequency histograms of nanofiber diameters. The results indicate that the average diameter of nanofibers produced solely from gelatin is the smallest, at 224±5nm. In contrast, incorporating additional components such as citric acid, glycerol, and PCL increases diameters of 250±6, 468±13, and 533±5 nm, respectively. The observed increase in nanofiber diameter follows the order of increasing molar mass of the components, which can explain the trend.

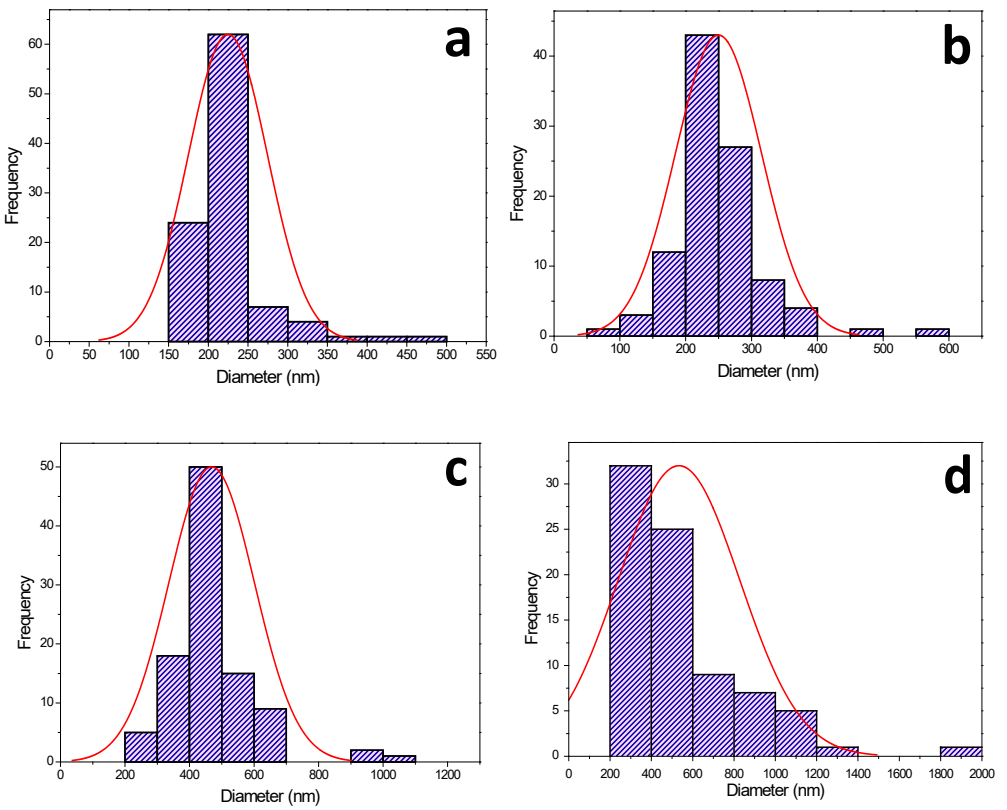

Figure 2. Frequency histograms of the distribution of diameters of the nanofibers obtained with Ge (a), GeCA (b), GeGL (c) and GePCL (d).

3.2. *FTIR Analysis*

Figure 3 displays the FTIR spectra of the nanofibers produced using gelatin (Ge), gelatin-citric acid (GeCA), gelatin-glycerol (GeGL), and gelatin-polycaprolactone (GePCL). Each spectrum shows characteristic signals that can be used for practical analysis, and the molecular structures of the nanofiber components were also included. Gelatin is a natural polymer and protein that produces well-defined signals, such as the peak at 3294 cm^{-1}, corresponding to the symmetric stretching vibrations of N-H amino groups belonging to primary amides. The signals at 2930 and 2850 cm^{-1} correspond to asymmetric and symmetric stretching vibrations of CH_2 groups, respectively. The intense PCL peak at 1724 cm^{-1} is a characteristic signal of carbonyl groups (C=O) in the ester-containing PCL in its chemical structure [30]. Likewise, a characteristic Ge signal can be observed at 1640 cm^{-1}, corresponding to the stretching vibrations of C=O groups belonging to primary

amide groups [31]. The amide signal confirms the presence of Ge in the GePCL nanofibers, which are highly hygroscopic due to their interaction with hydrogens [32]. This same signal is attributed to the random helix-like spiral conformation of the gelatin structure. In the GeCA and GeGL spectra, peaks are observed at the same wavenumbers as in the Ge spectrum, but with decreased intensities, likely due to the formation of fiber component interactions, which was corroborated by the high solubility of Ge in the solutions with CA and GL. The signal at 1526 cm^{-1} refers to bending vibrations of N-H amino groups presented by secondary amides and stretching vibrations of the C-N bond of the Ge structure. The signals at 1240 and 1160 cm^{-1} correspond to asymmetric stretching vibrations of the C-O-C bond of PCL, which are characteristic peaks of PCL, thereby confirming the incorporation of this polymer with Ge [33].

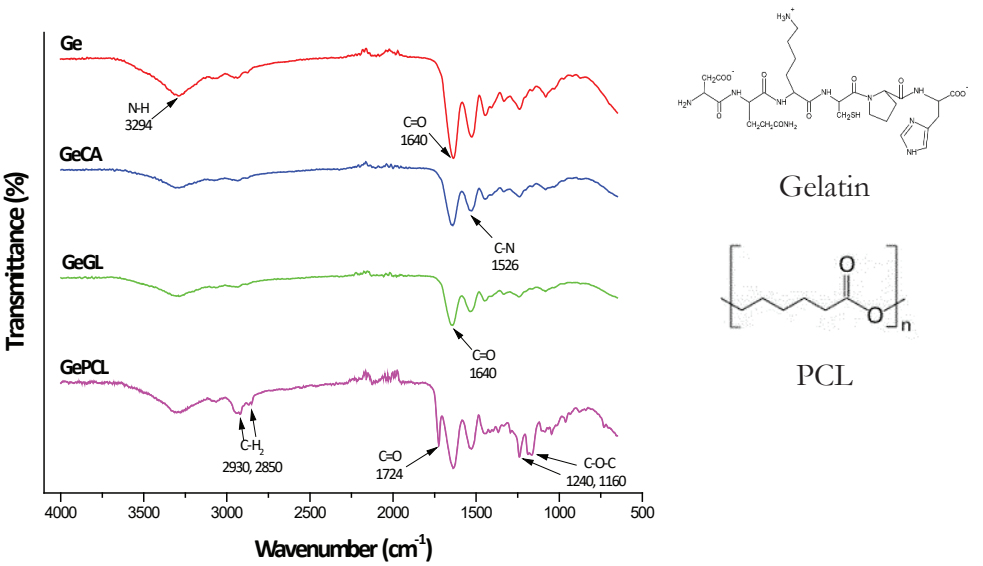

Figure 3. FTIR spectra corresponding to nanofibers of Ge, GeCA, GeGL and GePCL.

3.3. *Rheological Properties*

Viscosity is a crucial parameter in the electrospinning process, as it determines the formation of continuous and uniform fibers [8]. Figure 4 illustrates the viscosity behavior concerning a shear rate of 1–100 s^{-1}. The gelatin solution displayed behavior similar to that of a Newtonian fluid within the 1–60 s^{-1} range. However, at higher shear rates, the viscosity increased to 496 mPa.s, indicating a thickening shear behavior (rheopectic). GeCA and GeGL formulations showed similar behavior with the

same tendency but with a lower ratio than Ge. The GePCL mixture demonstrated almost Newtonian behavior throughout the shear range. The maximum viscosity – reached at a shear rate of 100 s^{-1} – was significantly higher in the Ge solution ($p<0.05$) than in GeCA and GeGL, which exhibited the lowest values.

The obtained flow curves were fitted to the Power Law model, and rheological parameters, including consistency coefficient (K) and flow behavior index (n), were calculated (Table 2). The Ge solution exhibited the highest value of K, while GePCL had the lowest value, as confirmed by the apparent viscosity results. In contrast, the n value of Ge was almost 1 within the 1–60 s^{-1} range, indicating similar Newtonian behavior. GeCA, GeGL, and GePCL solutions had values less than 1, indicating a shear-thinning behavior (pseudoplastic). This is favorable for nanofiber formation because, according to Mosayebi [34], polymers' arrangement during electrospinning is directly related to pseudoplastic behavior.

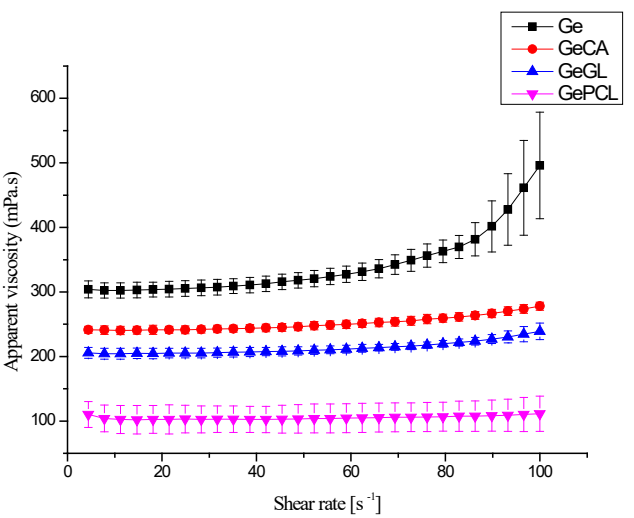

Figure 4. Flow curves of polymeric solutions: Ge, GeCA, GeGL and GePCL.

Table 2. Physical, mechanical and rheological parameters of nanofibers and Ge, GeCA, GL and GePCL solutions.

Formulation	Thickness (mm)	TS (MPa)	μ (mPa.s) [100 s^{-1}]	K (mPa.sn)	n
Ge	0.20 ± 0.02 [a]	0.96 ± 0.13 [b]	496.0 ± 0.08 [a]	279.15 ± 10.28 [a]	0.9616 ± 0.09 [a]
GeCA	0.10 ± 0.01 [b]	1.64 ± 0.16 [a]	278.0 ± 0.01 [b]	233.59 ± 6.71 [b]	0.3290 ± 0.09 [b]
GeGL	0.23 ± 0.01 [a]	1.38 ± 0.03 [a]	239.0 ± 0.01 [b]	198.24 ± 10.33 [c]	0.2686 ± 0.10 [b]
GePCL	0.06 ± 0.02 [c]	1.50 ± 0.11 [a]	111.3 ± 0.03 [c]	100.15 ± 20.23 [d]	0.0846 ± 0.04 [c]

TS=Tensile strength; K= Consistency coefficient; n= Flow behavior. Different letters in the same column indicate a significant difference ($p < 0.05$).

3.4. *Physical and mechanical tests*

Table 2 shows the thickness and TS values. Ge and GeGL formulations exhibited the highest thickness values, followed by GeCA and GePCL ($p < 0.05$), indicating that pure gelatin and its combination with glycerol promote the development of a thicker film. However, these formulations showed low TS values, possibly due to gelatin's high viscosity and rheological behavior. Furthermore, adding glycerol increases the nanofibers' plasticity and decreases the elastic modulus [35]. GePCL sample demonstrated a similar TS value to GeGL and the lowest thickness. GeCA had an intermediate thickness value (0.1 mm) and the highest TS value (1.86 MPa). Hence, in addition to the SEM images, GeCA may be considered the best nanofiber formulation due to citric acid facilitating better interaction between the molecules and increasing the hydrogen bond interactions between the carboxyl and amino groups of gelatin protein.

Citric acid has been investigated as a cross-linker, and successful results have been achieved in improving mechanical properties, increasing TS values, and decreasing the breaking point [36]. Although a low concentration of citric acid was used in this study, it likely enhanced these properties. However, a statistical difference was observed only in the Ge formulation.

4. Conclusions

Adding CA, GL, and PCL improved the final properties of the gelatin nanofibers. Gelatin nanofibers displayed good morphological characteristics, but their fiber diameters were the smallest, and their TS values were the lowest. On the other hand, the GeCA mixture presented the best physical characteristics by obtaining fibers close to those of Ge but with improved mechanical properties while maintaining pseudoplastic behavior. Similarly, the diameters of GeGL nanofibers were the most homogeneous and exhibited a similar rheological and physical behavior to GeCA. In conclusion, GeCA and GeGL formulations could be the best options for incorporating metabolites or active compounds into food.

Acknowledgement and Funding

Arias-Balderas and Gama-Castañeda wish to thank CONACYT Mexico (N° 2331328) for the financial support provided and IPN for the support in its facilities during the research study.

References

1. Chen K., Hu, H., Zeng, Y., Pan, H., Wang, S., Zhang, Y. *et al.* (2022). Recent advances in electrospun nanofibers for wound dressing. *European Polymer Journal*, 178. https://doi.org/10.1016/j.eurpolymj.2022.111490

2. Islam, M.S., Ang, B.C., Andriyana, A., & Afifi, A.M. (2019). A review on fabrication of nanofibers via electrospinning and teir applications. *SN Applied Sciences*, 1(10). https://doi.org/10.1016/j.carpta.2022.100262

3. Duan, M., Yu, S., Sun, J., Jiang, H., Zhao, J., Tong, C. *et al.* (2021). Development and Characterization of electrospun nanofibers based on pollulan/chitin nanofibers containing curcumin and anthocyanins for active-intelligent food packaging. *International Journal of Biological Macromolecules*, 187, 332-340. https.//doi.org/10.1016/j.ijbiomac.2021.07.140.

4. Hajikhani, M., & Lin, M. (2022). A review on designing nanofibers with high porous and rough surface via electrospinning technology for rapid detection of food quality and safety attributes. *Trends in Food Science & Technology*, 128, 118-128. https://doi.org/10.1016/j.tifs.2022.08.003

5. Shangguan, W., Li, S., Cao, L., Wei, M., Wang, Z., & Xu, H. (2022). Electrospinning and nanofibers: Building drug delivery systems and potential in pesticide delivery. *Materials Today Communications*, 33. https://doi.org/10.1016/j.mtcomm.2022.104399

6. Min, T., Zhou, L., Sun, X., Du, H., Zhu, Z., & Wen, Y. (2022). Electrospun functional polymeric nanofibers for active food packaging: A review. *Food Chemistry*, 391. https://doi.org/ 10.1016/j.foodchem.2022.133239

7. Shetty, K., Bhandari, A., & Yadav, K. (2022). Nanoparticles incorporated in nanofibers using electrospinning: A novel nano in nano delivery system. *Journal of Controlled Release*, 350, 421-434. https://doi.org/10.1016/j.jconrel.2022.08.035

8. Niu, B., Zhan, L., Shao, P., Xiang, N., Sun, P., Chen, H. *et al.* (2020). Electrospinning of zein-ethyl cellulose hybrid nanofibers with improved wáter resistance for food preservation. *International Journal of Biological Macromolecules*, 142. https://doi.org/10.1016/j.ijbiomac.2019.09.134

9. Yilmaz, A., Bozkurt, F., Cicek, P. K., Dertli, E., Durak, M. Z., & Yilmaz, M. T. (2016). A novel antifungal Surface-coating application to limit postharvest decay on coated apples: Molecular, termal and morphological properties of electrospun zein-nanofiber mats loaded with curcumin. *Innovative Food Science & Emerging Technologies*, 37, 74-83. https://dx.doi.org/10.1016/j.ifset.2016.08.008

10. Cui, C., Sun, S., Wu, s., Chen, S., Ma, J., & Zhou, F. (2021). Electrospun chitosan nanofibers for wound healing application. *Engineered Regeneration*, 2 82-90. https://doi.org/10.1016/j.engreg.2021.08.001

11. Surendran, G. & Sherje, A. P. (2022). Cellulose nanofibers and composites: An insight into basics and biomedical applications. *Journal of Drug Delivery Science and Technology*, 75. https://doi.org/10.1016/j.jobab.2020.10.001

12. Gulzar, S., Tagrida, M., Nilsuwan, K., Prodpran, T., & Benjakul, S. (2022b). Electrospinning of gelatin/chitosan nanofibers incorporated with tannic acid and chitooligosaccharides on polylactic acid film: Characteristics and bioactivities. *Food Hydrocolloids*, 133. https://doi.org/10.1016/j.foodhyd.2022.107916

13. Dehghani, S., Noshad, M., Rastegarzadeh, S., Hojjati, M., & Fazlara, A. (2020). Electrospun chia seed mucilage/PVA encapsulated with green cardamonmum essential oils: Antioxidant and antibacterial property. *International Journal of Biological Macromolecules*, 161, 1-9. https://doi.org/10.1016/j.ijbiomac.2020.06.023

14. Rashidi, M., Seyyedi Mansour, S., Mostashari, P., Ramezani, S., Mohammadi, M., & Ghorbani, M. (2021). Electrospun nanofiber based on Ethyl cellulose/Soy protein isolated integrated with bitter orange peel extract for antimicrobial and antioxidant active food packaging. *International Journal of Biological Macromolecules*, 193, B, 1313-1323. https://doi.org/10.1016/j.ijbiomac.2021.10.182

15. Mishra, K., & Sinha, S. (2023). Extended investigation of Ficus religiosa based PVA electrospun nanofiber for cosmeceutical application. *Materials Today: Proceedings*, 72(5), 2668-2680. https://doi.org/10.1016/j.matpr.2022.08.346

16. Ferreira, K. N., Oliveira, R. R., Castellano, L. R. C., Bonan, P. R. F., Carvalho, V., Pena, L. *et al.* (2022). Controlled release and antiviral activity of acyclovir-loaded PLA/PEG nanofibers produced by solution blow spinning. *Biomaterials Advances*, 136. https://doi.org/10.1016/j.bioadv.2022.212785

17. Kazemianrad, F., Koocheki, A., & Ghorani, B. (2023). Encapsulation of caffeine in sandwich structured *Alyssum homolocarpum* seed gum/PVA/gelatin nanofibers using electrospinning technique. *Food Hydrocolloids*, 140. https://doi.org/10.1016/j.foodhyd.2023.108604

18. Du, P., Chen, X., Chen, Y., Li, J., Lu, Y., Li, X. *et al.* (2023). *In vivo* and *in vitro* studies of a propolis- enriched silk fibroin-gelatin composite nanofiber wound dressing. *Heliyon*, 9. https://doi.org/10.1016/j.heliyon.2023.e13506

19. Gulzar, S., Tagrida, M., Prodpran, T., & Benjakul, S. (2022). Antimicrobial film base on polylactic acid coated with gelatin/chitosan nanofibers containing nisin extends the shelf life of Asian seabass slices. *Food Packaging and Shelf Life*, 34. https://doi.org/10.1016/j.fpsl.2022.100941

20. Lv, Y., Yu, Z., Li, C., Zhou, J., Lv, X., Chen, J. *et al.* (2022). Gelatin-based nanofiber membranas loaded with curcumin and borneol as a sustainable wound dressing. *International Journal of Biological Macromolecules*, 219, 1227-1236. https://doi.org/10.1016/j.ijbiomac.2022.08.198

21. Nilsuwan, K., Benjakul, S., & Prodpran, T., & de la Caba, K. (2019). Fish gelatin monolayer and bilayer films incorporated with epigallocatechin gallate: Properties and their use as pouches for storage of chicken skin oil. *Food Hydrocolloids*, 89, 783-779. https://doi.org/10.1016/j.foodhyd.2018.11.056

22. Alipal, J., Mohd Pu'ad, N. A. S., Lee, T. C., Nayan, N. H. ., Sahari, N., Basri, H. *et al.* (2021). A review of gelatin: Properties, sources, process, applications, and commercialisation. *MaterialsToday: Proceedings*, 42(1), 240-250. https://doi:10.1016/j.matpr.2020.12.922

23. Wonganu, B. (2020). Application of Gelatin Derived from Waste Tilapia Scales to an Antibiotic Hydrogel Pad. *E3S Web of Conferences*, 141, 03004. https://doi.org/10.1051/e3sconf/202014103004

24. Okutan, N., Terzi, P., & Altay, F. (2014). Affecting parameters on electrospinning process and characterization of electrospun gelatin nanofibers. *Food Hydrocolloids*, 39, 19-26. https://doi.org/10.1016/j.foodhyd.2013.12.022

25. Sajkiewicz, P., & Kołbuk, D. (2014). Electrospinning of gelatin for tissue engineering – molecular conformation as one of the overlooked problems. *Journal of Biomaterials Science, Polymer Edition*, 25(18), 2009-2022. https://doi.org/10.1080/09205063.2014.975392

26. Tarus, B., Fadel, N., Al-Oufy, A., & El-Messiry, M. (2016). Effect of polymer concentration on the morphology and mechanical characteristics of electrospun cellulose acetate and poly (vinyl chloride) nanofiber mats. *Alexandria Engineering Journal*, 55(3), 2975-2984. https://doi.org/10.1016/j.aej.2016.04.025

27. Li, M., Mondrinos, M. J., Gandhi, M. R., Ko, F. K., Weiss, A. S., & Lelkes, P. I. (2005). Electrospun protein fibers as matrices for tissue engineering. *Biomaterials*, 26(30), 5999-6008. https://doi.org/10.1016/j.biomaterials.2005.03.030

28. Li, M., Guo, Y., Wei, Y., Macdiarmid, A., & Lelkes, P. (2006). Electrospinning polyaniline-contained gelatin nanofibers for tissue engineering applications. *Biomaterials*, 27(13), 2705-2715. https://doi.org/10.1016/j.biomaterials.2005.11.037

29. Etxabide, A., Akbarinejad, A., Chan, E. W., Guerrero, P., de la Caba, K., Travas-Sejdic, J., & Kilmartin, P. A. (2022). Effect of gelatin concentration, ribose and glycerol additions on the electrospinning process and physicochemical properties of gelatin nanofibers. *European Polymer Journal*, 180, 111597. https://doi.org/10.1016/j.eurpolymj.2022.111597

30. Gautam, S., Sharma, C., Purohit, S.D., Singh, H., Dinda, A.K., Potdar, P.D. *et al.* (2021). Gelatin-polycaprolactone-nanohydroxyapatite electrospun nanocomposite scaffold for bone tissue engineering. *Materials Science and Engineering*, 119. https://doi.org/10.1016/j.msec.2020.111588.

31. Lim, Y. C., Johnson, J., Fei, Z. Farson, D., Lannutti, J.J., Choi, H.W., & Lee, L. (2009). Micropatterning and characterization of electrospun PCL/gelatin nanofiber tissue scaffolds by femtosecond laser ablation. *ICALEO 2009 - 28th International Congress on Applications of Lasers and Electro-Optics, Congress Proceedings*, 102, 1114-1123. https://doi.org/10.1002/bit.22914.

32. Bual, R., Kimura, H., Ikegami, Y., Shirakigawa, N., & Ijima, H. (2018). Fabrication of liver-derived extracellular matrix nanofibers and functional evaluation in in vitro culture using primary hepatocytes. *Materrialia*, 4, 518-528. https://doi.org/10.1016/j.mtla.2018.11.014.

33. KarbalaeiMahdi, A., Shahrousvand, M., Javadi, H. R., Ghollasi, M., Norouz, F., Kamali, M. *et al.* (2017). Neural differentiation of human induced pluripotent stem cells on polycaprolactone/gelatin bi-electrospun nanofibers. *Materials Science and Engineering: C*, 78, 1195-1202. https://doi.org/10.1016/j.msec.2017.04.083.

34. Mosayebi, V., Fathi, M., Shahedi, M., Soltanizadeh, N., & Emam-Djomeh, Z, (2022). Fast-dissolving antioxidant nanofibers base don Spirulina protein concentrate and gelatin developed using needleless electrospinning. *Food Bioscience*, 47, 101759. https://doi.org/10.1016/j.fbio.2022.101759

35. Nilsuwan, K., Benjakul, S., & Prodpran, T. (2018). Physical/thermal properties and heat seal ability of bilayer films based on fish gelatin and poly(lactic acid). *Food Hydrocolloids*, 77, 248-256. https://doi.org/10.1016/j.foodhyd.2017.10.001

36. Jiang, H., Sun, J., Li, Y., Ma, J., Lu, Y., Pang, J. *et al.* (2020). Preparation and characterization of citric acid crosslinked konjac glucomannan/surface deacetylated chitin nanofibers bionanocomposite film. *International Journal of Biological Macromolecules*, 164. https://doi.org/10.1016/j.ijbiomac.2020.08.138

Chapter 2 Food Area

EFFECT OF CHITOSAN, THYME ESSENTIAL OIL, AND PROPOLIS BASED NANOCOATINGS, ON TOMATO QUALITY DURING STORAGE AT CONTROLLED AND AMBIENT TEMPERATURES

Zormy Nacary Correa Pacheco[1*], María Luisa Corona Rangel[1], Silvia Bautista Baños[1], Laura Leticia Barrera Necha[1], Rosa Isela Ventura Aguilar[2], Mónica Hernández López[1]

[1]Centro de Desarrollo de Productos Bióticos, Instituto Politécnico Nacional, Carr. Yautepec-Jojutla Km. 8.5, San Isidro Yautepec, Morelos, 62731, Mexico.

[2]CONACYT-Centro de Desarrollo de Productos Bióticos, Instituto Politécnico Nacional, Carr. Yautepec-Jojutla Km. 8.5, San Isidro Yautepec, Morelos, 62731, Mexico.

zcorreap@ipn.mx

Correa Pacheco, Z. N., Corona Rangel, M. L., Bautista Baños, S., Barrera Necha, L. L., Ventura Aguilar, R. I., & Hernández López, M. (2023). Effect of chitosan, thyme essential oil, and propolis based nanocoatings, on tomato quality during storage at controlled and ambient temperatures. In E. San Martín-Martínez (Ed.). *Research advances in nanosciences, micro and nanotechnologies. Volume IV* (pp. 123-140). Barcelona, Spain: Omniascience.

Abstract

Nowadays, new alternatives for avoiding contamination due to the use of non-biodegradable packing and pesticides for fruit and vegetable preservation must be sought. In this work, three coatings based on chitosan nanoparticles, chitosan-thyme essential oil or chitosan-propolis nanoparticles were tested on inoculated and non-inoculated tomato with *Alternaria alternata*. The fruit was stored at 11 ± 2 °C for 14 days and at ambient temperature at 27 ± 2 °C for 7 days. The TEM and DLS showed a particle size in the range of 3.8 to 9 nm. The postharvest quality of tomato fruit was evaluated as firmness, weight loss, color and total soluble solids (TSS). It was obtained that the firmness decreased, the weight loss increased; and color and TSS were maintained over the storage days at both temperatures. The loss of firmness for the coated tomato fruit stored at 11 ºC was less than 1 N. On the other hand, the weight loss was less than 3 % and 8 % for the controlled and ambient temperature stored fruit, respectively, on day 7. It was concluded that the chitosan nanoparticles coating maintained a better postharvest quality of tomato, representing a natural alternative for the preservation of this important horticultural commodity.

Keywords: *Alternaria alternata*, *Lycopersicum esculentum L.*, nanoparticles, weight loss, firmness, color, postharvest preservation.

1. Introduction

Tomato (*Lycopersicum esculentum L.*) is the second important crop in Mexico with high nutritional value and uses in traditional cooking [1, 2]. According to data from the Food and Agriculture Organization of the United Nations Statistics Division (FAOSTAT), tomato represented 7.77 % of the export of the country by 2021, with a production of 4,149,240.67 ton [3, 4]. However, during storage, it is susceptible to various diseases caused by different microorganisms, among them, fungi such as *Alternaria alternata* that responsible for the black rot disease and bacteria deteriorating its postharvest quality [5].

Nowadays, nanotechnology has allowed the elaboration of coatings, in which the use of nanoparticles, enhances the fruit protection effect due to the highest surface area to volume ratio of the nanostructures, improving their activity [6]. Chitosan is a biocompatible and biodegradable polymer with a wide range of applications used for the elaboration of nanostructured coatings [7]. On this subject, Gutiérrez-Molina *et al.* [8] reported a nanostructured coating with 30 % of chitosan nanoparticles to preserve refrigerated tomatoes at 10±1 °C for 19 days. A weight loss of less than 13 % and a color change of less than 5 % were observed compared to the control (uncoated fruit). Firmness did not change with the storage days. On the other hand, chitosan nanoparticles (NPQs) and chitosan added with thyme essential oil (QS+NPTs) coatings for different concentration of nanoparticles (15, 30 and 45 %) were evaluated for controlling the bacterium *Pectobacterium carotovorum* in tomatoes, stored for 7 days at 10 °C having a relative humidity of c.a. 70 %. In this study, there were differences in the variable color in fruit coated with QS+NPTs 30 %, especially in the luminosity and chroma values on the inoculated tomatoes. Regarding the hue value, the highest variation was for the fruit coated with QS+NPQs 45 %. For firmness, the lowest loss was for tomatoes treated with QS+NPQs 15 %. The values of TSS presented a difference between 3 and 5 % and of weight loss between 0.7 and 1.2 % [9]. The aim of this study was to assess the effect of three nanostructured coatings based on chitosan, chitosan-thyme essential oil and chitosan-propolis on the storage behavior of tomato at controlled and ambient temperature measuring the quality variables of weight loss, firmness, TSS, and color.

2. Materials and methods

2.1. *Materials*

The reagents used for nanoparticles' elaboration (NPs) were medium molecular weight chitosan with a deacetylation degree of 75-85 % (Sigma-Aldrich Corp., St. Louis, MO, United States) which was dissolved in acetic acid (Fermont,

Monterrey, N.L., Mexico) and distilled water (0.05 %). For the incorporation of the thyme essential oil (Essential Oils-Essencefleur, Mexico City, Mexico) or the aqueous extract of propolis (10 %) (REDSA, Cuernavaca, Morelos, Mexico) to the nanoparticles, methanol (JT Backer, Phillipsburg, NJ, United States) and Tween 20 (Hycel, Zapopan, Jal., Mexico) were used. For the nanocoatings elaboration, high molecular weight chitosan (América Alimentos, Zapopan, Jal., México) and deacetylation degree of 91 % (1 %) was used as matrix.

2.2. *Methods*

2.2.1. Nanoparticles elaboration

The nanoparticles were elaborated using the nanoprecipitation method [10]. Two phases were prepared, one aqueous and one organic. The aqueous phase consisted of a solution of medium molecular weight chitosan (0.05 % w/v) in a solution of glacial acetic acid and distilled water (1 % v/v). For the organic phase, Tween 20 (1 %) was dissolved in 40 mL of ethanol. The concentration of both the essential oil of thyme and the aqueous extract of propolis added to the organic phase was 5 %. Then, by using a peristaltic pump (MasterFlex, Vernon Hills, IL, USA), 2.5 mL of the aqueous phase was added dropwise to the organic phase, stirring for 10 min. Next, a rotary evaporator (model 300, Büchi, Flawil, St. Gallen, Switzerland) was used to concentrate the NPs solution at 40 °C and 40 rpm. Final volume was 2 mL, being stored at 4 °C.

2.2.2. Nanocoatings elaboration and application

Based on 33 % chitosan nanoparticles (NPQ), chitosan-thyme nanoparticles (NPT) or chitosan-propolis nanoparticles (NPP), 66.7 % of chitosan (1 %) and 0.3 % of glycerol (JT Backer, Phillipsburg, NJ, United States), three formulations were elaborated and two controls were considered: inoculated tomato fruit with *A. alternata* C(+) and non-inoculated tomato fruit C(−). The coatings were elaborated following the methodology of Gutiérrez-Molina *et al.* [10]. The order of components addition was as follows: glycerol was added to chitosan (1 %) and mixed using a homogenizer (Virtis, model 45, Los Angeles, CA, United States) for 5 min at 10,000 rpm. Next, the NPs were added and stirred for another 5 min [11].

The tomatoes were purchased at a local market in Cuautla, Morelos. Fist, the fruit were washed with distilled water and disinfected with a sodium hypochlorite solution (3 %) for 3 min. They were rinsed again with water and the formulations

were sprayed on the fruit and allowed to dry. Then, disks of 5 mm of diameter containing the fungus were placed inside 4 holes of 2 mm in diameter. The *A. alternata* isolate was obtained from infected bell pepper and previously cultivated in potato dextrose agar culture medium (PDA) (BD Bioxon, State of Mexico, Mexico) for 7 days. The effect of the nanocoating was evaluated on fruit stored at 11 ± 2 °C for 14 days and at 27±2 °C for 7 days.

2.3. *Nanoparticles characterization by transmission electron microscopy (TEM) and dynamic light scattering (DLS)*

NPs morphology was observed using a transmission electron microscope (JEOL-JEM 2010, Tokyo, Japan) at an acceleration voltage of 200 kV placing a drop of nanoparticles solution on a copper grid. IMAGEJ software (National Institutes of Health, Bethesda, MD, USA) was used to calculate the average particle size. For the particle size distribution measurement, a Zetasizer Nano-ZS90 (Malvern Instruments, Worcestershire, UK) was employed, placing 3 mL of the NPs solution in a quartz cuvette. Before measurement, the NPs solution was sonicated for 10 min.

2.4. *Effect of nanostructured coating on tomato quality essays*

2.4.1. Weight loss

To determine the tomato fruit weight loss, a portable digital scale (OHAUS, Parsippany, NJ, U. S. A.) was used. The difference between the initial weight and the final weight of the tomato fruit was calculated and expressed as percentage.

2.4.2. Firmness

The firmness was measured on both sides of the tomato fruit using a penetrometer (Lutron FR-5120, Coopersburg, PA, USA) and results were reported in Newtons (N).

2.4.3. Total soluble solids (TSS)

For TSS determination, a drop of tomato fruit juice was placed in a refractometer (Atago N-1E, Fukaya-shi, Saitama, Japan). The results were expressed as percentage.

2.4.4. Color

The color was measured in two opposite sides of the tomato fruit using a colorimeter (Konica Minolta Sensing® 9992–995 BC 10, Chiyoda, Tokyo, Japan). The results were expressed as hue angle ($Hue=\tan^{-1} b^*/a^*$), chromaticity ($C^*=\sqrt{(a^*)^2+(b^*)^2}$) and lightness ($L^*$) [11].

2.5. *Statistical analysis*

The measurements for all variables were made in 5 fruit for treatment. The data obtained from the experimentation were analyzed using the InfoStat software (InfoStat, Sacramento, CA, 2018) with a double analysis of variance (ANOVA) and Tukey's mean comparison test ($p<0.05$).

3. Results and discussion

3.1. *Nanoparticles characterization by transmission electron microscopy (TEM) and dynamic light scattering (DLS)*

In Figure 1, the morphology of the nanoparticles can be seen. For the NPQ a more homogeneous distribution is observed (Figure 1a). On the other hand, the NPQ and NPP showed different sizes or possible agglomerates as seen in Figures. 1b) and 1c), respectively. The nanoparticles range was between 3.8 and 6 nm as calculated by Image J.

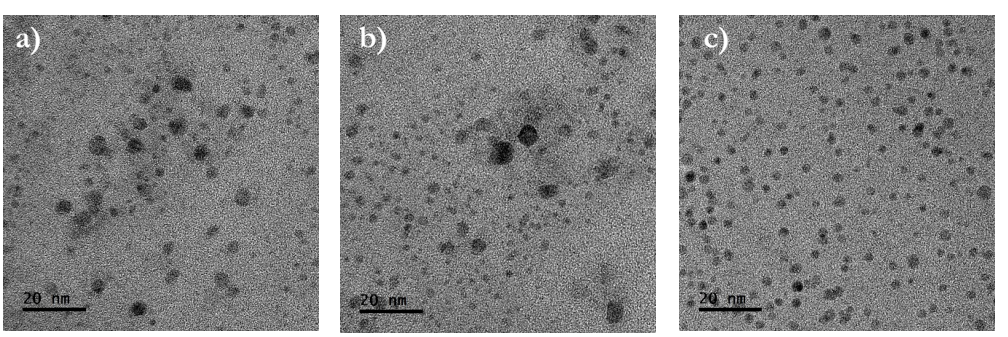

Figure 1. TEM of a) NPQ, b) NPT, and c) NPP. NPQ=chitosan nanoparticles, NPT=chitosan-thyme nanoparticles, NPP=chitosan-propolis nanoparticles.

Figure 2 shows the results of the DLS for the NPQ, NPT and NPP. A bimodal distribution is observed for the NPQ (Figure 2a) with the smallest particles in the range of 3.8 to 9 nm and the largest between 60 and 120 nm. Similarly,

the NPT presented a bimodal distribution with two populations. The first was between 8 and 15 nm and the second between 300 and 600 nm. Finally, the NPP showed a larger particle size with a unimodal distribution between 220 and 2000 nm. According to Sreekumar *et al.* [12] the presence of the second peak with the largest particle size may be related to aggregates. These results agreed with those previously published by our research group [13 – 16]. A possible reason for the formation of aggregates in the NPP coating could be related to the effect of propolis loading. It has been found that non-encapsulated propolis attached to the NPQ surface, increases the hydrophobicity and the interaction between NPQ and propolis with their subsequent aggregation [17].

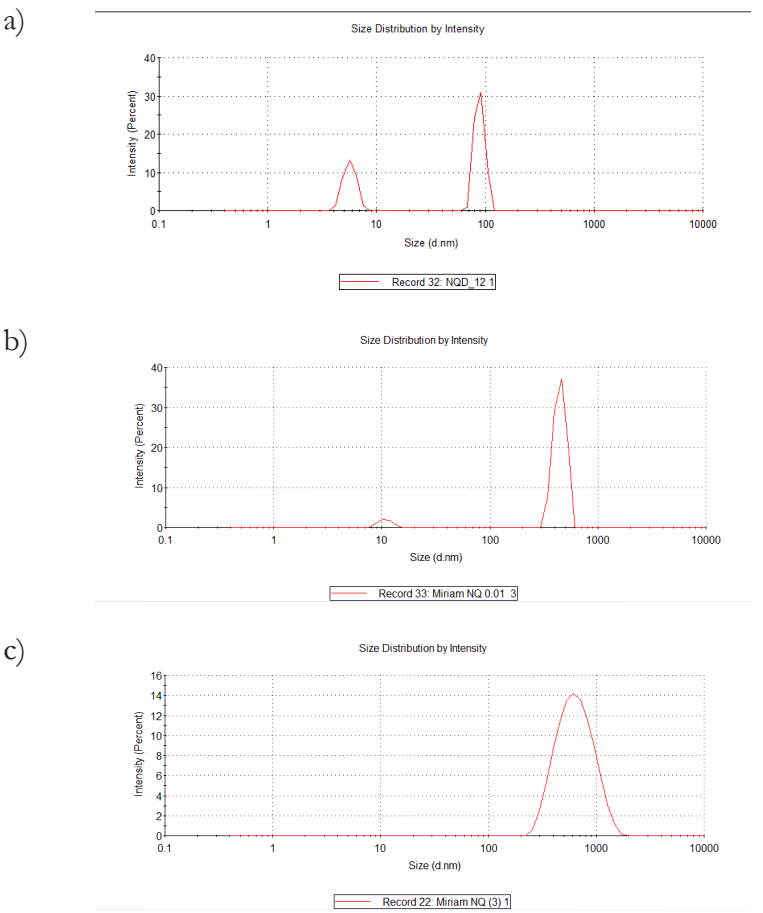

Figure 2. Particle size distribution (d=diameter) for: a) NPQ, b) NPT, and c) NPP. NPQ=chitosan nanoparticles, NPT=chitosan-thyme nanoparticles, NPP=chitosan-propolis nanoparticles.

3.2. *Effect of nanostructured coating on tomato quality*

3.2.1. Weight loss

In Figure 3, the weight loss of the tomato fruit refrigerated (Figure 3a) and stored at ambient temperature (Figure 3b) are shown. In general, weight loss is increased over time.

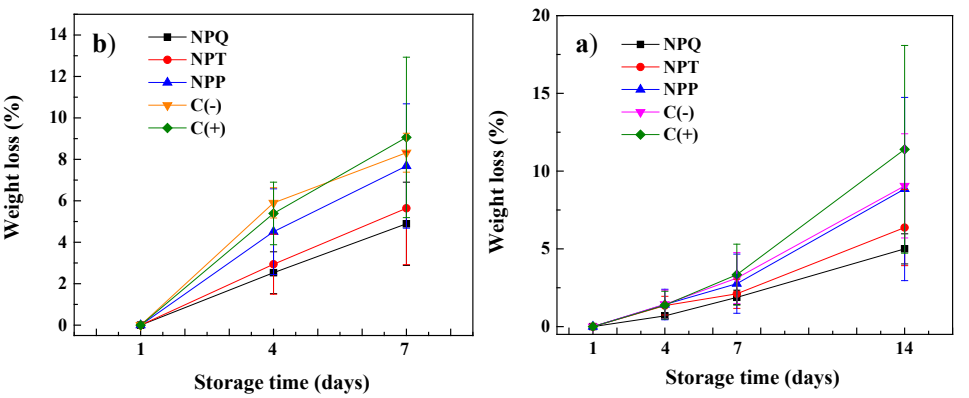

Figure 3. Weight loss of tomatoes coated with NPQ, NPT, and NPP and two controls, and stored at a) 11±2 °C for 14 days and b) 27±2 °C for 7 days. Error bars show the standard error of the mean. NPQ=chitosan nanoparticles; NPT=chitosan nanoparticles encapsulating thyme essential oil; NPP=chitosan nanoparticles encapsulating aqueous extract of propolis; C(−)=fruit not inoculated; C(+)=inoculated fruit.

Regarding the refrigerated tomatoes (Figure 3a) on day 7, the weight loss was between 2-3 %, less than for the tomatoes stored at ambient temperature. No significant statistical differences ($p<0.05$) were found between formulations (not shown). Moreover, the weight loss for coated tomatoes was lower than for the controls. On the other hand, on day 14, the weight loss values were between 5-11 %, being 9 % less than the coated fruit. Similar behavior to fruit stored at ambient temperature.

For the samples stored at ambient temperature for 7 days (Figure 2b), there was a weight loss of less than 8 % for the coated fruit. The weight loss of the coated tomato fruit was slightly lower than the controls, being higher for the inoculated tomato fruit, although no significant statistical differences were observed ($p<0.05$). Among the coated fruit, the highest weight loss was for NPP, then for NPT and finally for NPQ, However, the values were similar. Therefore, there was no significant weight loss of the fruit during the storage period.

Refrigeration of fruit and vegetable is a technique that has been used over the years to preserve the horticultural products for an extended time [18]. Kibar *et al.* (2018) [19] used 0.5, 1.0 and 2.0 % chitosan solutions to extend the postharvest quality of tomatoes stored at two different temperatures (at 5 °C with relative humidity of c.a. 90 % and at 21 °C with relative humidity of c.a. 65 %). There was a reduction in weight loss for the chitosan-coated tomato fruit with a more evident effect for the solution with a concentration of 1 % having a weight loss value of less than 2 % after 10 days of refrigerated storage and with a loss of less than 4 % after 7 days of storage at ambient temperature. Also, a higher percentage of weight loss was observed for the non-coated fruit. This is related to the barrier property of the coating on the fruit that prevents further dehydration and therefore the weight loss [20]. Azmai *et al.* (2019) [21] found weight loss values for tomatoes stored at ambient temperature for 12 days at concentrations of 0.5, 0.75 and 1 % of chitosan of 7.5, 6.7, and 7.2 %, respectively, and of 6.5 % for the untreated tomatoes. These values were lower than those obtained in this present research for a longer storage time perhaps because of the degree of ripening (just changing color from green to red) of the tomato used by cited authors. For tomatoes refrigerated at 6 °C and coated with chitosan solutions at different concentrations, Sucharitha *et al.* [22] reported tomato weight loss of about 0.54, 1.3 and 3.9 % with concentrations of 0.25 %, 0.5 % and the control, respectively, after 6 days of storage. Similar to this study, values of 2-3 % for the coated fruit and higher than 3 % for controls were obtained with a lower value of weight loss of the coated fruit compared to the control. On the other hand, Mustafa *et al.* [23] reported a weight loss of 7 % for fruit stored at 15 °C with a R.H. of c.a. 80 % using a coating based on chitosan particles of 400, 600, and 800 nm, after 20 days of storage. A similar value obtained for the 14 days of storage of this work.

Compared with our previous research where nanostructured coatings were used, for tomatoes stored for 7 days at 10 °C, a weight loss of less than 2 % was obtained for NPQ coated fruit at different concentrations of nanoparticles in the formulation (15 %, 30 %, and 45 %). For the NPT coated fruit and the same concentrations, the weight loss was also less than 2 % [14]. On the other hand, for tomatoes refrigerated at 10 °C, the weight loss value for coated fruit with NPQ (30 %) was less than 3 % on day 8 of storage [8].

Firmness results are shown in Figure 4. For the tomato fruit stored at controlled temperature (Figure 4a) and ambient temperature (Figure 4b) there was a decrease in firmness over time. The decrease in firmness with ripening in tomato

is attributed to moisture loss due to transpiration and enzymatic changes. These changes cause cell wall deterioration in tomato tissues [24].

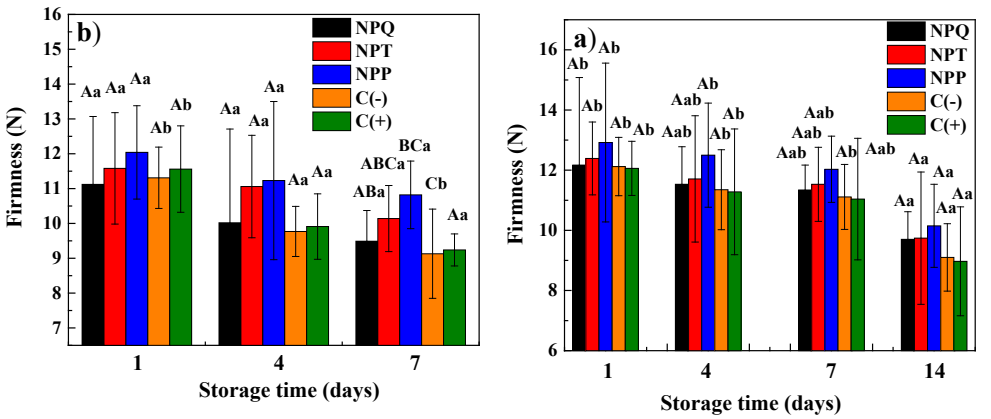

Figure 4. Firmness of tomatoes coated with NPQ, NPT, and NPP and two controls stored at: a) 11±2 °C for 14 days and b) 27±2 °C for 7 days. Different letters show statistical differences between formulations (upper case letters) and between days (lower case letters) calculated by ANOVA and Tukey's test ($p<0.05$). Initial firmness value=11.7±0.8 N. Error bars show the standard error of the mean. NPQ=chitosan nanoparticles; NPT=chitosan nanoparticles encapsulating thyme essential oil; NPP=chitosan nanoparticles encapsulating aqueous extract of propolis; C(−)=fruit not inoculated; C(+)=inoculated fruit.

The loss of firmness was lower for the refrigerated fruit (Figure 4a). On day 7 of storage the same trend was observed, with similar values. The highest loss of firmness was for the NPP coated tomato fruit (Δ=0.89 N), followed by the NPT-coated one (Δ=0.86 N), and finally for the coated NPQ tomato fruit (Δ=0.83 N). The uncoated tomato fruit showed a higher loss of firmness, with a variation of approximately 1 N for both controls. On day 14 the same trend was observed as for day 7. However, there was a higher difference in loss of firmness, almost approximately 3 N with higher values than the non-refrigerated fruit, although no significant statistical differences were found ($p<0.05$). For the tomatoes stored at ambient temperature (Figura 4b), the highest loss of firmness was for NPP coated fruit with values decreasing from 11.1 N to 9.4 N (Δ=1.63 N), followed by NPT coated fruit with values from 11.5 N to 10.1 N (Δ=1.44 N), and finally, for those coated with NPQ from 12.0 N to 10.8 (Δ=1.22 N). The controls showed a higher loss of firmness, being this value higher for the inoculated fruit with a variation of Δ=2.18 N compared to the non-inoculated fruit (Δ=2.32 N). Firmness values were higher than those for the coated tomato. For both storage

conditions, no significant statistical differences were observed ($p<0.05$) among coatings and during storage the days.

In a previous work [14], after 7 days at 10 °C, firmness values between 17 and 24 N were obtained in fruit refrigerated for different NPQ and NPT concentrations (15, 30, and 45 %) in the coating. For the controls, values were 18.8 N for C(−) and 28.5 N for C(+). Similarly, in other study, for tomatoes stored at 10 °C, on day 8, firmness values of 22 N were obtained for coated fruit (30 % of nanoparticles) compared to the initial value of 20 N [8]. A slight change in the value of firmness was observed like the values obtained in this research for tomatoes stored at controlled temperature. The difference between those values and the values obtained in this work is related the ripening grade of the fruit. In another study, for coated tomatoes with chitosan (0.5, 1, and 2 %) Kibar *et al.* [19] reported an initial firmness of 20 N for fruit stored at 5 °C and at 21 °C. For fruits stored at ambient temperature on day 7, the values of firmness were between 8 and 11 N for the coated fruit and of 12 N for the control fruit. Final values between 13 and 17 N were obtained for the coated refrigerated fruit and of 16 N for the control. The loss of firmness was lower for refrigerated fruit like the reported in this research. However, the variation of firmness with storage was higher. However, the. On the other hand, Azmai *et al.* [21] reported variations of firmness values of Δ=1.8 N for tomatoes stored at ambient temperature for 12 days treated with 0.5 % chitosan coating and of Δ=1.1 N for chitosan concentrations of 0.75 and 1 %, with a progressive decrease in firmness with storage time. For the control, the firmness variation was much higher (Δ=0.5 N). Except for the control, the results of the coated fruit were similar to those obtained in this work.

In Figure 5, the TSS data is shown. In both cases, no differences between treatments and storage days were observed as well as statistical differences ($p<0.05$). For the refrigerated fruit (Figure 5a), the values were between 4.0 % and 4.2 % for the coated tomatoes with a value of 4.2 % for C(−) and 4.0 oBrix for C (+) on day 7. On day 14, the values were between 4.0 % and 4.1 % for the coated tomato fruit and 4.0 % for C(−) and 4.1 % for C (+) on day 14. At ambient temperature (Figure 5b), the values for the coated tomato fruit ranged between 3.9 % and 4.0 % and for the controls they were 3.8 % for C(−) and 4.0 % for C(+) for day 7.

In previous work carried out on NPQ coated tomatoes and stored for 7 days at 10 °C, the TSS value reported for NPs concentrations of 15, 30, and 45 % were between 3 % and 4 % and for fruit with NPT coatings a value of 4 % was found, like those obtained in this work [14]. For fruit stored at ambient

temperature for 12 days with chitosan coating of 0.5 %, 0.75 %, and 1 %, Azmai *et al.* [20] obtained values between 3.2 % and 3.8 % for the coated fruit and of 3.3 % and 3.4 % for the controls without significant variations of these values with storage time. Sree *et al.* [25] obtained values between 4-4.5 % after 7 days of storage for fruit coated with chitosan at 0.5 %, 1 %, 2 %, and 2.5 % and 4.2 % for the control, although there was a tendency to increase this value over storage time. In this work, values similar to those reported by these authors were obtained, without significant variations during storage time.

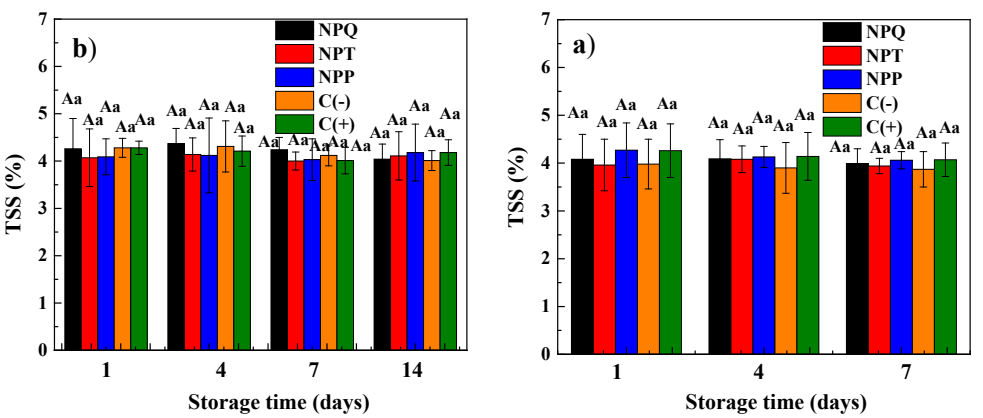

Figure 5. Tomatoes TSS coated with NPQ, NPT, and NPP and two controls, and stored at: a) 11±2 °C for 14 days and b) 27±2 °C for 7 days. Different letters represent statistical differences between formulations (upper case letters) and between days (lower case letters) calculated by ANOVA and Tukey's test ($p<0.05$). Initial TSS value=4.0 oBrix. Error bars show the standard error of the mean. NPQ=chitosan nanoparticles; NPT=chitosan nanoparticles encapsulating thyme essential oil; NPP=chitosan nanoparticles encapsulating aqueous extract of propolis; C(−)=fruit not inoculated; C(+)=inoculated fruit.

In Figure 6, the results for chroma, hue, and luminosity color parameters for tomatoes stored controlled temperature (Figures 5a, b, c) and ambient temperatures (Figures 6d, 6e, 6f) can be seen. No significant statistical differences ($p<0.05$) were observed between treatments or for the storage days; therefore, the color variation in the fruit was not affected by the application of the coating. This could be associated with the harvesting ripening stage of the tomato (full red) [26, 27]. Compared to previous works published by our group, for tomatoes stored at 10 ºC for 7 days, the values between 29-31 for chroma, 48-54 for hue and 37-39 for luminosity were for tomatoes with NPQ coatings (15, 30, and

45 %) and between 26-29 for chroma, 47 for hue and between 37-38 for luminosity for tomatoes coated with NPT (15, 30, and 45 %) [14].

On the other hand, Gutiérrez-Molina *et al.* [8] reported values of luminosity between 39-45, similar to those reported in this present research. Also, Sucharitha *et al.* [22] found no differences with the storage days in coated tomatoes with 0.25 % and 0.5 % of chitosan solutions and stored for 30 days at 5 °C, similar data to that obtained in this research.

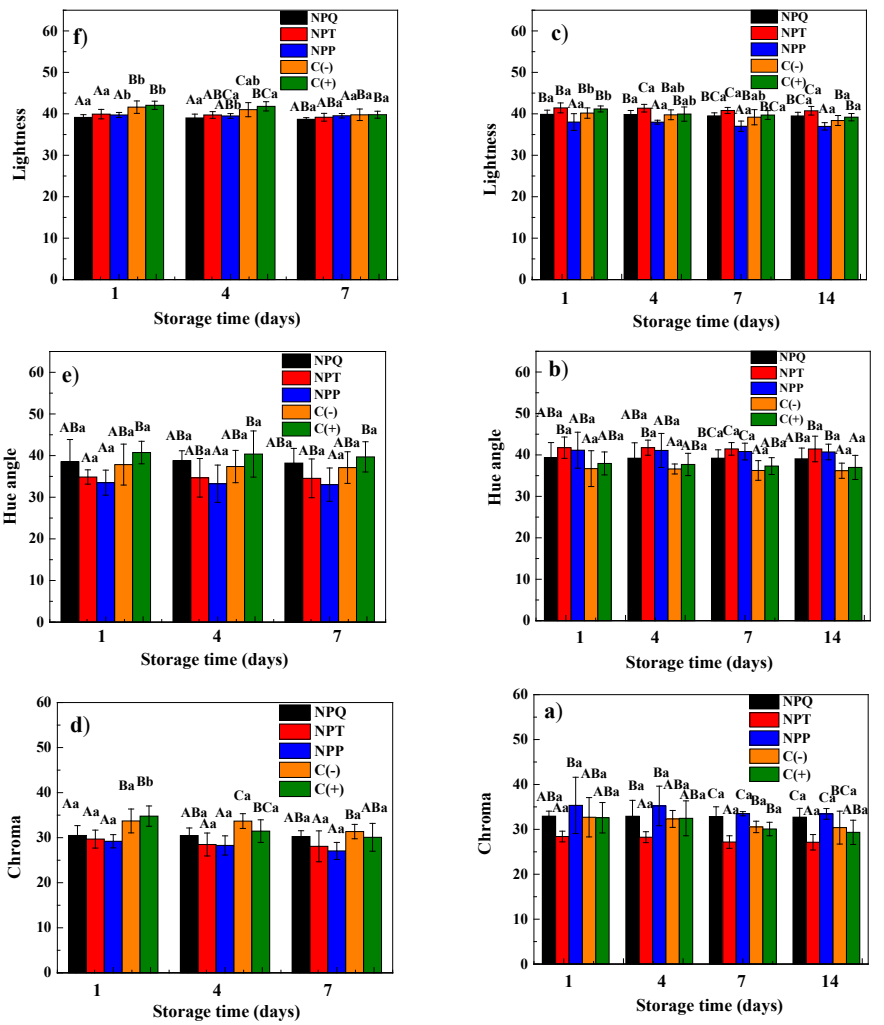

Figure 6. Change of tomato color coated with NPQ, NPT, and NPP and two controls C (+) and C(−), stored at 11 ºC±2 for 14 days: a) chroma C*, b) hue angle h, and c) lightness L* and at 27 ºC±2 for 7 days: d) chroma C*, e) hue angle h and f) lightness L*.

Different letters represent statistical differences between formulations (upper case letters) and between days (lower case letters) calculated by ANOVA and Tukey's test ($p<0.05$). Initial chroma value= 8.76±1.27. Initial hue value=40.0±2.5. Initial luminosity value=40.8±0.5. Error bars show the standard error of the mean. NPQ=chitosan nanoparticles; NPT=chitosan nanoparticles encapsulating thyme essential oil; NPP=chitosan nanoparticles encapsulating aqueous extract of propolis; C(−)=fruit not inoculated; C(+)=inoculated fruit.

4. Conclusions

From DLS measurements the NPQ showed the most homogeneous distribution. On the overall, the nanoparticles were spherical in shape according to TEM observation. Considering the quality essays, the most effective coating for tomatoes preservation was the NPQ followed by the NPT and NPP due to lower weight loss and loss of firmness for the refrigerated and ambient temperature stored tomato. No significant changes were observed for color change or TSS. It would be useful to carry out microbiological tests considering variables such as severity and disease incidence to achieve a whole evaluation of the performance of nanocoatings. It will be the subject of further research.

Acknowledgement

The authors would like to thank Dr. Nicolás Cayetano from Nanoscience and Micro Center and Nanotechnologies-IPN and Dr. Eduardo San Martín from CICATA-Legaria for TEM and DLS measurements, respectively.

References

1. García-Estrada, R. S., Diaz-Lara, A., Aguilar-Molina, V. H., & Tovar-Pedraza, J. M. (2022). Viruses of economic impact on tomato crops in Mexico: From diagnosis to management: A review. *Viruses*, 14 (1251), 1-16. https://doi.org/10.3390/v14061251

2. Valerino-Perea, S., Lara-Castor, L., Armstrong, M.E.G., & Papadaki, A. (2019). Definition of the traditional mexican diet and its role in health: A systematic review. *Nutrients*, 11(2803), 1-33. https://doi.org/10.3390/nu11112803

3. Montaño, I., Valenzuela, I., & Villavicencio, K. (2021). Competitiveness of the Mexican red tomato in the international market: analysis 2003-2017. *Revista Mexicana de Ciencias Agrícolas*, 12(7), 1185-1197. https://doi.org/10.29312/remexca.v12i7.2531

4. FAOSTAT, Mexican tomato production (2020). https://www.fao.org/faostat/en/#home. Accessed 27 September 2020.

5. Blancard, D. (2012). *A Color Handbook. Tomato Diseases. Identification, Biology and Control.* Second edition. Academic Press, USA. https://doi.org/10.1201/b15145

6. Khan, I., Saeed, K., & Khan, I. (2019). Nanoparticles: Properties, applications and toxicities. *Arabian Journal of Chemistry*, 12(7), 908-931. https://doi.org/10.1016/j.arabjc.2017.05.011

7. Jiménez-Gómez, C. P., & Cecilia, J. A. (2020). Chitosan: A natural biopolymer with a wide and varied range of applications. *Molecules*, 25(3981), 1-43. https://doi.org/10.3390/molecules25173981

8. Gutiérrez-Molina, J., Corona-Rangel, M. L., Ventura-Aguilar, R. I., Barrera-Necha, L. L., Bautista-Baños, S., & Correa-Pacheco, Z. N. (2021). Chitosan and *Byrsonima crassifolia*-based nanostructured coatings: Characterization and effect on tomato preservation during refrigerated storage. *Food Bioscience*, 42(101212), 1-9. https://doi.org/10.1016/j.fbio.2021.101212

9. Correa-Pacheco, Z. N., García-Paniagua, K. D., Bautista-Baños, S., & Corona-Rangel, M. L. (2019). Efecto de nanorecubrimientos de quitosano-aceite esencial de tomillo sobre la calidad postcosecha en frutos de jitomate. *Revista Mexicana de Fitopatología*, 37(1), 29-36. https://doi.org/10.18781/R.MEX.FIT.1903-5

10. Luque-Alcaraz, A., Lizardi-Mendoza, J., Goycoolea, F., Higuera-Ciapara, I., & Argüelles-Monal, W. (2016). Preparation of chitosan nanoparticles by nanoprecipitation and their ability as a drug nanocarrier. *RSC Advances*, 6, 59250-59256. https://doi.org/10.1039/C6RA06563E

11. Martínez-González, M. C., Bautista-Baños, S., Correa-Pacheco, Z. N., Corona-Rangel, M. L., Ventura-Aguilar, R. I., Del Río-García, J. C. *et al.* (2020). Effect of nanostructured chitosan/propolis coatings on the quality and antioxidant capacity of strawberries during storage. *Coatings*, 10(90), 1-12.
https://doi.org/10.3390/coatings10020090

12. Sreekumar, S., Goycoolea, F., Moerschbacher, B., & Rivera-Rodriguez, G. (2018). Parameters influencing the size of chitosan-TPP nano- and microparticles. *Scientific Reports*, 8 (4695), 1-11.
https://doi.org/10.1038/s41598-018-23064-4

13. Sotelo-Boyás, M. E., Correa-Pacheco, Z. N., Bautista-Baños, S., & Corona-Rangel, M. L. (2017). Physicochemical characterization of chitosan nanoparticles and nanocapsules incorporated with lime essential oil and their antibacterial activity against food-borne pathogens. *LWT*, 77, 15-20.
https://doi.org/10.1016/j.lwt.2016.11.022

14. Correa-Pacheco, Z. N., Bautista-Baños, S., Marquina-Valle, M. A., & Hernandez-López, M. (2017). The effect of nanostructured chitosan and chitosan-thyme essential oil coatings on *Colletotrichum gloeosporioides* growth *in vitro* and on cv Hass Avocado and fruit quality. *Journal of Phytopathology*, 165(5), 297-305.
https://doi.org/10.1111/jph.12562

15. Barrera-Necha, L. L., Correa-Pacheco, Z. N., Bautista-Banos, S., Hernández-Lopez, M., Martínez-Jiménez, J. E., & Morán Mejía, A. F. (2018). Synthesis and characterization of chitosan nanoparticles loaded botanical extracts with antifungal activity on *Colletotrichum gloeosporioides* and *Alternaria* species. *Advances in Microbiology*, 8, 286-296.
https://doi.org/10.4236/aim.2018.84019

16. González-Saucedo, A., Barrera-Necha, L. L., Ventura-Aguilar, R. I., Correa-Pacheco, Z. N., Bautista-Baños, S., & Hernández-López, M. (2019). Extension of the postharvest quality of bell pepper by applying nanostructured coatings of chitosan with Byrsonima crassifolia extract (L.) Kunth. *Postharvest Biology and Technology*, 149, 74-82.
https://doi.org/10.1016/j.postharvbio.2018.11.019

17. Zhang, H., Fu, Y., Niu, F., Li, Z., Ba, C., Jin, B. *et al.* (2018). Enhanced antioxidant activity and in vitro release of propolis by acidinduced aggregation using heat-denatured zein and carboxymethyl chitosan. Food Hydrocolloid, 81, 104-112.
https://doi.org/10.1016/j.foodhyd.2018.02.019

18. Duan, Y., Wang, G., Fawole, O. A., Verboven, P., Zhang, X., Wu, D. *et al.* (2020). Postharvest precooling of fruit and vegetables: A review. *Trends in Food Science & Technology*, 100, 278-291.
https://doi.org/10.1016/j.tifs.2020.04.027

19. Kibar, H. F., & Sabir, F. K. (2018). Chitosan coating for extending postharvest quality of tomatoes (*Lycopersicon esculentum Mill.*) maintained at different storage temperatures. *AIMS Agriculture and Food*, 3(2), 97-108. https://doi.org/10.3934/agrfood.2018.2.97

20. Peralta-Ruiz, J., Grande-Tovar, C. D., Sinning-Mangonez, A., Coronell, E. A., Marino, M. F., & Chaves-Lopez, C. (2020). Reduction of postharvest quality loss and microbiological decay of tomato "chonto" (*Solanum lycopersicum L.*) using chitosan-E essential oil-based edible coatings under low-temperature storage. *Polymers*, 12(1822), 1-22. https://doi.org/10.3390/polym12081822

21. Azmai, W. N. S. M., Latif, N. S. A., & Zain, N. M. (2019). Efficiency of edible coating chitosan and cinnamic acid to prolong the shelf life of tomatoes. *Journal of Tropical Resources and. Sustainable Science*, 7(1), 47-52. https://doi.org/10.47253/jtrss.v7i1.509

22. Sucharitha, K. V., Beulah, A. M., & Ravikiran, K. (2018). Effect of chitosan coating on storage stability of tomatoes (*Lycopersicon esculentum Mill*). *International Food Research Journal*, 25(1), 93-99.

23. Mustafa, M. A., Ali, A., & Manickam, S. (2013). Application of a chitosan based nanoparticle formulation as an edible coating for tomatoes (*Solanum Lycoperiscum L.*). *Acta Horticulturae* 1012, 445-452. https://doi.org/10.17660/ActaHortic.2013.1012.57

24. Al-Dairi, M., Pathare, P. B., & Al-Yahyai, R. (2021). Effect of Postharvest Transport and Storage on Color and Firmness Quality of Tomato. *Horticulturae*, 7(7), 163. https://doi.org/10.3390/horticulturae7070163

25. Sree, K. P., Sree, M. S., & Samreen, P. S. (2020). Application of chitosan edible coating for preservation of tomato. *International Journal of Chemical Studies*, 8(4), 3281-3285. https://doi.org/10.22271/chemi.2020.v8.i4ao.10157

26. Kasampalis, D. S., Tsouvaltzis, P., & Siomos, A. S. (2020). Chlorophyll fluorescence, non-photochemical quenching and light harvesting complex as alternatives to color measurement, in classifying tomato fruit according to their maturity stage at harvest and in monitoring postharvest ripening during storage. *Postharvest Biology and Technology*, 161(111036), 1-9. https://doi.org/10.1016/j.postharvbio.2019.111036

27. Khairia, A. N., Falaha, M. A. F., Suyantohadia, A., Takahashib, N., & Nishinab, H. (2015). Effect of Storage Temperatures on Color of Tomato Fruit (*Solanum lycopersicum Mill.*) Cultivated under Moderate Water Stress Treatment. *Agriculture and Agricultural Science Procedia*, 3, 178-183. https://doi.org/10.1016/j.aaspro.2015.01.035

CHAPTER 3 FOOD AREA

NANOENCAPSULATION OF RIBOFLAVIN IN BIODEGRADABLE POLYMERIC MATRICES USING NANOSPRAY DRYING

Mónica Rosalía Jaime-Fonseca[1], Violeta Mancilla-Dávalos[1], Pedro López-Ordaz[2,3], Jorge Yáñez-Fernández[2*]

[1]Centro de Investigación en Ciencia Aplicada y Tecnología Avanzada Unidad Legaria, Instituto Politécnico Nacional. Legaria 694 Col. Irrigación, 11500, Ciudad de México, México

[2]Unidad Profesional Interdisciplinaria de Biotecnología, Instituto Politécnico Nacional, Departamento de Biotecnología Alimentaria. Av. Acueducto S/N Col. Barrio la Laguna, Ticomán, C.P. 07340, Ciudad de México, México.

[3]División Química Biológicas, Universidad Tecnológica de Tecámac, Carretera Federal México-Pachuca Km 37.5, Col. Sierra Hermosa, C.P. 55740, Tecámac, Estado de México, México.

* jyanezfe@ipn.com

Jaime Fonseca, M. R., Mancilla-Dávalos, V., López-Ordaz, P., & Yáñez-Fernández, J. (2023). Nanoencapsulation of riboflavin in biodegradable polymeric matrices using nanospray drying. In E. San Martín-Martínez (Ed.). *Research advances in nanosciences, micro and nanotechnologies. Volume IV* (pp. 141-154). Barcelona, Spain: Omniascience.

Abstract

In this work, riboflavin (vitamin B_2) was encapsulated in a matrix of alginate, chitosan, and a combination of both polymers, and the morphological properties of the nanocapsules and the release of riboflavin were studied. The nanocapsules were obtained through a nano spray dryer using alginate, and chitosan as protection or wall material, the concentration of the fed solution was 0.125 % (w/v) of each polymer with a 4 μm microfilter at a temperature of 120 °C. The structure of the nanocapsules was observed by Scanning Electron Microscopy (SEM), the SEM images were used to estimate the size of the nanocapsules by the image analysis methodology with ImageJ. The average size of the nanocapsules was 500-700 nm, observing a homogeneous spheroidal morphology. The interaction of the nanocapsules was determined using a nanozetasizer. The Z potential (ζ) of the alginate-chitosan nanocapsules ranged from 3.50 to 3.75 mV. The interaction of the carboxyl group (-COO) of alginate with the amino group ($-NH^{3+}$) of chitosan was observed by using FT-IR spectroscopy. In addition, the release of riboflavin was evaluated in an in-vitro system, showing that the alginate-chitosan mixture released riboflavin within the first 30 minutes.

Keywords: Nano drying, alginate, chitosan, nanoencapsulation, riboflavin, release.

1. Introduction

Vitamins are essential bioactive compounds for good health, they are defined as a group of micronutrients that are not usually synthesized by the human body [1]. Currently, there are more than 18 compounds classified as vitamins, divided into two large groups: fat-soluble (A, D, E, and K) and water-soluble such as thiamine (B_1), riboflavin (B_2), niacin (B_3), pantothenic acid (B_5), pyridoxine (B_6), biotin (B_7), folic acid (B_9), cyanocobalamin (B_{12}) and C [2 − 4]. Vitamin deficiency can lead to serious diseases, such as scurvy, beriberi, ariboflavinosis, dermatitis, enteritis, and blindness, therefore, the consumption of vitamins is necessary to regulate metabolism and prevent diseases [5]. Riboflavin (vitamin B_2) is soluble in water and stable in acidic solutions [6 − 8] but can be degraded in alkaline solutions and is sensitive to light [9], non-toxic [10], and biocompatible [11]. The molecular formula of riboflavin is $C_{17}H_{20}N_4O_6$ and it consists of a heterocyclic isoalloxazine ring attached to the sugar alcohol ribitol, this molecule has a molecular mass of 376.36 g/mol (Figure 1). Riboflavin is used in food additives and supplements such as dyes and nutrients for human health [8], riboflavin is found in legumes, asparagus, spinach, lettuce, broccoli, cabbage, cereals, milk, eggs, and meat [12]. However, the obstacle that prevents the commercial use of riboflavin in the food industries its photosensitivity at a wavelength of 445 nm, causing a degradation of 79.9 % during the first 20 minutes [13, 14].

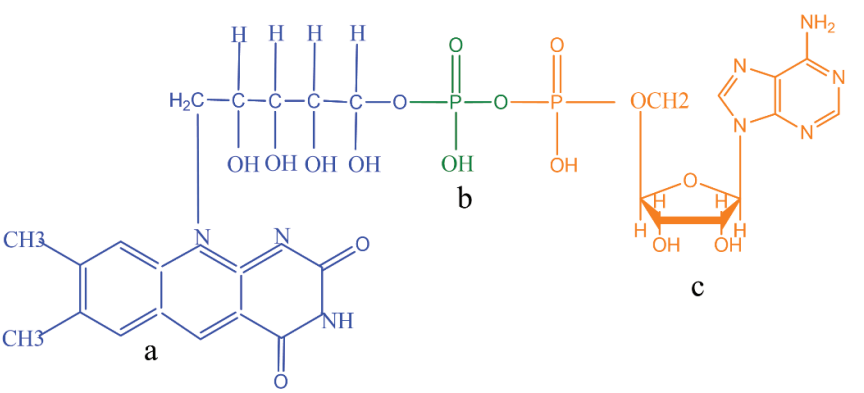

Figure 1. Chemical structure of riboflavin and its active forms, a) riboflavin; b) riboflavin phosphate (FMN); c) flavin adenine dinucleotide (FAD)

Encapsulation is a process used in the food and pharmaceutical industry to preserve bioactive compounds from environmental factors such as humidity, air, oxygen, light, and pH, increasing the useful life of the products [15]. The most

widely used biopolymers in the food and pharmaceutical industry are starch, pectin, maltodextrin, gelatin, alginate, cellulose acetate, ethyl cellulose, gum aarabic, K-carrageenan and chitosan [16 − 18]. Encapsulation can be carried out by nano spray drying, obtaining micro and nanometric scale particles. This technique is used in the food industry to transform liquids (solutions, suspensions, and emulsions) into solid powders such as milk, coffee, tomato, and glucose [19 − 22]. Nanoencapsulation performs nutrient entrapment at the nanoscale, providing much higher nutrient uptake and transport compared to microencapsulation [23, 24]. Therefore, the objective of this work was to develop riboflavin nanocapsules using alginate and chitosan as wall material. In addition, its morphology and particle size were characterized, and the controlled release of riboflavin was evaluated.

2. Methodology

2.1. *Materials and methods*

The materials used in the riboflavin nanoencapsulation were sodium alginate purchased by Sigma S.A. C.V. (Mexico), low-density chitosan, purchased from Sigma S.A. C.V. (Mexico), glacial acetic acid (ACS) provided by Fermont (Productos Químicos Monterrey S.A. C.V.) and riboflavin as active compound, purchased from Sigma S.A. C.V. (Mexico).

2.2. *Preparation of the solutions*

The solutions of the biopolymers from alginate and chitosan were prepared at a concentration of 0.125 % (w/v) separately, and then they were homogenized for 5 minutes using an ELMA brand (Germany) model D-78224 ultrasound equipment, with a frequency of 25 kHz. Finally, 0.185 mM M riboflavin was added.

2.3. *Riboflavin nanoencapsulation by nano drying*

Riboflavin nanoencapsulation was carried out using the Nano Spray Dryer B-90 brand equipment (BÜCHI, Switzerland), keeping the temperature at 120 °C according to the methodology reported by Kyriakoudi and Tsimidou [26]. The ratio of the concentration of alginate and chitosan was 0.125 and 0.25 % (w/v), respectively. The polymer solutions were fed to the nano dryer by a peristaltic pump at a flow rate of 7.5 ml/min using a nozzle of 4 μm.

2.4. *Zeta potential*

The Z potential (ζ) of the nanocapsules was determined using a Nano Zetasizer ZS unit (Malvern Instruments Ltd., Malvern, Worcestershire, UK), coupled to a Doppler laser velocimeter. The interaction of the nanocapsules was determined according to the methodology described by Porras *et al.* [27]. The samples were diluted to 43µL and placed in a cell with 2 electrodes that allowed the determination of the electrostatic charge of the particle.

2.5. *Characterization of nanocapsules by scanning electron microscopy (SEM)*

The morphology and size of the nanocapsules were analyzed using a scanning electron microscope (JSM-LV6390 JEOL, Japan). Samples were silver coated by sputtering (Desk IV, Denton Vacuum, USA) and viewed at 10,000 to 15,000X magnification establishing an accelerating voltage of 20 KV.

Furthermore, a study of nanocapsules stability was performed, changes were observed in the SEM and this process was carried out incorporating alginate and chitosan nanocapsules at different humidity environments of 33, 75 and 93 %, for 24 hours.

2.6. *Fourier Transform Infrared (FTIR)*

The FTIR spectra were obtained by means of a FTIR-spectrophotometer (Shimadzu Fourier Transform Infrared Spectrophotometer IRAffinity-1, Corporation Kyoto, Japan). For each sample 32 scans were performed in a range of wavelengths from 400 cm^{-1} to 4000 cm^{-1} and a resolution of 4 cm^{-1} using a 36X objective with a 2 mm diameter diamond crystal.

2.7. *Riboflavin release*

To release riboflavin, 0.015 g of the nanocapsules were taken and placed in a 2000 Dalton dialysis membrane, 11.5 mm in diameter, with a volume of 2.0 ml of distilled water. The riboflavin was released by adding a volume of 50 ml. The released concentrations of riboflavin were measured by UV-Vis spectroscopy (Multiskan GO from Thermo Scientist, Japan) at a wavelength of 200-450 nm following the modified methodology described by Abraham [28].

2.8. *Design of experiments and statistical analysis*

Experiments were performed using a 2k factorial design (k=3). Significant differences ($p<0.05$) were verified by ANOVA using Design Expert software (version 7.1.6, Minnesota, USA). All measurements were performed by triplicate.

3. Results and discussion

3.1. *Alginate-chitosan interaction at different pH*

The ζ potential is a measure of the stability of the nanocapsules, particles with a zeta potential greater than +30 mV and less than −30 mV are considered generally stable [29, 30]. In addition, the ζ potential also provides information on the surface charge of the nanocapsules. Figure 2 shows the effect of pH on the ζ potential of polymeric materials. In the alginate-chitosan solution, the ζ potential values reached their greatest interaction, allowing an adhered and resistant structure. The greatest interaction between alginate-chitosan was with an electrical potential of -35 mV for alginate and 35mV in chitosan at pH 3.3. These results contributed to the formation of nanocapsules as observed in (Figure 3). Azevedo *et al.* [30], reported similar values (−30.9±0.5 and −29.6±0.1 mV) for nanoparticles without and with riboflavin, respectively, indicating that from these values the nanoparticles have good stability [29]. The zeta potential values are significantly different ($p<0.05$), which shows that the riboflavin charge can influence the ζ potential of the nanocapsules; this behavior is generated by the positive charge of riboflavin in solutions at low pH [31].

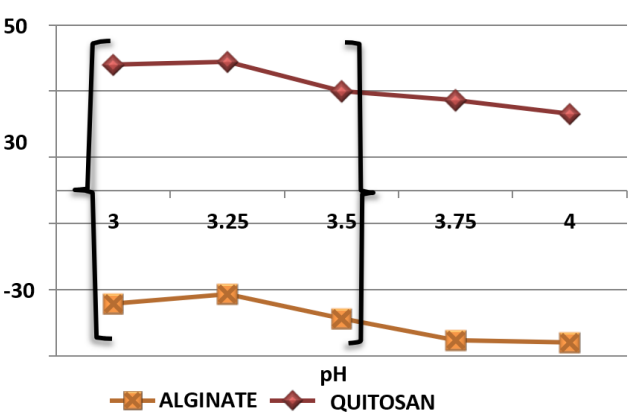

Figure 2. Variation of electrostatic charges as a function of pH for alginate-chitosan.

3.2. *Morphology of riboflavin (vitamin B_2) nanocapsules*

The nanocapsules were analyzed by SEM showing a spherical morphology (Figure 3) with an average size of 514.41±161.74 and 572.98±323.35 from alginate and chitosan, respectively. The average size of nanocapsules with riboflavin was 493.87±161.74 nm and 615.94 ± 168.80 nm when alginate and chitosan were used as a wall material, respectively, while alginate-chitosan-riboflavin nanocapsules were an average size of 621.06±270.94.

The sizes vary depending on the polymer that is being used, it is observed that when incorporating riboflavin, the size of the chitosan nanocapsules increases, however with alginate the size decreased, this may be due to a greater interaction of riboflavin and alginate, developing more compact nanocapsules after drying.

Compared to other works using similar biopolymers, the size of nanocapsules developed proved to be according to those reported by other authors, which range between 700 and 4000 nm [32, 33]. On the other hand, Goycoolea *et al.* [34] reported that insulin-loaded alginate/chitosan nanoparticles ranged from 200 to 300 nm. Furthermore, Sarmento *et al.* [35] indicated that when the pH decreases from 5.2 to 4.7, the mean particle size decreased. However, an important part of the alginate initiates an aggregation process which may contribute to the increase in mean particle size [35, 36]. Besides Goycoolea *et al.* [34] and Sarmento *et al.* [35], observed that the alginate load increase could contribute to the instability of the nanocapsules and, consequently, increase their size.

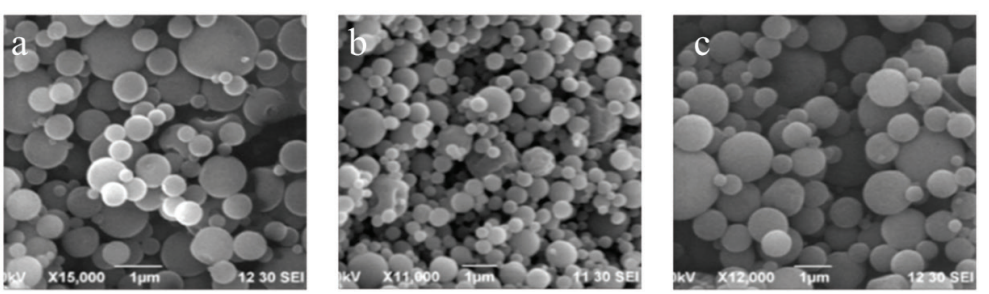

Figure 3. Micrographs of nanocapsules a) alginate; b) chitosan; c) alginate-chitosan.

On the other hand, Figure 4 shows the differences in the stability of the nanocapsules at different humidity levels (33 and 75 %) for 24 h. Therefore, it is observed that alginate and chitosan nanospheres are stable up to 75 % humidity in the first 24 hours of exposure, however at 93 % humidity the nanospheres of alginate (figure not shown) and chitosan were hydrated and agglomerated.

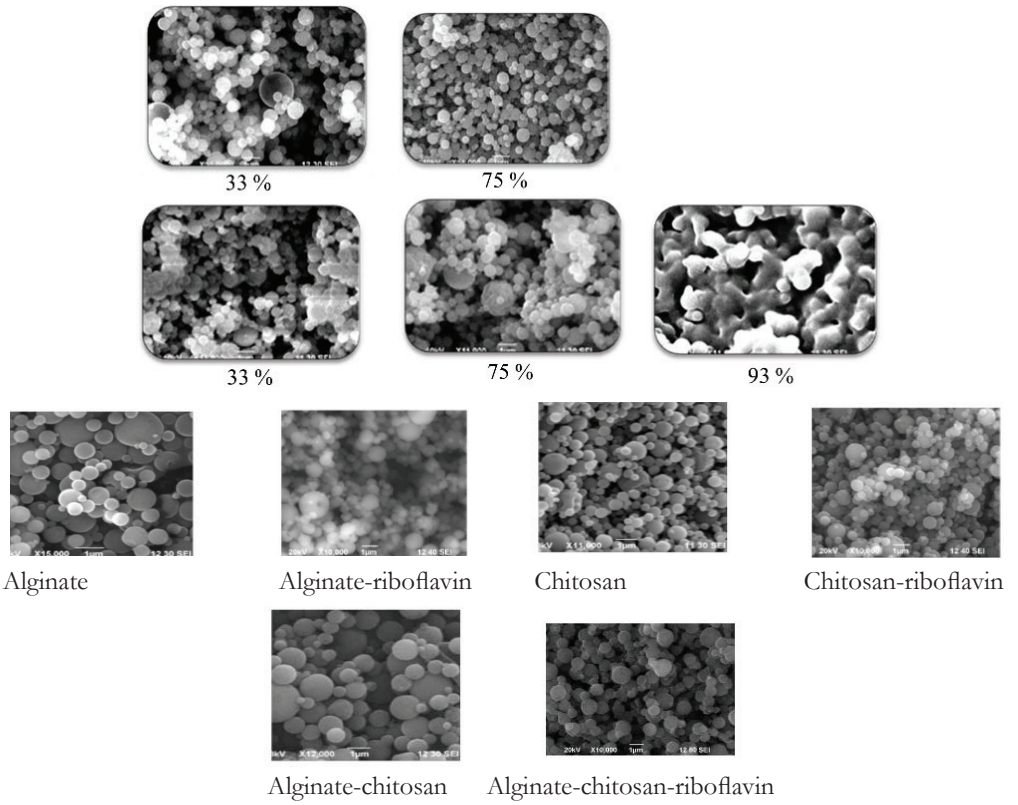

Figure 4. Micrographs of the nanocapsules at different humidity percentages after 24 h, stability analysis.

3.3. *FTIR*

FTIR was used to characterize the intermolecular interactions between alginate-chitosan-riboflavin. The spectra of the alginate-chitosan-riboflavin combination are shown in Figure 5. In the spectrum, the peaks of the carboxyl group of the alginate can be observed near 1605 cm^{-1} due to its symmetrical shape and stretch vibration (COO^-). However, at 1414 cm^{-1} the asymmetric presence and stretching vibration of the COO- are manifested. The chitosan spectrum shows a protonated amino peak at 1562 cm^{-1}, this peak agrees with that reported by Sarmento *et al.* [35] and Neiras *et al.* [38]. The chitosan- alginate interaction shows a displacement in the amino group at 1562 cm^{-1}, in addition, the presence of the carbonyl group (C=O) is observed due to the C6 stretching of the primary alcohol expressed in the 1069 cm^{-1} peak, this peak agrees with that reported by Thawatchai *et al.* [39]. Sarmento *et al.* [35] reported that chitosan under 75 % deacetylation conditions presents a spectral peak of 1641 cm^{-1} corresponding to the amide bond. The interaction of

alginate-chitosan in the nanocapsules was expressed in the 1579 cm^{-1} peak, characteristic of the amide groups that are formed in both polymers [39, 40]. The spectral peaks observed in the alginate-chitosan-riboflavin combination at 2916-3000 cm^{-1} are attributed to the stretching vibration of the –OH group. This peak often overlaps with the N- H bond of the amino group. The peaks observed ranged from 1579, 1410, and 1033 cm^{-1} and are attributed to C-O stretching vibration asymmetry and C-O symmetry of chitosan, respectively [41].

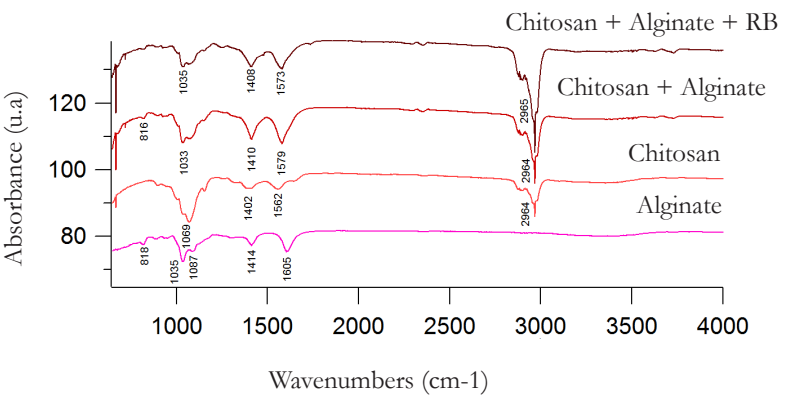

Figure 5. Infrared spectra of the alginate-chitosan-riboflavin combination.

3.4. *Riboflavin release*

Riboflavin release evaluation was performed for each biopolymer: alginate, chitosan, and their combination, separately. Release of alginate-encapsulated riboflavin began within the first hour (Figure 6a). After the first hour, a linear release trend was observed until the third hour, therefore, no significant change was observed, achieving a stable concentration in the solution within a release rate of 0.1215 mM/min. In the chitosan nanocapsules (Figure 6b) the release of riboflavin was observed after 20 minutes and after three hours the highest riboflavin release rate was reached (0.2064 mM/min). Likewise, in the biopolymer mixture (Figure 6c) a linear trend was observed starting at 30 minutes up to 3 hours and later reaching a maximum release rate of riboflavin of 0.1746 mM/min.

According to Azevedo *et al.* [30], in the transport mechanism for the release of riboflavin, not only the Bro5wnian movement is involved, that is, it does not follow the Fick behavior, but it is more related to the relaxation phenomenon, also called Case II transport. Thomas *et al.* [37] proposed a strong dependence of the solubility parameter and diffusion coefficient on concentration. However, they recognized that some independent material property must control the

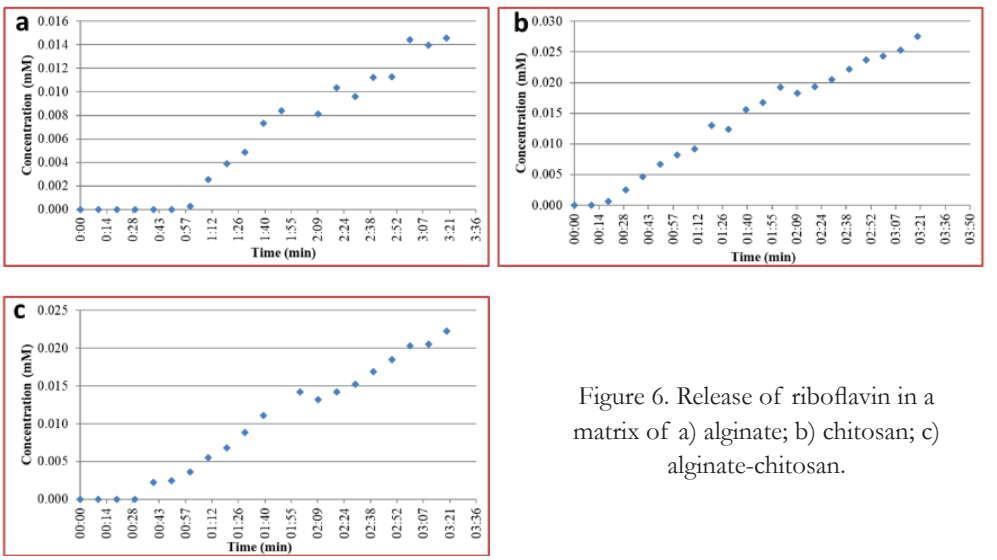

Figure 6. Release of riboflavin in a matrix of a) alginate; b) chitosan; c) alginate-chitosan.

velocity of the front and suggested time-dependent rupture and disentanglement of molecular chains as possible processes. This phenomenon may result in the loss of the structure of the nanocapsules with a more rapid release of riboflavin. When alginate/chitosan nanoparticles are mixed, the negatively charged carboxylate groups of the alginate begin to protonate to form uncharged COOH groups. It reduces the degree of electrostatic interactions between the alginate and chitosan chains within the nanocapsules [32, 37].

4. Conclusions

In this work, it was possible to form nanocapsules with homogeneous spheroidal morphology with a size of 500-700 nm through nano spray drying. Chitosan nanocapsules showed the fastest release of riboflavin with a release rate of 0.206 mM/min, compared to the mixture of alginate-chitosan. On the other hand, the alginate-chitosan nanocapsules presented a higher retention at 30 minutes with retention (0.175 mM/min). It indicates that a mix of alginate-chitosan allows a more delayed release than chitosan nanocapsules.

Acknowledgment and Funding

The authors thank CONACYT for the scholarship awarded, as well as the financial support provided for project 2542765 in the 2022 academic modality postdoctoral stay.

References

1. Ottaway, P. B. (1993). Stability of vitamins in food. In P. B. Ottaway (Ed.). *The Technology of Vitamins in Food* (pp. 90-113). Boston, MA: Springer US.
2. Teleki, A., Hitzfeld, A., & Eggersdorfer, M. (2013). 100 Years of vitamins: The science of formulation is the key to functionality. *KONA Powder and Particle Journal*, 30, 144-163.
3. Sebrell, W. H., & Harris, R. S. (2014). *The vitamins: chemistry, physiology, pathology, methods*. Academic Press, New York.
4. Mellidou, I., Georgiadou, E. C., Kaloudas, D., Fotopoulos, V., & Kanellis, A. K. (2019). Vitamins. *In Postharvest Physiology and Biochemistry of Fruits and 836 Vegetables*.
5. 5. Lešková, E., Kubíková, J., Kováčiková, E., Košická, M., Porubská, J., & Holčíková, K. (2006). Vitamin losses: retention during heat treatment and continual changes expressed by mathematical models. *Journal of Food Composition and Analysis*, 19(4), 252-276.
6. Patel, M., Vadlapatla, R. K., Pal, D., & Mitra, A. K. (2012). Molecular and functional characterization of riboflavin specific transport system in rat brain capillary endothelial cells. *Brain Research*, 1468, 1-10. https://doi.org/10.1016/j.brainres.2012.05.052
7. Yonezawa, A., & Inui, K. (2013). Novel riboflavin transporter family RFVT/SLC52: identification, nomenclature, functional characterization and genetic diseases of RFVT/SLC52. *Molecular Aspects of Medicine*, 34, 693-701. https://doi.org/10.1016/j.mam.2012.07.014
8. Sugimoto, T., Kato, T., & Park, E. Y. (2014). Functional analysis of cis-aconitate decarboxylase and trans-aconitate metabolism in riboflavin-producing filamentous *Ashbya gossypii*. *Journal of Bioscience and Bioengineering*, 117(5), 563-568. https://doi.org/10.1016/j.jbiosc.2013.10.020
9. Aguilar, L., & Gaona, V. G. (2012). Riboflavina (Vitamina B2) Pinto, J. T., & Zempleni, J. (2016). Riboflavin. *Advances in Nutrition*, 7(5), 973-975. https://doi.org/10.3945/an.116.012716
10. Allowances, N. R. C. C. O. D., Food, N. R. C. & Board, N. (1980). *Recommended dietary allowances*, National Academies.
11. Fawzy, A. S., Nitisusanta, L. I., Iqbal, K., Daood, U., Beng, L. T. & Neo, J. (2013). Chitosan/Riboflavin-modified demineralized dentin as a potential substrate for bonding. *Journal of the Mechanical Behavior of Biomedical Materials*, 17, 278-289. https://doi.org/10.1016/j.jmbbm.2012.09.008

12. Sanches, S. C., Ramalho, L. N., Mendes-Braz, M., Terra, V. A., Cecchini, R., Augusto, M. J. *et al.* (2014). Riboflavin (vitamin B^{-2}) reduces hepatocellular injury following liver ischaemia and reperfusion in mice. *Food and Chemical Toxicology*, 67, 65-71. https://doi.org/10.1016/j.fct.2014.02.013

13. Pan, Y. L., Pinnick, R. G., Hill, S. C., Niles, S., Holler, S., Bottiger, J. R. *et al.* (2001). Dynamics of photon-induced degradation and fluorescence in riboflavin microparticles. *Applied Physics B*, 72, 449-454. https://doi.org/10.1007/s003400100532

14. Gallardo, C. (2011). Estabilización de disoluciones acuosas de riboflavina por solapamiento espectral. *Revista Cubana de Farmacia*, 45, 515-523.

15. Lupo, P. B., González, A. C. & Maestro, G. A. (2012). Microencapsulación con alginato en alimentos. Técnicas y aplicaciones. *Revista Venezolana de Ciencia y Tecnología de Alimentos*, 3, 130-151.

16. Estevinho, B. N., Rocha, F., Santos, L. & Alves, A. (2013). Microencapsulation with chitosan by spray drying for industry applications – A review. *Trends in Food Science & Technology*, 31, 138- 155. https://doi.org/10.1016/j.tifs.2013.04.001

17. He, X., & Hwang, H.-M. (2016). Nanotechnology in food science: Functionality, applicability, and safety assessment. *Journal of Food and Drug Analysis*, 24, 671-681. https://doi.org/10.1016/j.jfda.2016.06.001

18. Peters, R. J., Bouwmeester, H., Gottardo, S., Amenta, V., Arena, M., Brandhoff, P. *et al.* (2016). Nanomaterials for products and application in agriculture, feed and food. *Trends in Food Science & Technology*, 54, 155-164. https://doi.org/10.1016/j.tifs.2016.06.008

19. Maupoey, P. F., Grau, A. M. A., Sorolla, A. M. A. & Baviera, J. M. B. (2001). *Introducción al secado de alimentos por aire caliente*. Ed. Univ. Politéc. Valencia.

20. Gouin, S. (2004). Microencapsulation. Trends in Food Science & Technology, 15, 330-347. Büchi 2006. Manual de instrucción Nano Spray Dryer B-90. *In:* BUCHI (ed.). https://doi.org/10.1016/j.tifs.2003.10.005

21. Li, X., Anton, N., Arpagaus, C., Belleteix, F., & Vandamme, T. F. (2010). Nanoparticles by spray drying using innovative new technology: the Büchi nano spray dryer B-90. *Journal of Controlled Release*, 147(2), 304-310. https://doi.org/10.1016/j.jconrel.2010.07.113

22. Schafroth, N., Arpagaus, C., Jadhav, U. Y., Makne, S. & Douroumis, D. (2012). Nano and microparticle engineering of water insoluble drugs using a novel spray-drying process. *Colloids and Surfaces B: Biointerfaces*, 90, 8-15. https://doi.org/10.1016/j.colsurfb.2011.09.038

23. Lopez-Rubio, A., Gavara, R., & Lagaron, J. M. (2006). Bioactive packaging: Turning foods into healthier foods through biomaterials. *Trends in Food Science & Technology*, 17, 567-575.
https://doi.org/10.1016/j.tifs.2006.04.012

24. Katouzian, I., & Jafari, S. M. (2016). Nano-encapsulation as a promising approach for targeted delivery and controlled release of vitamins. *Trends in Food Science & Technology*, 53, 34-48.
https://doi.org/10.1016/j.tifs.2016.05.002

25. Mora, H. C. E., Fessi, H., & Elaissari, A. (2010). Polymer-based nanocapsules for drug delivery. *International Journal of Pharmaceutics*, 385, 113-142.
https://doi.org/10.1016/j.ijpharm.2009.10.018

26. Kyriakoudi, A., & Tsimidou, M. Z. (2018). Properties of encapsulated saffron extracts in maltodextrin using the Büchi B-90 nano spray-dryer. *Food Chem*., 266, 458-465.
https://doi.org/10.1016/j.foodchem.2018.06.038

27. Porras-Saavedra, J., Palacios-González, E., Lartundo-Rojas, L., Garibay-Febles, V., Yáñez- Fernández, J., Hernandez-Sanchez, H. *et al.* (2015). Microstructural properties and distribution of components in microparticles obtained by spray-drying. *Journal of Food Engineering*, 152, 105-112.
https://doi.org/10.1016/j.jfoodeng.2014.11.014

28. Abraham, S. M. (2001). *Investigation of the physicochemical stability of chlordiazepoxide in poly (d, l-lactide-co-glycolide) microspheres*. University of Connecticut.

29. Silva, M. S., Cocenza, D. S., Grillo, R., De Melo, N. F. S., Tonello, P. S., DeOliveira, L. C. *et al.* (2011). Paraquat-loaded alginate/chitosan nanoparticles: preparation, characterization and soil sorption studies. *Journal of Hazardous Materials*, 190, 366-374.
https://doi.org/10.1016/j.jfoodeng.2014.11.014

30. Azevedo, M. A., Bourbon, A. I., Vicente, A. A., & Cerqueira, M. A. (2014). Alginate/chitosan nanoparticles for encapsulation and controlled release of vitamin B2. *International Journal of Biological Macromolecules*,71, 141-146.
https://doi.org/10.1016/j.ijbiomac.2014.05.036

31. Choe, E., & Min, D. B. (2005). Chemistry and reactions of reactive oxygen species in foods. *Journal of food science*, 70(9), R142-R159.
https://doi.org/10.1111/j.1365-2621.2005.tb08329.x

32. Sarmento, B., Ribeiro, A. J., Veiga, F., Ferreira, D. C., & Neufeld, R. J. (2007). Insulin-loaded nanoparticles are prepared by alginate ionotropic pre-gelation followed by chitosan polyelectrolyte complexation. *Journal of Nanoscience and Nanotechnology*, 7(8), 2833-2841.
https://doi.org/10.1166/jnn.2007.609

33. Zhang, N., Li, J., Jiang, W., Ren, C., Li, J. Xin, J. *et al.* (2010). Effective protection and controlled release of insulin by cationic β-cyclodextrin polymers from alginate/chitosan nanoparticles. *International Journal of Pharmaceutics*, 393(1-2), 212-218. https://doi.org/10.1016/j.ijpharm.2010.04.006

34. El-Ghaffar, M.A.A., Hashem, M.S., El-Awady, M.K., & Rabie, A.M. (2012). pH-sensitive sodium alginate hydrogels for riboflavin controlled release. *Carbohydrate Polymers*, 89(2), 667-675. https://doi.org/10.1016/j.carbpol.2012.03.074

35. Goycoolea, F. M., Lollo, G., Remunán-López, C., Quaglia, F., & Alonso, M. J. (2009). Chitosan- alginate blended nanoparticles as carriers for the transmucosal delivery of macromolecules. *Biomacromolecules*, 10(7), 1736-1743. https://doi.org/10.1021/bm9001377

36. Sarmento, B., Ferreira, D., Veiga, F. & Ribeiro, A. (2006). Characterization of insulin-loaded alginate nanoparticles produced by ionotropic pre-gelation through DSC and FTIR studies. *Carbohydrate Polymers*, 66(1), 1-7. https://doi.org/10.1016/j.carbpol.2006.02.008

37. Bajpai, S. K., & Tankhiwale, R. (2006). Investigation of dynamic release of vitamin B2 from calcium alginate/chitosan multilayered beads: Part II. *Reactive and Functional Polymers*, 66(12), 1565-1574. https://doi.org/10.1016/j.reactfunctpolym.2006.05.007

38. Neiras, Pinilla, P. A. & Henao, M. J. A. (2011). Arcilla bentonítica modificada con quitosano para materiales compuestos biodegradables. *Dyna*, 167, 59-65.

39. Phaechamud, T., Koizumi, T., & Ritthidej G. C. (2000). Chitosan citrate as film former: compatibility with water-soluble anionic dyes and drug dissolution from coated tablet. *International Journal of Pharmaceutics*, 198(1), 97-111. https://doi.org/10.1016/S0378-5173(99)00460-3

40. Bigucci, F., Luppi, B., Cerchiara, T., Sorrenti, M., Bettinetti, G., Rodriguez, L. & Zecchi, V. (2008). Chitosan/pectin polyelectrolyte complexes: selection of suitable preparative conditions for colon-specific delivery of vancomycin. *European Journal of Pharmaceutical Science*, 35(5), 435-441. https://doi.org/10.1016/j.ejps.2008.09.004

41. Su, L., Huang, J., Li, H., Pan, Y., Zhu, B., Zhao, Y., & Liu, H. (2021). Chitosan-riboflavin composite film based on photodynamic inactivation technology for antibacterial food packaging. *International Journal of Biological Macromolecules*, 172, 231-240. https://doi.org/10.1016/j.ijbiomac.2021.01.056

CHAPTER 1 ENERGY AREA

GLYCEROL ELECTROOXIDATION FOR ENERGY CONVERSION USING METAL NANOPARTICLES

Martin Daniel Trejo Valdez*, Luciana López Escobar, María Elena Manríquez Ramírez, Rodrigo Andrés Espinosa Flores

[1]Instituto Politécnico Nacional, Escuela Superior de Ingeniería Química e Industrias Extractivas (ESIQIE), Laboratorio de Investigación en Nanomateriales y Energías Limpias, Zacatenco, Edificio Z5 P.B., 07300, Ciudad de México.

mtrejov@ipn.mx

Trejo Valdez, M. D., López Escobar, L., Manríquez Ramírez, M. E., & Espinosa Flores, R. A. (2023). Glycerol electrooxidation for energy conversion using metal nanoparticles. In E. San Martín-Martínez (Ed.). *Research advances in nanosciences, micro and nanotechnologies. Volume IV* (pp. 155-176). Barcelona, Spain: Omniascience.

Abstract

Glycerol, also called glycerin, propanetriol or trihydroxypropane, is an alcohol with three -OH groups, which is obtained as a by-product in the production of biodiesel and is currently generated in quantities that exceed demand. In addition, crude glycerol causes significant pollution, as it contains methanol residues, which can be toxic to organisms present in aquifers. Glycerol can be transformed into other value-added products by chemical or enzymatic catalysis. Its transformation by electrochemical route is more attractive since it can be applied to the development of alkaline direct glycerol fuel cells (ADGFC). Transition element metal nanoparticles and some of its metallic oxides are commonly used as electrocatalysts in the anode of ADGFCs due to their high chemical stability and excellent catalytic activity. Therefore, the present work deals with the synthesis of metal nanoparticles of Gold, Platinum, Nickel and their bimetallic combinations to study their electrocatalytic activity in the oxidation of glycerol and to analyze their potential application in the development of ADGFC fuel cells. The electrocatalytic properties of metal nanoparticles were evaluated by using cyclic voltammetry and chronoamperometry coupled to ATR-FTIR spectroscopy (Attenuated Total Reflection- Fourier Transform Infrared Spectroscopy).

Keywords: Metal nanoparticles, alkaline glycerol fuel cells, glycerol oxidation, Chronoamperometry coupled to ATR-FTIR.

1. Introduction

Glycerol ($C_3H_8O_3$) is an alcohol with three hydroxyl groups, at room temperature it has a viscous, colorless appearance, is odorless, hygroscopic, insoluble in hydrocarbons and has a slightly sweet taste, commercially known as Glycerin. It is a pH-neutral substance (does not release hydronium or hydroxyl cations when dissolved in water) and is chemically stable under stable storage and handling conditions [1, 2]. It has a boiling point at 290 °C, at this temperature it decomposes generating Acrolein (a highly toxic compound). Generally, glycerol is used in medical preparations, pharmaceuticals, cosmetics, food additives and various products such as glycolic acid, oxalic acid, acetic acid, formic acid, glyceric acid, dihydroxyacetone, tartronic acid, and hydroxypyruvic acid. Glycerol has had a growing production over the years, since it is a by-product in the manufacture of biodiesel, therefore, due to these large volumes generated, which are greater than those demanded are, it has become an important pollutant of wastewater and aquifers [3, 4].

The development of Alkaline Direct Glycerol Fuel Cells (ADGFCs) is quite attractive given their high energy density whose theoretical value is close to 6.4 kW*h/L, which is advantageous in its application since it also reduces its environmental impact by transforming it into additional value-added products. The main challenge in the commercialization of ADGFC cells lies in the kinetics of the glycerol oxidation reaction, i.e. the breaking of covalent C-C bonds and its complete oxidation to CO_2 [5, 6].

Due to their chemical stability and high catalytic activity, Pt nanoparticles are commonly used in research works dealing with primary anode electrolysis of ADGFCs. However, Pt is a naturally scarce and expensive material and suffers from CO poisoning [7]. Moreover, the technological development leading to the commercialization of Anion Exchange Membrane-Direct Glycerol Fuel Cells (AEM-DGFCs) is slowed down by technical issues such as high platinum group metal loading on the anode electrode, low selectivity and poor long-term stability of the catalyst. In addition, the electrooxidation of glycerol conducted by platinum metal leads to the formation of several by-products, which are associated with multiple reaction steps. For example, several works report the formation of C3 products such as glyceraldehyde, dihydroxyacetone, tartronate, glycerate and mesoxalate; C2 products such as glycolate, glyoxylate and oxalate; and C1 products such as formate and CO_3^{2-} [8 –12]. In this sense, international research

groups focused their works on optimizing the catalyst chemical composition, particle size and morphology, structure and metal-support interaction to achieve excellent electrocatalytic performance of the glycerol oxidation reaction in an alkaline environment [13 – 17]. For instance, an alternative approach is the use of Pt catalysts modified with other metals such as Pd, Cu, Au, Ag and Sn, or by combining with metal oxides such as NiO, CuO, MnO_2 and CeO_2 [18 – 25].

Among the above-mentioned metals, nickel is a low-cost and earth-abundant element, and its crystalline structure and lattice parameters are comparable with those of platinum, thereby allowing the facile formation of well-defined alloyed structures. Thus, in this work we focused on the study of the electrooxidation of glycerol using bimetallic PtNi nanoparticles in alkaline medium. The results obtained with this material are compared with those obtained using gold and platinum nanoparticles. Electrochemical kinetic of glycerol oxidation was evaluated by means of cyclic and linear hydrodynamic voltammetry techniques.

2. Experimental

2.1. *Materials and reagents*

Sodium Borohydride $NaBH_4$ (Fluka Analytical ≥99.0 %, Lot # STBC6399V), Sodium citrate tribasic dehydrate $Na_3C_6H_5O_7 \cdot 2H_2O$ (Sigma-Aldrich ≥99.0 %, Lot # SLBP0031V), Gold (III) Chloride Trihydrate $HAuCl_4 \cdot 3H_2O$ (Sigma-Aldrich ≥99.9 % Lot # MKCJ4933), Potassium Iodide KI (Baker ≥99.0 % Lot # A39C76), Nickel (II) nitrate hexahydrate $Ni(NO_3)_2 \cdot 6H_2O$ (Sigma-Aldrich ≥97.0 % Lot # BCBR5231V), Chloroplatinic acid hexahydrate $H_2PtCl_6 \cdot 6H_2O$ (Sigma-Aldrich ≥99.9 %), Vulcan Carbon Black VXC-72R (Gently furnished by Química Rana S.A. DE C.V. Lot # 4267369, Mizu Técnica), Sílice < 0.5, Isopropilic alcohol (ACS FERMONT, 99.9 % Lot # 039131), Nafión™ 117 containing solution ~5 % in a mixture of lower aliphatic alcohols and water (Sigma-Aldrich Lot # BCCF9827). The chemical reagents were used as received and all solutions were prepared using bidestilled and deionized water.

2.2. *Catalysts preparation*

For the preparation of Pt-Ni nanoparticles supported on carbon, a two-step method was used. In a first step, a volume of 160 μL of 0.1 M $Ni(NO_3)_2$ solution and 260 μL of a platinum standard solution of concentration 0.0025 g/ml were

added to a beaker containing 10 mL of deionized H_2O. This mixture was placed on a magnetic stirring plate and stirred with the aid of a magnetic stir bar. Then, 0.005 g of Vulcan charcoal was added into the solution and stirring was continued until a homogeneous dispersion was obtained. A volume of 250 μL of 0.1 M sodium citrate was then added as surfactant. Finally, a volume of 250 μL of reducing agent sodium borohydride was added. The solution was left to stir for 30 minutes and the resulting dispersion of carbon nanoparticles was poured into test tubes and centrifuged for 20 minutes to separate the supernatant. The material with the NPs was washed repeatedly with absolute ethanol. In a final step the carbon supported metal particles were centrifuged and dispersed in only 1 mL of absolute ethanol. This dispersion was used to prepare an ink that was placed on the surface of a rotating glassy carbon disk electrode for electrocatalytic study of the material. The ink was prepared by mixing 250 uL of the nanoparticles dispersion with 50 μL of Nafion and 150 μL of acetone. The mixture was homogenized in an ultrasonic bath by sonicated for a time of 10 minutes.

In order to compare the electrokinetic performance of Pt-Ni bimetallic particles, Pt and Au metallic nanoparticles were also synthesized. The synthesis of Pt particles supported on Vulcan carbon was performed in a similar manner than PtNi catalyst by adding only the corresponding volume of precursor solution. On the other hand, and like the synthetic route of bimetallic particles, a volume of 250 μL of a 0.01 M $HAuCl_4$ aqueous solution was used for the synthesis of Au nanoparticles.

2.3. *Working electrode preparation*

The surface of a disk carbon glass of 1.2 cm^2 diameter was used as substrate for the electrochemical test. First, the carbon electrode was previously polished with a commercial silica alumina solution (Masterpolish) and after this, the surface was then rinsed with distilled water and with isopropyl alcohol. The dry and clean electrode was weighed on an analytical balance and then coated with 50 μL of the ink containing carbon supported nanoparticles. The solvents of the ink were evaporated, and the electrode was coated a couple of times with the ink. Once the excess of solvents was evaporated the coated electrode was used for electrochemical test.

2.4. *Electrochemical Test and Product Analysis*

Cyclic voltammetry (CV) and Electrochemical Impedance Spectroscopy (EIS) were carried out on an AUTOLAB potentiostat/galvanostat PGSTAT302 N, in

a three-electrode configuration cell using an ink-coated glass carbon electrode as the working electrode, a platinum wire as the counter electrode, and a Silver/Silver Chloride (Ag/AgCl) as the reference electrode in a 0.1 M KOH aqueous electrolyte. For Cyclic Voltammetry (CV): scans were performed in the potential range from -0.7 to + 0.5 V vs SHE.

Chronoamperometry coupled to ATR-FTIR spectroscopy was used to analyze glycerol oxidation products. This test was carried out on an AUTOLAB potentiostat/galvanostat PGSTAT302 N but with a different cell arrangement. A custom-made three electrode cell that fitted on top of the ATR crystal was machined from polytetrafluoroethylene (PTFE) fitted with a glassy carbon rod as counter electrodes and quasi-reference. The working electrode was a 3 mm diameter graphite electrode (GE). Since inorganic nitrate ions provide a broad and intense IR band near 1400 cm^{-1}, resulting from out-of-phase stretching for nitrate-containing compounds, for these spectro electrochemical tests the electrolyte was 0.1 M KOH electrolyte, since the spectrum obtained will not have interfering bands. It is indeed worth mentioning that a background was subtracted before collecting the ATR-FTIR scans. An aqueous solution containing 0.1 M KOH electrolyte was degassed beforehand under sonication for 20 min, and then N_2 was bubbled into the electrolyte for 20 minutes to purge O_2. This N_2-saturated solution was transferred to the custom-made PTFE three-electrode cell and a background spectrum was collected at this point.

2.5. *Structural samples characterization*

The morphology of the samples was observed using a transmission electron microscopy (JEM-ARM200CF) which was operated in TEM or STEM mode with acceleration voltages of 80–200 kV. It was installed with a cold electron gun cathode and spherical aberration corrector for the STEM mode. The microscope had coupled detectors for surface chemical analysis of the selected area by X-ray.

3. Results and discussion

3.1. *Electrocatalytic activity of gold nanoparticles (Au-NPs)*

The Au-NPs were applied as a conductive ink on a glassy carbon disk electrode as described in the experimental part and adapted as a working electrode in a three-electrode electrolytic cell. An Ag/AgCl electrode was used as reference and

a platinum wire as auxiliary electrode. 0.1 M KOH solution was placed in the cell as the supporting electrolyte and saturated with nitrogen gas to displace dissolved oxygen. After purging with N_2 gas, a voltammogram was plotted starting from an initial potential (Ei) of -698 mV to an intermediate potential (E_1) of +500 mV (anodic sweep) from which the direction of the applied potential was reversed in the cathodic direction to a final potential value (E_f) identical to E_i. In Figure 1 were shown the different voltammograms obtained from the scans varying, for each test, the potential sweep rates from 5 to 20 mV/s. This figure also shows the voltammogram obtained from the support electrolyte (KOH 0.1M) in which the evolution of the anodic capacitive current in the range -0.698 to +0.5 V is observed. For this anodic zone it is deduced that, when increasing the potential, only a slight oxidation of the nanoparticles appears at 0.5 V which determines the anodic limit of the working electrode. However, when the direction of the applied potential is changed to cathodic scanning, a reduction wave between -0.2 and -0.5 V is observed, which is related to the reduction of surface gold ions in the metallic nanoparticles.

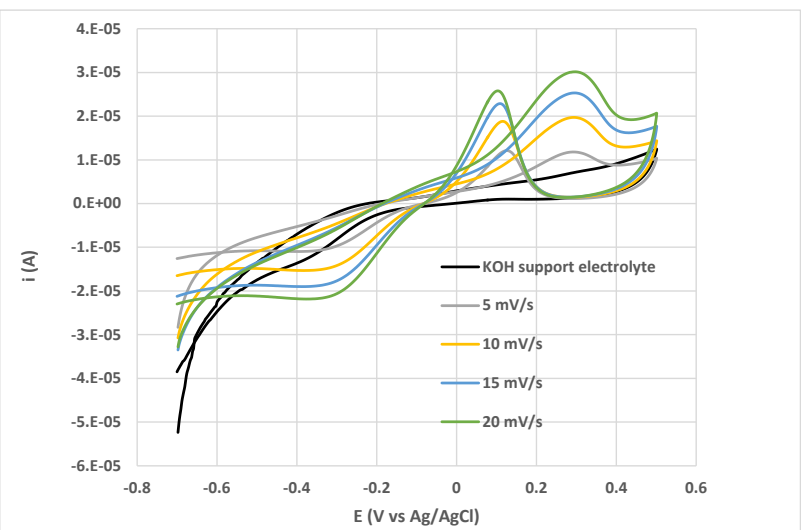

Figure 1. Cyclic Voltammograms obtained from the analysis of glycerol catalyzed by Au NPs. Measurement conditions: 0.1M KOH, Ei=-0.698 V, E1=+ 0.5 V, Ef=-0.698 V, [Glycerol]=2.4 mM.

Once the glycerol is added to the supporting electrolyte, Figure 1 shown that between Ei and -0.2 V a shift of the glycerol measurement currents with respect to the target occurs. This is caused by a capacitive current which is not associated with the electrochemical reaction itself, but with the formation of an electrical double layer on the electrode surface. For voltammograms with glycerol, in the

anodic zone a peak appears at 0.35 V indicating that its oxidation is taking place as an electroactive species, while, when the potential sweep is reversed at 0.1 V, a very pronounced peak appears corresponding to the decomposition of the product formed on the electrode surface.

Cyclic voltammetry was used to explore the ranges of sweep speed and working potential intervals in which oxidation or reduction of the gold nanoparticles does not occur. Moreover, with this technique is seen that the system behaves irreversibly since the ratio between its anodic and cathodic peak intensities is different from the unit. Furthermore, it was evidenced that the glycerol oxidation product formed decomposes when trying to reduce it by reversing the sweep potential direction. Electrode mechanisms are commonly described by using the Testa and Reinmuth notation [26], where letter E is used to denote a heterogeneous electron transfer step, and the letter C to indicate a homogeneous chemical step. In some cases, an electron transfers yields a product that is unstable, and this should be involved in a homogeneous irreversible reaction yielding an electrochemically inactive product:

$$A + e^- \rightleftarrows B \qquad (1)$$

$$B \rightarrow C \qquad (2)$$

Such a case is defined as an EC reaction and its electrochemical analysis is characterized by voltammograms such as those shown by glycerol electrooxidation using the carbon supported Au-Nps.

The results obtained with cyclic voltammetry indicate that it is possible to follow only the glycerol oxidation process. Then, for this process, the electrodynamic kinetic parameters such as the diffusion coefficient and the number of electrons transferred can be determined by using the Randles-Sevcik equation [27]:

$$I_p = 0.496\sqrt{\alpha}\, nFA[G]_{bulk}\sqrt{\frac{FDv}{RT}} \qquad (3)$$

Where:

I_p = peak current intensity [A]

F = Faraday constant [96485.33 C/mol]

n = number of transferred electrons

A=Electrode surface area [cm^2]

D = Diffusion coefficient of the electroactive species [cm^2s^{-1}]

$[G]_{bulk}$= Bulk concentration of electroactive species [$mo^l\ cm^{-3}$]

v = sweep speed [Vs^{-1}]

α = Transfer coefficient (~0.5)

The linear voltammetry technique using a rotating disk electrode (RDE) provides the means to vary the concentration profile at the electrode, since the faster the rotation, the thinner the diffusion layer becomes and the greater the transport-limited flux. The Levich equation models the diffusion and flow conditions of the solution around a rotating disk electrode (RDE), which is characterized by the dependence on the rotational velocity $\varpi^{0.5}$ according to the Eq.4 [26]:

$$I_{lim} = 0.62nFAD^{\frac{2}{3}} \rho^{-\frac{1}{6}} \varpi^{\frac{1}{2}} [G]_{bulk} \ldots\ldots\ldots \quad (4)$$

Where:

I_{lim} = limit current intensity [A]

A = electrode surface area [cm^2]

ρ = dissolvent kinematic viscosity $\left[\frac{cm^2}{s}\right]$

ω = electrode angular rotational speed $\left[\frac{rad}{s}\right]$

and the rest of the constants that have already been defined.

The sweep speed parameter is fixed at 5 mV/s for measurements using the RDE voltammetry and by varying the concentration of glycerol in the cell. The results are shown in Figure 2a where it is observed that the diffusion limit current increases with the addition of glycerol in the electrolytic cell. As is shown in Figure 2b, an absolute standard calibration curve was plotted by taking values in each curve where the limit current is minimum. From this plot, it is concluded that the maximum concentration of glycerol that can be used for working linear hydrodynamic voltammetry is up to 0.7 mol/cm^3. Then, a concentration of 0.662 mol/cm^3 of glycerol is chosen for the hydrodynamic voltammetry experiments but now varying the angular velocity ϖ (see the Figure 3a). According to Levich's postulate, the limiting current densities, j (mA/cm^2*g) should be plotted

as a function of the root of the angular velocity in rad/s, as shown in Figure 3b. Calculating the linear regression of the points in Figure 5 gives a correlation coefficient of 0.9934, which leads to the conclusion that the system behaves linearly according to Levich's equation. By using the eq. 4, the slope of Figure 3b is consistent with n =2 and D=5.75x10^{-6} cm^2/s

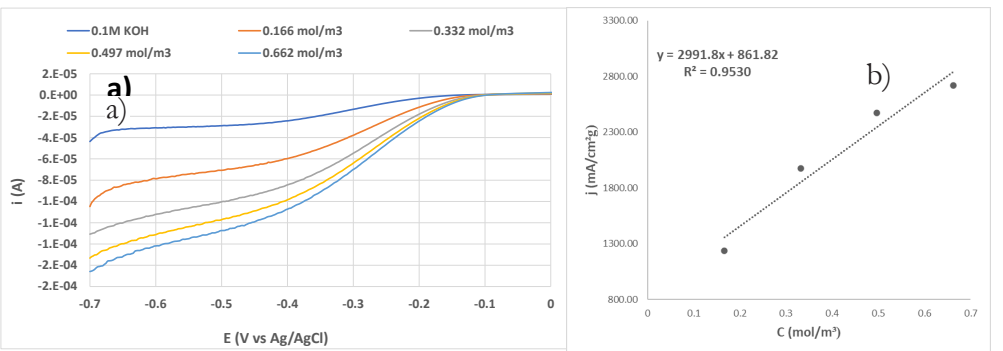

Figure 2. a) RDE Voltammograms obtained by varying the concentration of glycerol and catalyzed by using Au NPs. Measurement conditions: E_i=-0.7 V, Ef=0 V, ω=1500 rpm, υ=0.005 V/s. b) Glycerol calibration curve obtained from the limiting diffusion current values of RDE voltammograms.

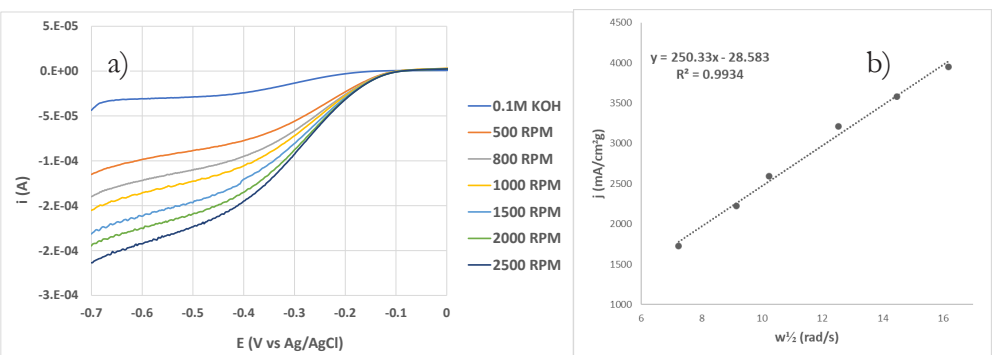

Figure 3. a) RDE Voltammograms obtained by varying the rotational speed of the electrode and catalyzed by using Au-NPs. Measurement conditions: E_i=-0.7 V, Ef=0 V, υ=0.005 V/s, [Glycerol]=6.62 mM. b) The Levich curve obtained from the current limit values.

3.2. *Electrocatalytic activity of platinum nanoparticles (Pt-NPs)*

For this study, the conductive ink applied to the glassy carbon electrode contained Platinum nanoparticles, with which the cyclic voltammograms of Figure 4 were obtained. For each test, the potential sweep rates were increased for a range from 5 to 20 mV/s. The voltammogram of the supporting electrolyte (0.1M

KOH) from a potential value (E_i)=-698 mV to potential (E_1)=+500 mV is seen flat, without any curvature since there is no oxidation or reduction alteration in the material in that potential range. On the other hand, in the measurements with glycerol we observe that the electro-oxidation takes place in a range of -0.1 to -0.2 V when the anodic sweep is being carried out, which is a lower voltage compared to the NP's-Au. The big difference between the first and subsequent sweeps is that from a sweep speed value of 10 mV/s a second oxidation peak is seen at a voltage of -0.2 V, which is evidence that a step transfer of electrons from the glycerol takes place, which is not observed in the case of electrodes modified with the Au-NPs. When the sweep changes to cathodic direction and the applied potential approaches to -0.3 V, only one cathodic peak is observed, which results from an irreversible mechanism. It is evident that the mechanism of glycerol oxidation catalyzed by supported Pt particles is not a simple EC mechanism. As will be discussed later, this electrocatalysis process involves the formation of more than two products.

A 0.662 mM concentration of glycerol is also chosen for the linear hydrodynamic voltammetry experiments by varying the angular velocity. As shown in Figure 5a, the increase of the diffusion current limit is observed with the increase of the angular velocity of the electrode given a correlation coefficient of 0.9933. The slope of plot shown in Figure 5b is consistent with n=6 and $D=6.95x10^{-6}$ cm^2/s.

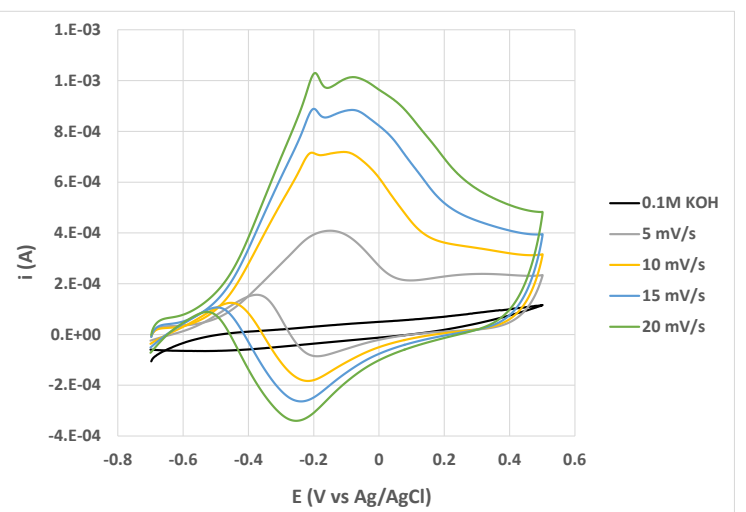

Figure 4. Cyclic voltammograms obtained from the electrocatalysis of glycerol using the Pt-NPs. Measurement conditions: E_i=-0.698 V, E_1=+0.5 V, E_f=-0.698 V, [Glycerol]=2.4 mM.

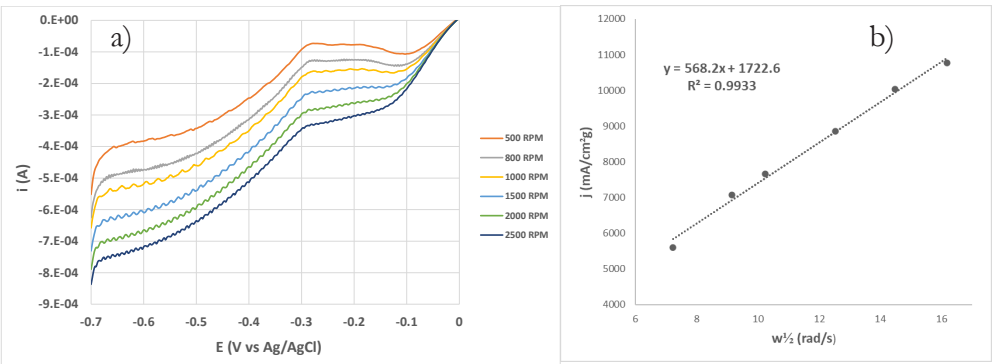

Figure 5. a) RDE Voltammograms obtained by varying the rotational speed of the electrode and catalyzed by using the Pt NPs. Measurement conditions: E_i = -0.7 V, E_f = 0 V, υ =0.005 V/s, [Glicerol] = 6.62mM. b) The Levich curve obtained from the current limit values.

3.3. *Electrocatalytic activity of platinum-nickel nanoparticles (PtNi-NPs)*

In the voltammogram obtained from the supporting electrolyte (see the Figure 6) the evolution of the anodic capacitive current from a potential of -698 mV to 698 mV shows slight oxidation of the bimetallic nanoparticles. However, when the direction of the potential changes to a cathodic sweep, unlike the Pt NP's, a significant reduction of one of the elements composing the PtNi nanoparticles is seen at a potential range of -0.2 to -0.5 V. As soon as glycerol was added to the electrolysis cell and the scanning starts, an anodic peak at -0.18 V

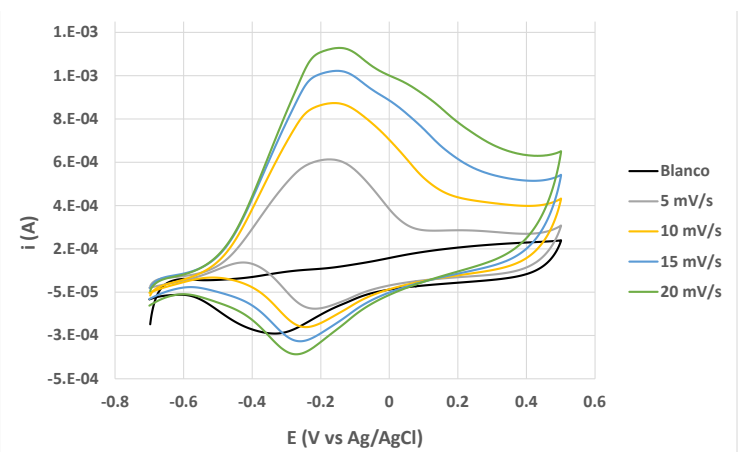

Figure 6. Cyclic Voltammograms obtained from the analysis of glycerol catalyzed by using the Pt-Ni NPs. Measurement conditions: 0.1M KOH, Ei=-0.698 V, E1=+ 0.5 V, Ef=-0.698 V, [Glycerol]=2.4 mM.

is observed, indicating that the oxidation of glycerol as an electroactive specie is taking place. At the highest sweep speed of 20 mV/s, a slight curvature is evident in the anodic zone at approximately 0.1 V, which it can be assumed as an additional oxidation peak, which can involve a second reaction mechanism. Also, when applied potential is inverted to cathodic direction none cathodic signals of glycerol products were observed in voltammogram which is associated with an irreversible chemical mechanism.

As shown in Figure 7a, the increase of the diffusion current limit is observed with the increase of the angular velocity of the electrode given a correlation coefficient of 0.995. The slope of Figure 7b is consistent with n=2 and D=1.75x10^{-7} cm^2/s.

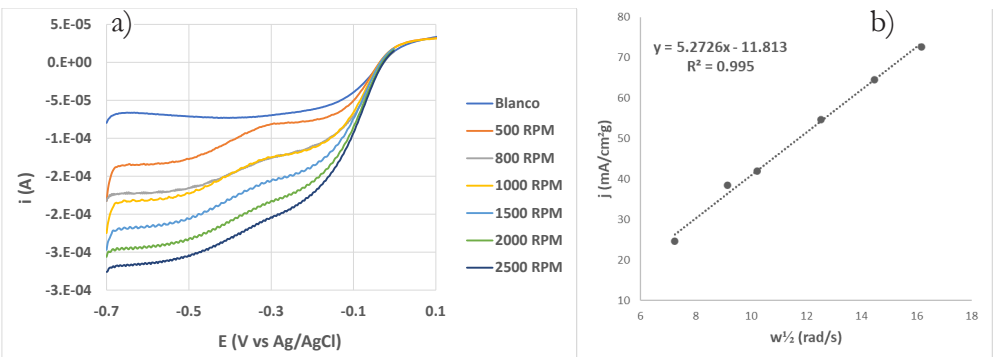

Figure 7. a) Cyclic voltammograms obtained by varying the rotational speed of the electrode and catalyzed by using the Pt-Ni NPs. Measurement conditions: Ei = -0.7 V, Ef = 0 V, υ = 0.005 V/s, [Glicerol] = 6.62 mM. b) The Levich curve obtained from the current limit values.

3.4. *Comparison of Glycerol electro-oxidation kinetics*

The glycerol oxidation process using the different synthesized metal nanoparticles materials (Au, Pt, and PtNi) is shown in the Figure 8. In this figure, the peak current density values were taken from voltammograms of Figures 1, 6 and 7 were plotted against the sweep speed $\nu^{1/2}$ (mV/s). The slope of this plot is related to the standard electrochemical rate constant by means of the dimensionless parameter proposed by Matsuda and Ayabe [28]:

$$\Lambda\sqrt{\frac{FD}{RT}}\,\upsilon^{\frac{1}{2}} = k^{0} \quad (5)$$

From the Figure 8 is appreciated that Pt-Nps shown the highest slope and hence the highest kinetic reaction constant. In addition, as is shown in table 1,

the highest diffusion coefficient of glycerol is obtained by using platinum nanoparticles supported on carbon.

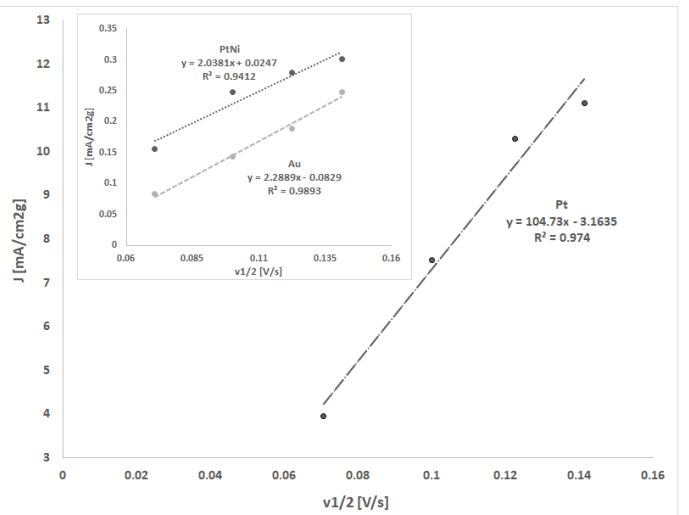

Figure 8. Forward peak current (i_p)versus scan rate for the glycerol oxidation by using the Pt-Nps. The insert corresponds to results obtained by using the Au-Np and PtNi-Nps.

Table 1. Electrochemical parameters of glycerol electrooxidation using the metal nanoparticles.

Metal nanoparticle	n (e-)	D [cm^2s^{-1}]
Au-NPs	2	$3.8296x10^{-7}$
Pt-NPs	6	$4.4852x10^{-7}$
PtNi-NPs	2	$4.48x10^{-7}$

The values of glycerol diffusion coefficient shown in Table 1 are within the range of those reported by D'Errico and co-workers in ref. [29] that were measured by using the Taylor dispersion and Gouy interferometric techniques.

3.5. *Infrared/ATR spectro-electrochemical characterization*

The goal of synthesizing bimetallic NPs with Nickel was due to the possibility of making cheaper catalysts and with less amount of precious metals such as Platinum. Although the electrocatalytic performance of NiPt bimetallic particles followed a very similar pattern to that shown by platinum particles, the electrocatalytic kinetics of the latter turns out to be far superior to that of the former material. Therefore, in this section we focus on the structural characterization of the reaction products on the electrode surface using platinum nanoparticles.

For the identification of the products, infrared spectroscopy tests were performed on the molecules resulting from the anodic reaction of Glycerol with Platinum NPs. Thus, every 5 minutes a spectrum of the oxidized solution was taken for comparison with the initial spectrum at zero time. As can be seen in Figure 9, in the first spectrum is appreciated the signal of the unreacted glycerol solution (t=0), and as the oxidation progresses is shown how progressively a peak appears at a wave number of 1654 cm^{-1}, which is attributed to the formation of a carbonyl group (C=O tension). On the other hand, we also observe the broadening of a tension signal representative of the -OH group from 3654 to 3123 cm^{-1} due to the formation of hydrogen bridges. In addition, we can notice another characteristic absorption band of C-O stress vibrations at 1315 cm^{-1}.

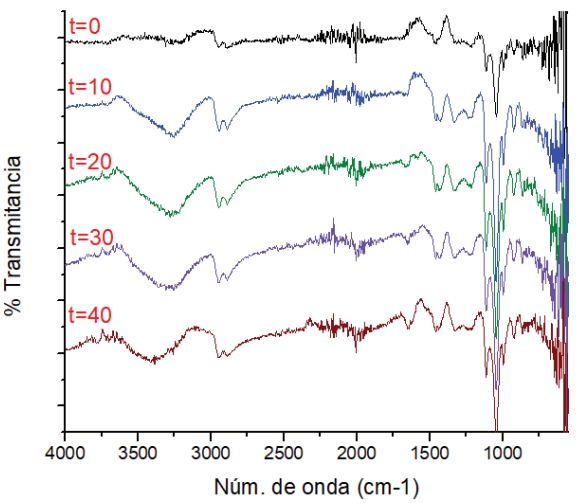

Figure 9. ATR-FTIR spectra of glycerol reduction reaction by using Pt-Nps +0.2 V vs. Ag/AgCl. The acquisition time in minutes was indicated in each spectrum.

From this spectra analysis, and by using a transfer of 6 electrons with the platinum nanoparticles; it is deduced that the glycerol did not only form an aldehyde, but the produced specie was full oxidized to form a carboxylic acid. The proposed electrooxidation mechanism can be similar as that proposed by Coutanceau et. al. [30] which is depicted in the Figure 10. In the initial step, the glycerol in solution travels toward the solution and comes in contact with the electrode surface. Once the glycerol arrives to electrode surface, the oxidation of the primary alcohol by transferring first 2 electrons to form glyceraldehyde. In a second step, this aldehyde formed at the electrode-solution interface is oxidized to glyceric acid via a second transfer of another two electrons. Finally, the Tartronic acid was formed by the oxidation of the glyceric acid via a third transfer of two electrons.

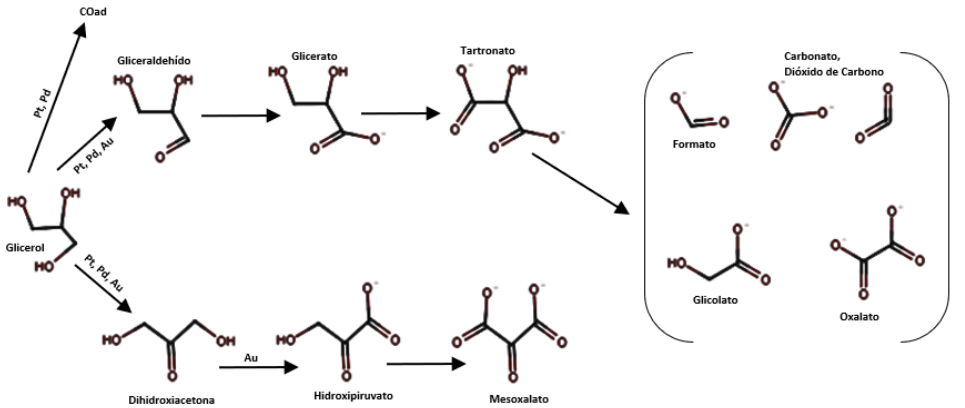

Figure 10. The reaction pathways proposed by Coutanceau *et al.* [30] for electro-oxidation of glycerol on Pt.

3.6. *TEM nanoparticles characterization*

The images obtained by Transmission Electron Microscopy and the analysis performed in the Digital Micrograph Software to measure the interplanar

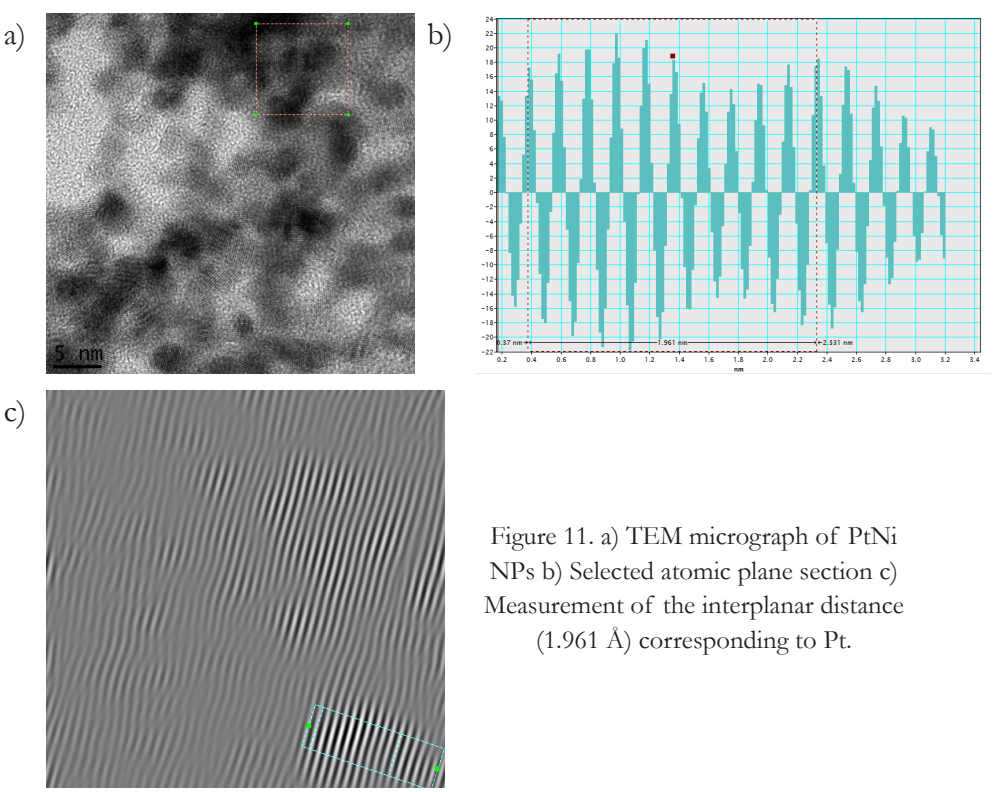

Figure 11. a) TEM micrograph of PtNi NPs b) Selected atomic plane section c) Measurement of the interplanar distance (1.961 Å) corresponding to Pt.

distances of the Platinum nanoparticles are shown in Figures 11. The Figure 11c) show interplanar distances of 1.961 and 2.244 Å, which according to the crystallographic chart of Platinum, correspond to 2θ of 46.2° and 39.76, with which we obtain the diffraction planes of (200) and (111) of Pt respectively.

4. Conclusions

The electrochemical activity of nanoparticles of three metallic nanoparticles (Pt, Au and PtNi) in the electro-oxidation of glycerol was studied to determine which of these materials was the best catalyst for this purpose. The synthesis of such NPs was carried out by a simple chemical method where the precursor solutions of each metal were reduced in situ on to vulcan carbon substrate. The characterization by electroanalytical techniques such as Cyclic Voltammetry and Hydrodynamic Voltammetry (RDE) allowed to visualize the behavior of the NPs in a potential range from -0.7 to 0.7 V(vs Ag/AgCl). It was obtained that all materials shown an irreversible electrode kinetics reaction giving the decomposition of the as formed oxidation product of Glycerol. The diffusion coefficients of glycerol were estimated by hydrodynamic voltammetry whose graphical analysis fitted well to Levich's model, obtaining a number of exchanged electrons of 2 for Au particles, 6 for Pt and 2 electrons by using PtNi bimetallic particles. The reaction mechanism for the electrooxidation of Glycerol was proposed from results obtained by using Pt-NPs and ATR spectroscopy coupled to chronoamperometric analysis. It was deduced that the product formed is a carboxylic acid, which could be tartronic acid.

Acknowledgment and Funding

The authors acknowledge the financial support for developing this work from the Instituto Politécnico Nacional (IPN) through the projects: SIP2241, SIP20230209, and EDI grants. We are grateful for the technical support of the IPN's Centro de Nanociencias y Micro y Nanotecnologías (CNMN).

References

1. Yang, F., Hanna, M. A., & Sun, R. (2012). Value-added uses for crude glycerol–a byproduct of biodiesel production. *Biotechnology for Biofuels* 5, 13. https://doi.org/10.1186/1754-6834-5-13

2. Veljković, V. B., Biberdžić, M. O., Banković-Ilić, I. B., Djalović, I. G., Tasić, M. B., Nježić, Z. B., *et al.* (2018). Biodiesel production from corn oil: a review. *Renewable Sustainable Energy Reviews*, 91, 531-548. https://doi.org/10.1016/j.rser.2018.04.024

3. Tan, H. W., Abdul Aziz, A. R., & Aroua, M. K. (2013). Glycerol production and its applications as a raw material: A review. *Renewable and Sustainable Energy Reviews*, 27, 118-127. https://doi.org/10.1016/j.rser.2013.06.035

4. Md. Rahim, S. A. N., Lee, C. S., Abnisa, F., Aroua, M. K., Daud, W. A. W., Cognet, P. *et al.* (2020). A Review of Recent Developments on Kinetics Parameters for Glycerol Electrochemical Conversion – A by-product of Biodiesel. *Science of the Total Environment*, 705, Article 135137. https://doi.org/10.1016/j.scitotenv.2019.135137

5. Yahya, N., Kamarudin, S. K., Karim, N. A., Masdar, M. S., Loh, K. S., & Lim, K. L. (2019). Durability and performance of direct glycerol fuel cell with palladium-aurum/vapor grown carbon nanofiber support. *Energy Conversion and Management*, 188, 120-130. https://doi.org/10.1016/j.enconman.2019.02.087

6. Geraldes, A. N., Da Silva, D. F., Silva, L. G. A., Spinacé, E. V., Neto, A. O., Dos Santos, M. C. (2015). Binary and ternary palladium based electrocatalysts for alkaline direct glycerol fuel cell. *Journal of Power Sources*, 293, 823-830. https://doi.org/10.1016/j.enconman.2019.02.087

7. Kim, M., Lee, C., Ko, S. M., & Nam, J. M. (2019). Metal alloy hybrid nanoparticles with enhanced catalytic activities in fuel cell applications. *Journal of Solid State Chemistry*, 270, 295-303. https://doi.org/10.1016/j.jssc.2018.11.014

8. Huang, L., Sun, J.-Y., Cao, S.-H., Zhan, M., Ni, Z.-R., Sun, H.-J. *et al.* (2016). Combined EC-NMR and In Situ FTIR Spectroscopic Studies of Glycerol Electrooxidation on Pt/C, PtRu/C, and PtRh/C. *ACS Catalysis*, 6(11), 7686-7695. https://doi.org/10.1021/acscatal.6b02097

9. Velazquez-Hernández, I., Oropeza-Guzmán, M. T., Guerra-Balcázar, M., Alvarez-Contreras, L., & Arjona, N. (2018). Electrocatalytic Promotion of Pt Nanoparticles by Incorporation of Ni(OH)2 for Glycerol Electro-Oxidation: Analysis of Activity and Reaction Pathway. *ChemNanoMat*, 5(1), 68-78. https://doi.org/10.1002/cnma.201800317

10. Wang, C.-Y., Yu, Z.-Y., Li, G., Song, Q.-T., Li, G., Luo, C.-X. *et al.* (2019). Intermetallic PtBi Nanoplates with High Catalytic Activity towards Electro-oxidation of Formic Acid and Glycerol, *ChemElectroChem*, 7(1), 239-245. https://doi.org/10.1002/celc.201901818

11. Kwon, Y., & Koper, M. T. M. (2010). Combining Voltammetry with HPLC: Application to Electro-Oxidation of Glycerol. *Analytical Chemistry*, 82(13), 5420-5424. https://doi.org/10.1002/celc.201901818

12. Martins, C. A., Giz, M. J., & Camara, G. A. (2011). Generation of carbon dioxide from glycerol: Evidences of massive production on polycrystalline platinum. *Electrochimica Acta*, 56(12), 4549-4553. https://doi.org/10.1002/celc.201901818

13. Wang, W., Jing, W., Wang, F., Liu, S., Liu, X., & Lei, Z. (2018). Amorphous ultra-dispersed Pt clusters supported on nitrogen functionalized carbon: A superior electrocatalyst for glycerol electrooxidation. *Journal of Power Sources*, 399, 357-362. https://doi.org/10.1016/j.jpowsour.2018.07.120

14. Zhang, Y., Gao, F., Song, P., Wang, J., Song, T., Wang, C. *et al.* (2019). Superior liquid fuel oxidation electrocatalysis enabled by novel bimetallic PtNi nanorods. *Journal of Power Sources*, 425, 179-185. https://doi.org/10.1016/j.jpowsour.2019.04.001

15. Wu, F., Zhang, L., Lai, J., Niu, W., Luque, R., & Xu, G. (2019). PtCu-O Highly Excavated Octahedral Nanostructures Built with Nanodendrites for Superior Alcohol Electroxidation. *Journal of Materials Chemistry A.*, 14, 8568-8572. https://doi.org/10.1039/C9TA01236B

16. Zhou, Y., Shen, Y., & Xi, J. (2019). Seed-mediated synthesis of PtxAuy@Ag electrocatalysts for the selective oxidation of glycerol. *Applied Catalysis B: Environmental*, 245, 604-612. https://doi.org/10.1016/j.apcatb.2019.01.009

17. Sieben, J. M., Alvarez, A. E., & Sanchez, M. D. (2023). Glycerol electrooxidation on carbon-supported Pt-CuO and PtCu-CuO catalysts. *Electrochimica Acta*, 439, 141672. https://doi.org/10.1016/j.electacta.2022.141672

18. Lv, H., Sun, L., Xu, D., Suib, S., & Liu, B. (2019). One-pot aqueous synthesis of ultrathin trimetallic PdPtCu nanosheets for the electrooxidation of alcohols. *Green Chemistry*, 9, 2367-2374. https://doi.org/10.1039/C9GC00741E

19. Castagna, R. M., Sieben, J. M., Alvarez, A. E., & Duarte, M. M. E. (2019). Electrooxidation of ethanol and glycerol on carbon supported PtCu nanoparticles. *International Journal of Hydrogen Energy*, 44(12), 5970-5982. https://doi.org/10.1016/j.ijhydene.2019.01.090

20. Dai, C., Sun, L., Liao, H., Khezri, B., Webster, R. D., Fisher, A. C. *et al.* (2017). Electrochemical production of lactic acid from glycerol oxidation catalyzed by AuPt nanoparticles. *Journal of Catalysis*, 356, 14-21. https://doi.org/10.1016/j.jcat.2017.10.010

21. Garcia, A. C., Ferreira, E. B., Silva de Barros, V. V., Linares, J. J., & Tremiliosi-Filho, G. (2017). PtAg/MnOx/C as a promising electrocatalyst for glycerol electro-oxidation in alkaline medium. *Journal of Electroanalytical Chemistry*, 793, 188-196. https://doi.org/10.1016/j.jelechem.2016.11.053

22. Li, Z., Qiu, G., Jiang, Z., Zhuang, W., Wu, J. & Du, X. (2018). Tuning concave Pt-Sn nanocubes for efficient ethylene glycol and glycerol electrocatalysis. *International Journal of Hydrogen Energy*, 43(50), 22538-22547. https://doi.org/10.1016/j.ijhydene.2018.10.132

23. Sieben, J. M., Alvarez, A. E., & Sanchez, M. D. (2022). Platinum nanoparticles deposited on Cudoped NiO/C hybrid supports as high-performance catalysts for ethanol and glycerol electrooxidation in alkaline medium. *Journal of Alloys and Compounds*, 921, 166112. https://doi.org/10.1016/j.jallcom.2022.166112

24. Li, Z.-.Y., Zhou, J., Tang, L.-S., Fu, X.-P., Wei, H., Xue, M. (2018). Hydroxyl-rich Ceria Hydrate Nanoparticles Enhancing the Alcohol Electrooxidation Performance of Pt catalysts. *Journal of Materials Chemistry A*, 6(5), 2318-2326. https://doi.org/10.1039/C7TA09071D

25. Velázquez-Hernández, I., Zamudio, E., Rodríguez-Valadez, F. J., García-Gómez, N. A., Álvarez-Contreras, L., Guerra-Balcázar, M. *et al.* (2020). Electrochemical valorization of crude glycerol in alkaline medium for energy conversion using Pd, Au and PdAu nanomaterials. *Fuel*, 262, 116556. https://doi.org/10.1016/j.fuel.2019.116556

26. Richard G. Compton, R. G., & Banks, C. E. (2018). *Understanding voltammetry*. (3rd Ed.). New Jersey: World Scientific. https://doi.org/10.1142/q0155

27. Bard, A. J.; & Faulkner, L. R. (2004). *Electrochemical methods: Fundamentals and applications*. Wiley India Pvt. Ltd. Chpt. 6.

28. Matsuda, H., & Ayabe, Y. (1955). Zur Theorie der Randles-Sevčikschen Kathodenstrahl-Polarographie. *Zeitschrift fuer Elektrochmie and Angewandte Physikalische Chemie*, 59(6), 494-503. https://doi.org/10.1002/bbpc.19550590605

29. D'Errico, G., Ortona, O., Capuano, F., & Vitagliano, V. (2004). Diffusion Coefficients for the Binary System Glycerol + Water at 25 °C. A Velocity Correlation Study. *Journal of Chemical & Engineering Data*, 49(6), 1665-1670. https://doi.org/10.1021/je049917u

30. Coutanceau C., Baranton, S., & Bitty Kouamé, R. S. (2019). Selective Electrooxidation of Glycerol into Value-Added Chemical: A Short Overview. *Frontiers in Chemistry*, 7, article 100. https://doi.org/10.3389/fchem.2019.00100

CHAPTER 2 ENERGY AREA

INCORPORATION OF FE-F6 BLOCKS INTO LAMINAR HYDROXIDES OF FE, NI: EXPLORING ON THE WATER OXIDATION REACTION

Ariel Guzmán Vargas*[1], María de Jesús Martínez Ortiz[1], Carlos Felipe Mendoza[2], Enrique Lima[3]

[1]Instituto Politécnico Nacional-ESIQIE-SEPI-DIQI-LiMpCa-QuF, UPALM, Zacatenco, CDMX, 07738, CDMX, Mexico.

[2]Instituto Politécnico Nacional –CIIEMAD- D. de Biociencias e Ingeniería, CDMX 07340, Mexico.

[3]Universidad Nacional Autónoma de México- LaFReS, IIM, Circuito Exterior s/n, Cd. Universitaria, Coyoacán, CDMX 04510, Mexico.

aguzmanv@ipn.mx

Guzmán Vargas, A., Martínez Ortiz, M. J., Felipe Mendoza, C., & Lima, E. (2023). Incorporation of Fe-F6 blocks into laminar hydroxides of Fe, Ni: Exploring on the water oxidation reaction. In E. San Martín-Martínez (Ed.). *Research advances in nanosciences, micro and nanotechnologies. Volume IV* (pp. 177-190). Barcelona, Spain: Omniascience.

Abstract

Nanostructured materials offer important characteristics to be applied in different fields of research, for example, in renewable and clean energy production processes in electrolyzers for the generation of hydrogen from water, reaction known as water splitting or oxidation. In the present work, the studies carried out with Ni, Fe layered double hydroxides (LDH) are reported, modified with the introduction of FeF_6 blocks containing fluoride (Fe-F) with 10 and 20 %w, in the brucite-type layers, which will partially occupy structural positions of the Fe-hydroxyl groups (Fe-OH). The method of synthesis used was coprecipitation at low saturation with the aim to obtain nanocrystals. The incorporation of Fe in the structure of nanomaterials was made in its Fe^{3+} form as M^{3+} cation, and nickel as M^{2+} cation, respectively, maintaining a M^{2+}/M^{3+} = 3 molar ratio. The physicochemical properties of the materials were characterized by different techniques such as: XRD, ^{19}F-NMR, IR, TGA/DSC, nitrogen physisorption. The results revealed well-ordered materials, structural modifications and changes in the thermal and adsorption properties, as a consequence of the incorporation of Fe-F_6 species in the brucite-type sheets.

The electrocatalytic properties of the materials as electrodes, were evaluated in the oxygen evolution reaction (OER) in an alkaline medium, determining the parameters such as: overpotential, Tafel slope, activation energy, electrochemically active surface area (ECSA) and stability. All samples exhibited responses on the OER, the fluorinated samples showed an overpotential of 1.16 -1.22 V and a Tafel slope of 285 - 331 mV/decade.

Keywords: Fluorinated LDH; OER; Water Oxidation; Electrocatalysis.

1. Introduction

Two dimensional nanostructured materials as Layered Multihydroxides (LMH or LDH) are formed by brucite-type layer with positive charge which is compensated by anionic species in the interlaminar or interlayer region. Their molecular formula is $[M^{II}_{1-x} M^{III}_{x} (OH)_2]^{x+} (A^{n-})_{x/n} \cdot mH_2O$, and their composition should be include a wide variety of divalent metal ions octahedrally coordinated to hydroxyl groups in the brucite-type layers (M^{II}=Mg^{2+}, Co^{2+}, Cu^{2+}, Ni^{2+} or Zn^{2+}), these cations should be isomorphically replaced by trivalent cations as (M^{III}=Al^{3+}, Fe^{3+}, Mn^{3+}, Cr^{3+} or Ga^{3+}) [1, 2]. In this context, the basicity attributed to the OH- can be tailored by the presence of electronegative species. For this purpose, the first reports showed the impregnation method to introduce fluorinated species on the layer´s surface in order to increase the basicity properties [3]. Thus, Lima *et al.* reported the first LDH material incorporating F as $(AlF_6)^{3-}$ blocks in the brucite-type layer, replacing $Al(OH^-)_6^{3-}$ by $(AlF_6)^{3-}$ blocks, obtaining a new class of material with different properties as acid-base [4]. With this aim, as an alternative to RuO_2 and IrO_2 materials, NiFe LDHs have been presented good response on the OER [5 – 8], which is the rate determining step (RDS) on the water splitting or oxidation to produce hydrogen from industrial electrolyzers, as alternative source of green and renewable energy from non-fossil origin in the context of the environmental crisis and the energy transition [9 – 11]. In this work, we reported the preparation of LDH containing F species, incorporating $(FeF_6)^{3-}$ instead of $Fe(OH^-)_6^{3-}$ blocks in the layer or sheet. As first approach, the solids were evaluated on OER process to prove some electrocatalytic aspects of this kind of nanomaterials.

2. Experimental

2.1. *Synthesis and electrode preparation*

The NiFe LDHs were prepared by coprecipitation method usingas source of flour and precursors of metal cations were $Ni(NO_3)_2 \cdot 6H_2O$, and $Fe(NO_3)_3 \cdot 9H_2O$; two samples with 10 and 20 %w of Fe-F, and one sample without F, all solids with a Ni/Fe = 3 molar ratio, the equipment used to perform the synthesis of the materials was a pH STAT Titrino (Metrohm). The work electrodes were obtained by mixing the prepared LDHs in a solution of nafion and ethanol, this suspension was sonicated for 30 min, then, around 80 μL were deposited on a

piece of glassy carbon to form a uniform film and dried at room temperature. The samples were labeled as NiFe-10F, NiFe-20F and NiFe.

2.2. *Characterization and Electrochemical Tests*

Powder X-ray diffraction analysis (PXRD) were carried out in an X'Pert PRO with a CuKα=1.5406 Å (45 kV and 40 mA) in the interval of 5 to 80 (2θ). The diffractograms were acquired with the step of 0.02 and 0.4 s for each point. FTIR spectra were obtained using a Frontier Perkin Elmer spectrometer with an ATR accessory, acquisition was performed between 500 and 4000 cm^{-1}, with a resolution of 2 cm^{-1}. The ^{19}F MAS NMR spectra were measured in an Avance 300 Bruker instrument operating the spectrometer at 376.3 MHz, using π/2 pulses of 6 ms with a recycle delay of 1 s; ^{19}F chemical shifts were referenced to those of $CFCl_3$ at 0 ppm. Thermal analyses were carried out employing a STA 6000 TGA/DSC Perkin Elmer apparatus in the range of temperature between 25 to 900 °C, in a N_2 atmosphere as carrier gas. Textural properties were measured in Autosorb iQ Station Quantachrome Instruments. The solids were previously out gassed in N_2 at 160 °C for 2 h, adsorption-desorption isotherms were collected in the range of 0.015 a 0.99 for P/Po.

The supported films were then used as working electrode in a three-electrode one compartment standard electrochemical cell. Graphite and Hg/HgO NaOH 0.1 M (0.164 V vs RHE) electrodes were employed as counter and reference electrode, respectively. Electrochemical analyses were carried out at room temperature in a multichannel PGstat302N potentiostat-galvanostat (Autolab). Rotating Disk Electrode method was employed for electrocatalytic evaluation at 1600 rpm, in the window of 0 V to 1.6 V at scan of 10 mV/s. For all set of experiments, linear voltammetry was reported with compensated cell resistance (iR). The Reversible Hydrogen Electrode (RHE) scale was calculated based on the formula: VRHE=VSCE+VSCE (vs NHE)+(0.059* pH).

3. Results and Discussion

3.1. *Structural Characterization*

Typical LDH crystalline structure was confirmed by XRD patterns for samples containing a mixture of Fe-F and Fe-OH groups and the sample without Fe-F species (Figure 1). For the three samples, the patterns show LDH phase with the usual hexagonal lattices and R3m rhombohedral symmetry (JCPDS 22-0700) [12, 13].

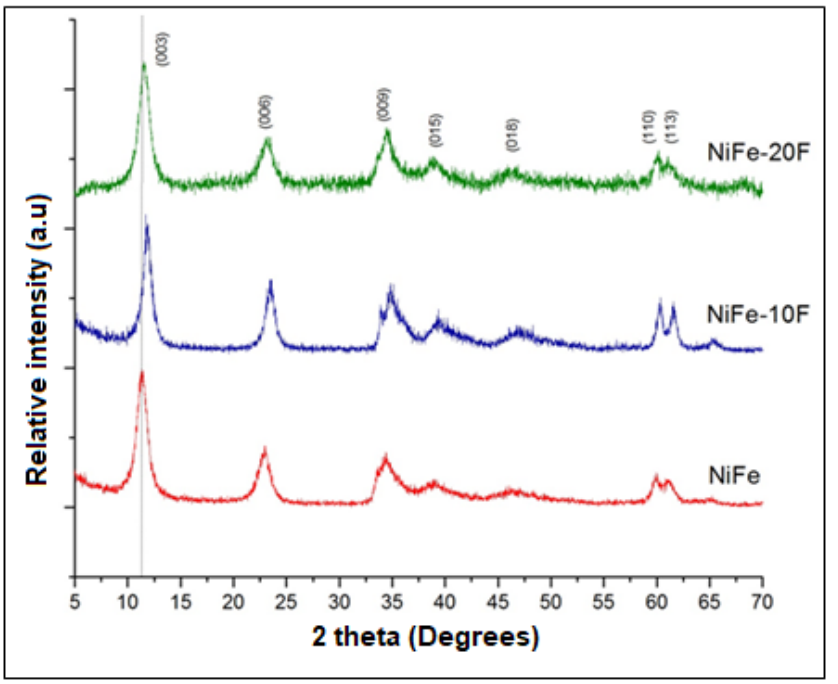

Figure 1. XRD patterns of layered materials with FeF6 incorporated blocks, the solid NiFe is without flour.

All samples exhibit well-defined peaks for the (003), (006) and (009) planes, related to the interlayer space. Furthermore, it should be remarked that the peaks for sample NiFe-10F sample are broader compared to the other two samples.

Moreover, the peak in the plane (003) was slightly shifted for the samples containing F, this is associated to the strong interaction between fluorine, the cations in the brucite-like layers and the anions in the interlayer space [4]. This is also in accord to the values of $\boldsymbol{c}$ and $\boldsymbol{d_{003}}$ parameters as shown in the table 1, both parameters decrease when Fe-F species are present, while the cell parameter **a**, related to the distance between adjacent cations in the layer, is similar for all samples.

Table 1. Cell parameters of LDH samples.

Sample	d_{003} (Å)	d_{110} (Å)	a (Å)	c (Å)
NiFe	7.82	1.54	3.09	23.47
NiFe-10F	7.56	1.53	3.07	22.67
NiFe-20F	7.69	1.54	3.08	23.08

IR spectra are exhibited in Figure 2. OH^- groups from water in the interlayer region and on the sheets are described by the presence of band around 3000-3600 cm^{-1}, specially, in the samples fluorinated this stretching vibration band is broader and more intense due to the dipolar moment indicating that these samples are more hydrated. The band at 1630 cm^{-1} is attributed to the deformation plane of water. C-O asymmetric stretching vibration of CO_3^{2-} is observed at 1360 cm^{-1}. In the range between 1000 to 500 cm^{-1} the bands are associated to M-O, M-O-M and O-M-O bonds in the brucite-like layers, typical bands of these kind of materials. For these samples, they correspond to the Ni-oxygen and Fe-oxygen lattice vibrations [14].

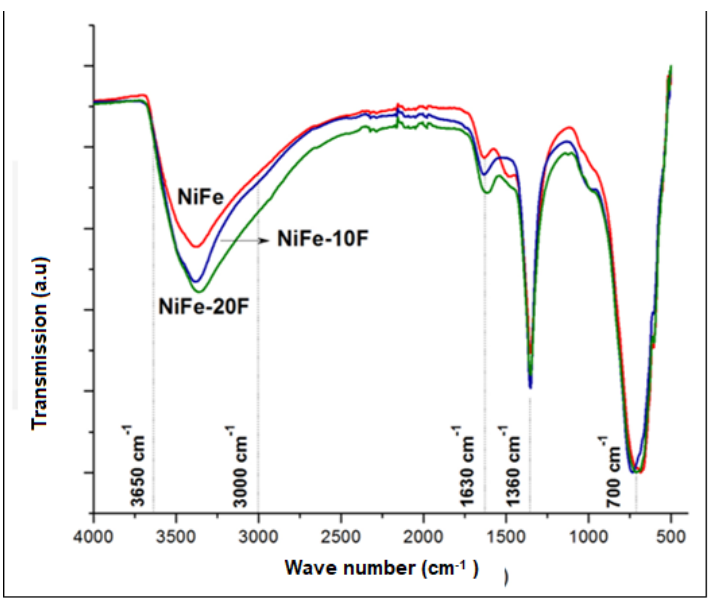

Figure 2. FTIR spectra of LDH solids with and without flour.

In order to verify the incorporation of Flour (Fe-F_6 blocks) in the brucite type layer, substituting partially OH- groups (Fe-OH), ^{19}F NMR studies were carried out. The spectra of ^{19}F nuclei are shown in Figure 3 for the samples. Three main signals were observed, a shoulder around -147, at -133 and -93 ppm. The peak at -147 ppm is associated to $(FeF_6)^{3-}$ species as it is was previously reported [15, 16]. In addition, other resonances a lower field (-133 and -93 ppm) suggest the existence of octahedral blocks type $(FeF_{6-x}(OH)_x)^{3-}$ which means that the $(FeF_6)^{3-}$ blocks are randomly mixed with $Fe(OH)_6)^{3-}$ or $(Ni(OH)_6)^{4-}$ blocks in the layer sheet. Thus, the main signal at -147 ppm point out the presence of domains rich in fluorinated blocks combined with zones rich in OH^-.

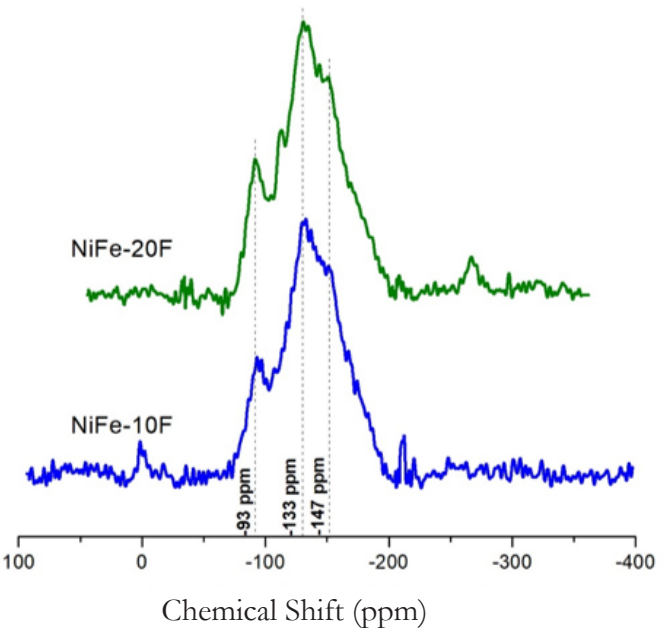

Figure 3. ^{19}F NMR spectra of NiFe-20F and NiFe-10F.

3.2. *Thermal Analysis, morphology, and textural properties*

Profiles of thermal analyses are shown in Figure 4, three zones of mass loss are clearly observed. The first around 100 °C, is associated to desorption of water on the surface. The second between 170 °C and 305 °C is attributed to the loss of water in the interlayer space and dehydroxylation. It is observed that the samples containing F show a fast loss of weigh, considering these materials

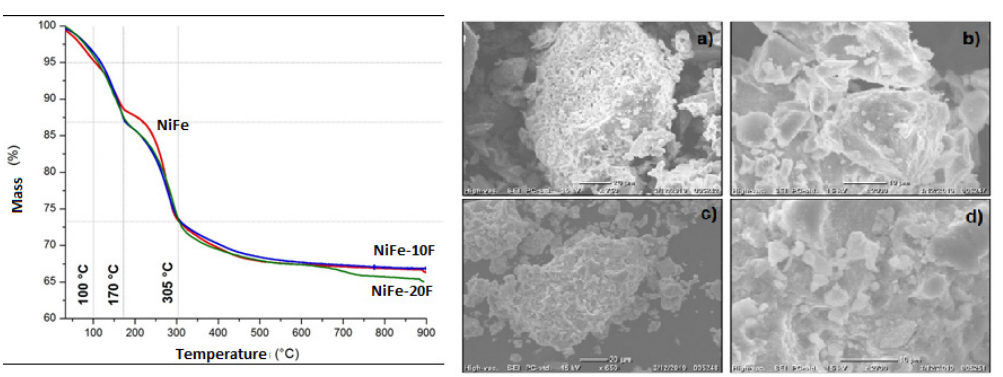

Figure 4. Thermal profiles of NiFe LDH and SEM images of a) and b) NiFe-10F, c) and d) NiFe-20F.

are more hydrated as above discussed. Besides, in the last zone up to 305 °C, the process of decarbonation takes place at the same time that the dihydroxylation is completed [17]. In general, all the samples exhibited the same percent of weight loss. Finally, the total mass loss was similar for all samples, the presence of flour has not important influence on the thermal stability at higher temperatur

Figure 4 a) to d) shows SEM images of the F containing samples, the form observed was flakes or irregular plaques, typical for layered materials, with sizes between 10-100 μm, there is not important influence of flour presence on the morphology.

Adsorption-desorption isotherms are shown in Figure 5; the profile of all samples corresponds to type IV, showing H2 type hysteresis loop according to IUPAC classification, typical for mesoporous materials showing desorption pore blocking effects [18]. This last phenomenon was more marked on the flour samples; it can be associated with the strong interaction of fluorinated species and

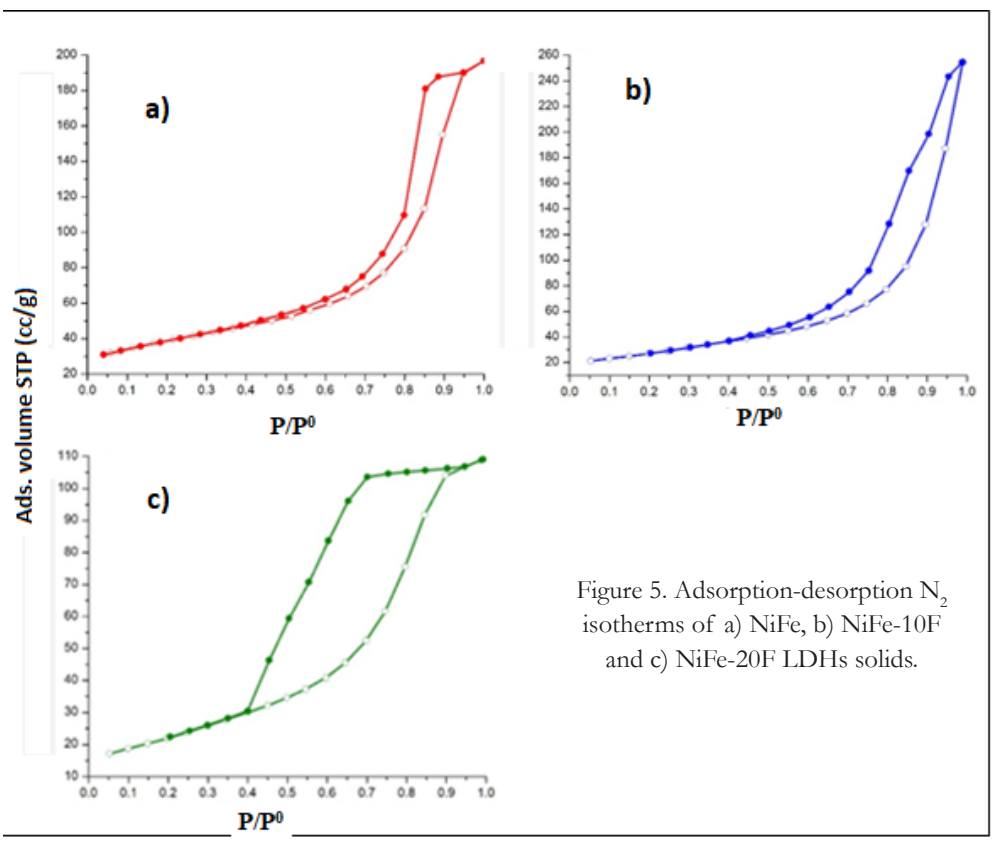

Figure 5. Adsorption-desorption N_2 isotherms of a) NiFe, b) NiFe-10F and c) NiFe-20F LDHs solids.

the higher degree of hydration, as reported in TGA studies. The profiles can also be associated with different sizes of pores.

Regarding the shape of the hysteresis loops, for the sample in red (see Figure 5), the pores are of similar sizes, causing slight pore blockage during desorption. In contrast, more significant pore blockage is appreciated in the green isotherm. On the other hand, the null pore blockage is evident in the blue isotherm due to the gradual filling and emptying of the pores.

For the results of a specific surface, the solid without F exhibited the largest values, and the samples with F showed a lower surface. This agrees with adsorption-desorption isotherms; the presence of F can block some part of the porous structure provoking the decrease of the area BET, volume and radius of the pore, as it is reported in Table 2.

Table 2. Textural properties of LDH samples.

Sample	ABET (m^2/g)	Pore Vol.* (cm^3/g)	Pore Radius Å
LDH NiFe SF	132.00	0.263	61.76
LDH NiFe 10 % F	43.56	0.394	48.65
LDH NiFe 20 % F	80.25	0.169	17.15

3.3. *First Approach: Exploring the electrocatalytic properties on the water oxidation reaction (OER)*

This kind of materials have been reported as electrocatalysts for the water oxidation reaction, in some studies Ni was founded that it acts as catalytic center protected by Fe, taking into account the adsorption of OH- as principal step [6, 19]. From this, we reported as first approach to examine some properties of this kind of materials, the performance on OER or water oxidation.

The overpotential (η) is a parameter to measure the catalytic activity, it is reported to reach current density (j) of 10 mA/. Figure 6 shows the profiles for the samples. Clearly, a positive effect due to the Fe-F species is observed. The best performance was for NIFe-20F with the lowest value around 868 mV. This behavior can be attributed to the formation of more catalytic sites when F is present and it is was corroborated determining the electrocatalytic surface area (ECSA) where the sample NiFe-20F showed a value of 0.530 cm^2, while the sample without F was 0.47 cm^2.

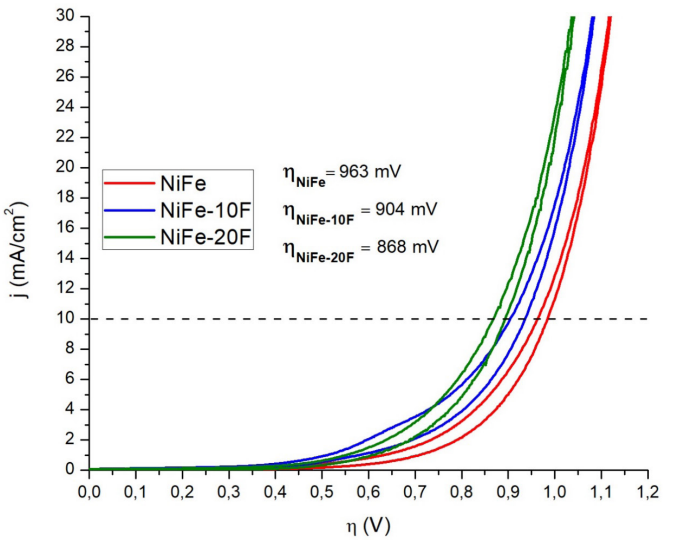

Figure 6. Overpotential on the OER process of LDH samples at j=10 mA/cm2.

NiFe fluorinated LDHs revealed overpotential values around 300 mV. Some aspects could be considered to explain this behavior. It is well known the electronegativity associated to the presence of flour, and the OER mechanism is mainly associated to the OH^- adsorption, although, it is possible the strong adsorption of the OH-. Species limiting the electron transfer due to the force of the electronegativity. To solve this inhibition, the presence of another kind of catalytic site i.e Co or improve the distribution of Fe-F blocks so as not creates richest zones of these species. Testing these kind of materials in reactions where strong electronegativity and basicity plays an important role as in some processes i.e. C-C bond formation [20].

4. Conclusions

Nanostructured Layered hydroxides of NiFe (NiFe-LDH) were obtained incorporating Fe-F6 blocks, which partially substituted to the Fe-OH or Ni-OH blocks in the brucite-type sheets using the coprecipitation method. The main goal of this study was achieved in order to demonstrate the introduction of iron fluorinated species in the layers to obtain a new kind of material. This was demonstrated by different techniques, from the XRD results typical diffraction patterns of layered hydroxide materials were obtained and corroborated with the

values of **a** and $\mathbf{d_{003}}$ parameters. The presence of fluorinated species was confirmed by ^{19}F NMR showing characteristic bands associated to flour interactions. Adsorption-desorption Isotherms were of mesoporous solids, a strong adsorption was observed due to the Fe-F_6 blocks. As first approach, the electrocatalytic properties were evaluated in the OER process in alkaline media.

Funding

This study was partially supported by the Projects SIP-IPN 20211169 and 20220802.

References

1. Cavani, F., Trifirò, F., & Vaccari, A. (1991). Hydrotalcite-type anionic clays: Preparation, properties and applications. *Catalysis Today*, 11, 173-301. https://doi.org/10.1016/0920-5861(91)80068-K

2. Shao, M., Zhang, ., Li, Z., Wei, M., Evans, D. G., & Duan, X. (2015). Layered double hydroxides toward electrochemical energy storage and conversion: design, synthesis and applications. *Chemical Communications*, 51, 15880-15893. https://doi.org/10.1039/C5CC07296D

3. Choudary, B. M., Kantam, M. L., Neeraja, V., Rao, K. K., Figueras, F., & Delmotte, L. (2001). Layered double hydroxide fluoride: a novel solid base catalyst for C–C bond formation. *Green Chemistry*, 5, 257-260. https://doi.org/10.1039/b107124f

4. Lima, E., Martínez-Ortiz, M. J., Gutiérrez Reyes, R. I., & Vera, M. (2012). Fluorinated Hydrotalcites: The Addition of Highly Electronegative Species in Layered Double Hydroxides To Tune Basicity. *Inorganic Chemistry*, 51(14), 7774-7781. https://doi.org/10.1021/ic300799e

5. Gong, M., & Dai, H. (2015). A mini review of NiFe-based materials as highly active oxygen evolution reaction electrocatalysts. *Nano Research*, 8, 23-29. https://doi.org/10.1007/s12274-014-0591-z

6. Carrasco, J. A., Romero, J., Varela, M., Hauke, F., Abellán, G., Hirsch, A. *et al.* (2016). Alkoxide-intercalated NiFe-layered double hydroxides magnetic nanosheets as efficient water oxidation electrocatalysts. *Inorganic Chemitry, Frontiers*, 3, 478-487. https://doi.org/10.1039/C6QI00009F

7. Guzmán-Vargas, A., Vazquez-Samperio, J., Oliver-Tolentino, M. A., Ramos-Sánchez, G., Flores-Moreno, J. L., & Reguera, E. (2017). Influence on the Electrocatalytic Water Oxidation of M2+/M3+ Cation Arrangement in NiFe LDH: Experimental and Theoretical DFT Evidences. *Electrocatalysis*, 8, 383-391. https://doi.org/10.1007/s12678-017-0383-9

8. Lu, Z., Xu, W., Zhu, W., Yang, Q., Lei, X., Liu, J. *et al.* (2014). Three-dimensional NiFe layered double hydroxide film for high-efficiency oxygen evolution reaction. *Chemical Communications*, 49, 6479-6482. https://doi.org/10.1039/C4CC01625D

9. Long, X., Li, J., Xiao, S., Yan, K., Wang, Z., Chen, H. *et al.* (2014). A strongly coupled graphene and FeNi double hydroxide hybrid as an excellent electrocatalyst for the oxygen evolution reaction. *Angewandte Chemie*, 126, 7714-7718. https://doi.org/10.1002/ange.201402822

10. Dresp, S., Luo, F., Schmack, R., Kuhl, S., Gliech, M., & Strasser, P. (2016). An efficient bifunctional two-component catalyst for oxygen reduction and oxygen evolution in reversible fuel cells, electrolyzers and rechargeable air electrodes. *Energy & Environmental Science*, 9, 2020-2024.
https://doi.org/10.1002/ange.201402822

11. Long, X., Wang, Z., Xiao, S., An, Y., & Yang, S. (2016). Transition metal based layered double hydroxides tailored for energy conversion and storage. *Materials Today*, 19, 213-226.
https://doi.org/10.1016/j.mattod.2015.10.006

12. Di Cosimo, J. I., Díez, V. K., Xu, M., Iglesia, E., Apesteguía, C. R. (1998). Apesteguía, Structure and Surface and Catalytic Properties of Mg-Al Basic Oxides. *Journal of Catalysis*, 178(2), 499-510.
https://doi.org/10.1006/jcat.1998.2161

13. Shanon, R. D. (1976). Revised Effective Ionic Radii and Systematic Studies of Interatomie Distances in Halides and Chaleogenides. *Acta Cryst.*, A32, 751-767.
https://doi.org/10.1107/S0567739476001551

14. Liao., F., Yang., G., Cheng., Q., Mao., L., Zhao, X., & Chen, L. (2022). Rational design and facile synthesis of Ni-Co-Fe ternary LDH porous sheets for high-performance aqueous asymmetric supercapacitor. *Electrochimica Acta*, 428, 140939.
https://doi.org/10.1107/S0567739476001551

15. Asseid, F. M., Duke, C. V. A., Miller, J. M. (1990). A 19F magic angle spinning nuclear magnetic resonance and infrared analysis of the adsorption of alkali metal fluorides onto montmorillonite clay. *Canadian Journal of Chemistry*, 68(8), 1420.
https://doi.org/10.1139/v90-217

16. Scholz, G., Krahl, T., Ahrens, M., Martineau, C., Buzaré, J. Y., Jäger, C. *et al.* (2011). 115In and 19F MAS NMR study of (NH4)3InF6 phases. *Journal of Fluorine Chemistry*, 132(4), 244-249.
https://doi.org/10.1139/v90-217

17. Magri, V. R., Duarte, A., Perotti, G. F., & Constantino, V. R. L. (2019). Investigation of Thermal Behavior of Layered Double Hydroxides Intercalated with Carboxymethylcellulose Aiming Bio-Carbon Based Nanocomposites. *ChemEngineering*, 3(2) 55.
https://doi.org/10.1139/v90-217

18. Cychosz, K. A., & Thommes, M. (2018). Progress in the physisorption characterization of nanoporous gas storage materials. *Engineering*, 4(4), 559-566.
https://doi.org/10.1016/j.eng.2018.06.001

19. Abellán, G., Coronado, E., Martí-Gastaldo, C., Waerenborgh, J., & Ribera, A. (2013). Interplay between chemical composition and cation ordering in the magnetism of Ni/Fe layered double hydroxides. *Inorganic Chemistry*, 52(17), 10147-10157. https://doi.org/10.1016/j.eng.2018.06.001

20. Tichit, D., & Álvarez, M. G. (2022). Layered Double Hydroxide/Nanocarbon Composites as Heterogeneous Catalysts: A Review. *ChemEngineering*, 6(4), 45. https://doi.org/10.1016/j.eng.2018.06.001

CHAPTER 3 ENERGY AREA

INFLUENCE OF LANTHANUM SUBSTITUTION AT A-SITE ON STRUCTURAL, MORPHOLOGICAL AND ELECTRICAL PROPERTIES OF THE $La_{(0.7-X)}Ln_XCa_{0.3}MnO_3$ (LN = PR, SM, CE) NANOPARTICLES SYNTHESIZED BY PECHINI METHOD

J. Ramírez-Hernández[1], S. B. Brachetti-Sibaja[1*], A. M. Torres-Huerta[2*], M. A. Domínguez-Crespo[2], M. A. Aguilar-Frutis[3], J. Moreno-Palmerín[4], F. Gutierrez-Galicia[2]

[1]Tecnológico Nacional de México, IT de Ciudad Madero, D.E.P.I., Ave. Primero de Mayo S.N. Col. Los Mangos, Cd. Madero, C.P. 89449, Tamps, México.

[2]Instituto Politécnico Nacional, UPII-Hidalgo, km. 1+500, Carretera Pachuca, San Agustín Tlaxiaca, Actopan, Hgo, 42162, México.

[3]Instituto Politécnico Nacional, CICATA Unidad Legaria, Calzada Legaria 694, Miguel Hidalgo, CDMX, 11500, México.

[4]Departamento de Minas, Metalurgia y Geología, Universidad de Guanajuato, Ex Hacienda San Matías s/n, Guanajuato, Guanajuato, C.P. 36020, México.

atohuer@hotmail.com, bbrachetti@hotmail.com

Ramírez-Hernández, J., Brachetti-Sibaja, S. B., Torres-Huerta, A. M., Domínguez-Crespo, M. A., Aguilar-Frutis, M. A. *et al.* (2023). Influence of lanthanum substitution at A-site on structural, morphological and electrical properties of the $La_{(0.7-x)}Ln_xCa_{0.3}MnO_3$ (Ln= Pr, Sm, Ce) nanoparticles synthesized by Pechini method. In E. San Martín-Martínez (Ed.). *Research advances in nanosciences, micro and nanotechnologies. Volume IV* (pp. 191-212). Barcelona, Spain: Omniascience.

Abstract

Solid Oxide Fuel Cells (SOFC) are one of the highly efficient energy conversion devices; however, the typical operating temperature (800 to 1000 °C) represents a challenge by requiring materials that can withstand these conditions without losing their properties. For SOFCs, the most commonly used cathode materials are lanthanum-strontium manganites (LSM); however, this type of materials has disadvantages as they require a high polarization, which has prompted the development of perovskite-type structure materials (ABO_3), establishing that combining or substituting lanthanum with some other lanthanide $(La_{1-x}L_{nx})_{0.7}Ca_{0.3}MnO_3$ could reduce the overpotential at the cathode, and increase the electrocatalytic activity. In this work, the effect of cation substitution in non-stoichiometric perovskites $(La_{1-x}L_{nx})_{0.7}Ca_{0.3}MnO_3$ (Ln=Pr, Sm, Ce) on the structural, morphological, and electrical properties has been evaluated when the Pechini method is used as a synthesis method. The properties were analyzed in terms of potential applications as cathode materials in SOFCs varying the doping concentration (x=0.1, 0.3, 0.5 and 0.6). The Pechini method is a low-cost reproducible method that led to the production of phase-pure perovskite under certain experimental conditions. The electrical conductivities at room temperature ranged between 0.5 and 0.09 S cm^{-1}, which seems promising to be used as cathode at low-intermediate temperatures preserving the activity for oxygen reduction reaction.

Keywords: Solid oxide fuel cells, nanostructures, perovskites, Pechini method.

1. Introduction

Fuel cells are a great field of study due to their development as alternative energy sources, carrying out research that proposes different synthesis methods to obtain electrode materials that provide favorable characteristics for their operation. In recent years, different works have been published that serve as a basis for the different types of cells, such is the case of Selmi *et al.* [1], where a compilation about fuel cells is provided, giving information about the challenges they currently present and the benefits they provide, making a general analysis of the different types that exist and their cost-benefit, as well as, the efficiency that they could present and their possible applications. The progress of SOFC research, the evolution of new materials, and the development of advanced instruments have collectively led to the selection of parameters that, when controlled, directly affect the desired performance results in the energy production [2].

These types of devices are normally classified according to the electrolyte used, with the exception of the direct methanol fuel cell (DMFC), where methanol is fed directly to the anode and therefore, it is the electrolyte of this cell, the second classification is based on the operating temperature of the cells. These can be classified into high and low temperature fuel cells. Low temperature fuel cells are alkaline (AFC), proton exchange cells (PEMFC), direct methanol (DMFC) and phosphoric acid fuel cells (PAFC). High temperature cells operate at temperatures from 600-1000 °C, and these are: molten carbon (MCFC) and solid oxide fuel cell (SOFC) [3]. Then, a solid oxide fuel cell is a high temperature device with a solid oxide as electrolyte which has the characteristic that it needs to be operated at an elevated temperature to achieve enough power. Knowing this, the use of cheap catalysts may be a good way to reduce the cost of the fuel cell. On the other hand, the possibility of using biofuel instead of hydrogen could be considered an eco-friendly alternative [4].

It is well-known that the performance of the cell is highly influenced by the oxygen reduction reaction (ORR) in cathode part, which needs a high overpotential to work [5]. This condition makes the cathode selection much more important in comparison to the anode choice. Elementary reactions in the cathode generally happened at the triple phase boundary (TPB) at electrode/electrolyte interface [6]. The TPB is defined as the site where the gas phase, the ion conductor and the electronic conductor of the oxygen are in contact with each other [7, 8]. To be considered as a good electrode material, the cathode must have strong electrochemical performance that can be measured by its electronic conductivity and

oxygen diffusivity; these properties are influenced by the ORR that occurs at the TBP cathode.

The cathode must be able to resist any chemical degradation that may occur during fuel cell operation and that can be determined making a comparison between the thermal expansion coefficient (TEC) and the stability of the electrode [9 – 11]. The mentioned characteristics not only depend on the interaction between the components forming the material but are also influenced by the size of the nanostructure and the composition of the cathode [12, 13]. New synthesis routes and unconventional compounds are the popular used strategies to propose new cathode materials and used as an alternative way to improve the performance of solid oxide fuel cells. Among the methodologies for the synthesis of new materials to the cathode, we find that doping the original composition with another element to produce a deformation within the structure is the most used since allows a better diffusivity of the oxygen ion. For example, strontium, calcium and barium, group II elements that have been used as dopants, according to the literature, can increase the conductivity of materials. Also, transition elements such as zinc, molybdenum or vanadium have also been reported as dopant agent to the cathode material, reporting interesting results from electrical measurements and polarization resistance [12].

The alteration of the structure in this type of materials to SOFC, has become one of the fields most studied since nanometric oxide materials have a higher catalytic performance due to present an increase in the surface vacancies, electronic and ionic conductivities [14]. Other synthesis methods as infiltration or impregnation, allows the construction of the nanostructure of the cathode material, by depositing the nanoparticles on a pre-sintered backbone (at high temperature), in that way, the electrocatalytic properties and stability of the cathode material are reached, while the costs of the synthesis can be reduced [14 – 16]. Cathode nanomaterials have generally been synthesized via solid-state reaction or sol-gel methods. However, since the cathode thickness influences the performance of SOFCs, other techniques such as inkjet printing, screen printing (SP), and electrophoretic deposition have been also proposed to fabricate more complex cathode structures [17, 18]. Parameters such as the temperature, time during annealing and sintering stage were also investigated to optimize the size of nanostructures, microstructural, magnetic and optical properties of different perovskite manganites [18, 19]. Additionally, a comparison of different synthesis methods has also been carried out to determine changes in electrical, microstructural and surface properties. For example, Da Conceição *et al.*, and coworkers

synthesized a lanthanum strontium manganite, LSM=$La_{0.7}Sr_{0.3}MnO_3$, using the combustion, sol-gel and a solid state reaction methods [20]. The authors found that all materials exhibited a single LSM phase formation with crystallite sizes in the range of 12 - 20 nm, whereas porosity, particle size and microstructure of the LSM sintered at high temperature are very dependent of the synthesis method. In this context, the samples synthesized by the combustion and sol-gel methods, compared to the other techniques, presented smaller particle sizes and higher porosity after the sintering process than that obtained from solid state synthesis; however, the electrical conductivity was found quite similar under the same composition [21].

The most popular cathode materials enclose perovskite nanostructures. This material is a mineral that contains the structure of calcium titanate ($CaTiO_3$), adopting the general formula of ABO_3. Thus, a wide variety of oxide compounds can have this type of structure and the properties can be modulated according to the final requirements. The orthorhombic structure is the most common among ABO_3 perovskite nanostructures. This type of structure includes many $LnMO_3$ compounds in which Ln is a trivalent rare earth combined with other transition metals and M is a trivalent cation (Al, Fe, Mn, Ga, Cr, V) [22]. As mentioned above, the doping strategy has been widely adopted to improve the performance of this kind of cathode materials for SOFCs applications [23]. Particularly, strontium-doped lanthanum manganite ($La_{1-x}Sr_xMnO_{3\pm d}$, LSM) also known as LSM is one of the earliest cathode materials that fill out a lot of the requirement for high-performance SOFCs. LSM nanostructures have good chemical and thermal stability, high catalytic activity in the reduction of the oxygen, and high electronic conductivity [24]; their thermal expansion coefficient similar to the solid electrolyte of yttria stabilized zirconia (ZrO_2/Y_2O_3 – YSZ) reduces the possibility of thermomechanical degradation due to the mismatch of length when the material is expanding while heating. Unfortunately, at low temperature, LSM nanostructures exhibits a very high polarization loss which inhibits its usage for IT-SOFC and LT-SOFC applications [25].

Among the nanostructured materials that can help to solve this problem during SOFCs operation, $LaMnO_3$ compounds have been proposed the. The lattice of these perovskites can be suitable to be doped with a combination of rare earths (RE), improving the compatibility at the cathode- electrolyte interphase and the kinetics of the oxygen reduction reaction. It is also known that the substitution of lanthanum by another ion directly modifies its characteristics due to

new interactions in the La-O and Mn-O bonds. Bhalla *et al.* present a review of this type of perovskites evaluating their role in ceramic science and technology, showing this structure is one of the most versatile in the area [26].

In this context, the partial substitution of La at the A-site by other rare earth ions has shown an improvement in overall cell performance by reducing cathode polarization, operating temperature and ionic-electrical resistivity, through RE-O and Mn-O interactions [27 – 30]. For example, electronic properties of Pr, Sm and Ce as part of the lanthanide series have similar properties compared to La, but can enhanced the electronic interaction in the final nanostructured compound favoring a specific property. The new interactions lead to a weak bond between the surface and adsorbed oxygen species provoking a low diffusion barrier for oxygen ions, thus facilitating the oxygen reduction reaction. [31, 32].

Continuing with the contribution of the research group of the Instituto Politécnico Nacional at UPII-Hidalgo in collaboration with Tecnológico Nacional de México- IT de Ciudad Madero and other research centers, in the development of nanostructured materials for energy production; at this opportunity, advances are reported in the synthesis of ABO_3-type perovskites nanostructures. It has been explored the La-substitution in the A-site of $LaMnO_3$ perovskites by different RE materials such as Ce, Sm, Pr to evaluate structural, morphological and electrical changes evaluating the alternative as cathode material for SOFCs. Specifically, this research reports the synthesis of rare earth cathode electrode nanomaterials, $La_{(1-x)}Ln_xCa_{0.3}MnO_3$, by the Pechini method, using different stoichiometries in molar ratios (x=0.1, 0.3, 0.5 and 0.6; Ln=Ce, Sm, Pr). The crystal structure, morphological analysis and electrical measurements of the cathode materials were systematically investigated and discussed in terms of ORR activity.

2. Methodology

2.1. *Synthesis of perovskites nanoparticles*

Metal nitrates from Sigma Aldrich, were used as a precursors to the synthesis and consisted of lanthanum (III) nitrate hexahydrate ($La(NO_3)_3 * 6H_2O$, 99.99 % purity), praseodymium (III) nitrate hexahydrate ($Pr(NO_3)_3 * 6H_2O$, 99.9 % purity), samarium (III) nitrate hexahydrate ($Sm(NO_3)_3 * 6H_2O$, 99.9 % purity) calcium nitrate tetrahydrate ($Ca(NO_3)_3 * 4H_2O$, 99 % purity) and manganese (II) nitrate

tetrahydrate ($Mn(NO_3)_2 * 4H_2O$, 97.0 % purity). Stoichiometric amounts were calculated to obtain a nominal composition according to the chemical reaction to form $La_{0.7-x}Ln_xCa_{0.3}MnO_3$ (Ln=Sm, Pr, Ce; x=0.1, 0.3, 0.5 and 0.6) perovskites nanoparticles. The synthesis was performed as follows: first, the metal salts were placed in a matrass and mixed with the citric acid (CA) and deionized water, forming a 3:1 solution in relation to citric acid/metal cations. The solution was magnetically stirred for 10 min at 90 °C or 110 °C, respectively. Thereafter, ethylene glycol (EG) was added drop by drop (2 mL min^{-1}) up to reach a 2:1 ratio (EG/CA), maintaining the magnetic stirring for 4 or 5 h to obtain a gel. This gel was annealed at 450 °C for 3 h until the obtaining of powders which were grinded in an agate mortar. Finally, the samples were put through a heat treatment at 1000 °C for 6 h.

2.2. *Characterization*

The structural analysis of the as obtained nanoparticles was performed in an X-Ray diffractometer, Bruker D2 Phaser Lynx eye using a Bragg-Brentano (θ-2θ) configuration. Measurements were carried out with an applied voltage of 40 kV, current of 40 μA and a radiation Kα-Cu (λ=1.5406 Å). The scans were acquired in the θ-2θ range of 10° to 90°. The morphology of nanopowders was observed using a JEOL JSM-6701F microscope using 10 kV of accelerating voltage. Pellets were manufactured with the powders at 10 ton (1 cm^2) to carry out the electrical tests. These measurements were carried out using four-point probe method at room temperature with a surface resistivity meter (SRM-232).

3. Results and discussion

It has been well recognized that depending on the applied temperature and the oxygen present in the lattice, this type of nanomaterials can crystallize in different symmetries, being the most common the cubic, orthorhombic and monoclinic [33]. Figure 1 shows the XRD patterns of the as-prepared $La_{0.7-x}Ln_xCa_{0.3}MnO_3$ (Ln=Sm, Pr, Ce; x=0.1, 0.3, 0.5 and 0.6) nanopowders.

It was observed that regardless of the Ln amount, the patterns display typical reflections of an orthorhombic perovskite-type structure (PDF #49-0416). But a displacement of the main reflections is observed as the content of the cations (Pr, Sm, Ce) increases. This behavior has been observed in other kind of perovskites and it is related to the expansion of the cell volume. It is also recognized

that impurities in the composition or interface can influence the stability performance of the SOFCs devices. In some compositions small peaks of a probable secondary phase formed during the synthesis process are observed. To estimate the size crystallites in the obtained perovskite, the Scherrer´s equation was used. Measurements were carried out based on the most representative signal of each sample (121). The as-obtain samples of praseodymium show a crystallite size (C.S.) between 61.2 and 73.5 nm, while in the case of samarium the samples show a variation between 64.3 and 71.5 nm; finally, for cerium, the C.S. was obtained in a range between 63.0 to 72.1 nm. The C.S. did not show a clear trend with the substitution of different cations, however the three substitutions coincide that the composition x=0.3, presented the minimum size in the samples: Pr^{3+} (61.2 nm), Sm^{3+} (64.3 nm) and Ce^{3+} (63.0 nm).

The contradiction with other previously reported lanthanum perovskites nanostructures, where a progressive increase in crystal size is observed with the amount of cationic dopant (30-49 nm), highlights the importance of both the size of the ionic radii as the amount of cation during La substitution to form ABO_3-type perovskites, as well as the synthesis process [34 – 36]. It is important to highlight that the XRD analyzes were carried out before applying the sintering process, however, the diffractograms did not show any representative signal corresponding to the typical perovskite structure, so it was concluded that a high applied temperature (1000 °C in this case) is necessary to achieve the formation of the desired ABO_3 structure.

Rietveld analysis is a method in which various parameters are adjusted to match XRD crystallographic data, being one of the best approaches to characterize nanocrystalline materials and extract information about the unit cell and quantitative amount of the phase. To confirm the formation of the secondary phase, Rietveld refinement was carried out using the FullProf Suite 64 software and a pseudo-Voigt function to compensate for stress or size contributions to signal broadening. The analysis was carried out from an orthorhombic system with a space group Pnma, determining the different parameters of the unit cell, the positions and atomic coordinates x and z for the corresponding elements. Table 1 shows the refinement parameters obtained for the different samples (Pr, Sm, Ce).

The results showed a variation in the occupancy of the site that was reflected in a correlation between the occupancy and the molar quantity of these elements. The results also showed that there is a reduction in the cell volume of the

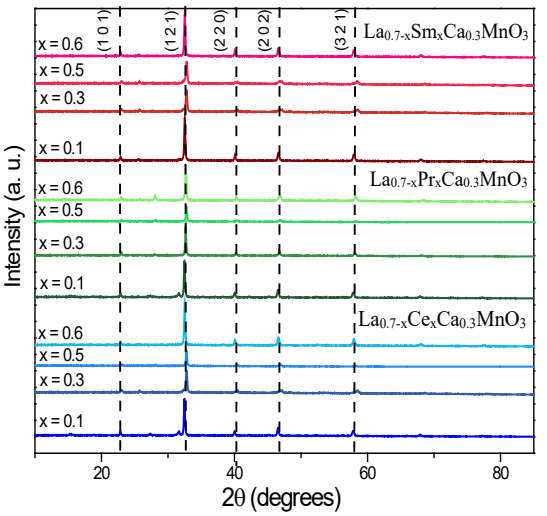

Figure 1. XRD patterns obtained for the $La_{(0.7-x)}Ln_xCa_{0.3}MnO_3$ (Ln = Sm, Pr, Ce; x=0.1, 0.3, 0.5 and 0.6) samples.

Table 1. Structural parameters obtained by Rietveld refinement

Sample	Composition	Phase	Cell Parameters			Volume (Å^3)	(χ^2)
			a (Å)	b (Å)	c (Å)		
Pr	0.1	Orthorhombic	5.433	7.667	5.467	227.76	3.48
	0.3		5.445	7.719	5.417	227.72	3.54
	0.5		5.428	7.666	5.476	227.92	4.03
	0.6		5.418	7.720	5.444	227.75	4.41
Sm	0.1	Orthorhombic	5.447	7.724	5.412	227.761	3.60
	0.3		5.450	7.723	5.404	227.518	4.28
	0.5		5.434	7.732	5.421	227.821	3.75
	0.6		5.445	7.735	5.409	227.849	5.31
Ce	0.1	Orthorhombic	5.678	7.722	5.601	245.57	5.718
	0.3		5.694	7.728	5.620	247.29	6.877
	0.5		5.512	7.731	5.419	235.181	4.92
	0.6		5.792	7.801	5.632	254.47	7.952

material by increasing the cation La cation substitution (*x* value) and therefore important differences in the lattice parameters depending on the composition. The increase of Pr, Sm or Ce in the synthesized nanocomposites causes an increase in the parameter a and a decrease in *b* and *c*, which confirms the existence

of distorted orthorhombic structures. From the obtained data, Vesta 3.5.7® software was used to represent the cell structure for each rare earth cation. Figure 2 a-c shows the cell for Pr, Sm and Ce at a composition of x=0.5, which were selected as representative.

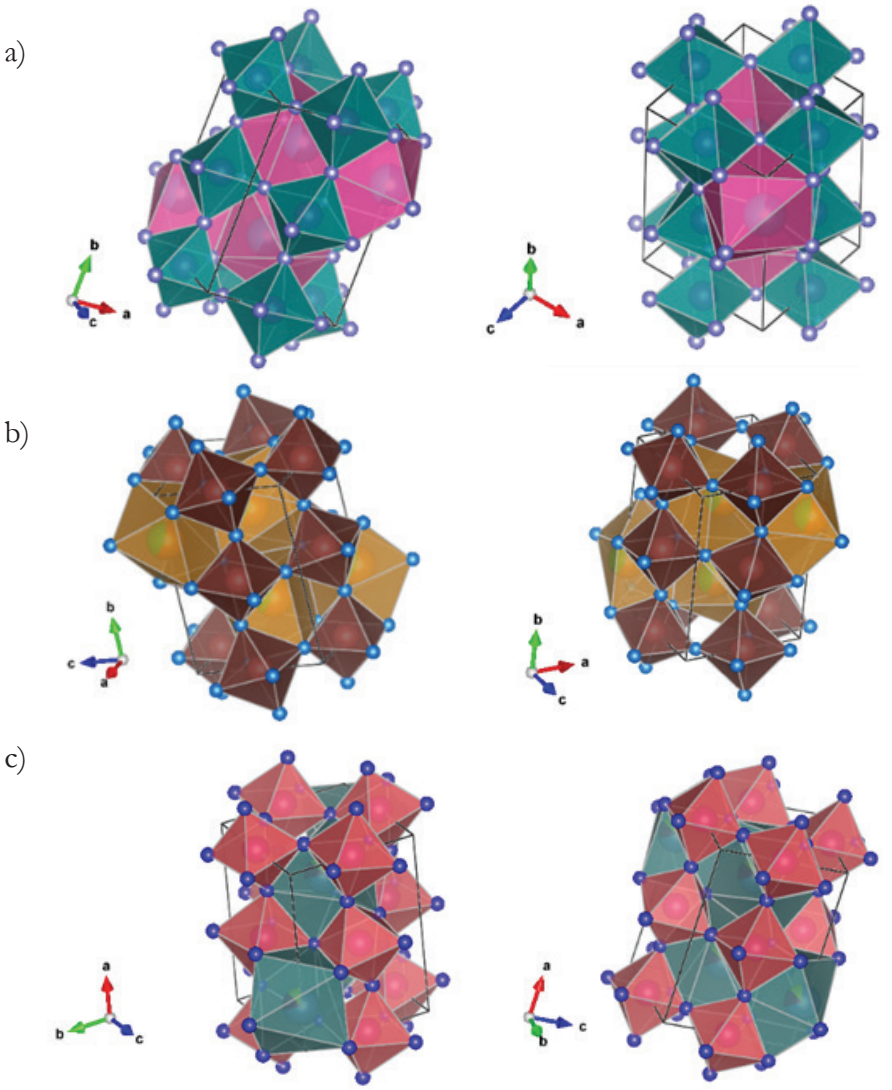

Figure 2. Unit cell drawn with the parameters obtained from Rietveld refinement: a) praseodymium b) samarium c) cerium

It was determined that the unit cell of the synthesized materials is orthorhombic, regardless of the amount of cation (Pr, Sm, Ce) used, however, when analyzing the cell with the values obtained for parameters *a*, *b* and *c*, important

differences were observed in the direction of the distortion depending on the amount and ionic radii that replaced La. A similar trend was previously reported for strontium-doped perovskites, where refinement showed that the unit cell parameters a and c increased with increasing amount of Sr [37], while b parameter decreased, obtaining a distorted orthorhombic structure; which in turn correlated with the Jahn-Teller (JT) effect that modifies the Mn^{+3} ion into the octahedral Mn. JT can be understood as the geometric distortion of a nonlinear system reducing its symmetry and energy, which in turn influence ionic and electrical properties. Jahn Teller proposed that nonlinear degenerate molecules cannot be stable and that any highly symmetric molecule will undergo geometric distortion to reduce its symmetry and, thus, lower its energy.

From this Figure, the distances in the Mn-O bond for each nanomaterial were also analyzed, since this parameter indicated the distortion degree, and the results can be seen in Table 2. Considering that the order in the ionic radii in these rare earths are La(1.189 *Å*)>Ce(1.155 *Å*)>Sm(1.086 *Å*)>Pr (1.069 *Å*). In each distorted orthorhombic structure six Mn-O bonds were identified; each Mn-O bond in the structure was labeled as I and varies from 1 to 6. It is clear that the distortion in the materials is giving in different directions without clear tendency, with respect to lanthanum substitution.

Table 2. Distance of Mn – O bonds.

Bond	Distance Mn-O / Å											
	$La_{0.7-x}Pr_xCa_{0.3}MnO_3$				$La_{0.7-x}Sm_xCa_{0.3}MnO_3$				$La_{0.7-x}Ce_xCa_{0.3}MnO_3$			
	0.1	0.3	0.5	0.6	0.1	0.3	0.5	0.6	0.1	0.3	0.5	0.6
I1	1.968	1.964	1.968	1.968	1.962	1.966	1.962	1.966	1.999	1.996	1.999	1.997
I2	1.960	1.951	1.962	1.963	1.954	1.952	1.951	1.951	1.940	1.942	1.940	1.941
I3	1.968	1.964	1.968	1.968	1.962	1.966	1.962	1.966	1.999	1.996	1.999	1.997
I4	1.960	1.951	1.962	1.963	1.954	1.952	1.951	1.951	1.940	1.942	1.940	1.941
I5	1.957	1.969	1.957	1.956	1.970	1.967	1.972	1.971	1.971	1.968	1.970	1.968
I6	1.957	1.969	1.957	1.956	1.970	1.967	1.972	1.971	1.971	1.968	1.970	1.968
Angle (º) O1		Mn-Ox-Mn			Mn-Ox-Mn				Mn-Ox-Mn			
	157.57	157.45	157.58	157.44	157.46	157.47	157.42	157.45	159.21	159.32	159.22	159.31
O2	156.56	156.91	156.52	156.81	156.87	156.89	156.94	156.95	158.76	158.81	158.79	158.77

The JT effect was observed to occur in the prepared nanostructured perovskites along the bonds of Mn^{+3} cation. In A-MnO_3 manganites, the conducting electrons reside in the 3d Mn^{+3} orbitals. Due to its structure, the Mn ion is located

in the octahedral center and the 3d degenerate orbitals of Mn are strongly hybridized with the 2p orbitals of O [38, 39]; which can explain the irregular variations in the Mn-O bonds with respect to the composition.

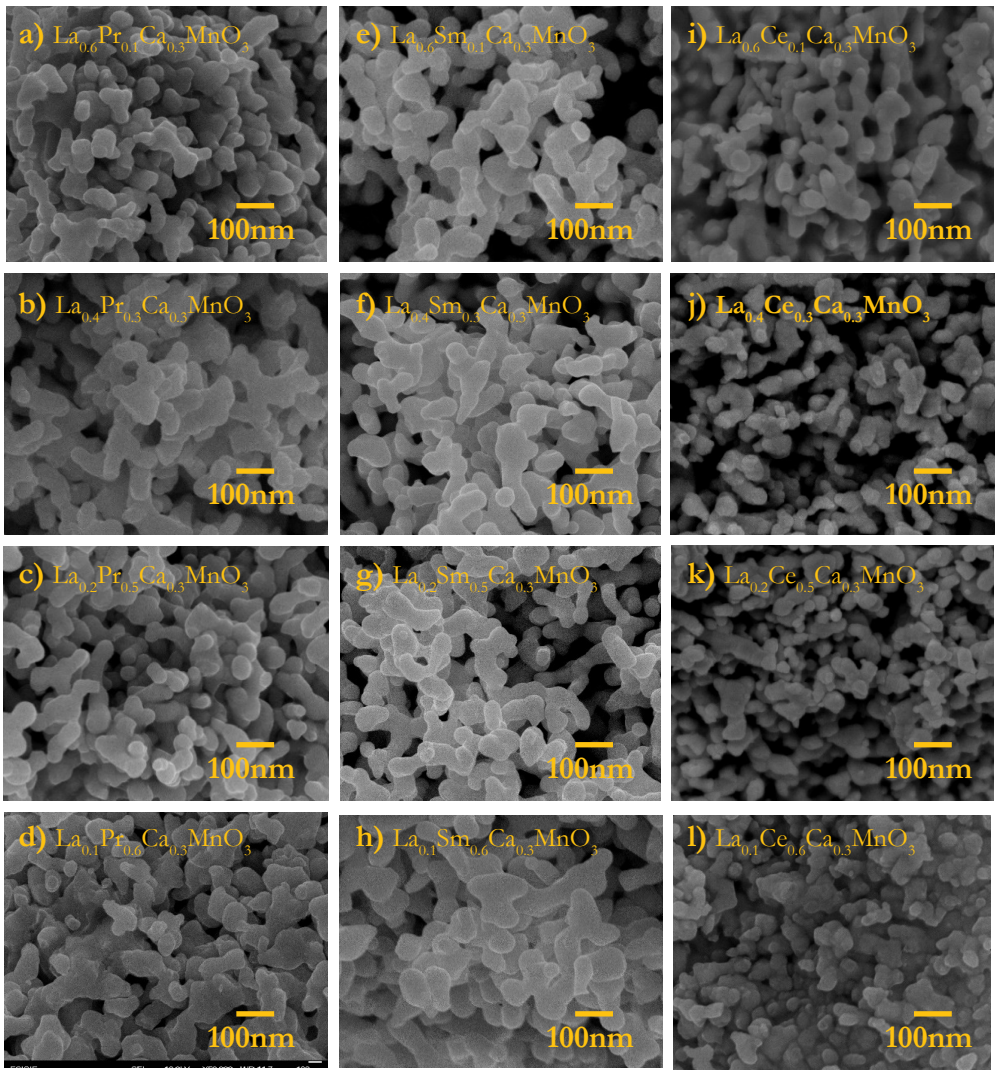

Figure 3. SEM observations for a-d) $La_{0.7-x}Pr_xCa_{0.3}MnO_3$, e-h) $La_{0.7-x}Sm_xCa_{0.3}MnO_3$ and, i-l) $La_{0.7-x}Ce_xCa_{0.3}MnO_3$ powders (x= 0.1, 0.3, 0.5, 0.6) after sintering process at 1000 °C.

The morphological analysis of the $La_{0.7-x}Pr_xCa_{0.3}$, $La_{0.7-x}Sm_xCa_{0.3}MnO_3$ and, $La_{0.7-x}Ce_xCa_{0.3}MnO_3$ powders sintered at 1000 °C can be seen in the Figure 2 a-l. From the micrographs, it is evident that that all samples present a granular structure, however a more compact morphology was obtained with the addition of

larger quantities of Pr, Sm or Ce ions. As a consequence, it can be observed that these assemblies present a less porous structure with well-connected agglomerate nanoparticles in the submicron size, which conditioned the gas diffusion towards the triple point boundary. Different materials with a similar microstructure have been reported indicating that they may be a suitable material for SOFC cathode at intermediate temperatures.

The electrical performance was analyzed using four-point probe, which is a common technique for evaluating the resistivity value of a layer in conductive nanomaterials that can be used in electrical devices. Then, measurements were carried out on green and sintered pellets (1 cm in diameter, 1000 °C, 4 h). Table 3 shows the parameters obtained to analyze the electrical performance in the perovskite-type nanostructures depending on the composition and ion substitution, as well as the potential application in SOFCs.

Table 3. Results obtained by the four-point probe.

Perovskite		Resistance (Ω sq^{-1})	Resistivity (Ω cm)	Conductivity (10^{-4} S cm^{-1})
$La_{0.7-x}Pr_xCa_{0.3}MnO_3$	0.1	36.6	4.76	2100.8
	0.3	35.5	4.54	2158.9
	0.5	79.7	10.30	970.8
	0.6	78.2	9.81	977.9
$La_{0.7-x}Sm_xCa_{0.3}MnO_3$	0.1	64	9.83	1017.1
	0.3	22.9	3.56	2803.3
	0.5	18.5	4.84	2064.3
	0.6	35.2	9.19	1087.5
$La_{0.7-x}Ce_xCa_{0.3}MnO_3$	0.1	28.8	3.80	2630.4
	0.3	26.4	3.46	2884.7
	0.5	---	---	---
	0.6	15.1	1.97	5070.2

The obtained values of conductivity for the praseodymium nanostructures are observed between 0.09 to 0.21 Scm^{-1}. For the Samarium samples, values from 0.10 to 0.28 Scm^{-1} were obtained. To the Cerium, the results present conductivity in a range of 0.26 to 0.5 Scm^{-1}. In general, the highest conductivity in the case of La substitution in the nanocomposites was observed with Pr and Sm at a composition of x = 0.3, showing a decrease in the values when the amount of the cation is higher. On the contrary, the behavior observed for Ce substituted

lanthanum, presents a tendency related to the doping applied, with the highest value reported at x=0.6 (0.5 Scm^{-1}). Previously, it has been found that in lanthanum-strontium-manganese (LSM) perovskites, the incorporation of Sr^{+2} in the ABO_3-type structure favors conductivity in relation to the amount of doping used, obtaining values in intervals greater than 200 Scm^{-1} with temperatures between 600-900 °C [39]. This behavior occurs at the expense of an increase in the content of Mn^{4+} in the final structure. Then, considering that measurements have been realized at room temperature and an important increased with the operating temperature of SOFCs is expected, the synthesized nanomaterials can be an alternative for scalable applications.

4. Conclusions

In this work, the synthesis of ABO_3-type perovskites has been analyzed, particularly $LaMnO_3$ nanoparticles by doping the A-site with other rare earth, as an efficient alternative cathode material for SOFCs. Then, this research reports the synthesis of rare earth cathode electrode materials, $La_{(1-x)}Ln_xCa_{0.3}MnO_3$, by the Pechini method, using different stoichiometries in molar ratios (x=0.1, 0.3, 0.5 and 0.6; Ln=Ce, Sm, Pr). From the above results the following results can be mentioned:

According to the crystallographic chart PDF490416, the observed signals are the characteristics of nanomaterials with an orthorhombic phase. XRD analyzes were performed before applying the heat treatment; however, the spectra did not show any representative signal of the sample, so it is concluded that the applied temperature is what leads to the formation of the desired nanostructured perovskite. From the results obtained through the Scherrer's equation for the crystallite size, it was observed that they present average values greater than 50 nm, but according to the consulted literature, they are within the reported interval.

After the Rietveld analysis, information was obtained on the unit cell of the perovskite type nanomaterial, the results represented a variation in the site occupation factor that was reflected in a correlation between the occupation and the molar quantity of these elements. It was determined that the unit cell of the synthesized nanomaterials is orthorhombic, regardless of the amount of cation (Pr, Sm, Ce) used and presenting a pure phase. The drawing of the cell with the values obtained for the lattice parameters *a*, *b*, *c* shows a distortion and cell

volume that depends on the ionic radii as well as the amount of the rare cation that replaces La. The observed micrographs show that the growth of the nanostructures is similar even when their stoichiometric ratio changes, being almost entirely homogeneous.

The values obtained by the four-point probe method did not show a clear trend; however, it is possible to appreciate that Sm (2803.3 x 10-4 S cm^{-1}) and Pr (2158.9 x 10-4 S cm^{-1}) at x=0.3 and displayed high conductivities whereas the highest electrical properties for Ce is observed at x=0.6. Test at high temperatures to evaluate coefficient of thermal expansion and electrochemical performance are ongoing to confirm this trend.

Acknowledgement

Jessica Ramírez-Hernández is grateful to CONACYT for her fellowship, Tecnológico Nacional de México, Instituto Tecnológico de Ciudad Madero.

Funding

The authors are thankful for the financial support provided by Instituto Politécnico Nacional through the SIP projects: 2023-0839, 2023-0842, 2022-1153, 2022-1155, and COFAA. This work has been also founded by SNI-CONACyT.

References

1. Selmi, T., Khadhraoui, A., & Cherif, A. (2022). Fuel cell–based electric vehicles technologies and challenges. *Environmental Science and Pollution Research*, 29, 78121-78131. https://doi.org/10.1007/s11356-022-23171-w

2. Fan, L., Tu, Z., & Chan, S. H. (2021). Recent development of hydrogen and fuel cell technologies: A review. *Energy Reports*, 7, 8421-8446. https://doi.org/10.1016/j.egyr.2021.08.003

3. Raza, T., Yang, J., Wang, R., Xia, C., Raza, R., Zhu, B. *et al.* (2022). Recent advance in physical description and material development for single component SOFC: A mini-review. *Chemical Engineering Journal*, 444, 136533. https://doi.org/10.1016/j.cej.2022.136533

4. Ahmad, M. Z., Ahmad, S. H., Chen, R. S., Ismail, A. F., Hazan, R. *et al.* (2022). Review on recent advancement in cathode material for lower and intermediate temperature solid oxide fuel cells application. *International Journal of Hydrogen Energy*, 47(2), 1103-1120. https://doi.org/10.1016/j.ijhydene.2021.10.094

5. Hauch, A., Küngas, R., Blennow, P., Hansen, A. B., Hansen, J. B., Mathiesen, B. V. *et al.* (2020) Recent advances in solid oxide cell technology for electrolysis. *Science*, 370(6513), aba6118. https://doi.org/10.1126/science.aba6118

6. Wang, M., & Feng, Z. (2021). Interfacial processes in electrochemical energy systems. *Chemical Communications*, 57, 10453-10468. https://doi.org/10.1039/D1CC01703A

7. Papac, M., Stevanović, V., Zakutayev, A., & Hayre, R. O'. (2020). Triple ionic–electronic conducting oxides for next-generation electrochemical devices. *Nature Materials*, 20, 301-313. https://doi.org/10.1038/s41563-020-00854-8

8. Sun, C., Alonso, J. A., & Bian, J. (2021). Recent Advances in Perovskite-Type Oxides for Energy Conversion and Storage Applications. *Advanced Energy Materials*, 11(2), 2000459. https://doi.org/10.1002/aenm.202000459

9. Abd Aziz, A. J., Baharuddin, N. A., Somalu, M. R., & Muchtar, A. (2020). Review of composite cathodes for intermediate-temperature solid oxide fuel cell applications. *Ceramics International*, 46(15), 23314-23325. https://doi.org/10.1016/j.ceramint.2020.06.176

10. Afroze, S., Reza, Md. S., Amin, M. R., Taweekun, J., & Azad, A. (2022). Progress in nanomaterials fabrication and their prospects in artificial intelligence towards solid oxide fuel cells: A review. *International Journal of Hydrogen Energy*. https://doi.org/10.1016/j.ijhydene.2022.11.335

11. Singh, M., Zappa, D., & Comini, E. (2021). Solid oxide fuel cell: Decade of progress, future perspectives and challenges. *International Journal of Hydrogen Energy*, 46(54), 27643-27674. https://doi.org/10.1016/j.ijhydene.2021.06.020

12. Gunkel, F., Christensen, D. V., Chen, Y. Z., & Pryds, N. (2020). Oxygen vacancies: The (in)visible friend of oxide electronics. *Applied Physics Letters*, 116, 120505. https://doi.org/10.1063/1.5143309

13. Zarabi Golkhatmi, S., Asghar, M. I., & Lund, P. D. (2022). A review on solid oxide fuel cell durability: Latest progress, mechanisms, and study tools. *Renewable and Sustainable Energy Reviews*, 161, 112339. https://doi.org/10.1016/j.rser.2022.112339

14. Tarancón, A., Burriel, M., Santiso, J., Skinner, S. J., & Kilner, J. A. (2010). Advances in layered oxide cathodes for intermediate temperature solid oxide fuel cells. *Journal of Materials Chemistry*, 19, 3799-3813. https://doi.org/10.1039/b922430k

15. Sreedhar, I., Agarwal, B., Goyal, P., & Agarwal, A. (2020). An overview of degradation in solid oxide fuel cells-potential clean power sources. *Journal of Solid State Electrochemistry*, 24, 1239-1270. https://doi.org/10.1007/s10008-020-04584-4

16. Ko, H. J., Myung, J.-h., Hyun, S.-H., & Chung, J. S. (2012). Synthesis of LSM–YSZ–GDC dual composite SOFC cathodes for high-performance power-generation systems. *Journal of Applied Electrochemistry*, 42, 209-215. https://doi.org/10.1007/s10008-020-04584-4

17. Rashidian Vaziri, M. R., Hajiesmaeilbaigi, F., & Maleki, M. H. (2011). Monte Carlo simulation of the subsurface growth mode during pulsed laser deposition. *Journal of Applied Physics*, 110, 043304. https://doi.org/10.1063/1.3624768

18. Xia, W., Wu, H., Xue, P., & Zhu, X. (2018). Microstructural, Magnetic, and Optical Properties of Pr-Doped Perovskite Manganite $La_{0.67}Ca_{0.33}MnO_3$ Nanoparticles Synthesized via Sol-Gel Process. *Nanoscale Research Letters*, 13, 135. https://doi.org/10.1186/s11671-018-2553-y

19. Baharuddin, N. A., Muchtar, A., Somalu, M. R., Anwar, M., Hameed, M. A. S. A. K. A., & Mah, J. (2017). Effects of sintering temperature on the structural and electrochemical properties of $SrFe_{0.5}Ti_{0.5}O_{3-\delta}$ perovskite cathode. *International Journal of Applied Ceramic Technology*, 15(2), 338-348. https://doi.org/10.1111/ijac.12825

20. da Conceição, L., Silva, C. R. B., Ribeiro, N. F. P., & Souza, M. M. V. M. (2009). Influence of the synthesis method on the porosity, microstructure and electrical properties of $La_{0.7}Sr_{0.3}MnO_3$ cathode materials. *Materials Characterization*, 60(12), 1417-1423. https://doi.org/10.1016/j.matchar.2009.06.017

21. Vismaya, J., Vinaya, J., Clementz Edwardraj, F. C., & Arputharaj S. N. (2022). Spinel-based electrode materials for application in electrochemical supercapacitors – present status and future prospects. *Inorganic and Nano-Metal Chemistry*, 52, 1449-1462. https://doi.org/10.1080/24701556.2021.1956968

22. Hwang, L., Heuer, A. H., & Mitchell, T. E. (1973). On the space group of $MgAl_2O_4$ spinel. *Philosophical Magazine*, 28, 241-243. https://doi.org/10.1080/14786437308217448

23. Zhang, Y., Yang, G., Chen, G., Ran, R., Zhou, W., & Shao, Z. (2016). Evaluation of the CO_2 Poisoning Effect on a Highly Active Cathode $SrSc_{0.175}Nb_{0.025}Co_{0.8}O_{3-\delta}$ in the Oxygen Reduction Reaction. *ACS Applied Materials & Interfaces*, 8(5), 3003-3011. https://doi.org/10.1021/acsami.5b09780

24. Jain, U., Soni, S., & Chauhan, N. (2022). Application of perovskites in bioimaging: the state-of-the-art and future developments. *Expert Review of Molecular Diagnostics*, 22(9), 867-880. https://doi.org/10.1080/14737159.2022.2135990

25. Ko, M.-H., Yoo, Y.-S., & Hwang, J.-H. (2015). Electrochemical estimation of GBCO(GdBaCo2O5+δ)/GDC(Gd_2O_3-doped CeO_2) cathode composites designed for intermediate-temperature solid oxide electrochemical cells. *Ceramics International*, 41(3), 4616-4620. https://doi.org/10.1016/j.ceramint.2014.12.005

26. Bhalla, A. S., Guo, R., & Roy, R. (2000). The Perovskite Structure – A Review of Its Role in Ceramic Science and Technology. *Material Research Innovations*, 4(1), 3-26. https://doi.org/10.1007/s100190000062

27. Frozandeh-Mehr, E., Malekzadeh, A., Ghiasi, M., Gholizadeh, A., Mortazavi, Y., & Khodadadi, A. (2012). Effect of partial substitution of lanthanum by strontium or bismuth on structural features of the lanthanum manganite nanoparticles as a catalyst for carbon monoxide oxidation. *Catalysis Communications*, 28, 32-37. https://doi.org/10.1016/j.catcom.2012.08.009

28. Solanki, S., Dhruv, D., Boricha, H., Zankat, A., Rathod, K. N., Rajyaguru, B. *et al.* (2020). Charge transport mechanisms and magnetoresistance behavior of $La_{0.6}Pr_{0.1}Ca_{0.3}MnO_3$ manganite. *Journal of Solid State Chemistry*, 288, 121446. https://doi.org/10.1016/j.jssc.2020.121446

29. Ferrel-Alvarez, A. C., Domínguez-Crespo, M. A., Cong, H., Torres-Huerta, A. M., Palma-Ramírez, D., & Irvine, J. T. S. (2021). Microwave irradiation synthesis to obtain La0.7-xPrxCa0.3MnO3 perovskites: Electrical and electrochemical performance. *Journal of Alloys and Compounds*, 851, 156882. https://doi.org/10.1016/j.jssc.2020.121446

30. Chourasia, R., & Shrivastava, O. P. (2012). Crystal structure and impedance study of samarium substituted perovskite: $La_{1-x}Sm_xMnO_3$ (x=0.1-0.3). *Solid State Sciences*, 14(3), 341-348. https://doi.org/10.1016/j.solidstatesciences.2011.12.007

31. Gu, Q., Wang, L., Wang, Y., & Li, X. (2019). Effect of praseodymium substitution on $La_{1-x}Pr_xMnO_3$ (x=0–0.4) perovskites and catalytic activity for NO oxidation. *Journal of Physics and Chemistry of Solids*, 133, 52-58. https://doi.org/10.1016/j.solidstatesciences.2011.12.007

32. Li, W., Xiong, C. Y., Jia, L. C., Pu, J., Chi, B., Chen, X. *et al.* (2015). Strontium-doped samarium manganite as cathode materials for oxygen reduction reaction in solid oxide fuel cells. *Journal of Power Sources*, 284, 272-278. https://doi.org/10.1016/j.solidstatesciences.2011.12.007

33. Hammond, C. (2015). Chapter 4. Crystal symmetry: point groups, space groups, symmetry-related properties and quasiperiodic crystals. In: C. Hammond (Ed.). The Basics of Crystallography and Diffraction. *Oxford University Press*. https://doi.org/10.1093/acprof:oso/9780198738671.003.0004

34. Ostroushko, A. A., Russkikh, O. V., & Maksimchuk, T. Y. (2021). Charge generation during the synthesis of doped lanthanum manganites via combustion of organo-inorganic precursors. *Ceramics International*, 47(15), 21905-21914. https://doi.org/10.1093/acprof:oso/9780198738671.003.0004

35. Dinamarca, R., Sepúlveda, C., Delgado, E. J., Peña, O., Fierro, J. L. G., & Pecchi, G. (2016). Electronic properties and catalytic performance for DME combustion of lanthanum manganites with partial B-site substitution. *Journal of Catalysis*, 338, 47-55. https://doi.org/10.1016/j.jcat.2016.02.011

36. Yue, C., Zhang, W., Wang, M., Liu, J., Zhang, J., & Hou, D. (2022). Crystal structure and octahedral deformation of orthorhombic perovskite ABO_3: Case study of $SrRuO_3$. *Journal of Solid State Chemistry*, 309, 122998. https://doi.org/10.1016/j.jssc.2022.122998

37. Nagaraja, B. S., Rao, A., Babu, P. D., & Okram, G. S. (2015). Structural, electrical, magnetic and thermal properties of $Gd_{1-x}Sr_xMnO_3$ ($0.2 \leq x \leq 0.5$) manganites. *Physica B: Condensed Matter*, 479, 10-20. https://doi.org/10.1016/j.jssc.2022.122998

38. Kamboj, V., & Ranjan, C. (2022). Chapter 11. Oxygen reduction reaction in solid oxide fuel cells. In: K. Sengupta, S. Chatterjee, K. Dutta (Eds.) *Oxygen Reduction Reaction*. Elsevier, pp. 379-426.
https://doi.org/10.1016/j.jssc.2022.122998

39. Moriche, R., Marrero-López, D., Gotor, F. J., & Sayagués, M. J. (2014). Chemical and electrical properties of LSM cathodes prepared by mechanosynthesis. *Journal of Power Sources*, 252, 43-50.
https://doi.org/10.1016/j.jpowsour.2013.11.093

CHAPTER 4 ENERGY AREA

PHOTOCATALYTIC GENERATION OF HYDROGEN USING TITANIUM AND BISMUTH OXIDE CATALYSTS

J. O. Peralta-Cruz[1], M. L. Hernández-Pichardo[1*], P. del Angel-Vicente[2]

[1] Instituto Politécnico Nacional, ESIQIE, Laboratorio de nanomateriales sustentables; Av. IPN S/N Col. Zacatenco, 07738, México City, México.

[2] Instituto Mexicano del Petróleo, Dirección de Investigación y Posgrado, Eje Central L. Cárdenas 152, 07730 México City, México.

mhernandezp@ipn.mx

Peralta-Cruz, J. O., Hernández-Pichardo, M. L., & del Angel-Vicente, P. (2023). Photocatalytic generation of hydrogen using titanium and bismuth oxide catalysts. In E. San Martín-Martínez (Ed.). *Research advances in nanosciences, micro and nanotechnologies. Volume IV* (pp. 213-230). Barcelona, Spain: Omniascience.

Abstract

Bismuth-based photocatalysts were prepared by a hydrothermal method. The binary $Bi_2Ti_2O_7/Bi_4Ti_3O_{12}$ nanocomposite was obtained by the coupling of both semiconductors. The heterojunction allows an efficient hydrogen generation under UV irradiation, which is superior to the TiO_2 and the Bi_2O_3 oxides. The interfaces observed by HRTEM are possibly in favor of the photoinduced-carriers transport between both semiconductors, assisting the separation of photogenerated electrons and holes. The enhanced photocatalytic hydrogen evolution activity was attributed to an increase of light absorption to generate more photoelectrons and an improved separation of photoinduced electrons and holes, which arises from the internal electric field formed by the heterojunction between $Bi_2Ti_2O_7$ and $Bi_4Ti_3O_{12}$.

Keywords: Hydrogen, photocatalysis, titanium oxide, bismuth oxide, $Bi_2Ti_2O_7/Bi_4Ti_3O_{12}$ nanocomposite.

1. Introduction

The United Nations estimates that the world population will increase by almost 2 billion in the next 30 years. Due to this increase in population and the economic growth associated, it is projected that global energy consumption will increase 2-fold by the midcentury [1]. These human activities will inevitably impact the environment without counting the imminent depletion of fossil fuels. Thus, the serious problem of environmental pollution coupled with the current energy crisis makes the development of clean and renewable energy sources a priority [2].

Therefore, one of the main global challenges is to find a sustainable energy source. Hydrogen, as a carbon-neutral energy carrier, is considered an environmentally friendly and regenerative energy vector [3]. However, most of the hydrogen presently generated is not coming from a clean energy source; the most common is gray or black hydrogen which is neither environmentally friendly nor economical [4, 5]. On the other hand, green hydrogen is produced from a clean source and is a more sustainable alternative. In this sense, solar energy is the most promising exploitable resource since it can provide the energy needed by humans in a year, just in one hour [1]. Thus, hydrogen production from water and solar energy by using a semiconductor is a promising idea that has attracted increasing attention [6, 7]. Photocatalytic production of hydrogen is one of the most promising ways, and the key part of this process is the development of active photocatalysts toward H_2 or O_2 evolution reactions under visible light.

Titanium dioxide (TiO_2) is one of the most widely used semiconductors in photocatalytic processes due to its ability to decompose pollutants into non-toxic substances related to its potential for the formation of photogenerated electrons and holes [8]. Nevertheless, the main drawbacks are wide band gap energy, high recombination of electron-hole pairs generated from visible light, as well as its low quantum efficiency [9]. Then, many efforts have been devoted to improving its efficacy. In this sense, TiO_2 nanostructures to increase the effective photocatalytic surface through the formation of Schottky junctions or heterojunctions have recently been developed [3].

In this regard, bismuth-based photocatalysts are good options for visible-light-driven catalysts [10 – 16]. Among them, bismuth titanates such as $Bi_2Ti_2O_7$ and $Bi_4Ti_3O_{12}$ are part of a large Bi–Ti–O family that have been shown to be effective UV-vis-light photocatalysts [12]. Both materials present a layered

perovskite structure and exhibit good photocatalytic activity due to their adequate bandgap energy and high electron-hole pair separation efficiency. $Bi_2Ti_2O_7$ possesses a bandgap energy of around 2.8 eV [14], which makes it suitable for the photocatalytic splitting of water and degradation of organic contaminants under ultraviolet light irradiation. Meanwhile, $Bi_4Ti_3O_{12}$, on the other hand, has a lower bandgap energy of around 2.9 eV [17], which allows it to respond to visible light in addition to ultraviolet light. It has been used for a variety of photocatalytic applications, including pollutant degradation, water splitting, and CO_2 reduction. Recent studies have shown that combining $Bi_2Ti_2O_7$ and $Bi_4Ti_3O_{12}$ can further enhance their photocatalytic performance, leading to better hydrogen evolution [18]. In this work, we describe the preparation of bismuth-based photocatalysts through and hydrothermal method. The $Bi_2Ti_2O_7/Bi_4Ti_3O_{12}$ heterojunction increased the generation of hydrogen through the improvement of charge separation of photogenerated charge carriers.

2. Experimental Methodology

2.1. *Photocatalysts Preparation*

2.1.1. Synthesis of the Bi_2O_3 by the hydrothermal method

The preparation of the bismuth oxides photocatalyst was done by using bismuth (III) chloride ($BiCl_3$, analytical grade, 98 %) as the precursor, which is dispersed in an aqueous sodium hydroxide solution (1.5 M). Then the hydrothermal process was carried out, transferring the solution to a 100 mL Teflon-lined stainless-steel autoclave at a constant temperature of 220 °C for 18 h. Once the hydrothermal process is complete, the autoclave is allowed to cool down to a temperature of 20 °C. The precipitate is collected by centrifugation for 20 min to separate the product formed. The product was washed with distilled water and finally dried at 100 °C for 6 h.

2.1.2. Synthesis of the $Bi_2Ti_2O_7/Bi_4Ti_3O_{12}$ nanocomposite

$Bi_2Ti_2O_7/Bi_4Ti_3O_{12}$ nanocomposite was prepared using bismuth (III) chloride ($BiCl_3$, analytical grade, 98 %) and titanium (IV) oxide (TiO_2, analytical grade, nanopowder, 21 nm primary particle size (TEM), ≥99.5 %) both dispersed in a caustic soda solution (1.5 M). The solution is transferred to a 100 mL Teflon-lined

stainless-steel autoclave and maintained at a constant temperature of 220 °C for a period of 18 h. Once the reaction is complete, the autoclave is allowed to cool to room temperature naturally. The precipitate is collected by centrifugation for 20 minutes at 7000 rpm to separate the product formed. The product was washed with distilled water and finally dried at 100 °C for 6 h. This sample was identified as BT2/BT4.

2.2. *Samples characterization*

The samples were characterized by X-ray diffraction by using a RIGAKU Miniflex 600 diffractometer with an X-ray tube with CuKα radiation (λ=1.5418 Å) with linear focus. The power used is 40 kV and 15 mA. An area Dtex high-speed detector is used to obtain high-quality diffraction patterns in less time. The step size is 0.02, and the speed is 5 °/min.

To carry out the X-ray photoelectric spectroscopy (XPS) analysis, a Thermo Scientific K-Alpha equipment with an AlK α source and a monochromator was used. The general spectra are obtained using a step energy of 160 eV and 60 eV for the high-resolution spectra using a load compensation system. Raman spectroscopy analyses were carried out using a HORIBA, Jobin Yvon spectrometer equipped with a CCD detector using a helium-neon laser (wavelength 633 nm). The UV-vis spectroscopy analysis was performed using a Perkin Elmer Lambda 365 UV-Vis equipment at 200-800 nm wavelength.

Finally, the samples were studied by high-resolution transmission electron microscopy (HRTEM), and the micrographs were obtained in a TITAN 80-300 with Schottky-type field emission gun operating at 300 kV. The point resolution and the information limit were better than 0.085 nm. HRTEM digital images were obtained using a CCD camera and Digital Micrograph Software from GATAN. In order to prepare the materials for observation, the powder samples were ultrasonically dispersed in ethanol and supported on holey carbon-coated copper grids.

2.3. *Photocatalytic Test for hydrogen production*

The photocatalytic behavior of the samples for the generation of H_2 was carried out using a water/methanol solution under UV irradiation. In a typical experiment, 0.01 g of the photocatalyst is dispersed in 150 mL of the water/methanol (1:1 volume) solution. The reactor is closed and irradiated with a Pen

Ray Hg UV lamp (254 nm, 4.4 mW/cm^2). The products were identified using a Perkin-Elmer model Clarus 480 chromatograph.

3. Results and discussion

3.1. *Physicochemical characterization of the samples*

Samples of bismuth oxide (Bi_2O_3) and the hybrid nanocomposite $Bi_2Ti_2O_7$/$Bi_4Ti_3O_{12}$ (BT2/BT4) were synthesized. The results were compared with commercial TiO_2. Figure 1 shows the diffraction patterns of the pure oxides of TiO_2 and Bi_2O_3. In the TiO_2 sample (Figure 1a), the diffraction peaks are identified as the anatase and rutile phases [19], while for the Bi_2O_3 sample (Figure 1b), the peaks were identified as the monoclinic (α- Bi_2O_3) and tetragonal (β- Bi_2O_3) phases [20].

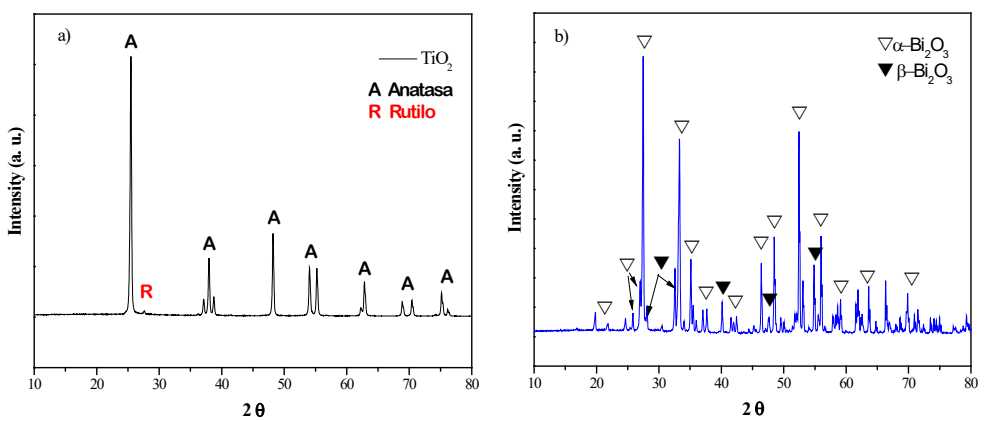

Figure 1. Diffraction patterns for the pristine oxides: a) TiO_2 and b) Bi_2O_3.

Also, Figure 2 shows the diffraction patterns of the three samples of TiO_2, Bi_2O_3, and BT2/BT4 in order to show the formation of the new bismuth titanate phases clearly. In the BT2/BT4 sample, the peaks corresponding to the cubic phases of $Bi_2Ti_2O_7$ (JCPDS-32-0118) and orthorhombic perovskite of $Bi_4Ti_3O_{12}$ (JCPDS-35-0795) [21] appear. The simultaneous presence of all the diffraction peaks of the $Bi_2Ti_2O_7$/$Bi_4Ti_3O_{12}$ phases in the BT2/BT4 sample indicates the formation of the nanocomposite. The fraction of the $Bi_4Ti_3O_{12}$ phase in BT2/BT4 was estimated using the Match ® program, and it was found that 56.9 % corresponds to $Bi_4Ti_3O_{12}$, while 43.1 % was assigned to the formation of $Bi_2Ti_2O_7$.

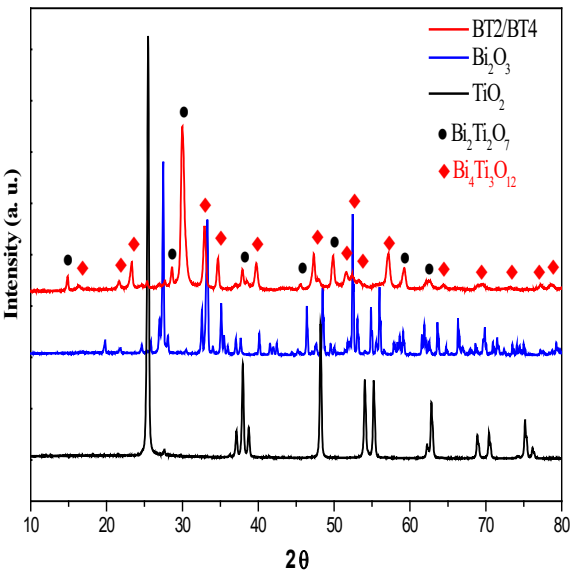

Figure 2. Comparison of the diffraction patterns of the individual oxides with the nanocomposite formed $Bi_2Ti_2O_7/Bi_4Ti_3O_{12}$ (BT2/BT4).

The surface composition and analysis of the chemical states of the BT2/BT4 hybrid composite were analyzed by XPS (Figure 3). Figure 3a shows the survey spectrum of the BT2/BT4 sample in which the peaks of the elements Bi, Ti, and O are observed. Likewise, the high-resolution spectra in the Bi 4f, Ti 2p, Bi 4d regions, and O 1s are shown in Figures 3b to 3d.

The high-resolution spectrum in the Bi 4f region is shown in Figure 3b. The presence of two peaks at 163.9 and 158.6 eV corresponding to the Bi $4f_{5/2}$ and $4f_{7/2}$ signals, respectively, indicating the presence of Bi^{3+} [20], is observed. In Figure 3c, the maximum signal of Ti $2p_{3/2}$ is observed at 457.5 eV, while the maximum signal of Ti $2p_{1/2}$ at 463.6 eV is partially covered by the maximum signal of Bi $4d_{3/2}$ at 465.7 eV, which leads to an overall maximum signal at about 465.5 eV. As shown in Figure 3d, the maximum signals at 529.26 eV and 531.08 eV are assigned to lattice oxygen and adsorbed oxygen. Therefore, with the previous results, there is evidence of the formation and presence of bismuth titanate on the catalyst surface.

Raman spectroscopy was used to verify the structure of the nanomaterials. Figure 4 shows the Raman spectrum of Bi_2O_3 between 100 and 700 cm^{-1} . It is observed that the spectrum presents many signals because α-Bi_2O_3 is a double

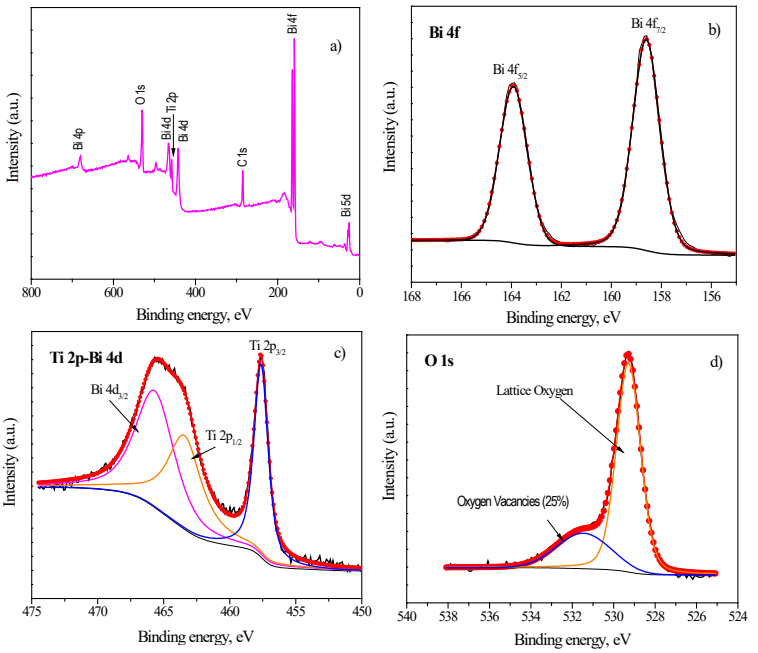

Figure 3. XPS spectra of the BT2/BT4 composite: a) Survey spectrum, b) Bi 4f region, c) Ti 2p-Bi 4d region, and d) O 1s region.

refraction biaxial crystal with a lower symmetry of the monoclinic structure. Ten typical Bi_2O_3 Raman peaks are observed above 100 cm^{-1} [22], confirming the formation of monoclinic α-Bi_2O_3. The mode at 119 cm^{-1} comes from the Ag symmetry caused mainly by the participation of Bi atoms. The 138 (Ag) and 153 cm^{-1} (Bg) modes can come from the displacements of the Bi and O atoms in the α-Bi_2O_3 lattice.

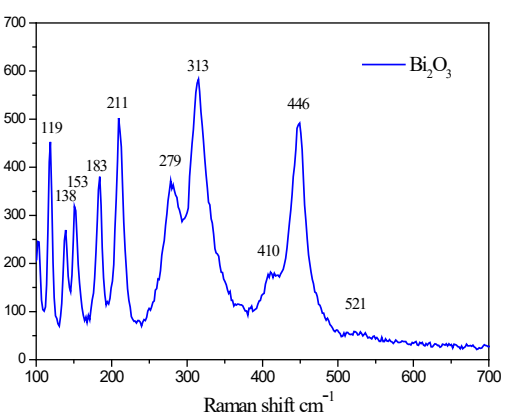

Figure 4. Raman spectra of Bi_2O_3 in the range of 100 to 700 cm-1.

On the other hand, Figure 5 shows the Raman spectrum of TiO_2 between 100 and 700 cm^{-1}. Four characteristic Raman active modes of anatase TiO_2 were observed with symmetries Eg, B1g, A1g, and Eg at 142, 394, 515, and 639 cm^{-1}, respectively, corresponding to the anatase TiO_2 phase [23]. No peaks corresponding to the formation of traces of rutile were observed due to the low amount of this phase in the material.

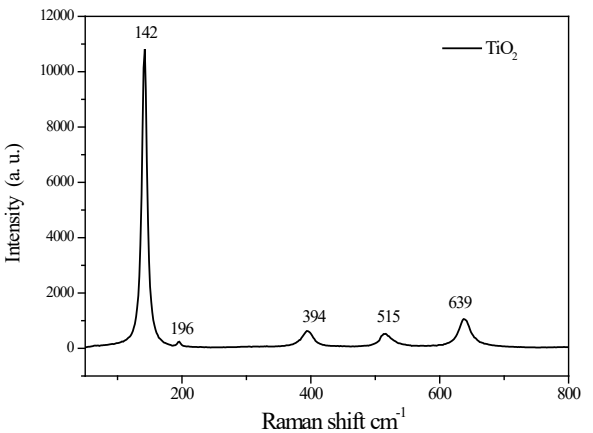

Figure 5. Raman spectra of TiO_2 in the range from 100 to 700 cm^{-1}.

Finally, Figure 6 shows the Raman spectrum of the BT2/BT4 composite between 100 and 1000 cm^{-1}. The spectrum exhibits signals at approximately 117, 142, 229, 271, 323, 537, 566, 617, and 850 cm^{-1}, which are attributed to the internal vibrational modes of $Bi_4Ti_3O_{12}$ [23]. The signals corresponding to $Bi_2Ti_2O_7$ were not observed since they overlap with the other titanate, $Bi_4Ti_3O_{12}$ [24].

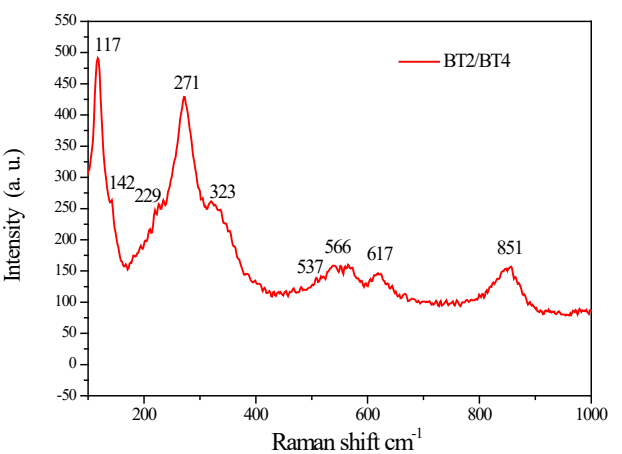

Figure 6. Raman spectra of composite BT2/BT4 in the range of 100 to 900 cm-1.

On the other hand, Figures 7a and 8a show the UV-vis absorption spectra of Bi_2O_3 and the BT2/BT4 composite, respectively, in the wavelength range of 200 to 800 nm in which deionized water has been used as a reference solvent. The optical bandgap has been calculated using the formula of the Tauc method, which relates the optical bandgap (Eg) to the absorption coefficient F(R) and the photon energy (hν) with respect to the relationship $(F(R)*h\nu)^n \propto (h\nu - Eg)$, where n is associated with the different types of electronic transitions, in which it can take values of 1/2 or 2 for direct and indirect transitions respectively [25]. Here we have calculated the optical band gap considering the direct transition allowed (n=1/2) because it presents the best fit to the data.

Figures 7b and 8b show a plot between F(R)*hν and the photon energy of bismuth oxide (Bi_2O_3) and the BT2/BT4 composite, respectively. The optical bandgap energy has been determined by extrapolating the linear portion of $[F(R)*h\nu]^{1/2}$ vs. hν to the x-axis (see Figures 7b and 8b). The Bi_2O_3 bandgap value

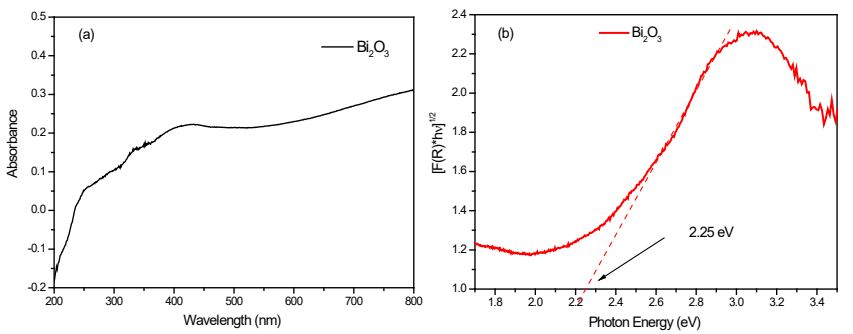

Figure 7. a) UV-vis spectra of Bi_2O_3 in the range 200 to 800 nm. b) Graph of the Tauc method for determining the optical band gap of Bi_2O_3.

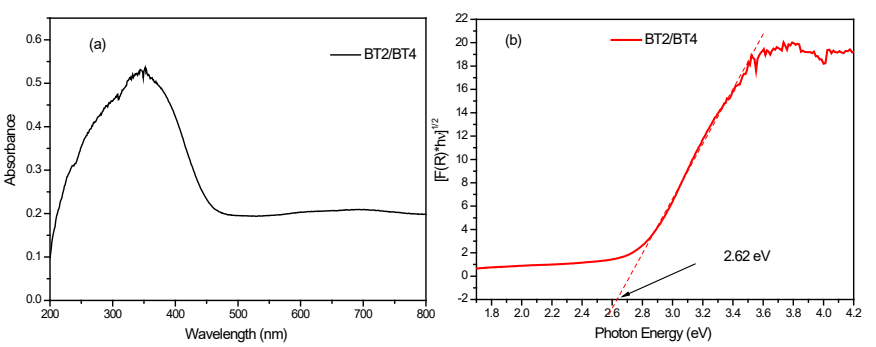

Figure 8. a) UV-vis spectra of the BT2/BT4 composite in the range 200 to 800 nm. b) Graph of the Tauc method for the determination of the optical band gap of the BT2/BT4 composite.

has been found to be 2.25 eV, while the BT2/BT4 composite shows a slightly narrower bandgap than the Bi_2O_3 nanoparticles, with a value of 2.62 eV; these values are close to the bandgap values previously reported [21, 22, 26, 27].

Finally, transmission electron microscopy indicates that the sample presents large crystals of more than 100 nm, which are in contact with nanocrystals of different sizes and shapes smaller than 30 nm, as observed in Figure 9.

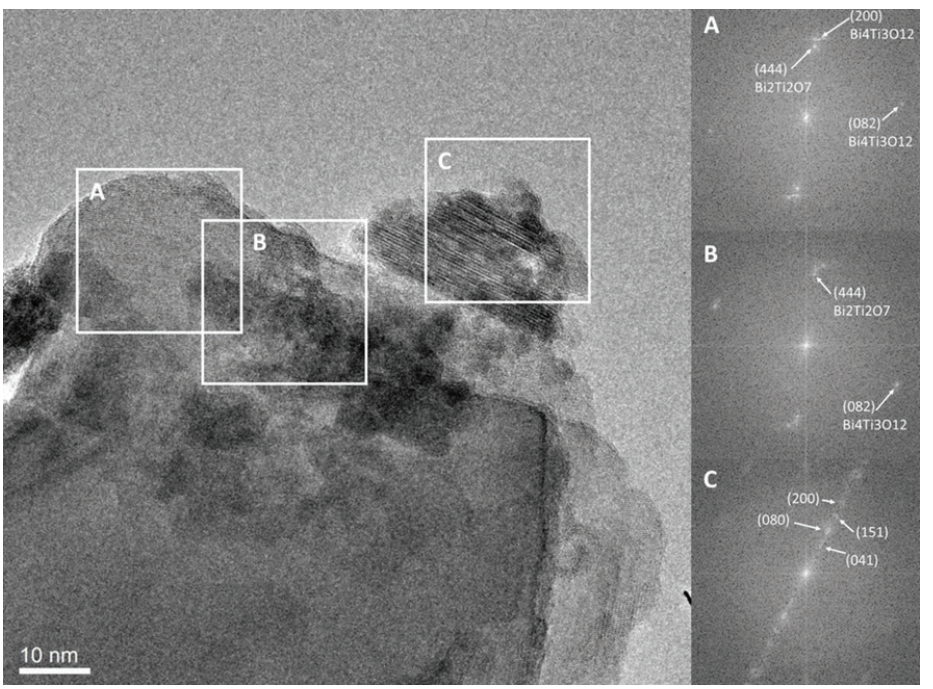

Figure 9. HRTEM image of the BT2/BT4 sample and its corresponding FFT in three zones. A) The FFT indicates that there are two phases, $Bi_2Ti_2O_7$ and $Bi_4Ti_3O_{12}$, B) The same phases were identified as $Bi_2Ti_2O_7$ and $Bi_4Ti_3O_{12}$, C) This crystal was identified as $Bi_4Ti_3O_{12}$; it is an "irregular laminar" crystal that contains planes from 5.5 Å down to less than 2 Å.

The large crystals correspond to the $Bi_2Ti_2O_7$ phase, while nanocrystals generally correspond to $Bi_4Ti_3O_{12}$. In the image, three zones were chosen, and the fast Fourier transform (FFT) of each of them was obtained. In regions A and B, the presence of both phases, $Bi_2Ti_2O_7$ and $Bi_4Ti_3O_{12}$, were identified, while in region C it was possible to analyze a single crystal with atomic planes that correspond to the $Bi_4Ti_3O_{12}$ phase. Here planes of 5.5 Å and 4.5 Å are observed, mainly observing a laminar formation. These interfaces observed by HRTEM are possibly in favor of the photoinduced-carriers transport between both semiconductors, assisting the separation of photogenerated electrons and holes.

3.2. *Photocatalytic performance of bismuth and titanium oxides for hydrogen production*

The photocatalytic performance of the TiO_2, Bi_2O_3, and BT2/BT4 composite for hydrogen production was evaluated under ultraviolet light. The obtained results are shown in Figure 10. The photocatalytic activity of these samples represents the study of four cycles, each cycle corresponding to a determined time of 1 hour, in which the photocatalytic activity of titanium oxide has been used as a reference. The results show that titanium oxide presents the lowest photocatalytic activity; despite this, it presents a constant hydrogen generation during the 4 hours. Bismuth oxide presents a better photocatalytic activity than titanium oxide; the drawback is that it presents a non-constant generation in the second cycle and stabilizes after this. Finally, the BT2/BT4 composite is the one with the highest photocatalytic performance in hydrogen generation, remaining constant during the 4 hours. This enhanced photocatalytic hydrogen evolution activity was attributed to an increase of light absorption to generate more photoelectrons and an improved separation of photoinduced electrons and holes, which arises from the internal electric field formed between the heterojunction between $Bi_2Ti_2O_7$ and $Bi_4Ti_3O_{12}$.

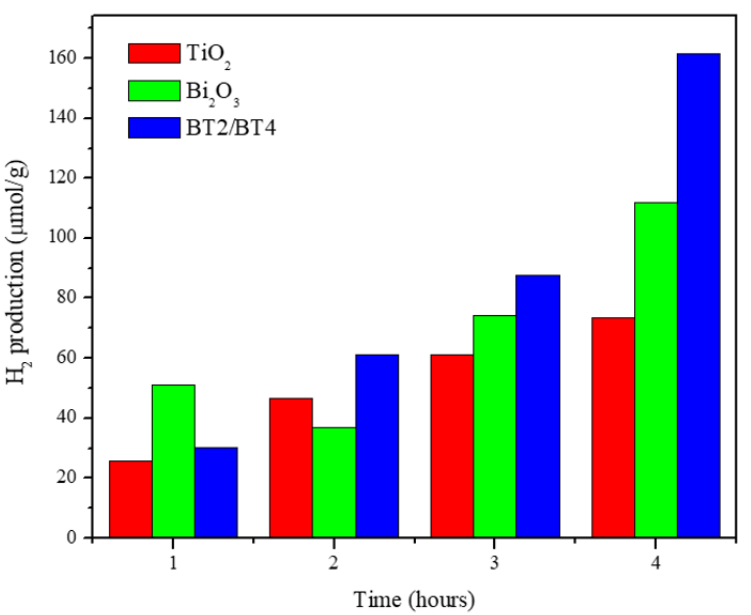

Figure 10. Hydrogen evolution amounts under UV irradiation for TiO2, Bi_2O_3, and the BT2/BT4 composite.

A possible route diagram of the $Bi_2Ti_2O_7/Bi_4Ti_3O_{12}$ composite for hydrogen evolution is shown in Figure 11. The conduction band (CB) and valence band (VB) potential of $Bi_4Ti_3O_{12}$ is more negative than that of $Bi_2Ti_2O_7$ [18]. When the composite is irradiated, producing photogenerated electrons and holes, the electrons in the CB of $Bi_4Ti_3O_{12}$ flow into the CB of $Bi_2Ti_2O_7$ due to closely contacted interfaces. The electric field formed by the heterojunction between $Bi_2Ti_2O_7$ and $Bi_4Ti_3O_{12}$ motivates the separation of the photogenerated electron-hole in both semiconductors. The hydrogen ions accept electrons and convert to hydrogen.

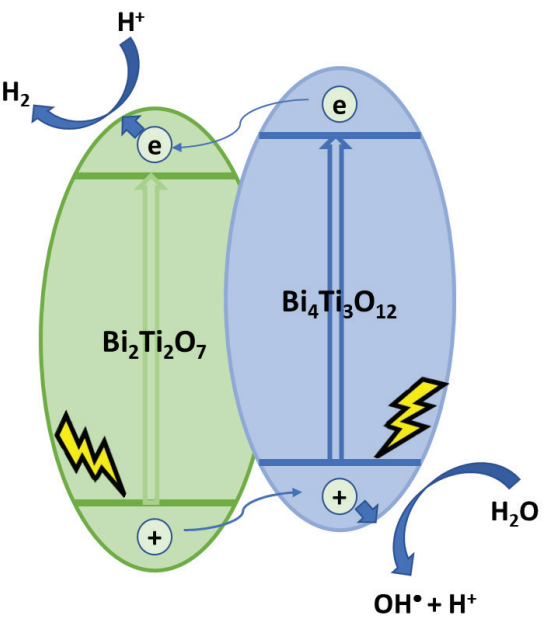

Figure 11. A possible route for the hydrogen evolution for the BT2/BT4 composite.

4. Conclusions

A $Bi_2Ti_2O_7/Bi_4Ti_3O_{12}$ composite was successfully obtained by a hydrothermal method. The composite is formed by the heterojunction of both phases in intimate contact, as XRD, Raman, XPS, and HRTEM showed. This enhanced photocatalytic hydrogen evolution activity was attributed to an increase of light absorption to generate more photoelectrons and an improved separation of photoinduced electrons and holes, which arises from the internal electric field formed by the heterojunction between $Bi_2Ti_2O_7$ and $Bi_4Ti_3O_{12}$.

Acknowledgment

The authors thank the CNMN of the Instituto Politécnico Nacional for the characterization of the samples.

Funding

This work has been supported by the multidisciplinary project IPN-SIP 20231007. JOPC thanks to CONACYT-Mexico for the doctorate fellowship (CVU: 1186295).

References

1. Lewis, N. S., & Nocera, D. G. (2006). Powering the planet: Chemical challenges in solar energy utilization. *Proceedings of the National Academy of Sciences of the United States of America*, 103(43),15729-15735. https://doi.org/10.1073/pnas.0603395103

2. Tian, J., Leng, Y., Zhao, Z., Xia, Y., Sang, Y., Hao, P. *et al.* (2015). Carbon quantum dots/hydrogenated TiO_2 nanobelt heterostructures and their broad spectrum photocatalytic properties under UV, visible, and near-infrared irradiation. *Nano Energy*, 11, 419-427. https://doi.org/10.1016/j.nanoen.2014.10.025

3. Cai, J., Huang, J., Ge, M., & Lai, Y. (2018). Multidimensional TiO_2 nanostructured catalysts for sustainable H2 generation. *Multifunctional Photocatalytic Materials for Energy*, 237-288. https://doi.org/10.1016/B978-0-08-101977-1.00012-0

4. Aditiya, H. B., & Aziz, M. (2021). Prospect of hydrogen energy in Asia-Pacific: A perspective review on techno-socio-economy nexus. *International Journal of Hydrogen Energy*, 46(71), 35027-35056. https://doi.org/10.1016/B978-0-08-101977-1.00012-0

5. Tarhan, C., & Çil, M. A. (2021). A study on hydrogen, the clean energy of the future: Hydrogen storage methods. *Journal of Energy Storage*, 40, 102676. https://doi.org/10.1016/j.est.2021.102676

6. Liu, G., Sheng, Y., Ager, J. W., Kraft, M., & Xu, R. (2019). Research advances towards large-scale solar hydrogen production from water. *EnergyChem*, 1(2), 100014. https://doi.org/10.1016/j.enchem.2019.100014

7. Guo, L., Chen, Y., Su, J., Liu, M., & Liu, Y. (2019). Obstacles of solar-powered photocatalytic water splitting for hydrogen production: A perspective from energy flow and mass flow. *Energy*, 172, 1079-1086. https://doi.org/10.1016/j.enchem.2019.100014

8. Nakata, K., & Fujishima, A. (2012). TiO_2 photocatalysis: Design and applications. *Journal of Photochemistry and Photobiology C: Photochemistry Reviews*, 13(3), 169-189. https://doi.org/10.1016/j.jphotochemrev.2012.06.001

9. Koe, W. S., Lee, J. W., Chong, W. C., Pang, Y. L., & Sim, L. C. (2020). An overview of photocatalytic degradation: photocatalysts, mechanisms, and development of photocatalytic membrane. *Environmental Science and Pollution Research*, 27, 2522-2565. https://doi.org/10.1007/s11356-019-07193-5

10. Zheng, C., Yang, H., Cui, Z., Zhang, H., & Wang, X. (2017). A novel $Bi_4Ti_3O_{12}$/Ag3PO4 heterojunction photocatalyst with enhanced photocatalytic performance. *Nanoscale Research Letters*, 12, article 608.
https://doi.org/10.1186/s11671-017-2377-1

11. Banerjee, A. M. (2012). Thesis: Synthesis, characterization and catalytic activity of novel mixed oxides for energy and environmental related reactions. *Homi Bhabha National Institute*.
http://shodhganga.inflibnet.ac.in/handle/10603/11595

12. Shi, H., Tan, H., Zhu, W.-B., Sun, Z., Ma, Y., & Wang, E. (2015). Electrospun Cr-doped $Bi_4Ti_3O_{12}$/$Bi_2Ti_2O_7$ heterostructure fibers with enhanced visible-light photocatalytic properties. *Journal of Materials Chemistry* A, 12, 6586-6591.
https://doi.org/10.1039/C4TA06736C

13. Zhang, Y., Gao, J., Chen, Z., & Lu, Z. (2018). Enhanced photocatalytic performance of $Bi_4Ti_3O_{12}$ nanosheets synthesized by a self-catalyzed fast reaction process. *Ceramics International*, 44(18), 23014-23023.
https://doi.org/10.1016/j.ceramint.2018.09.103

14. McInnes, A., Sagu, J. S., & Wijayantha, K. G. U. (2014). Fabrication and photoelectrochemical studies of $Bi_2Ti_2O_7$ pyrochlore thin films by aerosol assisted chemical vapour deposition. *Materials Letters*,137, 214-217.
https://doi.org/10.1016/j.ceramint.2018.09.103

15. Akihiko, K., & Satoshi, H. (1999). H_2 or O_2 evolution from aqueous solutions on layered oxide photocatalysts consisting of Bi^{3+} with $6s^2$ configuration and d^0 transition metal ions. *Chemistry Letters*, 28(10), 1103-1104.
https://doi.org/10.1246/cl.1999.1103

16. Yao, W. F., Xu, X. H., Wang, H., Zhou, J. T., Yang, Z. N., Zhang, Y. *et al.* (2004). Photocatalytic property of perovskite bismuth titanate. *Applied Catalysis B: Environmental*, 52(2), 109-116.
https://doi.org/10.1016/j.apcatb.2004.04.002

17. Liu, Z., An, Y., Zhang, W., Zhu, L., & Zhu, G. (2023). Au Nanoparticles Modified Oxygen-vacancies-rich $Bi_4Ti_3O_{12}$ Heterojunction for Efficient Photocatalytic NO Removal with High Selectivity. *Journal of Alloys and Compounds*, 942, 169018.
https://doi.org/10.1016/j.jallcom.2023.169018

18. Zhao, Y., Fan, H., Fu, K., Ma, L., Li, M., & Fang, J. (2016). Intrinsic electric field assisted polymeric graphitic carbon nitride coupled with $Bi_4Ti_3O_{12}$/$Bi_2Ti_2O_7$ heterostructure nanofibers toward enhanced photocatalytic hydrogen evolution. *International Journal of Hydrogen Energy*, 41(38), 16913-16926.
https://doi.org/10.1016/j.ijhydene.2016.07.162

19. Morad, I., Alshehri, A. M.M Mansour, A. F., Wasfy, M. H., & El-Desoky, M. M. (2020). Facile synthesis and comparative study for the optical performance of different TiO_2 phases doped PVA nanocomposite films. *Physica B: Condensed Matter*, 597, 412415. https://doi.org/10.1016/j.physb.2020.412415

20. Hou, J., Yang, C., Wang, Z., Zhou, W., Jiao, S., & Zhu, H. (2013). In situ synthesis of α–β phase heterojunction on Bi_2O_3 nanowires with exceptional visible-light photocatalytic performance. *Applied Catalysis B: Environmental*, 142-143, 504-511. https://doi.org/10.1016/j.apcatb.2013.05.050

21. Anu, & Yadav, K. (2020). Optical and dielectric properties of $Bi_2Ti_2O_7/Bi_4Ti_3O_{12}$ nanocomposite. *MaterialsToday: Proccedings*, 28(1), 153-157. https://doi.org/10.1016/j.matpr.2020.01.467

22. Ho, C.-H., Chan, C.-H., Huang, Y.-S., Tien, L.-C., & Chao, L.-C. (2013). The study of optical band edge property of bismuth oxide nanowires α-Bi_2O_3. *Optics Express*, 21(10), 11965-11972. https://doi.org/10.1364/OE.21.011965

23. Challagulla, S., Tarafder, K., Ganesan, R., & Roy, S. (2017). Structure sensitive photocatalytic reduction of nitroarenes over TiO_2. *Scientific Reports*, 7, article 8783. https://doi.org/10.1038/s41598-017-08599-2

24. Turner, C., Johns, P. M., Thatcher, E. M., Tanner, D. B., & Nino, J. C. (2014). Atomic displacive disorder in $Bi_2Ti_2O_7$. *Journal of Physical Chemistry C*, 118(49), 28797-28803. https://doi.org/10.1021/jp5095883

25. Makuła, P., Pacia, M., & Macyk, W. (2018). How to Correctly Determine the Band Gap Energy of Modified Semiconductor Photocatalysts Based on UV-Vis Spectra. *Journal of Physical Chemistry Letters*, 9(23), 6814-6817. https://doi.org/10.1021/acs.jpclett.8b02892

26. Liu, Z., An, Y., Zhang, W., Zhu, L., & Zhu, G. (2023). Au Nanoparticles Modified Oxygen-vacancies-rich $Bi_4Ti_3O_{12}$ Heterojunction for Efficient Photocatalytic NO Removal with High Selectivity. *Journal of Alloys and Compounds*, 942, 169018. https://doi.org/10.1016/j.jallcom.2023.169018

27. Nogueira, A. E., Longo, E., Leite, E. R., & Camargo, E. R. (2014). Synthesis and photocatalytic properties of bismuth titanate with different structures via oxidant peroxo method (OPM). *Journal of Colloid and Interface Science*, 415, 89-94. https://doi.org/10.1016/j.jcis.2013.10.010

Chapter 1 Environment Area

INFLUENCE OF CHEMICAL STRUCTURE OF ORGANIC COMPOUNDS IN THE ORGANOGEL FORMATION FOR REMOVAL OF ORGANIC SOLVENTS

Gabriela Martínez-Mejía[1,2], Brenda Afrodita Berméo-Solórzano[1], José Manuel del Río[2], Mónica Corea[2*], Rogelio Jiménez-Juárez[1*]

[1]Departamento de Química Orgánica, Escuela Nacional de Ciencias Biológicas, Instituto Politécnico Nacional, Prolongación de Carpio y Plan de Ayala S/N, Miguel Hidalgo, C.P. 11340, Ciudad de México, México.

[2]Escuela Superior de Ingeniería Química e Industrias Extractivas, Instituto Politécnico Nacional, San Pedro Zacatenco, Gustavo A. Madero C.P. 07738, Ciudad de México, México.

*mcorea@ipn.mx, rjimenezj@ipn.mx

Martínez-Mejía, G., Bermeo-Solórzano, B. A., del Río, J. M., Corea, M., & Jiménez-Juárez, R. (2023). Influence of chemical structure of organic compounds in the organogel formation for removal of organic solvents. In E. San Martín-Martínez (Ed.). *Research advances in nanosciences, micro and nanotechnologies. Volume IV* (pp. 231-248). Barcelona, Spain: Omniascience.

Abstract

In this work, the influence between two new organic compounds were compared: a carbamate and a urea to prepare organogels of low molecular weight (LMWGs). The reaction advance for the synthesis of carbamate and urea was followed by thin-layer chromatography. The compounds were tested for organic solvent removal in a model wastewater. The formed gels with the organic solvents were characterized by Fourier transformer infrared spectroscopy (FT-IR), nuclear magnetic resonance of proton (^{1}H-RMN), high resolution mass spectrometry (HR-MS) and scanning electron microscopy (SEM). The results showed the gel relation (molecules number of gelled solvent by gelator molecule) was lower for the urea (0.98-5.15 wt.%) than the carbamate (1.33-15.17 wt.%). The spectroscopy and microscopy studies showed that the urea gels formed spherical structures with appearance of entanglement fibers, and these were stronger than those made with carbamate, associated to hydrogen bonds.

1. Introduction

The pollution by organic solvents is a major environmental problem because these compounds are widely used in a wide variety of industrial and commercial processes, such as the production of paints, adhesives, cleaners, among others [1]. These solvents can be toxic and persistent in the environment, which can have negative effects on human health and the environment. For example, a way to eliminate the organic solvents of wastewater is adding amphiphilic compounds (low molecular weight organogelators) able to capture and remove them by filtration [1]. The chemical structure of amphiphilic compounds gives them hydrophilic and hydrophobic properties [2 – 4]. They have the ability to trap polar and non-polar solvents and to form supramolecular networks through weak donor-acceptor. That is "non-covalent" intermolecular interactions between "gellant-gellant", "gellant-solvent", "solvent-solvent" can be carried out [5 – 11]. These interactions can be done by hydrogen bonding, dipole-dipole, dipole-dipole interactions, van der Waals molecular interactions, molecular stacking π-π, C-H…π molecular interactions, solvophobic effects or molecular surface stress, among others [12].

The organogel form physical networks or supramolecular aggregates, which can be response to physical stimulus such as temperature, light, pH, ultrasound [13 – 16]. It has reported that these structures can used as carriers for drug delivery [16 – 18], tools for water organic contaminants removal [19] and scaffold for tissue regeneration [20]. The used groups to form supramolecular aggregates are peptides [21, 22], amides [15 – 23], ureas [24], carbamates and fatty acids [25].

In this work, two organic compounds were synthesized and characterized. The ability to form supramolecular aggregates and gel from four different solvents was compared.

2. Materials and Methods

2.1. *Materials*

Hexadecyl chloroformate (96 %), hexadecyl isocyanate (97 %), N,N-dimethylethylenediamine (99 %) as high purity chemicals (Sigma-Aldrich, United States). The chemicals were used without previous purification.

2.2. *Methods*

Melting points were determined by using an electrothermal apparatus A29003MB. Fourier transform infrared spectroscopy (FT-IR) was performed in a double beam Perkin-Elmer Model 1605 FT/IR spectrometer with ATR equipment. NMR spectra were recorded in CD Cl_3 or DMSO-d6 solution on a Varian Mercury spectrometer (300 or 500 MHz for ^{1}H NMR, 75 or 125 MHz for ^{13}C respectively). Chemical shifts were reported in parts per million relatives to Me_4Si as internal standard. Coupling constants J are expressed in Hz. High resolution mass spectroscopy (HR-MS) was analyzed on a micro TOF-Q II with electrospray ionization (ISI) (BrukerDaltonics, Billerica USA). All measurements were carried out by triplicate at room temperature. Purification of the reaction mixtures was carried out by column chromatography using silica gel (Merck 70-230 Mesh) as a solid support or by recrystallization. The progress of the reaction was followed by thin layer chromatography (TLC) on silica gel 60 F254 plates.

2.3. *Gelation test*

The gelation properties of each compound were tested for four different solvents. The gelation tests were carried out as follows: 1 mL of solvent was put and weighed in capped vial. The compound was added to solvent at intervals of 2 mg until saturation was reached. The mixture was heated with a thermal bath until the solid was dissolved into the solvent, then a clear solution was obtained. This solution was cooled until the observation of gel formation and this temperature was recorded. Finally, the test vial was inverted to check that no flow of the organic solvent out of the gel. The gel was weighed again, and the loss of solvent was calculated. After that the gel was heated and the temperature at which it broke drown was taken. The experiments were made by triplicate.

2.4. *Scanning Electron Microscopy*

A gel sample was deposited over the cooper sample holder and cooled with liquid nitrogen and sputtered with gold. Observations were carried out with in a Scanning Electron Microscope JEOL model JSM 7800F at 1 kV.

3. Results and Discussion

The carbamate **3** was synthesized according of scheme of Figure 1. The N,N-dimethylethylenediamine **2** (0.8 equiv.) was dissolved in dichloromethane (DCM) and put in a round-bottomed flask and stirred vigorously. Then, the hexadecyl chloroformate **1** (1 equiv.) in dichloromethane was added dropwise during 30 min at room temperature. The reaction progress was followed by thin layer chromatography (TLC). After two hours, the mixture reaction was extracted with 5v/v % aqueous hydrochloric acid solution (3 x15 mL) and water (2 x 15 mL). Organic phase was dried (Na_2SO_4), filtered and solvent was evaporated under reduced pressure. Reaction crude product was purified by recrystallization or by silica gel (70-100 mesh) column chromatography. The carbamate was obtained as white solid with a yield of 94 % and melting point of 79-80 °C.

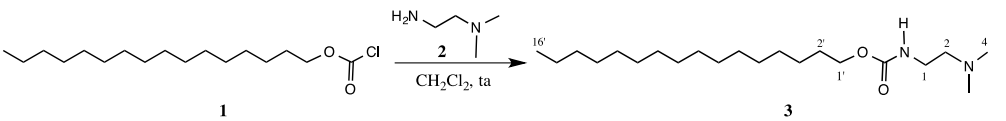

Figure 1. Scheme of reaction for synthesis of carbamate 3.

The urea **6** was synthesized from hexadecyl isocyanate **4** and phenylenediamine **5**, following the same procedure of carbamate (Figure 2). The urea was obtained as a white solid with a yield of 88 % and melting point of 109-110 °C.

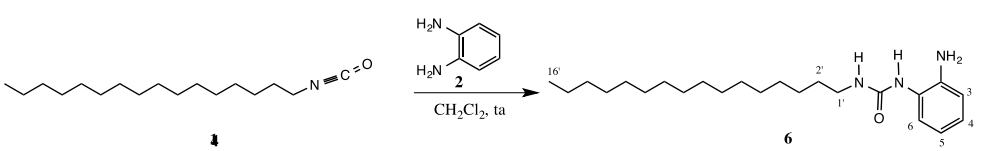

Figure 2. Scheme of reaction for synthesis of urea **6**.

The obtained compounds were analyzed by Fourier transform infrared spectroscopy (FT-IR), nuclear magnetic spectroscopy (NMR) and

high-resolution mass spectroscopy (HR-MS). The spectrum of carbamate **3** shows a wide absorption band around 3311 cm^{-1} attributed to the stretch of N-H group and intense absorption band at 1685 cm^{-1} attributed to carbonyl groups (C=O), (see Figure 3). This is according with the structures of carbamates compounds.

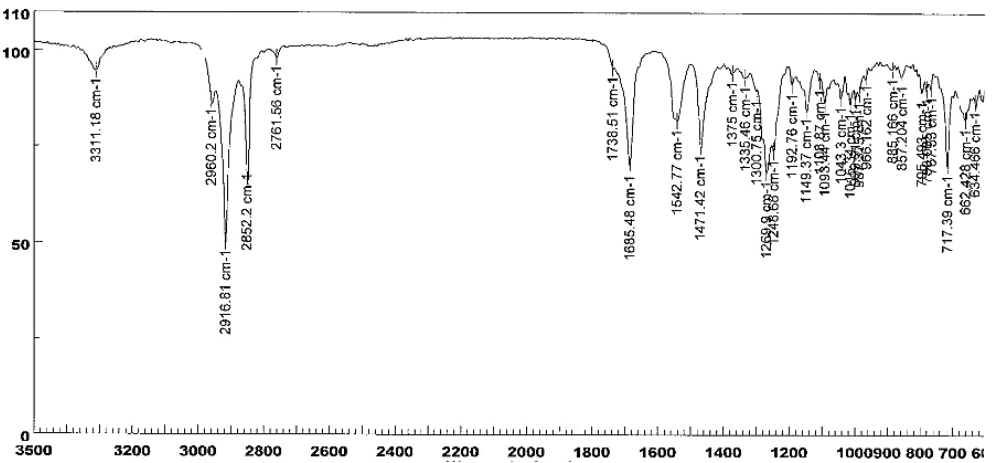

Figure 3. Infrared spectrum of carbamate 3.

Figure 4 presents the 1H-NMR spectrum of carbamate 3, and shows intense lines attributed to the deuterated solvent because the solvent was gelled by the organic compound. The characteristic signals of methylene protons bonded to oxygen CH_2-O are detected at 4.03 ppm, while the methylene from CH_2-N is shifted at 3.65 ppm.

The attributed signal to N,N-dimethylethylenediamine appears at 3.28 ppm due to H interaction from nitrogen; $(NCH_3)_2$ was observed as an intense line at 2.92 ppm. In the same way, the aliphatic chain shows three additional signals at 1.59 ppm attributed to H interaction from oxygen, 1.29 ppm attributed to the signal of $(CH_2)_{13}$, and 0.88 ppm corresponding to terminal methyl of chain.

The results of HR-MS of carbamate **3** showed an experimental m/z of 357.3486 (Figure 5) meanwhile the theoretical corresponds to 357.3481 as (M+1), confirming the formation of organic compound.

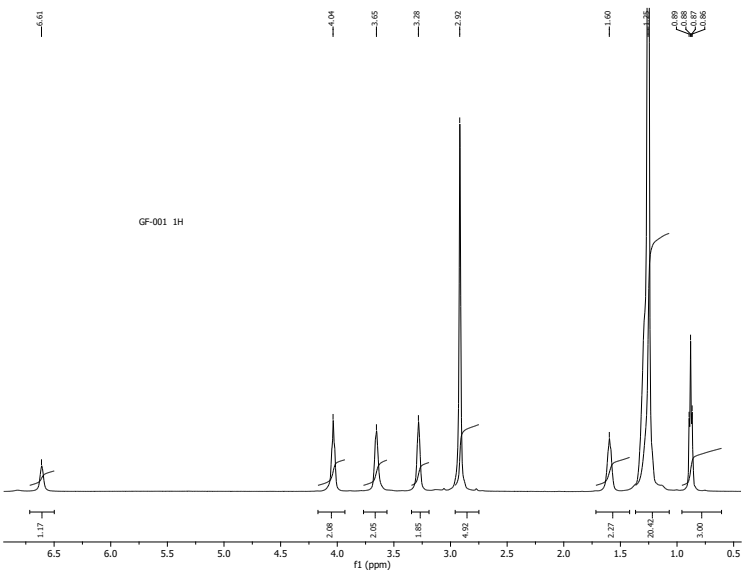

Figure 4. 1H NMR spectrum of carbamate **3**.

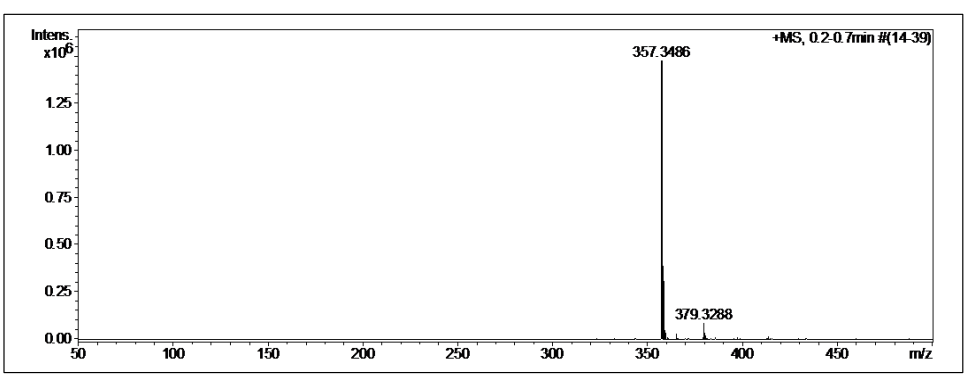

Figure 5. HR-MS spectrum of carbamate **3**.

In the same way, the urea compound was analyzed by the same techniques. The Figure 6 shows FT-IR spectrum for the urea 6, where a broad absorption band at 3280 cm^{-1} is observed, corresponding to NH and NH_2 groups and two intense bands at 1636 and 1556 cm^{-1} attributed to carbonyl groups (C=O).

The urea **6** also gelled the deuterated solvents. For this reason, the 1H MNR spectrum shows a quadruplet at 3.17 ppm by the protons of methylene group bonds to nitrogen (Figure 7). Other signals were also observed as: a quadruplet at

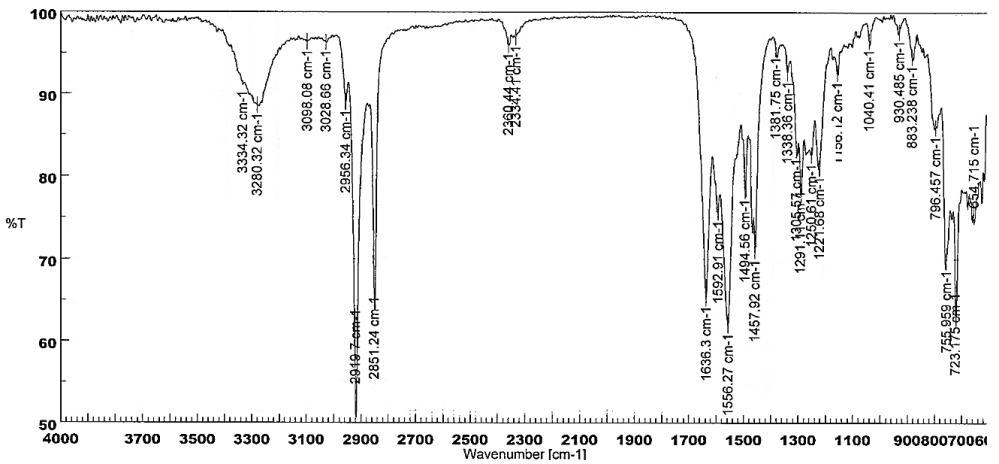

Figure 6. Infrared spectrum of urea 6.

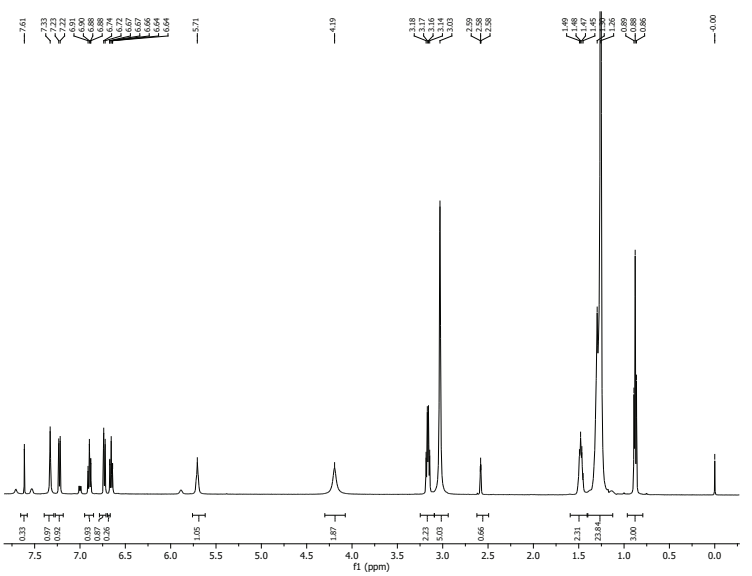

Figure 7. 1H NMR spectrum of urea 6.

1.26 ppm due to aliphatic chain and a triplet at 6.66 ppm (J=9 Hz, H_5), a doublet at 6.72 ppm (J=9 Hz, H_3), a triplet at 6.8 ppm (J=9 Hz, H_4) and a doublet at 7.23 ppm attributed to H_6, confirming the presence of urea compound.

The HR-MS spectrum of urea 6 showed an m/z experimental of 389.3142, while the theoretical was 398.3147 as sodium salt. However, an m/z experimental

of dimer (m/z 751.6576), trimer (m/z 1148.9628) and tetramer (m/z 1525.2926) were also obtained, attributed to the high ability of self-assemble of urea (Figure 8).

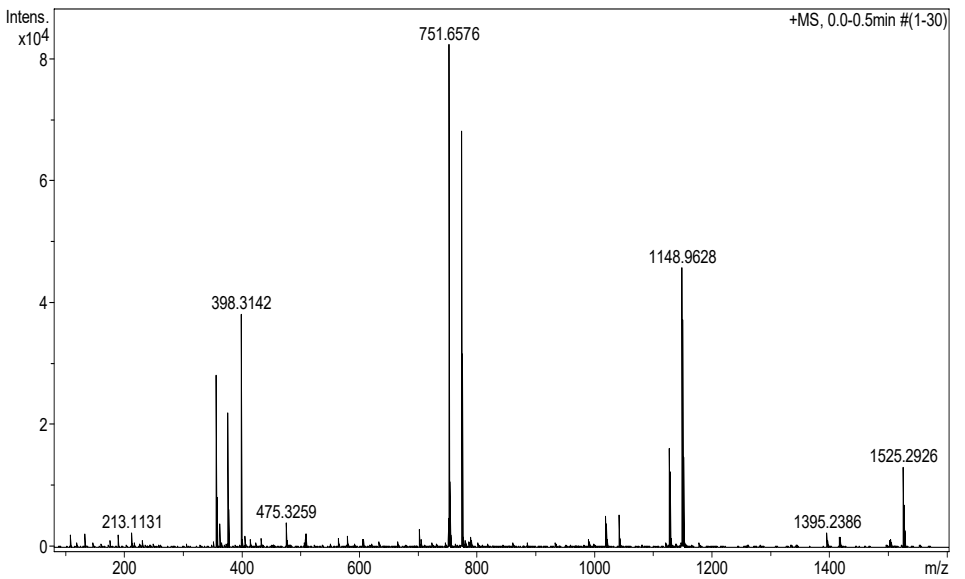

Figure 8. HR-MS spectrum of urea 6.

In this work, two organic compounds were synthesized: a urea and a carbamate. Both compounds have a hydrophilic part and a hydrophobic part [2 – 4], which allow that they can form supramolecular networks and interact in a non-covalent way, when they are in contact with solvents. For this reason, their ability to self-assemble was tested under four organic solvents and the determination of critical gelation concentration, defined as the minimum concentration required to obtain the molecular self-assembly to gel a solvent. The used solvents to carbamate were hexane, toluene, 1,4-dioxane and 2-propanol while the used solvent to urea were: carbon tetrachloride, xylene, toluene and 1,4-dioxane. The experiments consist of the addition of the organic compound at intervals of 2 mg in a volume of solvent previously weight. The mixture at each interval was heated until the solution turns transparent. After that, the mixture was cooled until the gel formation and the temperature was recorded. All the experiments were made by triplicate.

The photos of formed organogels with xylene, toluene and 1,4-dioxane with the carbamate is shown in Figure 9. The gels feature a semi-transparent appearance and colorless. This was observed to all solvents.

Figure 9. Carbamate gels obtained with: A) xylene; B) toluene; C) 1,4-dioxane.

The photos of obtained gels with urea in presence of xylene, toluene, 1,4-dioxane y carbon tetrachloride are presented in Figure 10. The results showed that the gels made with xylene and toluene had a transparent appearance, while the gels formed with dioxane and carbon tetrachloride were opaque and white in color.

Figure 10. Urea gels obtained with: A) xylene; B) toluene; C) 1,4-dioxane; D) carbon tetrachloride.

The results of supramolecular networks formation of carbamate with each solvent are summarized in Table 1, while the results for the urea are presented in Table 2.

Table 1. Conditions for the gel formation of carbamate with different solvents

Solvent	Solvent quantity (g)	Error	Carbamate quantity (g)	Error	Gel formation temperature (°C)	Gel breaking temperature (°C)	wt.%
Hexane	0.3262	0.0066	0.0767	0.0021	2	20	15.0
Xylene	0.3231	0.0101	0.0578	0.002	43	26	15.2
Toluene	0.9558	0.0175	0.0446	0.0019	10	20	4.46
1,4-dioxane	0.7542	0.006	0.0571	0.0011	2	20	7.04
2-propanol	0.5768	0.0186	0.0574	0.0014	0	9	9.05

Table 2. Conditions for the gel formation of urea with different solvents

Solvent	Solvent quantity (g)	Error	Urea quantity (g)	Error	Gel formation temperature (°C)	Gel breaking temperature (°C)	wt.%
Carbon tetrachloride	0.9944	0.0048	0.0178	0.0001	1	25	1.76
Xylene	1.0942	0.0492	0.0064	0.0001	12	12	0.58
Toluene	0.9883	0.0931	0.0615	0.0445	10	55	5.86
1,4-dioxane	0.9837	0.0545	0.0534	0.0002	5	35	5.15

Despite the formation of supramolecular networks for all solvents, their ability is limited because the higher quantities of carbamate to form gels compared with urea. It is likely the urea had great capacity of self-assemble and forming non-covalent networks. These results are coincident with the appearance and colors obtained in the organogels. For example, it was observed that the gel formed with urea in xylene was the one that used the least amount of organic compound (0.58 wt.%) and it had a transparent appearance, while the gels formed with toluene and 1,4-dioxane, the used concentration was 5.86 wt.% and 5.15 wt.%, respectively, and their appearance was semi-transparent and colorless. The urea in carbon tetrachloride formed a gel with a concentration of 1.76 wt.% of organic compound.

On the other hand, the best formed gel with carbamate was obtained with toluene, using a concentration of 4.46 wt.% of organic compound with a homogenous appearance of gel. The obtained concentrations in the organogel formation are coincident that those obtained in other works reported by bibliography [14, 26]. Due to the presented ability of carbamates and ureas to form organogels with organic solvents, it is possible that they can be applied as organic solvent trappers in the wastewater treatment. It is also possible that once the gel traps the solvent it can be reobtained by a filtering process, regenerated and reused several times the compound, which could be considered as an economical and sustainable treatment for water treatment.

The formation and breaking temperatures of gels were also measured. The results showed that carbamate gels with all solvent feature low temperatures of gel formation ($0<T/°C<10$) as compared with those gel formation from urea ($1<T/°C<12$). Concerning the breaking temperatures, urea has higher values ($12<T/°C<55$) than the carbamate, where the higher reached temperature was of 26 °C.

It has reported that the gel formation depends on number and interaction type between "gelator-gelator-solvent". These interactions can be identified as hydrogen bonding, van der Waals forces, π-π interactions and accepter-donator. Since the urea has two N-H bonding in its structure, while the carbamate only has one, the urea had the best ability to form organogels due to these supramolecular interactions. In addition, the adjacent polar groups as amine and/or hydroxyl (donor acids) increase the ability of functional groups to form organogels and trapping organic solvents. It has also reported that the gelling capacity of molecules with low molecular weight improves if in their structure have an aromatic part [7].

The gels of both organic compounds were analyzed by FT-IR. The spectra of carbamate and urea gels with toluene are presented in Figure 11, as an example. The results show that the intensity of the stretching in the vibrational bands of

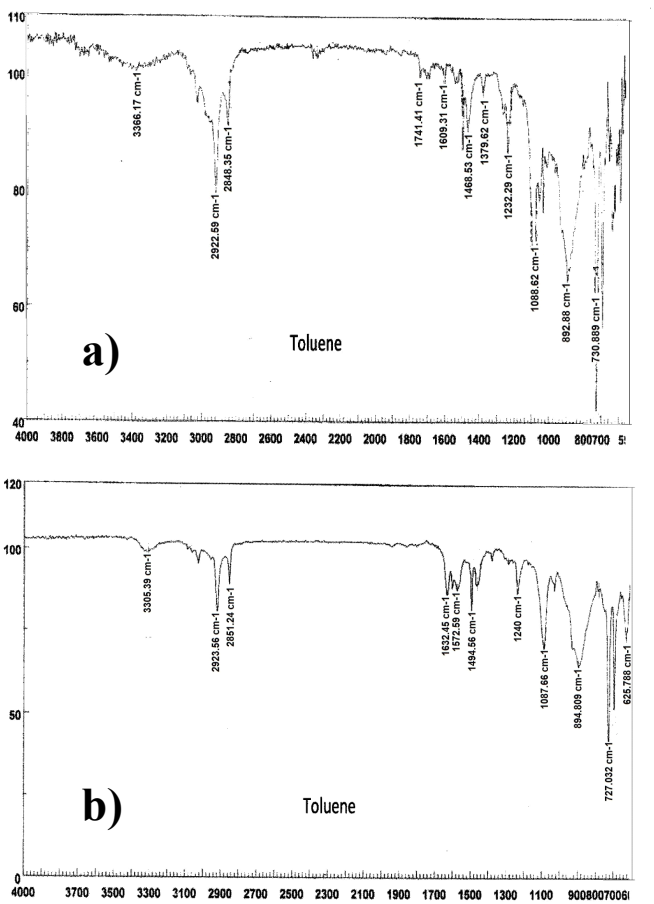

Figure 11. FT-IR gel spectra of a) carbamate with toluene and b) urea with toluene.

the NH_2, OH, CH and HNC=ONH bonds are reduced in the formed gels for both compounds. Additionally, the spectra showed very intense bands close to 890 cm^{-1}, because the bending vibrations (or deformation) of H-C-H causing intermolecular interactions by London dispersion.

According to FT-IR results a theoretical scheme of carbamate self-assemble to form the gel is presented in Figure 12, because it is possible assume that the organic compound stars to form non-covalent interactions between functional groups, creating supramolecular networks "gelator-gelator" and "solvent-gelator" in two and three dimensions. These interactions involve intermolecular forces as hydrogen-donor bond interactions (solvent acidity) or hydrogen-acceptor bond interactions (solvent basicity). These results can be coincident with the protein aggregation model developed by Boden [27] and the Hamilton model [28]. Both mechanisms explain that the gel formation follows three stages. In the first one, the primary structure is formed by a molecular recognition phenomenon that induces molecular aggregation or self-assembly, followed by the formation of a secondary structure through the anisotropic aggregate growth that define its morphology (micelles, vesicles, fibers corkscrews, disks, lamellae or tubules). Finally, a tertiary structure is created by the intersection of macro-nodes, generating aggregates that allow the gel stability. In this stage, the gel formation, the precipitation or crystallization of system is observed [29].

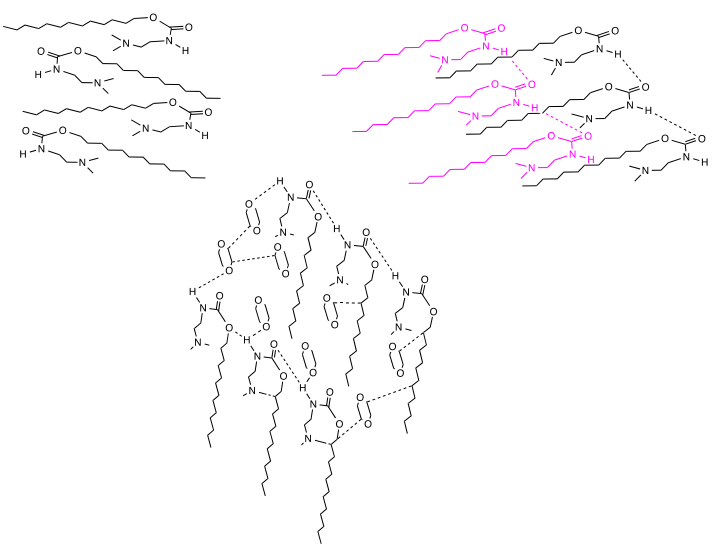

Figure 12. Scheme of non-covalent interactions in the gel formation.

Gel morphology was analyzed by scanning electron microscopy. The Figure 13 shows the micrographs of carbamate organogels produced with the different solvents where spheroidized clusters of fiber are observed. Now the structures less defined to carbamate gels were made with hexane and xylene (Figure 13a and 13b), while the gels prepared with 1,4-dioxane and 2-propanol, structures more defined were observed with diameters close to 20 μm.

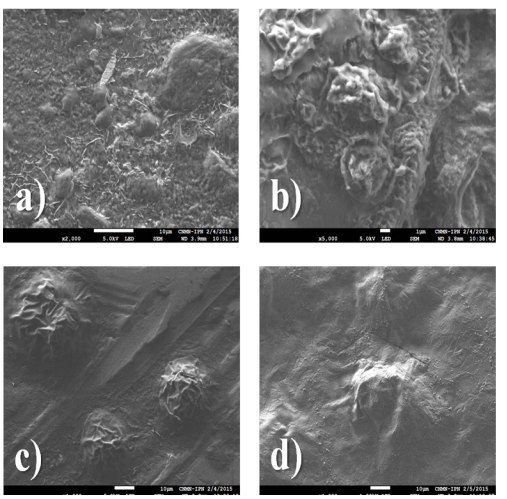

Figure 13. Carbamate organogels with a) hexane, b) xylene, c) 1,4-dioxane, d) 2-propanol.

The electron micrographs of urea gels with the solvents are present in Figure 14. Fiber clusters with spheroidized morphology are observed with mean diameter of 0.8μm.

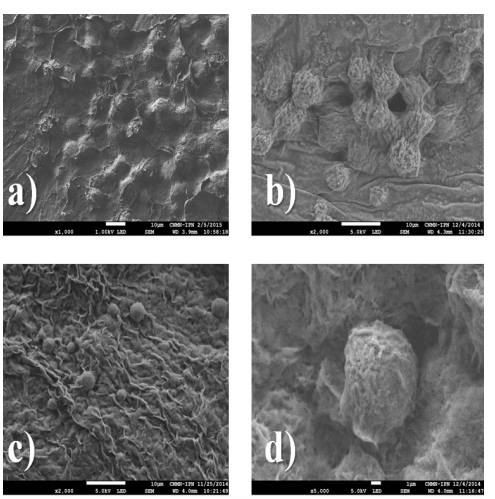

Figure 14. Urea organogeles with a) carbon tetrachloride, b) xylene, c) toluene, d) 1,4-dioxane.

4. Conclusions

In this work two organic compounds were synthesized: a carbamate and a urea. The carbamate 3 was obtained as an amorphous white solid with a yield of 94 %, melting point 89-90 °C, m/z 357.3486; while urea 6 was obtained as a white solid, yield 88 %, melting point 109-110 °C and m/z 398.3142.

The organic compounds were able to produce reversible gels with all tested organic solvents. The amount of used urea in the gel formation was lower than used for carbamate. This result is attributed to the interactions by hydrogen bonding between amino groups of urea in the self-assemble process of organogels. Finally, these organogels have great potential to be use in the removal of organic solvents from contaminated water.

References

1. Mohar, M., & Das, T. (2019). Phenylalanine-based low-molecular-weight gelator for the removal of metal ions and dyes from wastewater. *Soft Materials*, 17(4), 328-341. https://doi.org/10.1080/1539445X.2019.1600548
2. Kontantinova, T.V., Klykov, V.N., & Serebrennikova, G. A. (2001). The synthesis of cholesterol-containing cationic amphiphils with heterocyclic bases. *Russian Journal of Bioorganic Chemistry*, 27, 404-407. https://doi.org/10.1023/A:1012996921113
3. Ohkawabata, S., Kanemaru, M., Kuawahara, S.-Y., Yamamoto, K., & Kadokawa, J.-I. (2012) Synthesis of 6-o-hexadecyl- and 6-o-octylsucroses and their self-assembling properties under aqueous conditions. *Journal of Carbohydrate Chemistry*, 31(8), 659-672. https://doi.org/10.1080/07328303.2012.702250
4. Shimizu. T., Masuda, M., & Minamikawa, H. (2005). Supramolecular nanotube architectures based on amphiphilic molecules. *Chemical Reviews*, 105(4), 1401-1444. https://doi.org/10.1021/cr030072j
5. Sangeetha, N.M., & Maitra, U. (2005). Supramolecular gels: Functions and uses. Chemical Society Reviews, 34, 821-836. https://doi.org/10.1039/b417081b
6. Balamurugan, R., Zhang, Y.-S., Fitriyani, S. & Liu, J.-H. (2016). Click chemistry-assisted, bis-cholesteryl-appended, isosorbide-based, dual-responsive organogelators and their self-assemblies. *Soft Matter*, 12, 5214-5223. https://doi.org/10.1039/C6SM00447D
7. Curcio, P., Allix, F., Pickaert, G., & Jamart-Grégoire, B. (2011). A favorable, narrow, δh Hansen-Parameter domain for gelation of low molecular-weight amino acid derivatives. *Chemistry Europe*, 17(48), 13603-13612. https://doi.org/10.1002/chem.201101423
8. Zhu, G., & Dordick, J. S. (2006). Solvent Effect on Organogel Formation by Low Molecular Weight Molecules. *Chemistry of Materials*, 18(25), 5988-5995. https://doi.org/10.1021/cm0619297
9. Kamlet, M. J., Abboud, J. L. M., Abraham, M. H., & Taft, R. W. (1993). Linear solvation energy relationships. 23. A comprehensive collection of the solvatochromic parameters, .pi.*, .alpha., and .beta., and some methods for simplifying the generalized solvatochromic equation. *The Journal of Organic Chemistry*, 48(17), 2877-2887. https://doi.org/10.1021/jo00165a018
10. Wang, R., Geiger, C., Chen, L., Swanson, B., & Whitten, D. G. (2000). Direct Observation of Sol−Gel Conversion: The Role of the Solvent in Organogel Formation. *Journal of the American Chemical Society*, 122(10), 2399-2400. https://doi.org/10.1021/ja993991t

11. Sakurai, K., Jeong, Y., Koumoto, K., Friggeri, A., Gronwald, O., Sakurai, S. *et al.* (2003). Supramolecular Structure of a Sugar-Appended Organogelator Explored with Synchrotron X-ray Small-Angle Scattering. *Langmuir*, 19,20, 8211-8217. https://doi.org/10.1021/la0346752

12. Yang, L., Adam, C., & Cockrof, S. L. (2015). Quantifying Solvophobic Effects in Nonpolar Cohesive Interactions. *Journal of the American Chemical Society*, 137(32), 10084-10087. https://doi.org/10.1021/jacs.5b05736

13. Guo, M., Cao, X., Meijer, E. W., & Dankers, P. Y. W. (2013). Core-shell capsules base on supramolecular hydrogels show shell-related erosion and release due to confinement. *Macromolecular Bioscience*, 13(1), 77-83. https://doi.org/10.1021/jacs.5b05736

14. Wang, X., & Liu, M. (2014). Vicinal Solvent Effect on Supramolecular Gelation: Alcohol Controlled Topochemical Reaction and the Toruloid Nanostructure. *Chemistry – A European Journal*, 20(32), 10110-10116. https://doi.org/10.1021/jacs.5b05736

15. Luo, X., Li, Z., Xiao, W., Wang, Q., & Zhong, J. (2009). Self-assembled organogels formed by monochain derivatives of ethylenediamine. *Journal of Colloid and Interface Science*, 336(2), 803-807. https://doi.org/10.1016/j.jcis.2009.04.056

16. Minakuchi, N., Hoe, K, Yamaki, D., Ten-No, S., Nakashima, K., Goto, M. *et al.* (2012). Versatile supramolecular gelators that can harden water, organic solvents and ionic liquids. *Langmuir*, 28(25), 9259-9266. https://doi.org/10.1021/la301442f

17. Yang, Z., Xu, K., Wang, L., Gu, H., Wei, H., Zhang, M., & Xu, B. (2005). Self-assembly of small molecules affords multifunctional supramolecular hydrogels for topically treating simulated uranium wounds. *Chemical Communications*, 35, 4414-4416. https://doi.org/10.1039/b507314f

18. Liao, S. W., Rawson, J., Omori, K., Ishyama, K., Mozhdehi, D., Oancea, A. R. *et al.* (2013). Maintaining functional islets through encapsulation in an injectable saccharide-peptide hydrogel. *Biomaterials*, 34(16), 3984-3991. https://doi.org/10.1016/j.biomaterials.2013.02.007

19. Nicodemus., G. D., & Bryant, S. J. (2008). Cell encapsulation in biodegradable hydrogels for tissue engineering applications. *Tissue Engineering Part B: Reviews*, 14(2), 149-165. https://doi.org/10.1089/ten.teb.2007.0332

20. Sone, E. D., & Stupp, S. I. (2011). Bioinspired magnetite mineralization of peptide-amphiphile nanofibers. *Chemistry of Materials*, 23(8), 2005-2007. https://doi.org/10.1021/cm102985v

21. Bhattacharya, S., & Krishnan-Ghosh, Y. (2001). First report of phase selective gelation of oil from oil/water mixtures. Possible implications toward containing oil spills. *Chemical Communications*, 2, 185-186.
https://doi.org/10.1039/b007848o

22. Kumar, P., Kadam, M. M, & Gaikar, V. G. (2015). Low molecular weight organogels and their application in the synthesis of CdS nanoparticles. *Industrial & Engineering Chemistry Research*, 51(47), 15374-15385.
https://doi.org/10.1021/cm102985v

23. Hardy, J. G., Hirst, A.R., Ashworth, I., Brennan, C., & Smith, D. K. (2007). Exploring molecular recognition pathways within a family of gelators with different hydrogen bonding motifs. *Tetrahedron*, 63(31), 7397-7406.
https://doi.org/10.1016/j.tet.2007.03.120

24. Vemula, P. K., Aslam, U., Mallia, V. A., & John, G. (2007). In situ synthesis of gold nanoparticles using molecular gels and liquid crystals from vitamin-C amphiphiles. *Chemistry of Materials*, 19(2), 138-140.
https://doi.org/10.1021/cm062464n

25. Wang, X., Zhou, L., Wang, H., Luo, Q., Xu, J., & Liu, J. (2011). Reversible organogels triggered by dynamic K+ binding and release. *Journal of Colloid and Interface Science*, 353(2), 412-419.
https://doi.org/10.1016/j.jcis.2010.09.089

26. Aggeli, A., Nyrkova, I. A., Bell, M., Harding, R., Carrick, L., Meleish, T. C. B. *et al.* (2001). Hierarchical self-assembly of chiral rod-like molecules as a model for peptide α-sheet tapes, ribbons, fibrils, and fibers. *Applied Physical Sciences*, 98(21), 11857-11862.
https://doi.org/10.1073/pnas.191250198

27. Estroff, L. A., & Hamilton, A. D. (2004). Water gelation by small organic molecules. *Chemical Reviews*, 104(3), 1201-1218.
https://doi.org/10.1021/cr0302049

28. Shi X. (2013). Study on protein structure based on reverse Hamilton path models. *Proceedings of The Eighth International Conference on Bio-Inspired Computing: Theories and Applications (BIC-TA), Springer*, 623-627.
https://doi.org/10.1007/978-3-642-37502-6_75

29. Hardy, J.G.; Hirst, A.R.; Ashworth, I.; Brennan, C.; Smith, D.K. (2007). Exploring molecular recognition pathways within a family of gelators with different hydrogen bonding motifs. *Tetrahedron*, 63(31), 7397-7406.
https://doi.org/10.1016/j.tet.2007.03.120

Chapter 1 Semiconductors and materials Area

RELIABILITY OF FLEXIBLE AMORPHOUS IN-GA-ZN-O (A-IGZO) THIN-FILM TRANSISTORS

Isai S. Hernandez-Luna[1], Pablo Toledo[2], Francisco Hernandez-Cuevas[1], Norberto Hernandez-Como[1*]

[1]Centro de Nanociencias y Micro y Nanotecnologías, Instituto Politécnico Nacional, Mexico City, Mexico.

[2]Escuela Superior de Ingeniería Química e Industrias Extractivas, Instituto Politécnico Nacional, Mexico.

nohernandezc@ipn.mx

Hernandez-Luna, I. S., Toledo, P., Hernandez-Cuevas, F., & Hernandez-Como, N. (2023). Reliability of flexible amorphous In-Ga-Zn-O (a-IGZO) thin-film transistors. In E. San Martín-Martínez (Ed.). *Research advances in nanosciences, micro and nanotechnologies. Volume IV* (pp. 249-262). Barcelona, Spain: Omniascience.

Abstract

The application of flexible electronics will require a new class of electronic devices and systems with outstanding characteristics such as lightness and mechanical flexibility, giving the possibility of gradually entering in the daily people lives as human health monitors. Amorphous oxide semiconductors have been part of this type of application, becoming attractive materials for new generation flexible electronics. In this work we evaluate the scalability of our thin-film transistor technology for possible applications such as health monitors. The characterization of two identical TFT device fabrication processes is explored with the variant of being fabricated on two different substrates, rigid and flexible. Rigid substrate TFTs show slightly higher initial characteristics compared to flexible TFTs. The degradation in flexible devices is attributed to constant mechanical stress and roughness of the flexible substrate. Finally, in flexible devices under conditions of mechanical stress with a radius of curvature of 4 mm, present a combined behavior of a flexible device without mechanical stress to a device fabricate on a rigid substrate.

Keywords: flexible electronics, oxide TFT, InGaZnO (IGZO); compatible devices, reliability

1. Introduction

The growing demand for electronics with innovative features has recently oriented exploration towards new lines of technological research [1 – 4]. With features such as light weight, low cost, adaptability, and ease of use, flexible electronics have been a topic of special interest in the scientific research community in recent decades [4, 5]. In this sense, flexible electronics, which consists of devices and systems capable of displaying electrical functionality while mechanical stress is applied, has shown great promise in many practical applications, such as wearable devices, smart implants, folding screens, physiological monitoring, among many [6 – 9]. Similarly, thin-film electronics based on oxide semiconductors have recently attracted increasing interest due to the characteristics they share with flexible substrates [10 – 14]. This combination of properties, enabled using advanced materials and processes, has find the way for new applications in different fields, such as detection technologies and healthcare systems [15]. As active devices in such flexible systems, the reliability of oxide semiconductor thin-film transistors is a subject of study, which must withstand the combined stress of electrical and mechanical loads.

Since the use of amorphous metal oxides such as indium-gallium-zinc oxide, a-IGZO as the semiconductor material, or active layer, in thin-film transistors (TFTs) was shown by Nomura et al in 2004 [14], a huge effort has been put into the research of amorphous oxide semiconductor (AOS) TFT devices, especially for their application in new generation flat panel displays (FPDs) and now in alternative applications [16, 17]. Among the main advantages of amorphous semiconductor oxide materials are that it is possible to obtain them using conventional deposition methods, such as sputtering, pulsed laser, by atomic layers, even at room temperature [14, 18, 19]; in addition, its amorphous structure allows to maintain similar properties in devices fabricated even in large areas [20].

The characteristics of amorphous semiconductor oxides are mainly attributed to their electronic configuration, which presents a spherical symmetry of orbitals of their S-type energy sublevels, allowing a high degree of overlap between neighboring orbitals, forming a conduction path of free electrons despite its amorphous structure. Inherent to the material, there is the creation of oxygen vacancies, which affect the electrical properties of AOS [21, 22].

Regarding the electrical performance of AOS-based TFTs, the high field effect mobility observed with respect to hydrogenated amorphous silicon TFTs

(a-Si;H) or organic TFTs stands out, obtaining values around of 10 Vs, even if the AOS are processed at room temperature (RT), as well as good stability under polarization and lighting stress. The mentioned characteristics depend not only on the use of the semiconductor material, but also on the gate dielectric and the contact metal or metals within the TFT structure. Research on optimizing the cationic composition of compounds in semiconductor materials has been highlighted, as well as the variation in the methods used for their deposit, heat treatments after their deposit or at the end of transistor fabricated. In the use of dielectric materials, it is desired that they have dielectric constants higher than SiO_2, low leakage current, and good thermal stability. Additionally, the formation of an ohmic contact is essential for the fabrication of TFTs, in the drain and source regions have a significant influence on the performance of the device [23, 24].

The structure of the TFT can be coplanar or staggered type and bottom or top gate, depending on the position of the gate with respect to the semiconductor oxide. The coplanar structure generally means that the source/drain electrodes and the semiconductor material are in the same plane. The staggered configuration means that the metal electrodes and the semiconductor material are not in the same plane, but rather are interleaved. For sensor applications, the bottom gate structure is generally used, allowing semiconductor material to act as an active layer to the outside environment. In the application of the TFT as a sensor, there are other configurations such as the case of the extended gate TFT, where the gate metal is used to sense the medium and have less contact resistance [25].

A TFT is used as a three-terminal device to connect to an external circuit that acts as an electrical signal amplifier or switch. The transistor is the central device for data processing and transmission. The three electrodes of the transistors are gate, source, and drain, and their three positions are not fixed and can be adjusted according to different processes to prepare different device structures. Thin Film Transistors (TFTs) are recognized as key building blocks/tools for the implementation of electronic logic circuits.

The use of polyimide (PI) in the industry is the most widely used representative plastic substrate presenting excellent thermal, chemical, and mechanical resistance. PI substrates withstand the fabrication process of Low Temperature Polycrystalline Silicon (LTPS) TFTs and oxide semiconductor TFTs [26]. Parallel to this, PI allows high uniform and achieve device functionality under different mechanical conditions, it is crucial to establish fabrication protocols to support electronic functionality under different types of deformation, such as bending,

stretching, creasing [27]. When a device is bent, the force applied to the device varies depending on the direction of bending and the radius of curvature. Depending on the magnitude of the force applied to the device, defects and dislocations can form in the active layer, leading to cracks from the gate electrode to the PI substrate in severe cases. This non-ideal phenomenon leads to deterioration of the electrical characteristics and reliability of TFTs.

The strategy that is taken is the fabrication of devices in two different substrates, rigid and flexible to aim at the scalability of the device for large area systems and flexible electronics. Furthermore, the transistors are characterized to evaluate their functionality as sensor conditioning circuits for portable devices, and health devices. By proper design of the device structure, is possible to reduce the effect of mechanical deformation on the active layer, allowing the realization of highly deformable transistors.

2. Experimental part

Two fabrication processes of IGZO TFTs were carried out, A and B samples, the difference between the processes lies in the use of different substrates as mechanical support for devices. In process A, a square-shaped Corning Eagle XG, one inch per side and 0.7 mm thick, purchased by Corning Incorporated, is occupied, with the characteristic of being occupied up to 600 °C. For process B, a Kapton HN Polyimide (Pi) substrate with a square shape, two inches per side and 50 μm thick, purchased from DuPont, was used. Pi has the characteristic of being used up to 400 °C. For the use of Pi, a dehydration heat treatment was carried out in air at 300 °C for 1 h, this to prevent expanding or contracting during processing. The flexible substrate is supported throughout the fabrication process on a glass support using the surface tension provided by a few drops of water. Both substrates were cleaned with acetone, alcohol, and water in an ultrasonic bath, prior to use.

The fabricated structure of the TFTs for both samples is bottom gate and staggered type. To define the bottom gate electrode in process A, we use Cr/Au as bilayer with 10/50 nm of thickness, the electrode was deposited using the electron beam evaporation technique and defined by wet etching based on ceric ammonium nitrate/potassium iodide. In process B, we use aluminum (Al) with 150 nm of thickness deposited by thermal evaporation and defined with a

phosphoric acid solution. The difference between the gate metals is due to the possibility of Pi attack on the solutions that define the Cr/Au metals.

For both processes A and B, 22 nm of Al_2O_3 was used as the dielectric layer deposited by atomic layer deposition (ALD) at 150 °C, using trimethylaluminum (TMA) and H_2O as precursors. Afterwards, 15 nm of IGZO layer was deposited by sputtering at room temperature at 70 W in an argon plasma. HCl and BOE 6:1 was used to define the semiconductor and gate dielectric layers, respectively. Subsequently, 150 nm Al were deposited by sputtering as source and drain electrodes with 150 W in argon plasma. The definition of the drain and source metal is carried out through the Lift-off process to avoid possible deterioration of the top part of the semiconductor material. Finally, for both processes, 200 nm of polymethylmethacrylate (PMMA) was deposited by spin-coating as a passivation layer with a heat treatment at 150 °C in air. The definition of PMMA is carried out using the RIE in an oxygen environment with a power of 130 W.

We use lithography processes to define the areas that make up the TFT structure, these processes were carried out using the direct writing technique using a Heidelberg DWL66FS system and positive photoresist at 115 °C. The photoresist development process is carried out with a potassium hydroxide-based solution at room temperature. In the figure 1a) we show the bottom gate structure in staggered configuration of the fabricated TFT and b) optical microscope image of the completed device.

a) b)

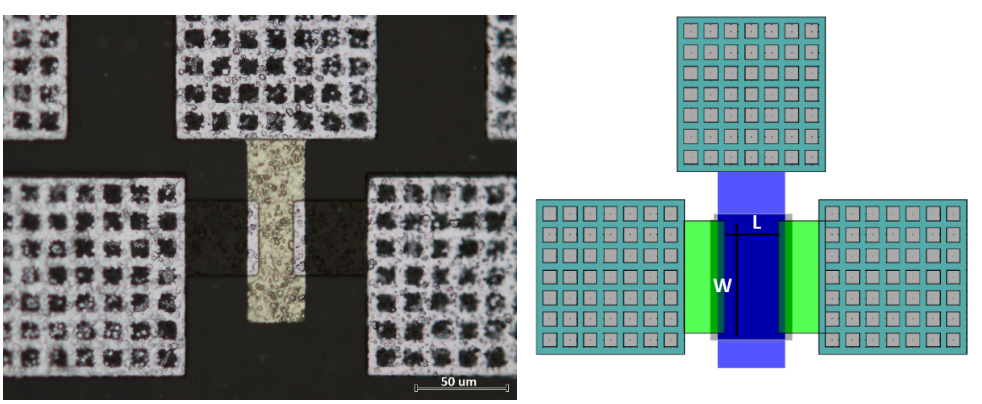

Figure 1. a) Shows the bottom gate structure in staggered configuration of the fabricated TFT and b) optical microscope image of the completed device.

The fabricated TFTs have two channel widths of 80 μm and 160 μm with two different channel lengths of 40 and 80 μm. In addition to the transistors, metal insulating metal (MIM) capacitors with dimensions of 80x80 μm per side were fabricated. Electrical characterization was performed with a Keithley 4200-SCS system at room temperature.

3. Results and discussion

According to the C-V characterization of MIM capacitors, the dielectric constant of Al_2O_3 was extracted, ki=6.4, this value is constant for the samples A (S-A) and B (S-B). Figure 2 shows the linear and saturation transference curves of a sample device A, measured at V_{DS}= 0.1 V and V_{DS}=5 V, correspondingly. A transistor with W=160 μm and L=40 μm is occupied. From the curves, the field effect mobility in the saturation region (μFET) of the transistor are extracted, μ_{FET}=11 cm^2/Vs, threshold voltage (V_{th}), V_{th}=0.84 V, both extracted from the linear fit of the graph IDS1/2 vs. VGS, according to the IDS formula in saturation [28]; Delta Vth (DV_{th}), which corresponds to the voltage window formed by measuring the negative to positive and reverse voltage, DVth=0.1V, the Ion/Ioff ratio of the transistor in the saturation transference curve, I_{ON}/I_{OFF}=6.8x10^7 and the subthreshold slope (SS), corresponds to the increase in V_{GS} necessary to increase the I_{DS} in a decade, SS=256 mV. The gate current (I_{GS}) is plotted which is below 10 nA.

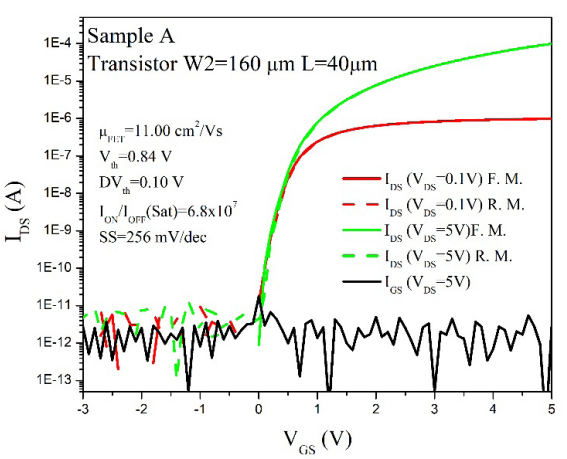

Figure 2. Shows the linear and saturation transference curves of a sample device A, with forward (F.M.) and reverse (R.M.) measurements.

In Figure 3a, the output characteristics of two devices with the same channel length L=40 μm and different channel width are shown, W1=80 μm and W2=160 μm. We can observe that I_{DS} with respect to its geometric relationship, there is a good coincidence of all the output characteristic curves, this indicates a good repeatability of the devices within the fabrication process. Figure 3b graphs the transference in saturation for four different devices, a good fit between them can be observed.

a) b)

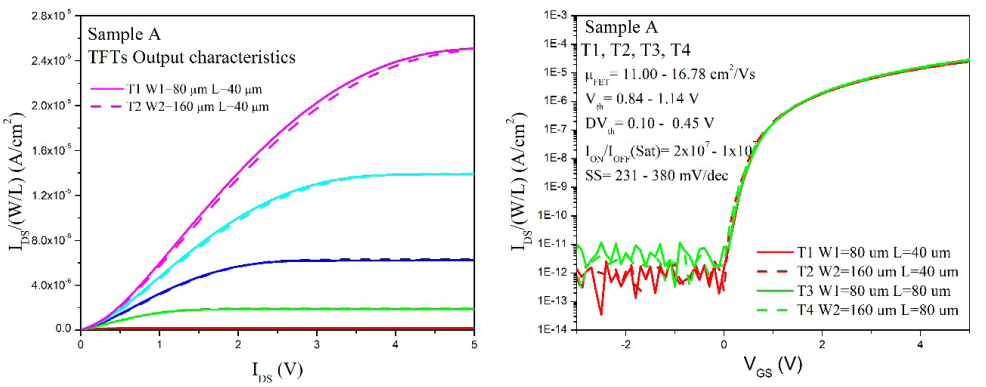

Figure 3. Show a) output characteristics and b) transfer curves for a device of sample A.

Figure 4 shows the linear and saturation transference graphs for a sample B device, measured in a flat state, occupying a rigid glass substrate as a support. The device presents a reduction of μ_{FET}=8.9 cm^2/Vs, a reduction in Vth and an increase in the value of SS with respect to the device of sample A. The values of the DV_{th} window for both sets of curves, the current gate and the I_{on}/I_{off} ratio of the transistor hold with respect to the device in sample A.

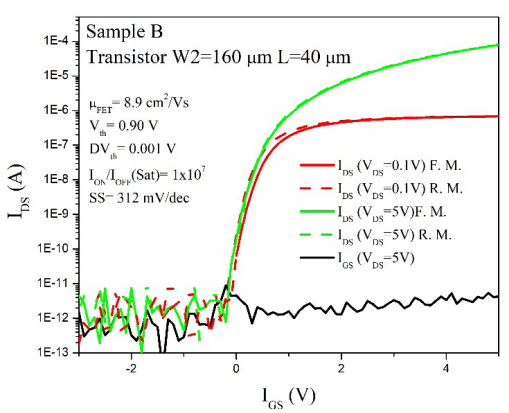

Figure 4. Shows the linear and saturation transference curves of a sample device A.

Figure 5 shows the graphs of the comparison of sample A and B for a device with the same geometric configuration. We can observe a slight reduction in the drain current for sample B. Figure 5a, shows an increase on origin resistor (Origin R) at V_{GS}=5 V for sample B. In figure 5b a reduction of the drain current is shown for sample B, the DV_{th} windows are kept in the same range of values. A general reduction of the drain current of around 15 to 20 % can be observed in sample B compared to sample A. This may be due to the roughness of the flexible substrate and the constant flexing that the substrate exhibited during the fabrication process.

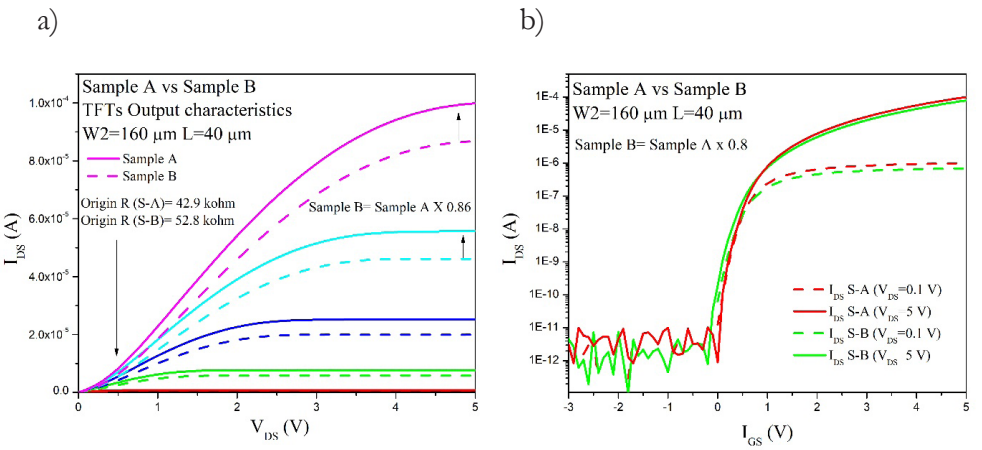

Figure 5. Shows the comparison of the a) output characteristics and b) transfer curves for devices of sample A and B without mechanical stress.

Figure 6 shows the transference curves for a device from sample B under conditions of mechanical stress with a bending radius of 4 mm. The device is completely new, which indicates that it has not been subjected to prior electrical characterization. A slight increase in field effect mobility is presented, and a reduction in V_{th} compared to a device without flexion. The values of SS, I_{ON}/I_{OFF} and I_{GS} are kept in close range for flexible devices. There is a slight increase in the DV_{TH} window for the linear transference curve, but not significant for the saturation transference curve.

Figure 7a shows the comparison of the saturation transference curves for a device from samples A, B and B with flexion of 4 mm radius. A clear shift of V_{th} towards negative values and an increase in ID_{max} current is observed for device B with flexion with respect to the device of sample A. The I_{GS} of the devices is plotted, where no notable variation is shown. Figure 7b shows the output characteristic curve for a value of V_{GS}=5 V, it highlights the behavior of devices B with

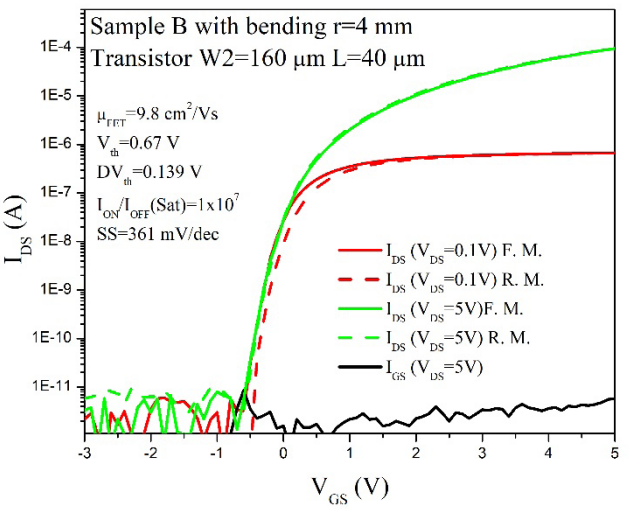

Figure 6. Show the transfer curves for a device of sample B with mechanical stress with a bending radius of 4 mm.

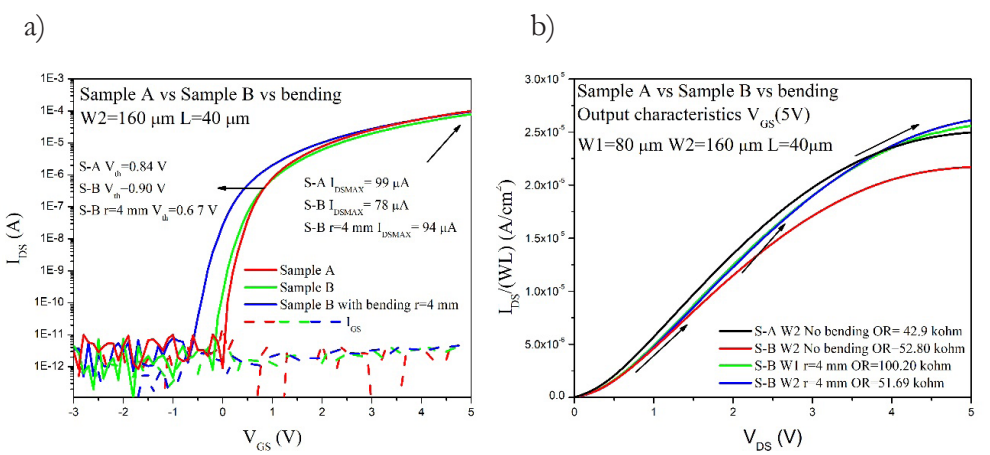

Figure 7. a) Transfer curves and b) output characteristics for devices of sample A, B, and B with bending

bending, which have an initial behavior corresponding to a flexible device without mechanical tension to a behavior of a device fabricated on a rigid substrate.

When comparing the results of two samples fabricated with the same technology, but changing their mechanical support, a reliability of the manufacturing process was obtained by seeing a good repeatability in their characteristic curves. For flexible substrates that show mechanical stress conditions with a radius of curvature of 4 mm, we can predict their use as health monitors in portable

applications that at least have a radius of curvature greater than 4 mm, for example the human finger has a radius of curvature of 12 mm, which may be feasible to use in this kind of applications.

4. Conclusions

In this work we evaluate the scalability of our thin-film transistor of fabrication process, when comparing the characterization of two identical TFT devices with the variant of being fabricated on two different substrates, rigid and flexible. Rigid substrate TFTs show slightly higher initial characteristics compared to flexible TFTs. The degradation in flexible devices is attributed to constant mechanical stress and roughness of the flexible substrate. Finally, in flexible devices under conditions of mechanical stress with a radius of curvature of 4 mm, present a combined behavior of a flexible device without mechanical stress to a device fabricate on a rigid substrate. We consider the use of this fabrication process for possible applications such as portable health monitors.

Acknowledgment

Isai Hernandez-Luna and Pablo Toledo would like to thank the CNMN-IPN for the experimental support in the realization of this work. Isai Hernandez-Luna would like to thank the program "Estancias Posdoctorales Académicas" by CONAHCYT.

Funding

This research was financially supported by SIP-IPN under grant 20230982 and 20231952.

References

1. Nathan, A., Ahnood, A., Cole, M. T., Lee, S., Suzuki, Y., & Hiralal, P. (2012). Flexible electronics: The next ubiquitous platform. *Proceedings of the IEEE*, 100(Special Centennial Issue), 1486-1517. https://doi.org/10.1109/JPROC.2012.2190168

2. Atwood, S. (2016). Mining the Vast Wealth of Display Week. *Information Display*, 32(5), 2-42. https://doi.org/10.1002/j.2637-496X.2016.tb00928.x

3. Wang, J., He, N., Fei, J., Ma, Z., Ji, Z., Chen, Z. *et al.* (2022). Flexible and wearable fuel cells: A review of configurations and applications. *Journal of Power Sources*, 551, 232190. https://doi.org/10.1002/j.2637-496X.2016.tb00928.x

4. Tee, B. C. K., Wang, C., Allen, R., & Bao, Z. (2012). An electrically and mechanically self-healing composite with pressure- and flexion-sensitive properties for electronic skin applications. *Nature Nanotechnology*, 7, 825-832. https://doi.org/10.1038/nnano.2012.192

5. Sharma, A., Ansari, M. Z., & Cho, C. (2022). Ultrasensitive flexible wearable pressure/strain sensors: Parameters, materials, mechanisms and applications. *Sensors and Actuators A: Physical*, 347, 113934. https://doi.org/10.1016/j.sna.2022.113934

6. Wang, Y., Guo, J., Xu, D., Gu, Z., & Zhao, Y. (2023). Micro-/nano-structured flexible electronics for biomedical applications. *Biomedical Technology*, 2, 1-14. https://doi.org/10.1016/j.bmt.2022.11.013

7. Liu, X., Wei, Y., & Qiu, Y. (2021). Advanced Flexible Skin-Like Pressure and Strain Sensors for Human Health Monitoring. *Micromachines*, 12(6), 695. https://doi.org/10.3390/mi12060695

8. Asghar, W., Li, F., Zhou, Y., Wu, Y., Yu, Z., Li, S. *et al.* (2020). Piezocapacitive Flexible E-Skin Pressure Sensors Having Magnetically Grown Microstructures. *Advanced Materials Technologies*, 5(2), 1900934. https://doi.org/10.1002/admt.201900934

9. Windmiller, J. R., & Wang, J. (2012). Wearable Electrochemical Sensors and Biosensors: A Review. *Electroanalysis*, 25(1), 29-46. https://doi.org/10.1002/elan.201200349

10. Cantarella, G., Catania, F., Munzenrieder, N., & Petti, L. (2022). Flexible, Scalable and Buckled Electronics based on Oxide Thin-Film Transistors. *In 4th IEEE International Flexible Electronics Technology Conference, IFETC 2022 - Proceeding, 2022.* https://doi.org/10.1109/IFETC53656.2022.9948509

11. Trung, N. D., & Kim, H. S. (2016). Oxide thin-film transistor for flexible display application. *In Proceedings - International NanoElectronics Conference, INEC*, Oct. 2016, vol. 2016-October.
https://doi.org/10.1109/INEC.2016.7589402

12. [12] Nakata, M., Tsuji, H., Fujisaki, Y., Nakajima, Y., Takei, T., Motomura, G. *et al.* (2015). Oxide thin-film transistor technology for flexible organic light-emitting diode displays. In *IEEE Industry Application Society - 51st Annual Meeting, IAS 2015, Conference Record*, 1-5.
https://doi.org/10.1109/IAS.2015.7356876

13. Petti, L. Münzenrieder, N., Vogt, C., Faber, H., Büthe, L., Cantarella, G. *et al.* (2016). Metal oxide semiconductor thin-film transistors for flexible electronics. *Applied Physics Reviews*, 3, 021303.
https://doi.org/10.1063/1.4953034

14. Nomura, K., Ohta, H., Takagi, A., Kamiya, T., Hirano, M., & Hosono, H. (2004). Room-temperature fabrication of transparent flexible thin-film transistors using amorphous oxide semiconductors. *Nature*, 432, 488-492.
https://doi.org/10.1038/nature03090

15. Zulqarnain, M., & Cantatore, E. (2021). Analog and Mixed Signal Circuit Design Techniques in Flexible Unipolar a-IGZO TFT Technology: Challenges and Recent Trends. In *IEEE Open Journal of Circuits and Systems*, 2, 743-756, Nov. 2021.
https://doi.org/10.1109/OJCAS.2021.3123206

16. Mativenga, M., & Haque, F. (2021). Highly Stable Thin-Film Transistors for Flexible and Transparent Displays. In *International Conference on Electrical, Computer, and Energy Technologies, ICECET 2021*, 2021.
https://doi.org/10.1109/ICECET52533.2021.9698710

17. Reza Chaji, G. (2008). Thin-film transistor integration for biomedical imaging and AMOLED displays. *UWSpace*, 47. [Online]. Available:
http://uwspace.uwaterloo.ca/handle/10012/3667

18. Chun, Y. S., Chang, S., & Lee, S. Y. (2011). Effects of gate insulators on the performance of a-IGZO TFT fabricated at room-temperature. *Microelectronic Engineering*, 88(7), 1590-1593.
https://doi.org/10.1016/j.mee.2011.01.076

19. Hsu, H. H., Chang, C.-Y., Cheng, C.-H., Chen, P.-C., Chiu, Y.-C. *et al.* (2014). High mobility field-effect thin film transistor using room-temperature high-$\varkappa$ gate dielectrics. In IEEE/OSA *Journal of Display Technology*, 10(10), 847-853.
https://doi.org/10.1109/JDT.2014.2331351

20. Wan, G. M., Ge, S. M., Gong, C., Li, S., & Lin, X. N. (2020). A stable FHD display device based on BCE IGZO TFTs. In *IOP Conference Series: Materials Science and Engineering*, Feb. 2020, 729, 012099.
https://doi.org/10.1088/1757-899X/729/1/012099

21. Kamiya, T., Nomura, K., & Hosono, H. (2010). Present status of amorphous In-Ga-Zn-O thin-film transistors. *Science and Technology of Advanced Materials*, 11(4), article 044305.
https://doi.org/10.1088/1468-6996/11/4/044305

22. Kamiya, T., Nomura, K., & Hosono, H. (2009). Origins of High Mobility and Low Operation Voltage of Amorphous Oxide TFTs: Electronic Structure, Electron Transport, Defects and Doping*. *Journal of Display Technology*, 5(12), 468-483.
https://doi.org/10.1109/JDT.2009.2034559

23. Wang, W., Li, L., Lu, C., Liu, Y., Lv, H., Xu, G. *et al.* (2015). Analysis of the contact resistance in amorphous InGaZnO thin film transistors. *Applied Physics Letters*, 107(6), 063504.
https://doi.org/10.1063/1.4928626

24. Wang, W., Li, L., Ji, Z., Lu, C., Liu, Y., Lv, H. *et al.* (2015). Analysis of the temperature dependent contact resistance in amorphous InGaZnO thin film transistors. In *IVNC 2015 - Technical Digest: 28th International Vacuum Nanoelectronics Conference*, Aug. 2015, 206-207.
https://doi.org/10.1109/IVNC.2015.7225585

25. Lee, J., Kim, M. J., Yang, H., Kim, S., Yeom, S., Ryu, G. *et al.* (2021). Extended-Gate Amorphous InGaZnO Thin Film Transistor for Biochemical Sensing. *IEEE Sensors Journal*, 21(1), 178-184.
https://doi.org/10.1109/JSEN.2020.3014447

26. Toledo, P., Hernandez-Pichardo, M. L., Garduño, S. I., Hernandez-Lopez, J. L., Hernandez-Cuevas, F., & Hernandez-Como, N. (2022). Threshold voltage reliability in flexible amorphous In–Ga–ZnO TFTs under simultaneous electrical and mechanical stress. *Flexible and Printed Electronics*, 7(2), 025015.
https://doi.org/10.1088/2058-8585/ac7186

27. Hong, S., Mativenga, M., & Jang, J. (2014). Extreme bending test of IGZO TFT. *In Proceedings of AM-FPD 2014 - The 21st International Workshop on Active-Matrix Flatpanel Displays and Devices: TFT Technologies and FPD Materials*, 125-127.
https://doi.org/10.1109/AM-FPD.2014.6867145

28. [28] Schroder, D. K. (2005). *Semiconductor material and device characterization*. (3rd Ed.).
https://doi.org/10.1002/0471749095

Chapter 2 Semiconductors and materials Area

SUPERHYDROPHOBIC NANOCOATING AND THEIR MECHANICAL STABILITY FOR BUILDINGS MATERIALS APPLICATION

J. Sanabria-Mafaile, E. San Martin-Martinez*

Centro de Investigación en Ciencia Aplicada y Tecnología Avanzada, Legaria 694. Instituto Politécnico Nacional. Colonia Irrigación, C.P. 11500, CDMX, México.

esanmartin@ipn.mx

Sanabria-Mafaile, J., & San Martin-Martinez, E. (2023). Superhydrophobic Nanocoating and Their Mechanical Stability for Buildings Materials Application. In E. San Martín-Martínez (Ed.). *Research advances in nanosciences, micro and nanotechnologies. Volume IV* (pp. 263-284). Barcelona, Spain: Omniascience.

Abstract

Superhydrophobic durability or robustness refers to the ability of a superhydrophobic coating to maintain its structure and resist external mechanical damage over time since it depends on this ability to be marketable. We developed a superhydrophobic coating surface based on a composite of SiO_2-nanoparticles, polystyrene (GPPS), and a non-solvent. The SiO_2/GPPS superhydrophobic composite coating has an apparent static contact angle (ASCA) with water of ~156.72±0.53° and a water slip angle of ~3.5±0.32°, these values are similar when the superhydrophobic coating are applied on different substrates surfaces. The durability of the superhydrophobic coating was investigated by applying different tests both in laboratory conditions and in natural environments. After each test, changes in the topography (mechanical wear) of the coating surface were examined by scanning electron microscopy. The superhydrophobic coating on quarry table tile substrate showed outstanding resistance against mechanical damage, including sticking, tangential abrasion, sharp scratching, thermal stability, and chemical corrosion while retaining its superhydrophobicity. The coated quarry table tile also showed excellent durability against the impact of water drops, but poor stability to ultraviolet (UV) radiation, and more importantly, the ceramic essentially showed high repellency to different liquids and, moreover, showed remarkable self-cleaning effect, highlighting its potential use in various practical applications.

Keywords: Superhydrophobicity, Polystyrene Nanocomposite, Self-cleaning Surface, Mechanical Durability, Spray Coating, Sol-Gel Method, Robust Coating.

1. Introduction

The ability of superhydrophobic surfaces to stay dry [1], self-cleaning [2], and anti-corrosion [3] is one of the most discussed topics at the present due to several practical applications across a wide range of areas, including buildings [4], textiles [5], medicine [6], drag reduction during fluid transportation [7, 8] and many others. It is well known that when water droplets get into contact with these surfaces, they must have high apparent static contact angles (> 150°) and low rolling-off angles (< 10°). This is possible for surfaces that have low-surface-energy chemistry and micro- or nanoscale surface roughness, which minimizes contact between the liquid and the solid surface [9 – 11]. Nevertheless, rough surfaces, where only a small fraction of the total area is in contact with the liquid, are very fragile and can be easily destroyed by light friction on the surface.

Up to date, most superhydrophobic surfaces have poor durability and tend to lose their anti-wetting properties even a slight friction or mechanical contact on the surface. The problem of durability or stability refers to wear by exploiting the hierarchical roughness or wear of the low surface energy coating or damage of both. However, mechanical contact not only causes damage to roughness topography but also surface contamination, which shortens the lifetime of superhydrophobic surfaces despite the self-cleaning effect. Thus, durability knowledge of a water-repellent surface is extremely important for applications in practical life, which determines whether superhydrophobic surfaces can be used in the area, and the performance of the devices in the long-term operation [12].

Nowadays, studies have begun to address the mechanical durability and a lot of characterization technique have been proposed, probing different aspects of durability on such surfaces (i.e., mechanical abrasion, dynamic impact, chemicals, severe environmental conditions, etc.) [13]. This in turn has led to the invention of new and more durable superhydrophobic surfaces. A few recent reviews exist which cover some aspects of characterization, enhancing the robustness of the hierarchical structure, and fabricating with hydrophobic materials. Several new strategies have been developed to address and solve this issue, for example, the use of a bonding layer [14, 15] strengthens the bond between the coating and the substrate, the random introduction of discrete microstructures [16 – 18] withstands the force of abrasion allowing the abrasion to wear away the top layers of the self-similar structure, these strategies have resulted in only modest improvements in robustness. To date, new strategic designs continue to be implemented to improve the mechanical

robustness of superhydrophobic coatings. Therefore, more efforts are still required to develop a highly robust superhydrophobic surface for industrial applications.

In this research, we successfully developed a semi-transparent, and mechanically stable superhydrophobic coating by Sol-Gel method. The product can be easily applied by Spray-coating technique on different kinds of solid substrates to create superhydrophobic surfaces with extremely high-water contact angles and low roll-off angles. The fabricated superhydrophobic surfaces were applied on different substrates, their repellency with different liquids was treated, and their self-cleaning effect was tested with water drops. The developed coatings were tested under adverse conditions such as tangential abrasion, temperature, tape peeling, sharp scratching, chemical corrosion, water droplet impact, and the severe environment.

The developed coating exhibits excellent stability for various wear tests and its self-cleaning effect promotes great potential for practical outdoor applications. In brief, the design and fabrication of durable and chemically stable superhydrophobic surfaces has become increasingly significant and practical.

2. Experimental Section

2.1. *Materials*

General Purpose Polystyrene granules (GPPS grade HF 777), melt flow index (MFI)=8 g/10 min obtained from Resirene S.A. of C.V. (CDMX, Mexico). Hydrophobic Fumed Silica (HFS, AEROSIL R972) (Silica, SiO_2) purchased from First Quality Chemicals, S.A. of C.V. (State of Mexico, Mexico) and used as received. AEROSIL R972 is a fumed silica after-treated with DDS (Dimethyldichlorosilane), it has a specific surface area of 90-130 m2/g and primary particle size of 16 nm. Tetrahydrofuran (THF) and Absolute Ethyl Alcohol (Ethanol, EtOH) were supplied from Merck (Darmstadt, Mexico) and used as received.

2.2. *Methods*

2.2.1. Preparation of the coating solution

The precursor coating solution was prepared as follows. GPPS solution at 2 wt% was prepared by dissolving GPPS granules into the solvent (THF) at

room temperature for 30 minutes, then, EtOH was slowly added to complete a solvent-nonsolvent ratio of 75:25 (THF/EtOH) and stirring for 15 minutes. Finally, a known amount of SiO_2-nanoparticles (36 wt%) were dispersed with the master solution while magnetically stirring for 1 hour until a homogeneous mixture was obtained.

The variables conditions for the superhydrophobic coating were content of SiO_2-nanoparticles at 36 wt%, substrate temperature at 150 °C, and substrate drying time at 50 min. Under these conditions, the surface is extremely rough, inducing non-wetting properties that are virtually unaffected by the underlaying substrate.

2.2.2. Deposition of the coating solution

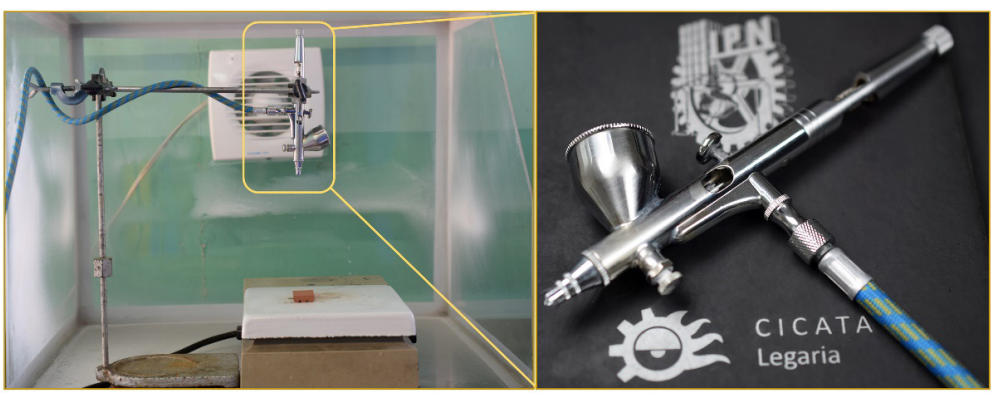

Figure 1. Image of the experimental spray coating set-up (airbrush + hot plate).

The coating solution were deposited by using the configuration in our previous paper. A simple commercial airbrush (Trupper Aero-35) system supplied by air compressor and fixed on a mechanic arm over a hot plate was used for the spray-coating. The spray distance from the substrate was held constant at 25 cm and air pressure at 45 psi. The solutions were sprayed onto clean substrates for 5 s. This procedure was repeated for 5 times with a time interval of 2 min. The airbrush was slowly moved laterally to make a uniform coating on the substrates. All films were made by this configuration technique. The representative image of the airbrush spray-coating setup is shown in Figure 1. For all substrates, the substrate temperature at 150 °C and the substrate drying time at 50 min. These precursor coating preparation conditions induce non-wetting properties that are virtually unaffected by the underlying substrate.

2.3. *Characterizations*

2.3.1. Superhydrophobic properties measurements

The surface roughness parameter (average roughness, Ra) was obtained by Dektak3 Surface Profilometer. The arithmetic average roughness value Ra reacts to hills and valleys, the measured length (ln) was 2000 μm at a speed of 2 μm/s. Apparent Static Contact Angle (ASCA) measurements of the superhydrophobic films were performed by the sessile drop method using a micro-pipette and tap water. The reported ASCAs are the mean values of measurements on a 10 μL water droplet at five different positions on each sample. Roll-off /Sliding Angles (SA) were determined by slowly tilting the sample stage until the 10 μL water droplet started to move. This measurement was performed 5 times for each sample, and all reported ASCA and SA are averages of the five measurements.

2.3.2. Superhydrophobic robustness tests

2.3.2.1. Adhesion test

Tape-peeling test was conducted to assess the adhesion stability of the hybrid superhydrophobic coating. The tape-peeling test was carried out using a 3M duct tape, based on the ASTM D3359-02 standard. The tape has a thickness of 0.19 mm and width of 46 mm which is just enough to cover the surface of the substrate. The pressure was laid by using a cylindrical aluminum block (5.0 kg) as a roller (Figure 2) across the coated surface to ensure a good contact with the coating, then slowly pulled away from the sample surface, and this process was repeated for 10 times at the sample place using a new tape. The non-wetting properties, i.e., apparent static contact angle (ASCA) and sliding angle (SA) are evaluated after each peeling cycle.

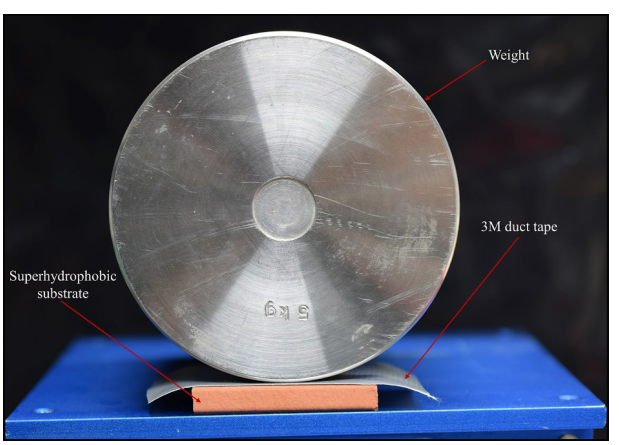

Figure 2. Photograph showing the tape-peeling test.

2.3.2.2. Tangential abrasion test

Wear abrasion test was conducted as illustrated in Figure 3. In this test, the sample is positioned on a 600-grit size sandpaper with the coated surface in contact with the sandpaper and on top of samples surface placed 320 g of weight is placed. In the first step, the sample travels a distance of 10 cm on the sandpaper, and then the sample is rotated 90°. In the second step, the sample returns to its original position with a travel distance of 10 cm. These two steps are considered as one abrasion cycle. A total of 10 abrasion test cycles are carry out that correspond to a total travel distance of 200 cm. The pressure applied on the surface during the test was approximately 2.33 kPa, according to the size of the piece of quarry table tile of 45 x 30 mm and 320 g of weight on it. After each abrasion, the superhydrophobic surfaces were cleaned by blown with air. The values of the ASCA and SA measurements were taken after every abrasion linear cycle on the material.

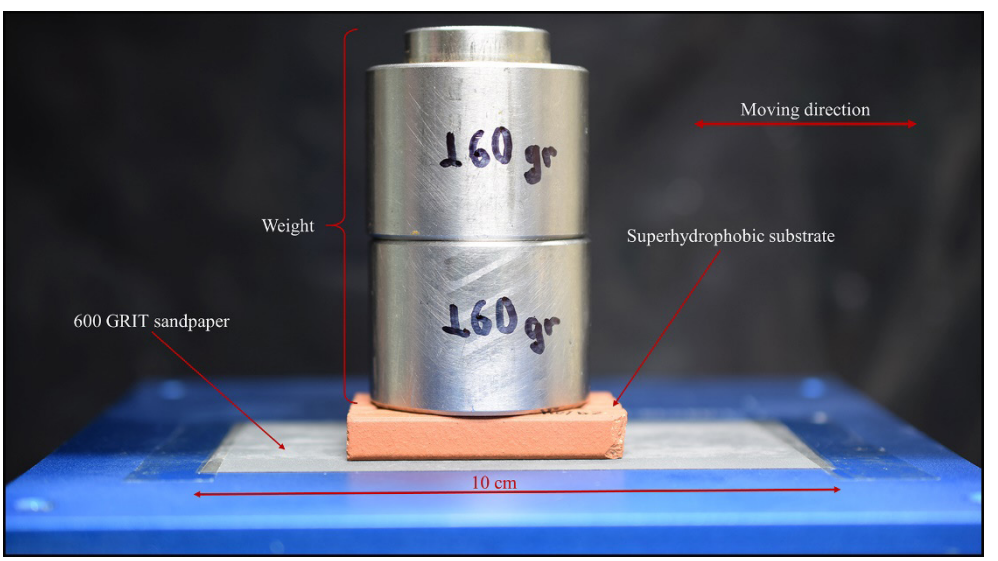

Figure 3. Photograph of the abrasion test of superhydrophobic surface.

2.3.2.3. Sharp scratch test

The sharp object scratch test was conducted by using a steel blade as the indenter. The coated samples were placed on a flat smooth stage. The flat steel blade was then dragged by hand in two directions perpendicular to the sample dimensions. In this test, the pressure applied to the top surface of the superhydrophobic film is sufficient to severe damage it.

2.3.2.4. Dynamic impact test

Water-droplet impact experiment was performed and the impingement process of water droplets on the surface was captured by a high-speed camera fitted with a macro lens. The continuous water drops apparatus was homebuilt as shown in Figure 4. The test was carried out following some steps as reported [19 – 21]. The superhydrophobic sample was mounted on a lab tripod stage and place at 35 cm below the shower head water drops exit. The water-droplet impact experiment is supplied with a laboratory peristaltic pump with a velocity of 10 rpm to create a water mass flow rate of 1.8 L/min. Droplets were impacted onto the superhydrophobic sample during 10 min. After drops impact interval, the samples are shaken by hand for 2 minutes to remove embedded drops on the surface, then the tested surface is blown with compressed air 1 minute from approximately 10 cm to remove the drops remaining, all this process was repeated 6 times for a same sample. After 6-time intervals, equaling a total of 60 minutes, the sample was heated at 100 °C for 40 min to evaporate any water trapped inside the surface asperities.

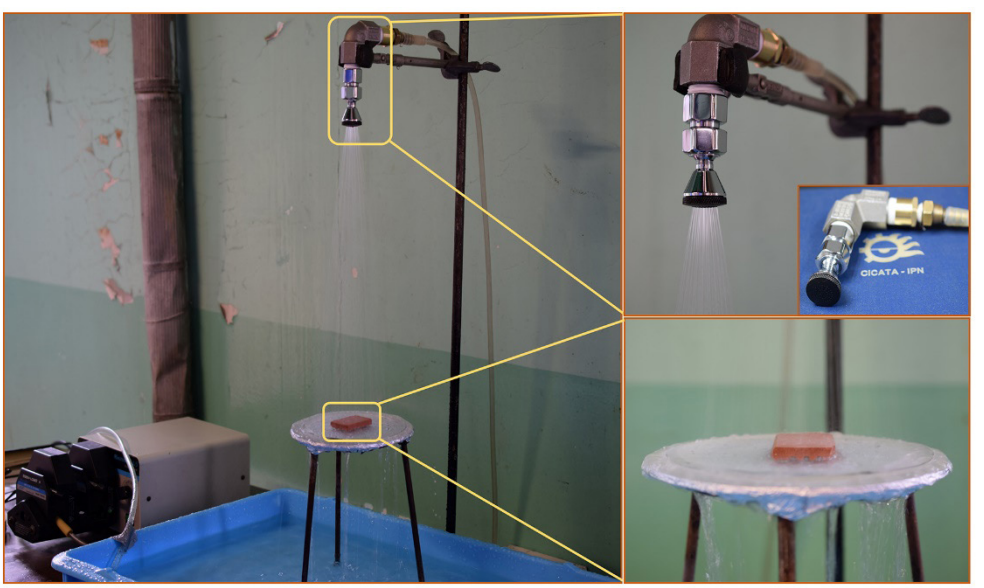

Figure 4. Photo of the water droplets impact test set-up.

2.3.2.5. Environmental test

In order to test the practical performance and durability of the superhydrophobic samples, outdoor weathering test was carried out for a testing period of 2 months (60 days) on the roof of a tall building in Mexico City. Samples were placed horizontally.

Under outdoor weathering, the superhydrophobic coating is exposed against harsh environmental ageing, i.e., heat, moisture, acidic rainfall, and UV radiation. The performance analysis of the superhydrophobic sample was caried out by analysis the ASCA and SA every 10 days till 60 days. ASCA and SA measurements were measured using the same set-up mentioned early at room temperature. The values to be reported are the average of five measurements made on different areas of the sample.

2.3.2.6. Thermal stability test

The effect of thermal stability was performed by heating the superhydrophobic coating into a muffle at a constant temperature. The superhydrophobic samples were exposed to temperatures of 100 °C for 20 days. ASCA and SA values were measured after cooling to room temperature every 5 days.

2.3.2.7. Chemical corrosion test

In this research, we evaluated the acid- and alkali-resistant ability of superhydrophobic of as-prepared material. The ASCAs of acidic and basic aqueous solutions with pH ranging from 1 to 14 were measured. For a pH value, five droplets were placed in different positions for each sample and the ASCA average value was taken as its ASCA value, all measurements were carried out at room temperature.

3. Finding and Discussion

3.1. *Wettability of the surfaces: Application on different substrates surfaces*

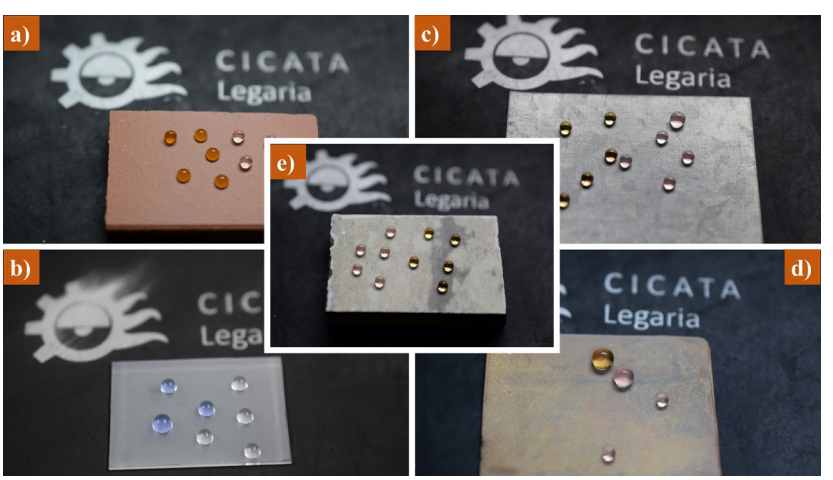

Figure 5. Photo of water droplets deposited on different substrates: a) quarry table tile, b) glass coverslip, c) galvanized steel sheet, d) copper sheet, and e) tile.

The methodology development presented has the advantage that it can be easily used to treat surfaces of several kinds of substrate. The evidence for this statement is provided in Figure 5 and Table 1, which show the experimental and observed results of ASCA, SR, and SA measurements, respectively, carry out treated surfaces of tile, galvanized steel sheet, and cooper sheet. For comparison, superhydrophobic properties on glass coverslip and quarry table tile, discussed previously reported, are also included.

Table 1. Superhydrophobic properties measured on different substrates.

Substrate	Predicted values		Superhydrophobic properties		
	ASCA (°)	SR (nm)	ASCA (°)	SR (nm)	SA (°)
Quarry table tile	156.51	54.62	157.19±0.33	55.79±0.35	3.2±0.15
Glass coverslip			156.76±0.52	54.32±0.63	3.4±0.45
Galvanized steel sheet			156.19±0.67	54.06±0.73	3.5±0.13
Cooper sheet			156.19±0.74	55.46±0.43	3.4±0.53
Tile			157.27±0.37	55.75±0.84	3.2±0.35

As we can see, the values of ASCA and SR that correspond to the five substrates are in agreement with the expected experimental value. ASCA, SR, and SA reported in Table 1 for various treated substrates show narrow ranges of variations, this could be attributed to the difference on the roughnesses of the substrate materials. We can say that our superhydrophobic coating deposited on these substrates are not affected by the type of substrate surface.

3.2. *Wettability of the surfaces: Application with different kinds of liquids*

We evaluated some common liquids, such as tea, orange juice, milk, Coca-Cola, and urine. In Figure 6 droplets of different liquids are shown in the shape of a sphere on the superhydrophobic substrate. The superhydrophobic character of the coated substrate was evaluated as performed a water droplet by measuring the ASCA and SA.

The results are shown in Figure 6, the ASCA of the liquids remained above 150° and the SA below 10°. However, we note that for milk, SA showed a slight increase, this may be due to the fact that the surface tension presented by this liquid is very close to the value of the surface tension of the coating.

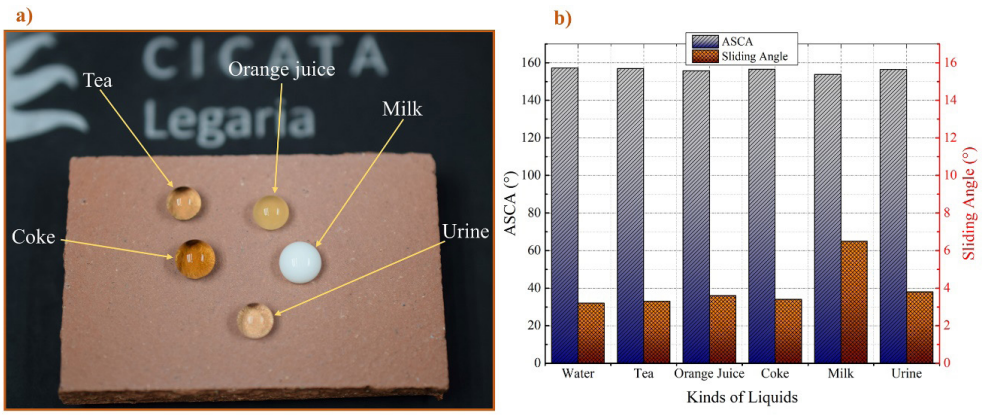

Figure 6. a) Photo of the different kinds of liquids on the superhydrophobic quarry table tile substrate, b) ASCA and SA of different kinds of liquids.

3.3. *Self-cleaning performance*

It is well known that the self-cleaning effect is a significant characteristic of superhydrophobic surface in real application. In this study, natural graphite particles were used as a contaminant to investigate the self-cleaning performance of coated surface. The photographs in Figure 7 illustrate the time sequence of self-cleaning ability. The superhydrophobic substrate was set at a ~8° tilt.

Figure 7a shows the superhydrophobic substrate clean, i.e., without natural graphite particles. While Figure 7b shows the natural graphite particles that were

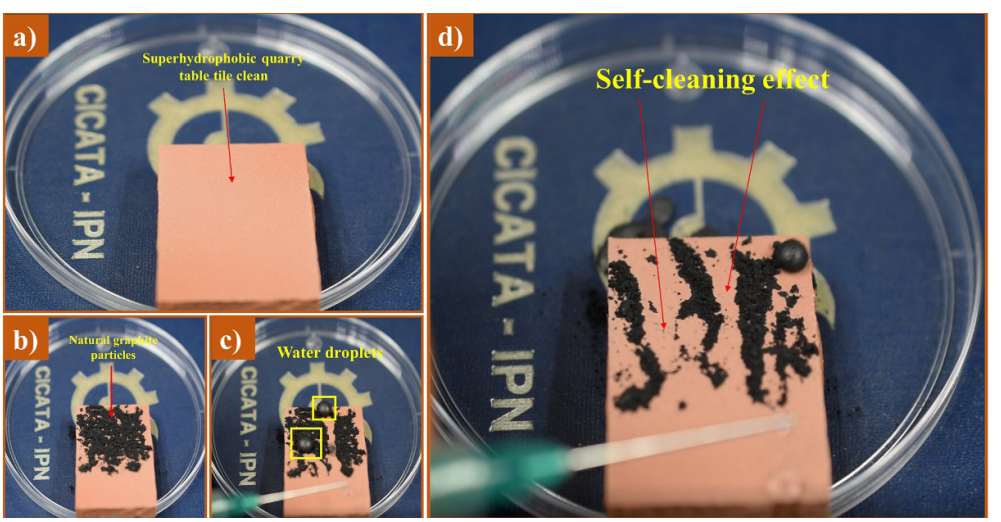

Figure 7. Time sequence of the self-cleaning test on the coated surface with ~8° tilt.

deliberately spread on the superhydrophobic coating surface. We observed that, as the water droplets were dropped to the coated surface, the droplets began to roll off swiftly taking away the contaminant particles (Figure 7c, 7d). This behavior is attributed to the joint action of the high capillary forces resulting from the water droplet and the weak adhesion of the contaminant particles to the superhydrophobic coated [7]. Therefore, our superhydrophobic film exhibits an excellent self-cleaning effect and expansive potential application prospects.

3.4. *Adhesion performance*

Testing the adhesion was the first measurement to be conducted in a test series regarding mechanical durability evaluation of the superhydrophobic film. The results are plotted in Figure 8. As we can see, the superhydrophobic of the hybrid coating can maintain until 8 peel cycles (ASCA ~150±0.30° and SA ~7.50, Figure 8a). Additionally, the inset photographs show remains of tape on the substrate and that when it was removed it stuck to the film or in any case to the substrate causing loss of superhydrophobicity. On the contrary, we noticed 9 and 10 peel-off cycles caused damage or detachment of the film. This negative trend is evidence of the observation that the film was peeling-off the substrate during latest cycles of testing (Figure 8b), indicating that a little hydrophobic SiO_2-nanoparticles were transferred to the tape surface, leading to an antiwetting performance degradation.

This mechanical adhesion stability indicated that the manufactured superhydrophobic layer had a good adhesion property to the quarry table tile substrate up to 8 peel cycles, proving that the coating could be considered as robust.

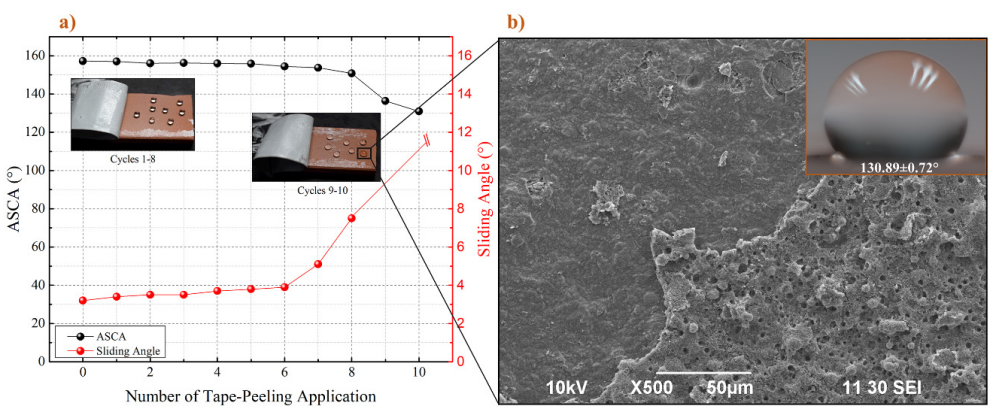

Figure 8. a) ASCA and SA measured tape-peeling cycles on the superhydrophobic sample. Insets: photographs of tape test and image of scotch tape surface. b) SEM image after peeling off sticky tape. Inset: ASCA of the coating after 10 tape-peeling cycles.

3.5. *Wear abrasion performance*

In this research work, the superhydrophobic layer was abraded by sandpaper with 10 abrasion cycles. Figure 9a shows the ASCA and SA for different friction cycles and the insets images of the static water droplets for the 1st and 10th abrasion cycles. It can be seen that as the friction cycles increased from 1 to 8 times under 320 g of weight, the ASCA of the material still maintained more than 150° and SA less than 10°. On the other hand, when the abrasion cycles reached 10 times, the surface lost its superhydrophobicity with a travel distance of 200 cm. Further abrasion of superhydrophobic sample makes it superhydrophobic stick and even large water droplets do not roll off at 90° tilt angles. This is due to physical abrasion and resultant polymer/nanoparticle wear and removal from the surface layer. Inspection of SEM images after 10 ties of wear abrasion cycles supports this statement (see Figure 9b).

After mechanical abrasion cycles, the tests results demonstrated a slight change in superhydrophobic properties, yet the special hybrid coating could efficiently withstand the abrasion cycles to some extent, maintaining its superhydrophobicity.

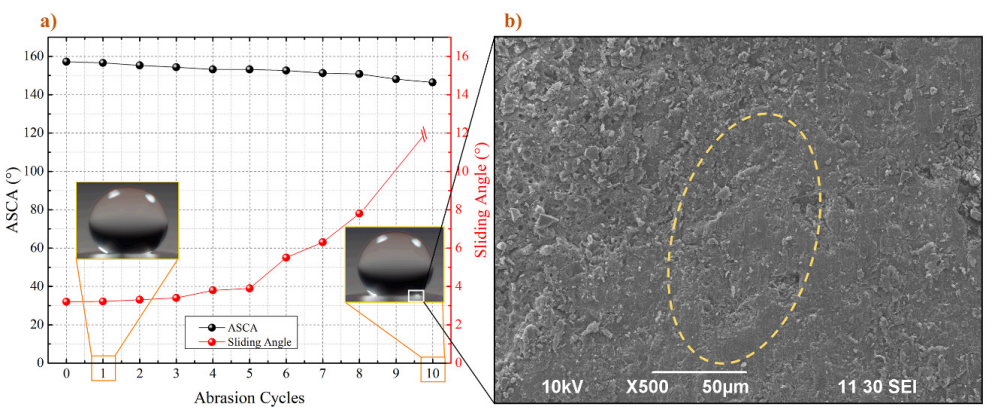

Figure 9. a) ASCA and SA measured for the abrasion cycles. Inset: shape of the water droplets on the surface. b) SEM image after 10 cycles of abrasion test.

3.6. *Sharp scratched performance*

To further study the mechanical durability of superhydrophobic films, a sharp scratch test was performed. As shown in Figure 10a, a series of sharp scratches on the as-prepared hybrid material are noticed, indicating that the

superhydrophobic material could not stand for sharp scratch test. However, the water droplets on the scratched superhydrophobic surface can still move freely as long as it does not hit a scratch. We also note that, after sharp scratched tests, severe abrasion scratches are observed at macro-scale on the superhydrophobic surface that even the hybrid material could be removed from the substrate. SEM images of the coating after sharp scratched tests showed significant alteration of superhydrophobic surface morphology (Figure 10b), so the superhydrophobic coating cannot pass the sharp scratch test.

The results demonstrate that superhydrophobic films which have a micro-scale topography is not tolerant to damage. In real application, the high sharp scratch can extend the applied range of the superhydrophobic materials.

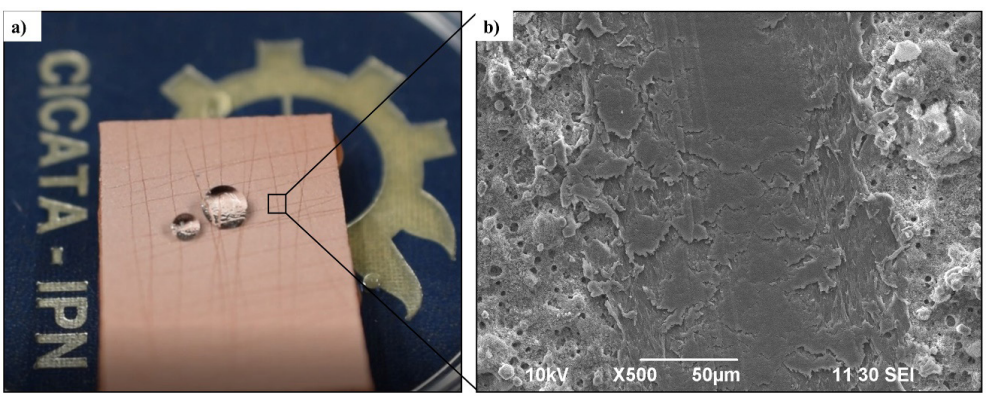

Figure 10. a) Image of the superhydrophobic coating after abrasion with sharp scratch. b) SEM micrographs of coated substrate after scratching with a knife.

3.7. *Water-droplet impact performance*

The durability of the superhydrophobic coating was also assessed by a high-speed droplet impact experiment. Figure 11a illustrates the effect of water on the ASCA and SA of the superhydrophobic film immediately after each spray droplet impact interval. It is evident that the average values of ASCA and SA did not experience significant changes after being sprayed for 20 min. After that exposure time, the sample lost its superhydrophobic performance (ASCA <150° and SA >10°). This indicates that the intense water droplet impact test damages the superhydrophobicity of the coating by either removing SiO_2-nanoparticles from the surface of the composite material or by degrading hydroxyl oxide functional groups or other low surface energy functional groups.

Upon heating the samples after the spray droplet impact test, the ASCA of the sample recovered to some degree but did not return to its initial value. This indicates that the loss superhydrophobicity property during droplet spraying was not due to mechanical erosion or change in surface morphology, but rather to saturation of the microstructured surface due to water, as can be seen in the SEM image in Figure 11b. This saturation might effectively change the coating surface from the superhydrophobic Cassie-Baxter state to the wetted Wenzel state [19, 22].

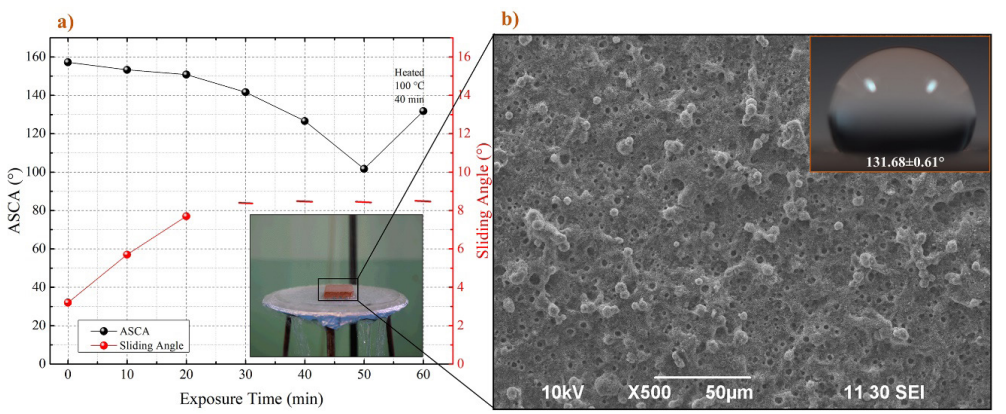

Figure 11. a) ASCA and SA details with respect to exposure time of water droplets impact. b) SEM image of surface after exposure to simulated rain.

Studies reported by Zhang *et al.* [16] conclude that when an external force is applied to the surface either by water jet impact, water drop impact, sand particle impact abrasion or direct shear abrasion, water or sand could impregnate into the grooves od the rough texture if the impact force is large enough and subsequently remove part or all of the coverage of the nanoparticle surface of the coating that does not have chemical bond with the substrate.

3.8. *Outdoor weather performance*

In order to assess the practical long-term performance of the superhydrophobic substrate, it was exposed to outdoor weathering for a 2-months period. For the outdoor weathering experiment, ASCA values are plotted in Figure 12a as a function of time (days), and the inset images show the surface change and degradation of the superhydrophobic film over the days. From Figure 12a, it is observed that the apparent static contact angles decrease abruptly linearly from 161.58±0.78° to 86.46±0.61° over two months of outdoor weathering.

We believe that the increase deterioration effect of the superhydrophobic film is due to either the accumulation of dust particles on the samples or the sticking of the dust particles after water droplets evaporate from the surface over time. Moreover, it can be clearly observed from Figure 12b that the coating shows some cracks which are the beginning of the deterioration phenomenon.

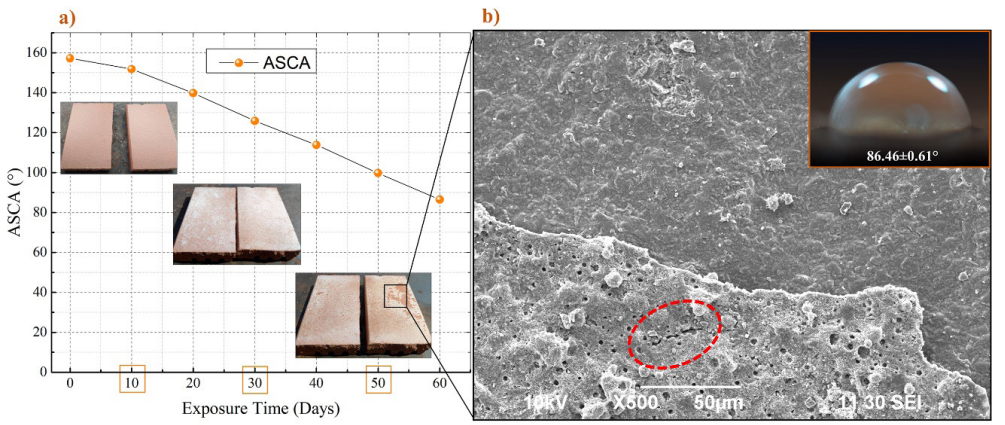

Figure 12. a) ASCA and SA with respect to exposure time in days. Inset: Photograph of the sample on a certain day. b) SEM image of the coated sample after outdoor exposure. Inset: Shape of the water droplet on the coated surface.

Studies conducted by Sakhuja *et al.* [23] report that the degradation effect caused by outdoor weathering on their superhydrophobic films decreases as long as they are mounted at an inclination of either 10° or 20°. They hypothesized that when the dirt particles come into contact with nanostructured substrates, they cannot penetrate the nanosized voids between two adjacent nanostructures, but instead settle on the nanostructures surface of the substrate. Therefore, the contaminant particles flow together with the water off the surface, allowing the coated substrates to exhibit a self-cleaning effect compared to horizontally placed samples where the contaminant particles mix with water and remain adhered to the surface of the nanostructured substrate. Thus, the improvement in the self-cleaning effect may be due to the inclination angle of the substrate. Inclination of the substrate has an important effect on self-cleaning behavior, allowing the water flowing over sample to provide a sheeting effect, removing dirt particles more easily during rains.

3.9. *Thermal stability performance*

The effect of thermal treatment on the wettability of the superhydrophobic coating was systematically studied. The superhydrophobic substrate was heated

at 100 °C for 20 days, the ASCA and SA values were measured at room temperature every 5 days, and the results are shown in Figure 13.

As can be clearly seen in Figure 13a, the composite coating remained superhydrophobic property till 15 days of exposure time into an oven and water drops rolled on the surface of the coating. However, as the exposure time increases to 20 days, ASCA dramatically decrease to 141.73±0.56° and SA increased to >10°, this could be attributed to the decomposition of GPPS in the coating composite, and some of the GPPS fragments volatilized leading to the water drops wetting the coating surface. Meanwhile, we believe that silica oxide hydroxyl groups could remain on the surface of hydrophobic SiO_2-nanoparticles reacting with each other, and this reaction might also occur between the substrate and the SiO_2-nanoparticles.

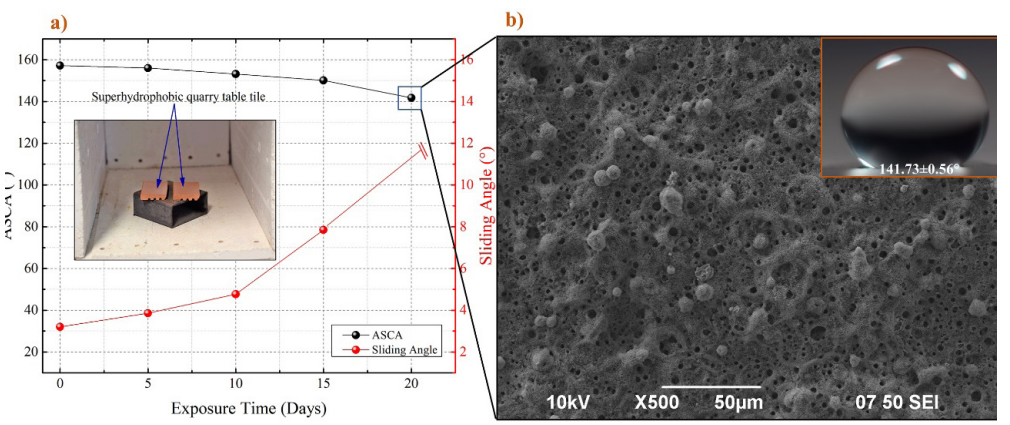

Figure 13. a) Effect of temperature on superhydrophobicity. b) SEM image of superhydrophobic coating after 20 days of heating exposure. Inset: ASCA for the sample.

Nevertheless, with the continuous decomposition of the hybrid nanocomposite and the condensation between hydroxyls, the Si-CH_3 groups lead to decomposition, and a mass of Si-OH generated, could result in the superhydrophobicity of the coating. In addition, we can note that the superhydrophobic coating does not suffer physical damage (Figure 13b) but chemical decomposition as we have just described. These results indicate that the thermal stability of our superhydrophobic film could be stable at least for 15 days.

3.10. *Chemical corrosion performance*

In our previous tests on mechanical stability, the apparent static contact angle (ASCA) and sliding angle (SA) measurements were evaluated by using pure water. However, in practical applications, the majority of liquids are not pure water only.

Thus, it is recommended to study the wettability properties of different liquids with different pH values on the superhydrophobic films. In this research, we evaluated the acid-and alkali-resistant ability of superhydrophobic GPPS film of different liquids with pH ranging from 1 to 14.

Figure 14a shows the relationship between pH values versus ASCA and SA, and the photograph inset shows the shapes of acidic and basic aqueous droplets on the superhydrophobic quarry table tile substrate. As can be seen, water droplets with pH range from 1 to 12 have no significant effect on the ASCA and SA. That is, the ASCASs are larger than 150° and SAs were still less than 10° for corrosive liquids. In addition, when the aqueous liquid droplets contacted with the porous superhydrophobic GPPS film after a short period of time, no decrease in ASCA was observed, this could be due to the mico/nanostructure of the coating did not deteriorate after being in contact with the aqueous solution droplets. Therefore, the water droplet can be moved easily when the surface is slightly tilted. However, for the pH values of 13 and 14, the ASCAs were 132.34±0.38° and 133.11±0.51°, respectively, and the SAs were not possible to measure it for those pH values. In this case, the less ASCA and the high SA observed in alkaline solution is attributed to the chemical wear degradation of the hybrid nanocomposites being faster than in acid solution. As can be seen in SEM image (Figure 14b), the superhydrophobic coating does not suffer physical damage, but the loss of the superhydrophobic property can be due to the chemical wear of the film, this statement must be corroborated by EDS or FTIR measurements, which are not shown in this study. From an experimental point of view, with respect to these results, our superhydrophobic GPPS is suitable for practical applications in corrosive liquids between the 1-12 pH range.

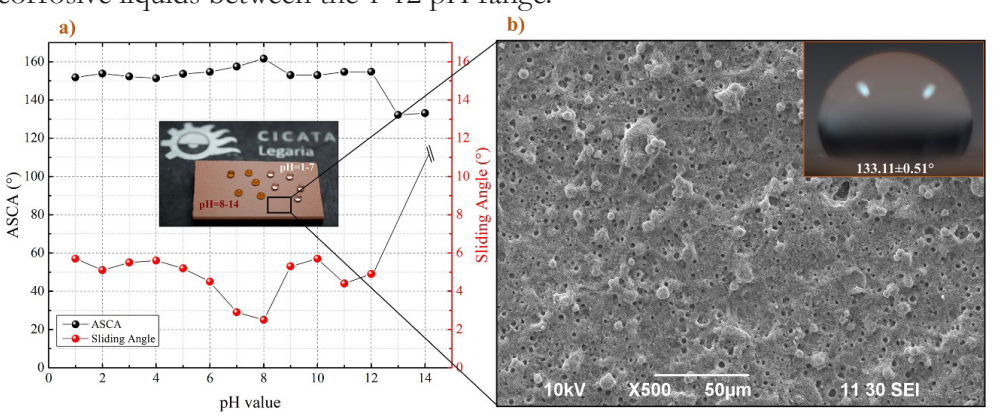

Figure 14. a) ASCA and SA on the superhydrophobic substrate. Inset: Image of the different pH value liquids on the superhydrophobic material. b) SEM image after chemical corrosion test.

The corrosion of strong acidic or basic liquids on a solid surface is known to be great. Therefore, the surface micro/nanostructure found on a solid substrate can be destroyed due to the strong corrosive property when suffering strong acidic or basic aqueous solutions, which may lead to the changes of ASCA and SA because the geometric micro/nanostructure of the surface is an important factor for the wettability of a solid [24, 25].

4. Conclusions

The superhydrophobic coating showed exceptional liquid-repellency to some liquids including water, tea, orange juice, milk, coke, and urine. The substrate shown to have almost no effect on the hydrophobic character of the applied coatings, which were produced on quarry tablet tile, glass coverslip, tile, galvanized steel and copper sheet.

The results demonstrated that the superhydrophobic films present a considerable mechanical resistance toward multi-fold, adhesion, wear abrasion, sharp scratch, water-droplet impact, thermal stability, outdoor weathering, and even chemical corrosion. Our design strategy could also be applied to different kinds of heat-resistant materials, brick, aluminum, or concrete, which are needed to retain effective self-cleaning, anti-fouling or anti-corrosion abilities in harsh operating environments.

A proper control of nanoparticles is one of the main challenges to produce a hierarchical rough surface and, moreover, the mechanisms that trigger the Cassie-Baxter and Wenzel regime transitions still need to be further investigated.

The Sol-Gel method and the Spray-Coating technique are simple and cheap, they demonstrate that the development of superhydrophobic surfaces can be obtained in the laboratory for future research and other application areas.

Acknowledgement and Funding

The authors acknowledge the financially supported by Consejo Nacional de Ciencia y Tecnología (CONAHCYT), Beca de Estímulo de Formación de Investigadores (BEIFI), and Secretaría de Investigación y Posgrado (SIP-IPN). We greatly appreciate to Centro de Investigación en Ciencia Aplicada y Tecnología Avanzada - Unidad Legaria. Especial thanks to Dr Miguel Angel Aguilar Frutis for his kind support.

References

1. Wang, D., Sun, Q., Hokkanen, M. J., Zhang, C., Lin, F.-Y., Liu, Q. *et al.* (2020). Design of robust superhydrophobic surfaces, *Nature*, 582, 55-59. https://doi.org/10.1038/s41586-020-2331-8

2. Wang, X.-Y., Zhang, C., Sun, S., Kalulu, M., Chen, L., Zhou, X. *et al.* (2019). Durable superhydrophobic coating based on inorganic/organic double-network polysiloxane and functionalized nanoparticles. *Colloids and Surfaces A: Physicochemical and Engineering Aspects*, 578, 123550. https://doi.org/10.1016/j.colsurfa.2019.06.016

3. Figueira, R. B., Sousa, R., & Silva, C. J. R. (2020). Chapter 3. Multifunctional and smart organic–inorganic hybrid sol–gel coatings for corrosion protection applications. In: A.S.H. Makhlouf, N.Y. Abu-Thabit (Eds.). *Advances in smart coatings and thin films for future industrial and biomedical engineering applications*. Elsevier, Amsterdam, 2019, 57-97. https://doi.org/10.1016/B978-0-12-849870-5.00008-2

4. Carrascosa, L. A. M., Facio, D. S., & Mosquera, M. J. (2016). Producing superhydrophobic roof tiles. *Nanotechnology*, 27, 095604. https://doi.org/10.1088/0957-4484/27/9/095604

5. Zahid, M., Heredia-Guerrero, J. A., Athanassiou, A., & Bayer, I. S. (2017). Robust water repellent treatment for woven cotton fabrics with eco-friendly polymers. *Chemical Engineering Journal*, 319 321-332. https://doi.org/10.1016/j.cej.2017.03.006

6. Hou, X., Wang, X., Zhu, Q., Bao, J., Mao, C., Jiang, L. *et al.* (2010). Preparation of polypropylene superhydrophobic surface and its blood compatibility. *Colloids and Surfaces. B: Biointerfaces*, 80, 247-250. https://doi.org/10.1016/j.colsurfb.2010.06.013

7. Bake, A., Merah, N., Matin, A., Gondal, M., Qahtan, T., & Abu-Dheir, N. (2018). Preparation of transparent and robust superhydrophobic surfaces for self-cleaning applications. *Progress in Organic Coatings*, 122, 170-179. https://doi.org/10.1016/j.porgcoat.2018.05.018

8. Li, K., Zeng, X., Li, H., Lai, X., & Xie, H. (2014). Effects of calcination temperature on the microstructure and wetting behavior of superhydrophobic polydimethylsiloxane/silica coating. *Colloids and Surfaces A: Physicochemical and Engineering Aspects*, 445, 111-118. https://doi.org/10.1016/j.colsurfa.2014.01.024.

9. Quéré, D. (2008). Wetting and Roughness. Annual Review of Materials Research, 38, 71-99. https://doi.org/10.1146/annurev.matsci.38.060407.132434

10. Butt, H.-J., Roisman, I. V., Brinkmann, M., Papadopoulos, P., Vollmer, D., & Semprebon, C. (2014). Characterization of super liquid-repellent surfaces. *Current Opinion in Colloid & Interface Science*, 19(4), 343-354.
https://doi.org/10.1016/j.cocis.2014.04.009

11. Liu, T.L., & Kim, C.-J. (2014). Repellent surfaces. Turning a surface superrepellent even to completely wetting liquids. *Science*, 346(6213), 1096-1100.
https://doi.org/10.1126/science.1254787

12. Verho, T., Bower, C., Andrew, P., Franssila, S., Ikkala, O., & Ras, R. H. A. (2011). Mechanically durable superhydrophobic surfaces. *Advanced Materials*, 23(5), 673-678.
https://doi.org/10.1002/adma.201003129

13. Milionis, A., Loth, E., & Bayer, I. S. (2016). Recent advances in the mechanical durability of superhydrophobic materials. *Advances in Colloid and Interface Science*, 229, 57-79.
https://doi.org/10.1016/j.cis.2015.12.007

14. Lu, Y., Sathasivam, S., Song, J., Crick, C., Carmalt, C. J., & Parkin, I. P. (2015). Robust self-cleaning surfaces that function when exposed to either air or oil. *Science*, 347(6226), 1132-1135.
https://doi.org/10.1126/science.aaa0946

15. Zhang, W., Xiang, T., Liu, F., Zhang, M., Gan, W., Zhai, X. *et al.* (2017). Facile Design and Fabrication of Superwetting Surfaces with Excellent Wear-Resistanc. *ACS Applied Materials & Interfaces*, 9(18), 15776-15784.
https://doi.org/10.1021/acsami.7b02158

16. Zhang, Y., Ge, D., & Yang, S. (2014). Spray-coating of superhydrophobic aluminum alloys with enhanced mechanical robustness. *Journal of Colloid and Interface Science*, 423, 101-107.
https://doi.org/10.1016/j.jcis.2014.02.024

17. Kondrashov, V., & Rühe, J. (2014). Microcones and nanograss: toward mechanically robust superhydrophobic surfaces. *Langmuir*, 30, 4342-4350.
https://doi.org/10.1021/la500395e

18. Zimmermann, J., Reifler, F. A., Fortunato, G., Gerhardt, L.-C., & Seeger, S. (2008). A Simple, One-Step Approach to Durable and Robust Superhydrophobic Textiles. *Advanced Functional Materials*, 18(22), 3662-3669.
https://doi.org/10.1002/adfm.200800755

19. Davis, A., Yeong, Y. H., Steele, A., Loth, E., & Bayer, I. S. (2014). Spray impact resistance of a superhydrophobic nanocomposite coating. *AIChE Journal*, 60(8), 3025-3032.
https://doi.org/10.1002/aic.14457

20. Sanabria-Mafaile, J., San Martin-Martinez, E., & Cruz-Orea, A. (2020). Thermal properties of superhydrophobic films applied in ceramic tiles. *Colloids and Surfaces A: Physicochemical and Engineering Aspects*, 607, 125524. https://doi.org/10.1016/j.colsurfa.2020.125524

21. Bhushan, B., & Jung, Y. C. (2011). Natural and biomimetic artificial surfaces for superhydrophobicity, self-cleaning, low adhesion, and drag reduction. *Progress in Materials Science*, 56(1), 1-108. https://doi.org/10.1016/j.pmatsci.2010.04.003

22. [22] Davis, A., Yeong, Y. H., Steele, A., Loth, E., & Bayer, I. S. (2014). Nanocomposite coating superhydrophobicity recovery after prolonged high-impact simulated rain. *RSC Advances*, 88, 47222-47226. https://doi.org/10.1039/C4RA08622H

23. [23] Sakhuja, M., Son, J., Yang, H., Bhatia, C. S., & Danner, A. J. (2014). Outdoor performance and durability testing of antireflecting and self-cleaning glass for photovoltaic applications. *Solar Energy*, 110, 231-238. https://doi.org/10.1016/j.solener.2014.07.003

24. [24] Sun, X. L., Fan, Z. P., Zhang, L. D., Wang, L., Wei, Z. J., Wang, X. Q. *et al.* (2011). Superhydrophobicity of silica nanoparticles modified with polystyrene. *Applied Surface Science*, 257(6), 2308-2312. https://doi.org/10.1016/j.apsusc.2010.09.094

25. [25] Chen, H., Yuan, Z., Zhang, J., Liu, Y., Li, K., Zhao, D. *et al.* (2009). Preparation, characterization and wettability of porous superhydrophobic poly (vinyl chloride) surface. *Journal of Porous Materials*, 16, 447-451. https://doi.org/10.1007/s10934-008-9217-8

FINAL CONCLUSIONS AND RECOMMENDATIONS

In this volume IV, researchers in energy have developed innovative methods for renewable and clean energy, in particular, in electrolyzers for the generation of hydrogen from water, a reaction known as water splitting or oxidation with the topics "Incorporation of Fe -F6 blocks into laminar hydroxides of Fe, Ni: exploring on the water oxidation reaction"; "Photocatalytic generation of hydrogen using titanium and bismuth oxide catalysts". Other topics for the development of solid fuel cells; "Evaluation of the partial substitution of the lanthanum A-site in ABO_3-type perovskites: structural and properties for solid-state fuel cells applications"; Or the use of by-products of biodiesel production "Glycerol electrooxidation for energy conversion using metal nanoparticles."

In the area of health, research is focused on the study of breast cancer with two investigations "Nanostructured lipid carriers for cancer treatment: effect of process parameters on particle size and polydispersity index using experimental design" and "Design of nanomaterials toward the contrast enhancement in mammography images for breast cancer diagnosis". Other investigations "Thermal study of nanocomposites for medical applications" and "Numerical simulation of a PDMS microfluidic channel compatible with biosensors", contribute to new medical devices to use as future tools.

Research in food seeks conservation through coating with nanostructured films and incorporating natural compounds that can improve conservation. They are also investigating the incorporation of nutrients in nanocapsules or nanofibers, which can later be administered in daily intakes.

The development of new materials such as "Reliability of flexible amorphous In-Ga-Zn-O (a-IGZO) thin-film transistors" and Superhydrophobic Nanocoating and Their Mechanical Stability for Buildings Materials Application, carry out research for applications in new areas, depending on of the entrepreneurial demands will be successful.

Readers and researchers in nanosciences will find in this volume IV of advances in micro nanosciences and nanotechnology of the RNMN network of the IPN, innovative and original research that covers most areas of knowledge, seeking to meet the needs of society (LA TÉCNICA AL SERVICIO DE LA PATRIA).

New challenges are coming for the National Polytechnic Institute, such as attending to nearshoring in Mexico, that is, the transfer of new factories from the country of origin to one close to the market, which will require research and training of new researchers in the field of semiconductors, for the manufacture of processors or CHIPS. Nanotechnology has and will have an important role in this task, which is why work on semiconductor materials and their applications in luminescence or photoluminescence, optoelectronics will move on to applications on semiconductor substrates and films aimed at manufacturing processors.

IPN researchers should also not neglect their activities aimed at the problems of water, alternative energy, health, food, communications, and the environment, which are still current in terms of the need for improvement and development of new nanometric materials. Therefore, in this volume IV of advances in micro nanoscience and nanotechnology, the results of these investigations are presented and now include an area of materials and semiconductors seeking to develop part of processors.

RED DE NANOCIENCIA
MICRO NANOTECNOLOGÍA DEL
INSTITUTO POLITÉCNICO NACIONAL

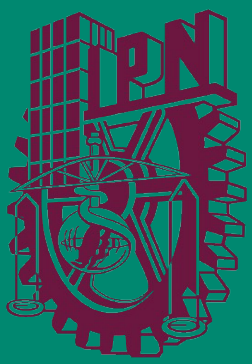

OmniaScience
Monographs

ISBN 978-84-126475-2-5